5-24-2012

The Ultrasonic Characterization of Shear Thickening Suspensions

Benjamin Johnson
Washington University in St. Louis

WASHINGTON UNIVERSITY IN SAINT LOUIS

Department of Physics

Dissertation Examination Committee:

James G. Miller, Chair
R. Martin Arthur
Philip V. Bayly
Mark S. Conradi
Mark R. Holland
Jonathan I. Katz

ULTRASONIC CHARACTERIZATION OF SHEAR THICKENING SUSPENSIONS

by

Benjamin Lenihan Johnson

A dissertation presented to the
Graduate School of Arts and Sciences
of Washington University in
partial fulfillment of the
requirements for the degree
of Doctor of Philosophy

August 2012

Saint Louis, Missouri

.

Abstract

This dissertation describes the characterization of an inherently inhomogeneous medium capable of shear thickening. An aqueous suspension of cornstarch represents an important exemplar of such physical systems. The physics underlying the behavior of such shear thickening suspensions is incompletely understood. Characterization of these suspensions may provide valuable clues into the underlying mechanisms that result in shear thickening behavior. The goal of this thesis is to characterize the acoustic properties of suspensions of cornstarch in density-matched cesium chloride aqueous solutions. A review of the literature indicated that almost no information concerning the ultrasonic characteristics of suspensions of starches had been reported other than studies monitoring the gelatinization of starches not relevant to the shear stiffening of ungelatinized suspensions. Each chapter began with a discussion and validation of the specific experimental techniques and methods of analysis necessary for each type of measurement. Ultrasonic measurement of the group velocity, the frequency-dependent attenuation properties, the frequency-dependent phase velocity, and the frequency-dependent backscatter properties of the suspensions of cornstarch are reported. Initially counterintuitive results including negative (phase velocity) dis-

persion and a decrease in the measured backscatter coefficient with increasing particle concentration are understood in terms of widely accepted physical models. In sum, these studies represent an advancement of the understanding of the physics underlying the interaction between ultrasound and suspensions and lay the groundwork for future studies probing the physics of the shear thickening.

Acknowledgments

I must begin this dissertation by thanking all of those who have made this work possible. I have spent the past several year of my life working in the Laboratory for Ultrasonics at Washington University under the mentorship of Dr. James Miller. Jim has had a profound influence on not only the scientist that I have become but also the person that I have become. Jim has always been there to listen and advise, regardless of whether the issue was a problem with my latest experiment or something more personal. I am lucky to have spent as much time as I have working with Jim.

I would also like to thank Mark Holland for everything that he has done over the past several years for me. Mark is one of the gentlest and most positive people that I know and I have been blessed to work with him as long as I have. His thoughtful advice has led to many a breakthrough in the process of this work and I am eternally indebted to him.

I am also grateful to Dr. Jonathan Katz for all of his help with this work. Jonathan's ideas led to the beginning of this project and provided much of the funding for it. Jonathan's brilliance goes far beyond just ideas though, and he was a constant source of inspiration and creativity throughout the process of this project.

Dr. Scott Handley is also very deserving of my thanks. Scott and I spent many hours together teaching the advanced labs during which time I learned innumerable important lab skills. I also spent my first summer in the lab under Scott's tutelage and the training he provided me was invaluable to all of the work I later completed. Scott has also always been there over the years to provide helpful advice or a word of encouragement when needed.

I also would like to thank all of the graduate postdoctoral students that I have worked with in the lab during my time here. Joe Hoffman especially deserves mention as the two of us worked closely together for several years. Joe was also always there to listen to my confusion and to help me figure out the many problems and issues that arise over the course of graduate school. I also would like to thank Chris Anderson, Adam Bauer, Allyson Gibson, Todd Krueger, Karen Marutyan, Michelle Milne, Chris Lloyd, and Amber Nelson. I truly enjoyed all of the time I spent with all of you and cannot thank you enough for all of your help.

I would also like to thank Hannah Sieber for all of her help with the rheological experiments. She has been a dedicated and enthusiastic experimentalist throughout the project.

The faculty and staff of the physics department have also proved invaluable over the years. Debbie Barco, Julia Hamilton, Sarah Hedley, Christine Monteith, Christina Saldivar, and Tammy White-Devine in the physics office have all helped me through this process in so many ways. Anthony Biondo, Todd Hardt, and Dennis Huelsman in the machine shop were invaluable to so many of the projects that I have worked

on in the lab. Their expertise and brilliance cannot be overstated and the success of many different aspects of my work is directly attributable to their help.

My family has supported me throughout not only graduate school, but my entire life. My parents, Eric Johnson and Patricia Hart, have always been everything I could have asked for as parents. Their continual love and support has allowed me to pursue my dreams and have helped me in every facet of my life. I hope I make them proud in all that I have done and can only hope to someday be exactly the type parent they were for me. My brother, Patrick Johnson, has also been a constant source of support and relief. I truly have to thank you for always being there for me and I hope you are as proud of me as proud as I am of you. I also need to thank my mother-in-law and father-in-law, Gloria and Bud Yanker and my sister-in-law, Maggie Yanker. Since they have come into my life, they have truly adopted me as their own and have taken such good care of me. Whether it's having me over for dinner every Sunday night, or just the countless thoughtful gifts and messages they have sent me I truly am lucky to be a part of their family.

Finally, I want to end by thanking my wife, Dawn. I truly am the luckiest man in the world to be spending the rest of my life with you and you've shown that again and again throughout this process. I love you so much and I can never thank you enough for everything that you've done for me.

Contents

List of Figures

List of Tables

Chapter 1

Introduction

1.1 Background and Motivation

The goal of the research reported in this dissertation is to contribute to the physics underlying the material properties of suspensions that exhibit shear thickening. The mechanisms underlying such shear thickening behavior are an active topic in the current physics literature (Brown *et al.*, 2010; Brown and Jaeger, 2011; Cheng *et al.*, 2011). Ultrasound provides a natural tool for studying suspensions of this sort. Suspensions of corn starch in water represent a useful system in which that underlying physics can be investigated. The ultrasonic characterization of static cornstarch suspensions provides a necessary first step toward using ultrasound to study the physics of suspensions under shear. By first developing a thorough understanding of the ultrasonic properties at rest, a more complete knowledge of the changes in these properties

with shear can be determined.

Materials that shear thin or thicken are of fundamental interest and are also of potential practical value. It is well known that flowing blood, which consists of liquid plasma and (soft-solid) formed elements, can exhibit shear thinning behavior (Chien *et al.*, 1970). Examples of the possible use of shear thickening fluids include their use as a means of capping blown-out oil wells (Beiersdorfer *et al.*, 2011) or as a component in body armor (Lee *et al.*, 2003).

The studies reported in this thesis characterize ultrasonically suspensions of cornstarch in water and in density-matched cesium chloride aqueous solutions over a range of concentrations. The measurements also lay the ground work for future ultrasonic studies.

1.2 Overview of the Dissertation

Chapter 2 consists of two parts, with the first section reviewing the literature involved in ultrasonic characterization of suspensions and slurries and with the second section discussing non-Newtonian fluid behavior, with a focus on shear thickening. The review of the literature examines previous work involving the ultrasonic characterization of suspensions of starch. The current understanding of the mechanisms underlying shear thickening behavior are also highlighted.

Chapter 3 presents a number of experiments that were necessary before the ultrasonic measurements could be completed and discusses the rheological measurements

that have so far been completed on the suspensions of cornstarch. The physical properties of the cornstarch itself, such as its particle size and density, are determined and the reproducibility of the suspension-making process is examined. Qualitative rheological measurements of cornstarch in water, cornstarch in a density-matched cesium chloride solution, and cornstarch in oil are described. The quantitative rheological measurements on suspensions of cornstarch in oil, as opposed to those on cornstarch in water, provide an approach for determining how interactions with the suspending fluid affect the behavior of the suspension.

Chapter 4 discusses the ultrasonic measurements of the group velocity and the sample thickness of a number of concentrations of cornstarch in suspension with both pure water and with a density-matched cesium chloride in water solution. These measurements, although interesting in their own right, were also necessary to permit ultrasonic measurements reported later in the thesis.

Chapter 5 describes the ultrasonic characterization of the attenuation in the cornstarch suspensions. The attenuation coefficient is of fundamental interest and is critical to the determination of the fully-reduced backscatter coefficient. A knowledge of the attenuation in samples is especially important in order to aid in the design of future experiments exploring the ultrasonic characterization of cornstarch suspensions under shear.

Chapters 6 and 7 discuss measurements of the phase velocity in the cornstarch suspensions. The experimental measurements of the dispersion in the phase velocity are not properly accounted for by predictions of dispersion obtained using the

band-limited, approximate Kramers-Kronig relations. In order to account for the negative dispersion measured in the samples, contributions from large resonances in the attenuation coefficient that lie well outside of the experimental bandwidth are required.

Chapter 8 reports the backscatter measurements made on the cornstarch suspensions. The backscatter coefficient was found to decrease as the concentration increased. This somewhat counterintuitive observation is well explained by a theory for determining the backscatter from relatively dense suspensions.

Chapter 9 includes a brief summary and some final remarks.

Bibliography

Beiersdorfer, P., Layne, D., Magee, E., and Katz, J. (**2011**). "Viscoelastic suppression of gravity-driven counterflow instability", Physical Review Letters **106**, 058301.

Brown, E., Forman, N., Orellana, C., Zhang, H., Maynor, B., Betts, D., DeSimone, J., and Jaeger, H. (**2010**). "Generality of shear thickening in dense suspensions", Nature Materials **9**, 220–224.

Brown, E. and Jaeger, H. (**2011**). "Through thick and thin", Science **333**, 1230–1231.

Cheng, X., McCoy, J., Israelachvili, J., and Cohen, I. (**2011**). "Imaging the microscopic structure of shear thinning and thickening colloidal suspensions", Science **333**, 1276–1279.

Chien, S., Usami, S., Dellenback, R., and Gregersen, M. (**1970**). "Shear-dependent deformation of erythrocytes in rheology of human blood", American Journal of Physiology **219**, 136–142.

Lee, Y., Wetzel, E., and Wagner, N. (**2003**). "The ballistic impact characteristics of kevlar woven fabrics impregnated with a colloidal shear thickening fluid", Journal of Materials Science **38**, 2825–2833.

Chapter 2

Background

2.1 Preface

This chapter summarizes the background knowledge necessary to undertake the rest of the studies described in this thesis. The first section of the chapter discusses the structure of a general starch particle. The next section details a number of ultrasonic studies that have already been completed on suspensions of starch and other similar materials. The last section describes in detail the mechanisms behind shear thickening and shear thinning behavior in the context of suspensions of cornstarch.

2.2 Starch

Starch is a storage polysaccharide for many plants and is typically in the form of partially crystalline water-insoluble granules (Lionetto *et al.*, 2006; Singh *et al.*, 2003) The size and the composition of the starch depends upon its source (wheat, rice, corn, etc.). Starch is primarily made up of two polysaccharides known as amylose and amylopectin (Singh *et al.*, 2003). Amylose is primarily a linear polymer that is insoluble in water and makes up anywhere from 15% to 30% of a typical starch (Lionetto *et al.*, 2006). Amylopectin on the other hand is a highly branched macromolecule that is soluble in water and is primarily responsible for the crystallinity of the granules of starch (Lionetto *et al.*, 2006; Singh *et al.*, 2003). A typical starch contains anywhere from 70% to 85% amylopectin.

2.3 Ultrasonic Measurements of Starch in the Literature

Ultrasound has been used to characterize cornstarch (and starches in general) for a number of different applications. The food industry has used ultrasound to examine certain properties of starches and flours for at least 25 years in order to study gelatinization (Lionetto *et al.*, 2006; Aparicio *et al.*, 2009; Letang *et al.*, 2001; Povey and Rosenthal, 1984; Cobus *et al.*, 2007; Garcia-Alvarez *et al.*, 2006; Lehmann *et al.*, 2004; Garcia-Alvarez *et al.*, 2011; Salazar *et al.*, 2002; Alava *et al.*, 2007). The

industry has been focused on the amplitude of the ultrasonic signal and the ultrasonic velocity with some measurements of the attenuation properties. The attenuation properties of very dilute suspensions of cornstarch in water have been measured in order to explore the effect of the porous nature of the particle on the attenuation (Koltsova *et al.*, 2008, 2010). Several papers have examined the flow properties of suspensions of cornstarch using ultrasonic methods (Birkhofer *et al.*, 2004; Ouriev and Windhab, 2003, 2002). Cornstarch has also been used as a scatterer in ultrasonic phantoms (King *et al.*, 2010; Rubin *et al.*, 1991). The effect of high intensity, lower frequency ultrasound on the structure and properties of cornstarch particles has also been studied (Jambrak *et al.*, 2010; Huang *et al.*, 2007). Ultrasound has been used to characterize dense slurries similar to the cornstarch suspensions described in this thesis (Xue *et al.*, 2009; Stolojanu and Prakash, 2001; Sung *et al.*, 2008). Ultrasonic measurements have also been made on other materials that exhibit shear thickening behavior including wormlike micellar fluids (Manneville *et al.*, 2008; Gladden *et al.*, 2010).

2.3.1 Ultrasonic Characterization of Slurries

Ultrasound has been used to characterize the properties of slurries containing solids suspended in a liquid. A slurry can be defined as a thick suspension of solids in a liquid (Stolojanu and Prakash, 2001). Although none of the research in the field has been directly applied to cornstarch suspensions, the measurement techniques employed are similar to those described in this thesis, so several relevant papers

will be highlighted. Slurry systems of glass beads in water with diameters ranging from 35 μm to 180 μm with concentrations of up to 45% have been ultrasonically characterized (Stolojanu and Prakash, 2001). Specifically, the attenuation coefficient and the velocity were measured as a function of glass bead concentration in these slurry systems (Stolojanu and Prakash, 2001). Another application of ultrasonic characterization of slurries was in the investigation of dense coal-water slurries with concentrations of up to 30% (Xue *et al.*, 2009). Ultrasonic measurements of the attenuation have also been used to characterize suspensions of kaolin and reservoir sediments in water (Sung *et al.*, 2008). Additional work in this field led to the proposal of a theory for estimating the ultrasonic attenuation and backscatter for suspended sand particles in the ocean (Thuraisingham, 1994).

2.3.2 Applications of Ultrasound in the Food Industry

The use of ultrasound in the food industry has led to several relevant studies of suspensions of starch particles. Lehmann et al. made three 25% suspensions of starch and water using cornstarch, rice starch, and wheat starch (Lehmann *et al.*, 2004). A 2% cornstarch-water suspension was also investigated. The ultrasonic velocity and attenuation were measured over a temperature range of 37 °C to 95 °C in order to characterize the gelatinization of the starches (Lehmann *et al.*, 2004). The measurements were made using a HR-US 101 ultrasonic spectrometer (Ultrasonic Scientific Ltd., Dublin) at frequencies of 4.5 MHz, 7.6 MHz, and 11.0 MHz (Lehmann *et al.*, 2004). Both the ultrasonic velocity and ultrasonic attenuation were presented on a

relative scale to help aid in the determination of several critical temperatures in the starch gelatinization process (Lehmann *et al.*, 2004). Another study monitored the gelatinization of a 15% cornstarch-water suspension and a 20% cornstarch-water suspension using a 1 MHz through transmission setup (Aparicio *et al.*, 2009). This study measured the amplitude of the ultrasonic signal as a function of temperature to determine the critical temperatures in the gelatinization of the cornstarch. Both of these studies focus only on cornstarch in water suspensions and only measured ultrasonic parameters at a few concentrations of cornstarch at a few frequencies. The investigations in this thesis represent an attempt to conduct a thorough and systematic study of the ultrasonic properties of cornstarch suspensions.

Ultrasound has also frequently been used to study the degradation of starch over time in order to determine the best methods of storage. One study used a 10 MHz transducer to measure the ultrasonic velocity and attenuation of a 66% suspension of wheat starch in water over a period of several days (Lionetto *et al.*, 2006). The authors found that as the wheat starch suspension was stored and slowly gelatinized, the ultrasonic velocity of the suspension increased continuously before eventually leveling off, while the ultrasonic attenuation increased initially before decreasing (Lionetto *et al.*, 2006). Another study measured the ultrasonic velocity and attenuation of a 5% suspension of wheat starch in water as the starch was being degraded by an enzyme (Povey and Rosenthal, 1984). As the enzyme degraded the suspension, the ultrasonic attenuation was found to decrease, while the ultrasonic velocity did not change appreciably (Povey and Rosenthal, 1984). A number of papers characterize

wheat flours and doughs by measuring their ultrasonic velocity and attenuation (Alava *et al.*, 2007; Garcia-Alvarez *et al.*, 2006, 2011; Letang *et al.*, 2001; Salazar *et al.*, 2002). One of the most relevant examples of these wheat flour studies used two 100 kHz transducers in a transmission setup to study the ultrasonic velocities and attenuations of 35 different wheat flours in water solutions (Garcia-Alvarez *et al.*, 2011). The study found that ultrasonic velocity and attenuation at these low frequencies could be used to differentiate between the different types of wheat flour doughs (Garcia-Alvarez *et al.*, 2011). Flour is distinct from starch, because it contains not only starch (made up entirely of starch polymers), but also gluten (Garcia-Alvarez *et al.*, 2011). Additionally, all of these studies looked at much more concentrated suspensions of flour in water than any of the suspensions studied in this thesis.

2.3.3 Attenuation Measurements in Dilute Cornstarch Suspensions

Two conference proceedings from the Russian Acoustical Society also ultrasonically characterized suspensions of cornstarch (Koltsova *et al.*, 2008, 2010). In the first study, the authors examined the ultrasonic attenuation at 3 MHz of 0.5% and 1.0% suspensions of cornstarch in water (Koltsova *et al.*, 2008). The authors were interested in modeling theoretically the ultrasonic attenuation in the cornstarch suspensions. They took into account the typical contributions to the attenuation from longitudinal-to-longitudinal scattering, thermal forces, and viscous relative motion.

An additional term was included that was due to the excess attenuation of porous particles resulting from dissipation due to the infiltration of water into the pores and the potential gradient that could be produced (Koltsova *et al.*, 2008). The study measured the attenuation as a function of time in an attempt to tease out the contribution to the attenuation from the porous dissipation term. The usual contributions to the attenuation do not change appreciably as a function of time, whereas the attenuation due to the porous dissipation would increase as more and more water made its way into the pores of the cornstarch particles (Koltsova *et al.*, 2008). The authors concluded that the contributions to the attenuation from this porous dissipation was a large enough effect that it could not be neglected or ignored when modeling theoretically the ultrasonic attenuation in porous particles (Koltsova *et al.*, 2008).

The second study from these authors measured the ultrasonic attenuation at 3 MHz in a 3% cornstarch-water suspension over a temperature range of 20 °C to 70 °C (Koltsova *et al.*, 2010). The cornstarch particles undergo an irreversible expansion when heated above a specific temperature, and this study used measurements of the ultrasonic attenuation to map out at what temperature that transition occurs (Koltsova *et al.*, 2010). Both of these studies made measurements of the ultrasonic attenuation in cornstarch suspensions, but the studies were done on much more dilute suspensions of cornstarch than those studied in this thesis. Additionally, the cornstarch suspensions detailed in these two papers were in water rather than in a density-matched aqueous solution.

2.3.4 Ultrasonic Monitoring of Fluid Flow

Another common use of ultrasound to investigate starches involves Doppler ultrasound measurements that study the rheometry of flowing liquids (Birkhofer *et al.*, 2004; Ouriev and Windhab, 2002, 2003). One study used this technique to measure the acoustic sound speed and ultrasonic signal amplitude for a 10% cornstarch suspension in a sucrose solution, silicone oil, and rapeseed oil (Birkhofer *et al.*, 2004). The study found that ultrasonic velocity in a fluid increased modestly with the addition of the cornstarch, but did not further explore the results (Birkhofer *et al.*, 2004). Another study used an ultrasonic pulse echo Doppler pressure difference technique to measure some of the rheological properties of a flowing starch in glucose suspension (Ouriev and Windhab, 2002)

Ultrasonic velocimetry is an ultrasonic technique already in use in the rheometry of complex fluids (Manneville *et al.*, 2008; Manneville, 2008; Gladden *et al.*, 2010). One application of this technique uses an ultrasonic transducer with a center frequency of 36 MHz to acquire backscattered signals from fluid in a rheometer with Couette geometry (Manneville, 2008). The ultrasonic speckle measured in the signals is cross-correlated over successive acquisitions in order to measure the displacement of the scatterers at various positions along the beam (Manneville, 2008). The technique (known as ultrasonic speckle velocimetery or ultrasound velocity profiling) has a spatial resolution of 40 μm and a temporal resolution between 20 ms and 2 s depending on the measurement (Manneville, 2008). Variations of the method have already been

used to study shear-thickening wormlike micelles and concentrated emulsions (Becu *et al.*, 2006, 2007).

2.3.5 Cornstarch in Ultrasonic Phantoms

Cornstarch particles have also been used as scatterers in clinical ultrasonic phantoms (King *et al.*, 2010; Rubin *et al.*, 1991). In both of these studies the cornstarch particles were used simply as scatterers to increase the backscattered ultrasonic signal. The ultrasonic properties of the cornstarch phantoms were not characterized in any systematic way.

2.3.6 Summary of Literature

The applications of ultrasonic measurements of starches appears to be very wide-ranging. However, a systematic characterization of the ultrasonic properties of cornstarch suspensions does not seem to have ever been completed. A thorough understanding of these properties may help to better understand the interesting and somewhat complicated physics that underlies these suspensions.

2.4 Basic Rheology

A fluid whose stress vs. strain rate curve is linear and passes through the origin is known as a Newtonian fluid (Kleinstreuer, 2010). The constant of proportionality between the stress and the strain curve is known as viscosity (Kleinstreuer, 2010).

Water is the most common example of a Newtonian fluid. Newtonian fluids will flow regardless of the forces acting upon them. A Bingham plastic is a material that exhibits Newtonian flow once a certain stress level is reached, but behaves as a solid below that level (Kleinstreuer, 2010). A common example of a Bingham plastic is toothpaste.

Fluids that do not have a linear stress vs. strain curve can display either shear thinning or shear thickening behavior (Brown and Jaeger, 2011). For shear thinning fluids, the viscosity decreases as the shear rate (or shear stress) increases, whereas in shear thickening fluids the viscosity increases as the shear rate (or shear stress) increases (Brown and Jaeger, 2011). Common examples of fluids that exhibit shear thinning are latex paint and ketchup, and a common example of a shear thickening fluid is a cornstarch in water suspension. Many suspensions display different flow behaviors depending on the shear rate (or shear stress) applied to the system displaying shear thinning behavior over one range of shear rates, Newtonian behavior over another, and shear thickening over a third (Brown and Jaeger, 2011). The response of a particular suspension depends on the sum of the stress contributions in that range of shear rates (Brown and Jaeger, 2011).

The cornstarch suspensions discussed in this thesis fall under the definition of a suspension: a heterogeneous mixture of a liquid with particles that are large enough to settle (Brown and Jaeger, 2010). In contrast, colloids have particles smaller than those that make up suspensions that will not settle out over time (Brown and Jaeger, 2010). In terms of particle diameter, the transition between a mixture being char-

acterized as a suspension or a colloid usually occurs when the particles are on the order of a micron (Brown and Jaeger, 2010). The particles in a suspension can separate out through a number of different mechanisms. Sedimentation typically occurs when the particles are denser than the suspension and settle to the bottom over time (Hunter, 2001). Creaming is the opposite of sedimentation in that the particles are typically less dense than the suspension and will rise to the top of the suspension over time (Hunter, 2001). Flocculation occurs when the particles are attracted together reversibly (the particles do not necessarily combine into larger particles, but stay as separate entities) (Hunter, 2001). Coalescence involves the particles coming together irreversibly to form larger particles (Hunter, 2001). In the case of the cornstarch suspensions, the main mechanism by which the particles separate out of the suspension is sedimentation, because the cornstarch granules are much more dense than water.

2.4.1 Shear Thinning

A material displays shear thinning behavior if the dominant stress in the system at low shear rates does not increase with shear as fast as the Newtonian viscous stress (Brown and Jaeger, 2011). Shear thinning can result from particle rearrangements (such as the particles organizing into layers so that they can slide over each other more easily) or from interparticle interactions (such as attractive forces between particles) (Brown and Jaeger, 2011). The magnitude of shear thinning due to interparticle interactions is typically larger than the magnitude of shear thinning that results from particle rearrangements (Brown and Jaeger, 2011). In a paper published in Science,

Cheng et al. studied the shear thinning behavior of a colloidal suspension of silica spheres of diameters of approximately a micron in a water-glycerin mixture (Cheng *et al.*, 2011). The shear thinning behavior in the system was due to the sum of a constant Newtonian contribution from the viscous stresses in the system and an entropic contribution from the pressure produced when thermal motion causes the particles to collide (Cheng *et al.*, 2011). For soft glassy materials, shear thinning can be understood in terms of the the free energy landscape of the system (Fall *et al.*, 2008). When the fluid is sheared, the shearing pulls it over energy barriers that the fluid would not otherwise be able to cross (Fall *et al.*, 2008). Crossing these energy barriers lowers the viscosity in the fluid (Fall *et al.*, 2008).

2.5 Shear Thickening

Shear thickening fluids display the opposite property of shear thinning fluids in that in shear thickening fluids the viscosity increases as the shear rate (or shear stress) increases (Brown and Jaeger, 2010). Similar to shear thinning behavior, shear thickening can be due to either particle rearrangements or to more complicated mechanisms. In the Cheng et al. paper, the shear thickening evident at higher shear rates in the colloidal suspension studied was due to the formation of hydroclusters (clusters of particles brought together by shear) (Cheng *et al.*, 2011). The shear thickening found in this system was modest when compared to shear thickening found in some other systems (such as cornstarch in water), and thus the mechanism for the shear

thickening behavior may be different in other systems (Cheng *et al.*, 2011; Brown and Jaeger, 2011). Shear thickening behavior can be generally classified into two subgroups: continuous shear thickening and discontinuous shear thickening (Brown and Jaeger, 2010).

2.5.1 Continuous Shear Thickening

Continuous shear thickening occurs when the viscosity increases with increasing shear rate, but not the orders of magnitude increase seen with some shear thickening fluids (Brown and Jaeger, 2010). Continuous shear thickening is not as dependent on packing fraction as discontinuous shear thickening (Brown and Jaeger, 2010). Continuous shear thickening behavior was seen in the colloidal suspension studied by Cheng et al. and attributed to the formation of hydroclusters (Cheng *et al.*, 2011). Fall et al. also studied a suspension of 40 micron polystyrene beads in a density-matched solution at a volume fraction of 59% that displayed continuous shear thickening behavior (Fall *et al.*, 2010). Interestingly, the suspension displayed a transient, much steeper shear thickening initially that was attributed to a shear-induced particle migration (Fall *et al.*, 2010). After the system had rearranged in this way though, a smaller, continuous shear thickening was consistently observed in the system (This presumably represents the steady state behavior of the system) (Fall *et al.*, 2010). In this system, as the shear rate was increased for a fixed volume fraction, the material transitioned from a viscous behavior (where the shear stress was proportional to the shear rate) to a shear thickening, Bagnoldian behavior (in which the shear stress is

proportional to the shear rate squared) (Fall *et al.*, 2010). In this Bagnoldian regime where the shear stress goes as the shear rate squared, grain inertia dominates over viscous forces and the continuous shear thickening is attributed to a behavior similar to the formation of the hydroclusters found in the Cheng et al. paper (Fall *et al.*, 2010). Cornstarch in water (or in a density-matched solution) does not display continuous shear thickening, but instead displays what is termed discontinuous shear thickening.

The Reynolds number of a fluid is the ratio of the inertial forces to the viscous forces in that fluid under a given flow condition (Brown and Jaeger, 2010). At high Reynolds number, the inertial forces are dominant and can lead to weak shear thickening in a system (Brown and Jaeger, 2010). Brown and Jaeger indicate that the steepest possible scaling for shear thickening due to these inertial effects is that the shear stress goes as the shear rate squared (the Bagnoldian regime) and thus the discontinuous shear thickening found in cornstarch suspensions in water (and other suspensions and colloids) must be due to some other mechanism (Brown and Jaeger, 2010). Brown et al. tested this idea by making viscosity measurements on a suspension of cornstarch in a viscous glycerol-water mixture. The viscosity in the fluid was approximately 80 times higher than water (Brown and Jaeger, 2010). In these suspensions, almost no shear thickening was found at low packing fractions (below 40%), but discontinuous shear thickening was still seen in suspensions at higher packing fractions. Thus, high Reynolds number flow is a separate phenomena from discontinuous shear thickening (Brown and Jaeger, 2010).

2.5.2 Discontinuous Shear Thickening

Discontinuous shear thickening can be characterized by stress scales, a diverging slope, and reversibility (Brown and Jaeger, 2010). One basic property of discontinuous shear thickening is that the boundaries of the shear thickening regime can be more easily defined in terms of stress rather than shear rate. This definition is convenient because stress is largely independent of packing fraction and the viscosity of the liquid (Brown and Jaeger, 2010). The stress at the onset of shear thickening for a particular system, τ_{min}, is defined as the onset of a positive slope in the viscosity as a function of shear stress. The maximum stress at which the system will display shear thickening, τ_{max}, is defined as the point where the slope of the viscosity as a function of shear stress transitions from positive to negative (Brown and Jaeger, 2010). Thus, for a particular system, τ_{min} and τ_{max} are consistent across different packing fractions and liquid viscosities. Another defining characteristic of discontinuous shear thickening fluids is the increase in the viscosity by orders of magnitude at the onset of shear thickening (Brown and Jaeger, 2010). This steep increase is only found for a small range of packing fraction and lessens considerably as the packing fraction decreases (Brown and Jaeger, 2010). The last defining characteristic of discontinuous shear thickening is that the thickening is reversible (the viscosity will be approximately the same whether the stress is ramped up or down) (Brown and Jaeger, 2010). Some examples of discontinuous shear thickening are transient (such as the suspension studied by Fall et al.), although these examples of discontinuous shear thickening may be due to

a different mechanism (Fall *et al.*, 2010).

Cornstarch suspensions exhibit discontinuous shear thickening. The mechanism of this discontinuous shear thickening in cornstarch suspensions (and in suspensions and colloids in general) is dependent on three characteristics of the system (Brown and Jaeger, 2010). The first property is that the particles must dilate when sheared. Dilatancy occurs because of collisions among the particles that cause the particles to roll over each other in order to flow (Fall *et al.*, 2008). For the particles to be able to roll over each other, the system must expand (dilate) in the direction of the gradient (Fall *et al.*, 2008). Dilation will typically only occur at a high packing fraction that is close the jamming transition for the suspension (Brown and Jaeger, 2010). The second critical characteristic that a system needs in order to display discontinuous shear thickening is a confining stress that produces a strain-dependent restoring force against the dilation of the system (Brown and Jaeger, 2010). This confining stress frequently comes from the surface tension of the fluid, but can also come from the walls surrounding the system or the particle stiffness itself (Brown and Jaeger, 2010; Fall *et al.*, 2008). The final characteristic necessary for discontinuous shear thickening is that this confining stress must be large enough to exceed all of the stresses within the system that could prevent shearing and dilation (such as interparticle interactions and the pressure due to gravity) (Brown and Jaeger, 2010). In the case of a cornstarch suspension, if the cornstarch particles are confined by the surface tension of the liquid, then the grains cannot move over each other to flow, potentially leading to a jamming of the system and discontinuous shear thickening (Fall *et al.*, 2008). Shear flow can

occur if the system is unconfined, because the suspension can expand and reduce the effective packing fraction (Fall *et al.*, 2008). If the stress from the confining stress is not dominant, then the stress increase from dilation will not be enough to result in discontinuous shear thickening (Brown and Jaeger, 2010).

2.5.3 Jamming Transitions

"Jamming" is a term for describing when frictional contact among particles prevents them from flowing like a fluid (Becu *et al.*, 2006). Jamming can occur if the system increases its volume fraction, lowers its temperature, or releases some external stress (Becu *et al.*, 2006). Jammed materials respond to stress differently depending on whether the external stress is above or below the yield stress of the system (Becu *et al.*, 2006). If the stress is below the yield stress, then the system remains jammed and responds elastically like a solid (Becu *et al.*, 2006). If the stress is above the yield stress, then the system flows like a liquid (Becu *et al.*, 2006). For stresses close to this yield stress, some systems will not flow at a uniform shear rate. Instead shear banding (also known as shear localization) occurs where part of the system flows while another part of the system remains in a jammed state (Becu *et al.*, 2006). As the shear rate is increased, more and more of the system begins to flow until eventually the entire suspension is flowing (Becu *et al.*, 2006).

Suspensions of cornstarch in water (or a density-matched liquid) display this jamming behavior (Fall *et al.*, 2008). At rest (no shearing), the cornstarch suspension has a small yield stress and thus behaves like a solid (Fall *et al.*, 2008). For a low shear

rate, the shear banding behavior described above will occur with more and more of the suspension flowing as the shear rate increases (Fall *et al.*, 2008). After the shear rate is high enough that all of the suspension is flowing, the material will suddenly become solid again, because the dilation in the grains and confinement of the system, and significant shear thickening will be observed (Fall *et al.*, 2008). To summarize, at low shear rates the shearing first "unjams" a jammed system by overcoming the yield stress (Fall *et al.*, 2008). As the stress increases eventually the shearing causes the unjammed, flowing suspension to jam because of the dilatant behavior of the cornstarch and the confinement of the surface tension in the system (Fall *et al.*, 2008).

2.5.4 Confining Stresses

The surface tension in the fluid is an important confining stress for many discontinuous shear thickening systems with high packing fractions. The surface tension produces normal stresses between the particles and the walls of the system that result in a shear stress due to friction (Brown and Jaeger, 2010). The confining stress due to surface tension was found to increase as the dilation in the system increases (Brown and Jaeger, 2010). The surface tension is an effective confining stress only if the particles in the system are densely packed (Brown and Jaeger, 2010). In this case, some of the particles are pushed out of the interior of the suspension and penetrate the edge of the suspension creating a curved liquid-air interface (Brown and Jaeger, 2010). This produces a stress from surface tension on the particles that scales with the particle diameter and pushes them back toward the inside of the suspension

(Brown and Jaeger, 2010). However, the tightly packed particles cannot be pushed back into the interior of the suspension (Brown and Jaeger, 2010). One potential way for the stress from the surface tension to be transmitted through the rest of the suspension is through a force chain (Brown and Jaeger, 2010).

Another characteristic of aqueous suspensions of granules is the transmission of stress through force chains (Liu *et al.*, 2010; Mueth *et al.*, 1998). Force chains were first observed in dry, granular media (Mueth *et al.*, 1998). A homogeneous solid would transmit an external stress through elastic deformation or plastic yield, whereas in a Newtonian liquid viscous dissipation would cause resistance in the fluid (Liu *et al.*, 2010). In an aqueous suspension of a granular medium on the other hand, the force is transmitted heterogeneously in a branching, chain-like way (Liu *et al.*, 2010). In contrast to viscous liquids which will dissipate an applied force throughout the medium, in these types of media the force is not dissipated throughout the medium, but is instead only distributed to an area on the scale of the size of the object which applied it (Liu *et al.*, 2010; Brown and Jaeger, 2009).

The importance of surface tension as a confining stress to discontinuous shear thickening suspensions was investigated by Brown et al. using a suspension of 100 micron diameter glass spheres in water at a packing fraction of 0.56 (below the critical packing fraction for this system) (Brown and Jaeger, 2010). The critical packing fraction is defined as the packing fraction at which the viscosity curve diverges because the system is jammed (Brown and Jaeger, 2009). The viscosity as a function of shear stress was measured in this system and then the measurement was repeated after

a surfactant was mixed in that decreased the surface tension in the system by a factor of approximately 3 (Brown and Jaeger, 2010). The maximum stress of shear thickening was found to decrease by a factor of about 2.4, a value that was was very close to the decrease found in the surface tension (Brown and Jaeger, 2010). Thus, the confining stress in this system was found to determine the upper stress limit of the shear thickening regime.

2.5.5 The Onset of Shear Thickening

The onset shear stress for shear thickening depends on the the size of the particles in the suspension of interest. If the particles are very small (creating a colloid because the particles won't settle out), then the onset stress for shear thickening is determined by the effects of Brownian motion and electrostatic interactions (Brown *et al.*, 2010). If on the other hand the particles are larger (suspensions), then gravity is the dominant effect in determining the level of the onset stress (Brown and Jaeger, 2010). In both cases, the onset of shear thickening can only occur if the shear stress is large enough to exceed the local stress barriers holding the particles in place. Once the stress is large enough to overcome these barriers, the particles begin to shear; this leads to dilation and increased confining stresses resulting in shear thickening (Brown and Jaeger, 2010). Shear thickening behavior is hidden until the stresses relevant to shear thickening are the dominant stress in the system (Brown and Jaeger, 2010). Because of this, many systems do not appear to exhibit shear thickening behaviors.

Brown et al. examined a suspension of glass spheres of diameter 90 microns with

a hydrophobic coating in water where the onset of shear thickening was hidden by interparticle interactions (Brown *et al.*, 2010). In a suspension of water, the coating on the spheres causes them to cluster (Brown and Jaeger, 2010). These clusters resist flow and require a significant stress in order to be pulled apart (resulting in a yield stress). If the viscosity of the system as a function of shear stress is measured for this system, no shear thickening behavior is observed (Brown and Jaeger, 2010). However, if a surfactant is added to the system eliminating the particle clustering (and thus the yield stress), then the suspension will display shear thickening behavior over a range of shear stresses. This is just one example of a system where the shear thickening behavior was hidden by some other stress. Brown et al. also examined dielectric glass spheres in mineral oil and magnetite-filled polyethylene glycol-acrylate rods suspended in polyethylene glycol. These materials were chosen because the attractions between these particles could be tuned depending on the strength of the external field (an electric field in the case of the former suspension and a magnetic field in the case of the latter suspension) (Brown and Jaeger, 2010). As the interparticle attractions increased, the yield stress in the suspensions increased which caused the shear thickening behavior to only be apparent over a smaller and smaller shear stress range (Brown and Jaeger, 2010). The attractions between the particles could even be increased to the point where no shear thickening behavior was evident. Although cornstarch particles do not display these large interparticle attractions, similar behavior was found in a suspension of cornstarch in water where the yield stress of the system was increased due to confinement as the packing fraction was increased (Brown

and Jaeger, 2010). The packing fraction could eventually be increased to the point where the whole system was jammed and no shear thickening behavior was apparent in the suspensions of cornstarch and water. Thus, the onset stress for shear thickening can be strongly dependent on the other stresses in the system whether they are from interparticle interactions, confinement, or some other mechanism (Brown and Jaeger, 2010).

For suspensions of larger particles, the stresses due to gravity are often the dominant stress in the system and thus determine the onset stress for shear thickening behavior (Brown and Jaeger, 2010). The stress due to gravity can be understood in the context of a system of glass spheres being measured using a parallel plate rheometer setup. If the system is not being sheared, then the particles will settle to the bottom plate due to gravity (Brown and Jaeger, 2010). At low shear stresses, the stress measured in the system would be due solely to flow of a thin fluid layer on top of the settled particles. If the shear stress is increased to the point that it exceeds the frictional force between the particles under gravity, then the upper layer of particles can be moved and the system begins to flow (Brown and Jaeger, 2010). This frictional force between the particles under gravity leads to the yield stress in the system. Density-matching the fluid to the particles in the system can lower the onset stress due to gravity (Brown and Jaeger, 2010).

The transition between the regime where the Brownian motion and interparticle interactions dominate and the regime where gravity dominates typically occurs at a diameter of approximately 10 μm (Brown and Jaeger, 2010). The specific particle

diameter at which the transition occurs depends on a number of factors such as the density of the particles, the type and size of the interparticle interactions, etc., but for a general system the transition between the two regimes occurs at a diameter on the order of 10 μm (Brown and Jaeger, 2010). As a result of this transition, the minimum stress required for shear thickening is lowest for particles of approximately this size (Brown and Jaeger, 2010). Interestingly, particles of this diameter are approximately at the transition point between a colloid and a suspension, thus the transition between a colloid and a suspension and the transition between where interparticle interactions are the dominant stresses and where gravity is the dominant stress may be related (Brown and Jaeger, 2010).

Cornstarch granules have a diameter very close to the optimal diameter for shear thickening. Cornstarch particles are also very hydrophilic, resulting in minimal particle-liquid surface tension (Brown and Jaeger, 2010). Minimizing particle-liquid surface tension decreases the shear thinning effect (Brown and Jaeger, 2010). Cornstarch suspensions display strong shear thickening behavior because of both the cornstarch granule's size and lack of interactions which result in shear thinning.

2.6 Conclusion

The discontinuous shear thickening behavior found in suspensions of cornstarch in water is due to the dilation of the grains under shear, the confining stress of the surface tension of the suspension, and the dominance of this confining stress over a

range of shear stresses. In general, the lowest stress that the stresses in the system must exceed to exhibit shear thickening is set by either interparticle interactions (for most colloids and some suspensions) or gravity (for many suspensions) (Brown and Jaeger, 2010). The maximum stress at which the system will exhibit shear thickening is set by surface tension (or other confining stress) and decreases with particle size. Brown and Jaeger indicate that a general framework for understanding the mechanisms behind discontinuous shear thickening (and other types of flow behaviors) exists, but much more work needs to be completed before the mechanisms can be completely understood. The hypothesis underlying this thesis is that ultrasonic attenuation and scattering could provide information about grain-grain contacts, force chains, and other interactions between particles in suspensions under shear. Thus, studying the ultrasonic characteristics of a cornstarch suspension under shear may serve to enhance the understanding of these complex phenomena.

Bibliography

Alava, J., Sahi, S., Garcia-Alvarez, J., Turo, A., Chavez, J., Garcia, M., and Salazar, J. (**2007**). "Use of ultrasound for the determination of flour quality", Ultrasonics **46**, 270–276.

Aparicio, C., Resa, P., Molina-Garcia, A., Martino, M., and Sanz, P. (**2009**). "Assessment of starch gelatization by ultrasonic and calorimetric techniques", Journal of Food Engineering **94**, 295–299.

Becu, L., Anache, D., Manneville, S., and Colin, A. (**2007**). "Spatio-temporal dynamics of wormlike micelles under shear", Physical Review E **76**, 011503.

Becu, L., Manneville, S., and Colin, A. (**2006**). "Yielding and flow in adhesive and nonadhesive concentrated emulsions", Physical Review Letters **96**, 138202–1 – 138202–4.

Birkhofer, B., Jeelani, S., Ouriev, B., and Windhab, E. (**2004**). "In-line characterization and rheometry of concentrated suspensions using ultrasound", Proceedings of the Ultrasonic Doppler Method for Fluid Mechanics and Fluid Engineering Symposium 65–68.

Brown, E., Forman, N., Orellana, C., Zhang, H., Maynor, B., Betts, D., DeSimone, J., and Jaeger, H. (**2010**). "Generality of shear thickening in dense suspensions", Nature Materials **9**, 220–224.

Brown, E. and Jaeger, H. (**2009**). "A dynamic jamming point for shear thickening suspensions", Phys Rev Lett **103**, 086001.

Brown, E. and Jaeger, H. (**2010**). "The role of dilation and confining stresses in shear thickening of dense suspensions", arXiv:1010.4921v1 1–43.

Brown, E. and Jaeger, H. (**2011**). "Through thick and thin", Science **333**, 1230–1231.

Cheng, X., McCoy, J., Israelachvili, J., and Cohen, I. (**2011**). "Imaging the microscopic structure of shear thinning and thickening colloidal suspensions", Science **333**, 1276–1279.

Cobus, L., Ross, K., Scanlon, M., and Page, J. (**2007**). "Comparison of ultrasonic velocities in dispersive and nondispersive food materials", Journal of Agriculture and Food Chemistry **55**, 8889–8895.

Fall, A., Huang, N., Bertrand, F., Ovarlez, G., and Bonn, D. (**2008**). "Shear thickening cornstarch suspensions as a reentrant jamming transition", Physical Review Letters **100**, 018301–1 – 018301–4.

Fall, A., Lemaitre, A., Bertrand, F., Bonn, D., and Ovarlez, G. (**2010**). "Shear thickening and migration in granular suspensions", Physical Review Letters **105**, 238303.

Garcia-Alvarez, J., Alava, J., Chavez, J., Turo, A., Garcia, M., and Salazar, J. (**2006**). "Ultrasonic characterization of flour-water systems: a new approach to investigate dough properties", Ultrasonics **44**, e1051–e1055.

Garcia-Alvarez, J., Salazar, J., and Rosell, C. (**2011**). "Ultrasonic study of wheat flour properties", Ultrasonics **51**, 223–228.

Gladden, J., Skelton, C., and Mobley, J. (**2010**). "Shear waves in viscoelastic wormlike micellar fluids", JASA Express Letters **128**, EL268–EL273.

Huang, Q., Li, L., and Fu, X. (**2007**). "Ultrasound effects on the structure and chemical reactivity of cornstarch granules", Starch **59**, 371–378.

Hunter, R. (**2001**). *Foundations of colloid science*, 2nd edition (Oxford).

Jambrak, A., Herceg, Z., Subaric, D., Babic, J., Brncic, M., Brncic, S., Bosiljkov, T., Cvek, D., Tripalo, B., and Gelo, J. (**2010**). "Ultrasound effect on physical properties of corn starch", Carbohydrate Polymers **79**, 91–100.

King, D., Hangiandreou, N., Tradup, D., and Stekel, S. (**2010**). "Evaluation of a low-cost liquid ultrasound test object for detection of transducer artefacts", Physics in Medicine and Biology **55**, N557–N570.

Kleinstreuer, C. (**2010**). *Modern fluid dynamics: basic theory and selected applications in macro and micro-fluidics* (Springer).

Koltsova, I., Deinega, M., and Polukhina, A. (**2008**). "Attenuation of ultrasound waves in suspensions of porous particles", Proceedings of the Russian Acoustical Society 328–331.

Koltsova, I., Polukhina, A., and Deynega, M. (**2010**). "Reversible and irreversible processes in biocomposites", Proceedings of the Russian Acoustical Society 301–303.

Lehmann, L., Kudryashov, E., and Buckin, V. (**2004**). "Ultrasonic monitoring of the gelatinisation of starch", Progr Colloid Polym Sci **123**, 136–140.

Letang, C., Piau, M., Verdier, C., and Lefebvre, L. (**2001**). "Characterization of wheat-flour-water doughs: a new method using ultrasound", Ultrasonics **39**, 133–141.

Lionetto, F., Maffezzoli, A., Ottenhof, M., Farhat, I., and Mitchell, J. (**2006**). "Ultrasonic investigation of wheat starch retrogradation", Journal of Food Engineering **75**, 258–266.

Liu, B., Shelley, M., and Zhang, J. (**2010**). "Focused force transmission through an aqueous suspension of granules", Physical Review Letters **105**, 188301–1 – 188301–4.

Manneville, S. (**2008**). "Recent experimental probes of shear banding", Rheol Acta **47**, 301–318.

Manneville, S., Becu, L., and Colin, A. (**2008**). "High-frequency ultrasonic speckle velocimetry in sheared complex fluids", Eur Phys. J. AP **28**, 361–373.

Mueth, D., Jaeger, H., and Nagel, S. (**1998**). "Force distribution in a granular medium", Physical Review E **57**, 3164–3169.

Ouriev, B. and Windhab, E. (**2002**). "Rheological study of concentrated suspensions in pressure driven shear flow using a novel inline ultrasound doppler method", Journal of Experiments in Fluids **32**, 204–211.

Ouriev, B. and Windhab, E. (**2003**). "Novel ultrasound based time averaged flow mapping method for die entry visualization in flow of highly concentrated shear-thinning and shear-thickening suspensions", Measurement of Science and Technology **14**, 140–147.

Povey, M. and Rosenthal, A. (**1984**). "Technical note: ultrasonic detection of the degradation of starch by alpha-amylase", Journal of Food Technology **19**, 115–119.

Rubin, J., Adler, R., Bude, R., Fowlkes, J., and Carson, P. (**1991**). "Clean and dirty shadowing at us: A reappraisal", Radiology **181**, 231–236.

Salazar, J., Alava, J., Sahi, S., Turo, A., Chavez, J., and Garcia, M. (**2002**). "Ultrasound measurements for determining rheological properties of flour-water systems", IEEE Ultrasonics Symposium Proceedings 877–880.

Singh, N., Singh, J., Kaur, L., Sodhi, N., and Gill, B. (**2003**). "Morphological, thermal, and rheological properties of starches from different botancial sources", Food Chemistry **81**, 219–231.

Stolojanu, V. and Prakash, A. (**2001**). "Characterization of slurry systems by ultrasonic techniques", Chemical Engineering Journal **84**, 215–222.

Sung, C., Huang, Y., Lai, J., and Hwang, G. (**2008**). "Ultrasonic measurement of suspended sediment concentrations: an experimental validation of the approach using kaolin suspensions and reservoir sediments under variable thermal conditions", Hydrological Processes **22**, 3149–3154.

Thuraisingham, R. (**1994**). "Theoretical estimates of high frequency acoustic attenuation and backscattering from suspended sand particles in the ocean and in an estuary", DSTO Aeronautical and Maritime Research Laboratory 1–16.

Xue, M., Su, M., Dong, L., Shang, Z., and Cai, X. (**2009**). "An investigation on characterizing dense coal-water slurry with ultrasound: theoretical and experimental method", Chemical Engineering Communications **197**, 169–179.

Chapter 3

Preliminary Studies

3.1 Preface

This chapter begins with an investigation of the cornstarch granule size using an optical microscope. The next section describes the efforts to use cesium chloride solutions to density match the cornstarch particles in suspension and the steps taken to characterize the cesium chloride solution. The procedure necessary for the creation of the cornstarch in density-matched cesium chloride suspensions is outlined. The details of the sample mold used for the ultrasonic measurements described later in the thesis are described. The next section details the studies completed examining the reproducibility of the experiments among samples and over time. The second part of the chapter describes some preliminary attempts to examine the rheology of suspensions of cornstarch in several liquids. This part begins with a description

of some of the qualitative measurements that were initially made in order to better understand the onset of shear thickening in a number of different suspensions. The second part of the section discusses some quantitative measurements of the apparent viscosity of suspensions of cornstarch in olive oil.

3.2 Granule Size

The cornstarch (Sigma Aldrich, St. Louis, MO) for all of the work of this thesis was made up of 27% amylose and 73% amylopectin as reported by Sigma Aldrich (Merkt *et al.*, 2004; Fall *et al.*, 2008). The average granule diameter was reported to be 14 μm in the literature (Fall *et al.*, 2008). As a check on the particle size, a series of optical images of the cornstarch granules were taken using a Nikon Eclipse TE2000-E microscope system (Nikon Corporation, Tokyo, Japan). An example image is shown in Figure 3.1.

Using ImageJ (ImageJ, National Institute of Health), the approximate particle diameter of seventy-five cornstarch particles was measured with the digital ruler feature. The particle diameters were collected in a histogram shown in Figure 3.2. The average particle size for these seventy-five particles was determined to be 13 μm $\pm$ 3 μm which is very close to the literature value of 14 μm (Fall *et al.*, 2008). The diameters measured were two dimensional projections of a three dimensional granule and may have underestimated the actual diameter.

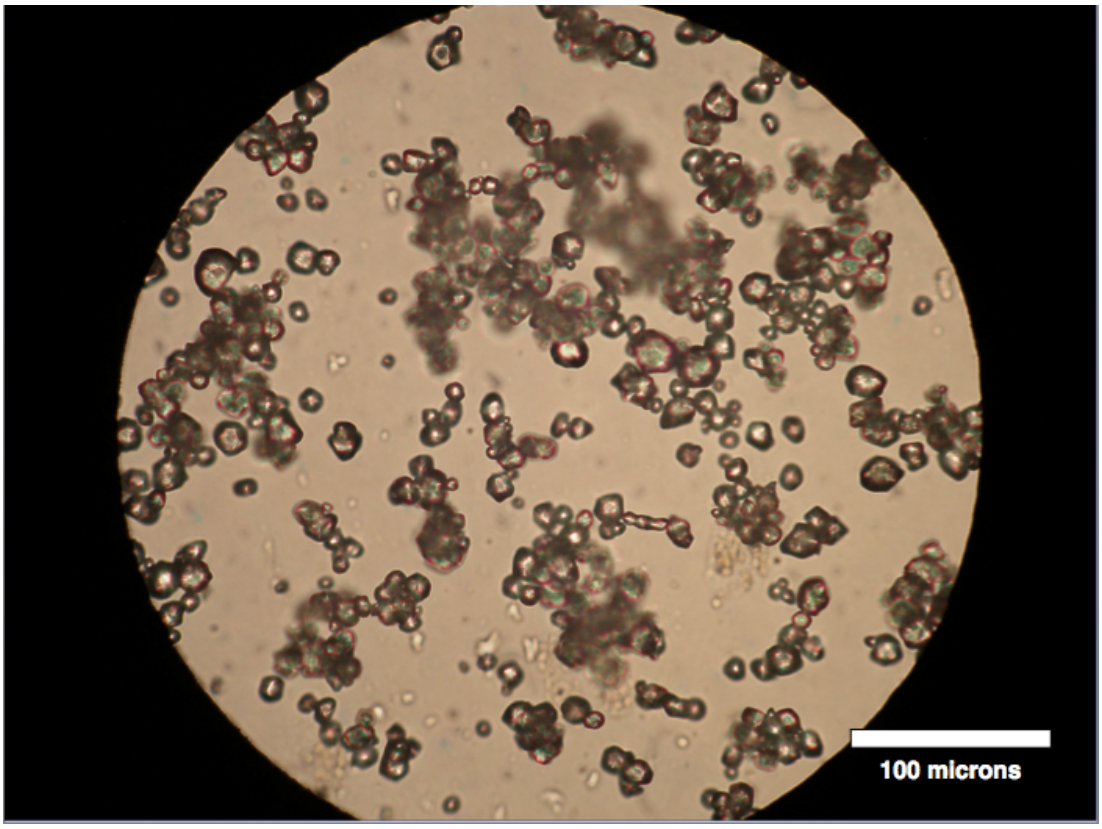

FIGURE 3.1: Cornstarch particles under microscope. Photography by Ben Johnson.

3.3 Density Matching

The cornstarch particles are more dense than water and settle in a matter of minutes in suspension with pure water. In order to perform ultrasonic experiments over a longer period of time, settling must be slowed by increasing the density of the water to more closely match the density of the cornstarch. The most common way of increasing the density of water involves mixing in cesium chloride (Merkt *et al.*, 2004; Fall *et al.*, 2008). The density of cesium chloride solutions as a function of concentration at a temperature of 25 °C is shown in Figure 3.3 (Washburn, 1928).

In the work of Brown and Jaeger, the leading group in the field, their procedure

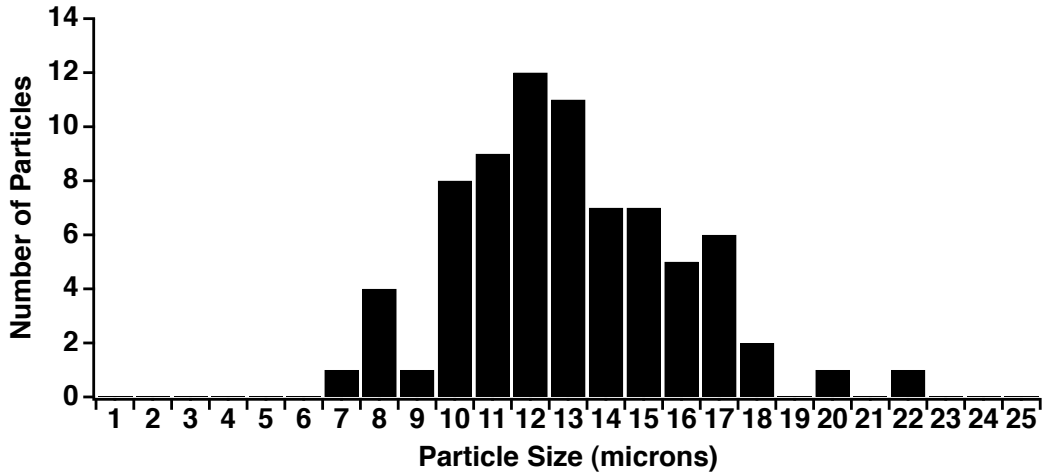

FIGURE 3.2: A histogram of the approximate particle diameters of seventy-five cornstarch particles.

used cornstarch right out of the container without any special drying procedure for all of their experiments (Brown and Jaeger, 2010). However, the density of cornstarch reported in the literature varies from 1.55 g/mL (White *et al.*, 2009) to 1.68 g/mL (Merkt *et al.*, 2004). These density differences may be the result of differences in the fraction of the weight of the cornstarch particles that is made up of absorbed water. The paper reporting the highest density describes a method to dehydrate the cornstarch as much as possible (Merkt *et al.*, 2004). Their procedure described how the cornstarch is dried at 50°C for a week and stored in a desiccator (Merkt *et al.*, 2004).

In order to determine the density of the cornstarch without any drying procedure, a series of suspensions was made containing 10% cornstarch in different concentrations of cesium chloride solutions (all concentrations are reported by mass unless otherwise indicated). The range of densities for cornstarch reported in the literature would

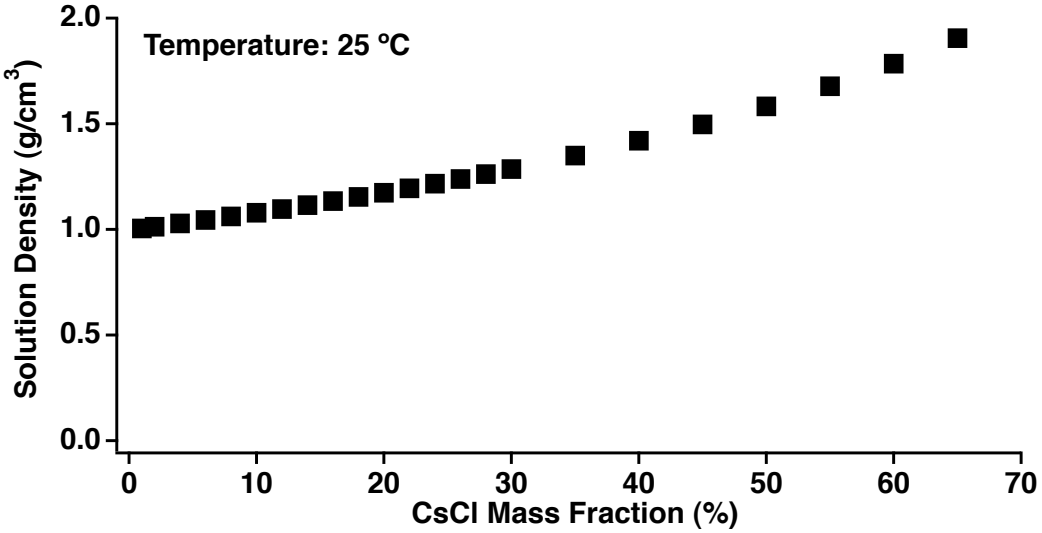

FIGURE 3.3: The density of cesium chloride solutions in water as a function of the mass fraction of cesium chloride. (Washburn, 1928)

require solutions of cesium chloride with concentrations between 50% and 55%, as can be seen from Figure 3.3.

Figure 3.4 shows a comparison between a 10% cornstarch solution in a 55% cesium chloride and water solution and a 10% cornstarch solution in a 50% cesium chloride and water solution. The 50% cesium chloride and water solution has a density of approximately 1.59 g/mL and the 55% cesium chloride solution has a density of approximately 1.68 g/mL. Both solutions were stored overnight allowing the suspensions to separate. The cornstarch can be observed to be more dense than the 50% cesium chloride solution and less dense than the 55% cesium chloride solution.

The experiment depicted in Figure 3.4 was repeated with ten percent cornstarch suspensions in solutions of cesium chloride with concentrations from 50% to 55% in one percent steps. These solutions were allowed to settle overnight as shown in Figure

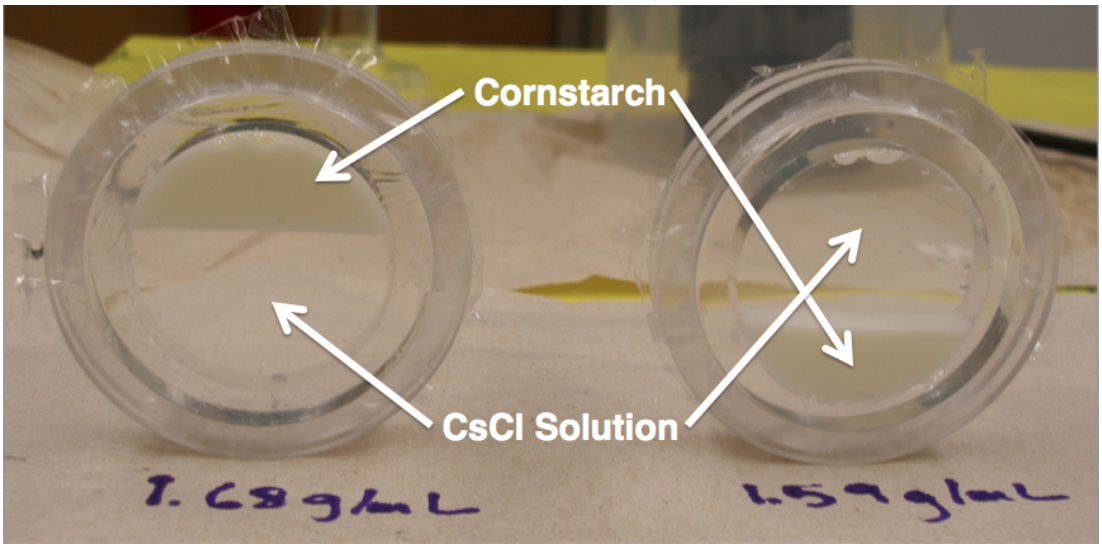

FIGURE 3.4: Two solutions containing 10% cornstarch in different concentrations of cesium chloride. The sample on the left contains a 55% cesium chloride solution and the sample on the right contains a 50% cesium chloride solution. The samples were stored overnight to allow the suspension to separate into its two components.

3.5. The cornstarch is observed to be less dense than the cesium chloride solutions for concentrations of cesium chloride above 53%. The cornstarch is observed to be more dense than the cesium chloride for concentrations of cesium chloride below 52%. The densities of the cornstarch and the cesium chloride solution appears to be approximately the same for the 52% cornstarch solution.

When the experiment was repeated, the cornstarch was found to be less dense than the cesium chloride solutions for the 52% to 55% concentrations. The cornstarch was found to be more dense than the 50% cesium chloride solution and the two components of the suspension were approximately density-matched for the 51% cesium chloride solution. Based on the results of these two experiments, it was determined to use a 51.5% concentration of cesium chloride in distilled water as a density matching

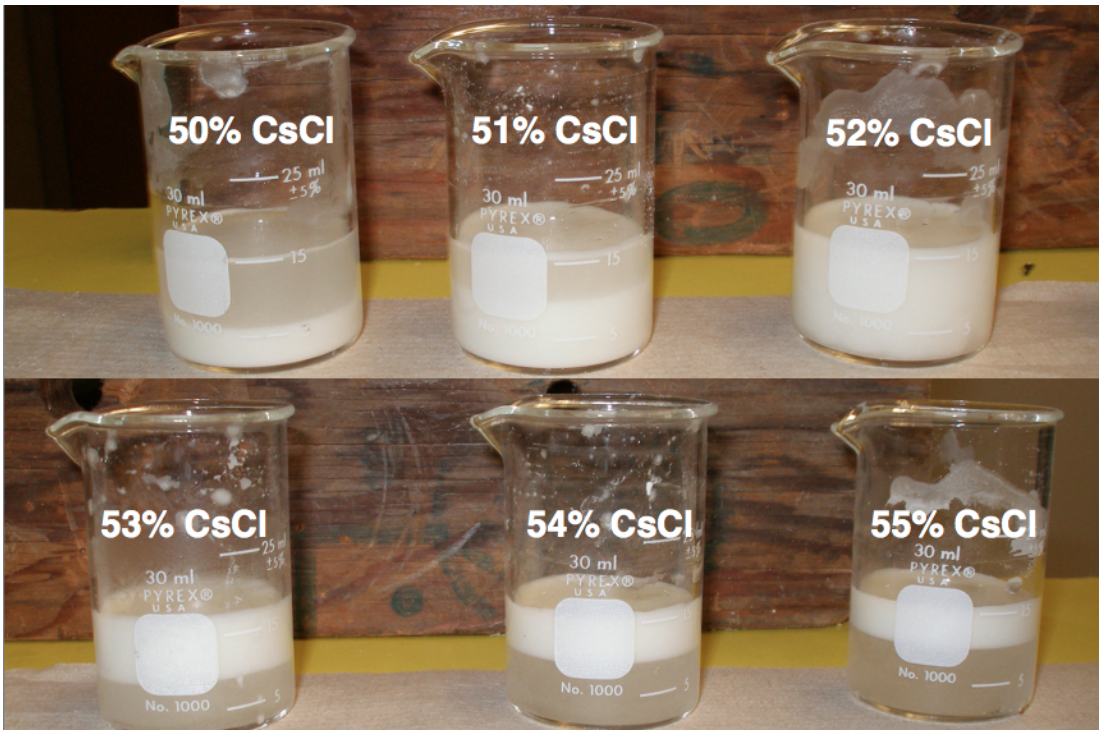

FIGURE 3.5: A series of solutions containing 10% cornstarch in different concentrations of cesium chloride. The samples' cesium chloride concentration ranges from 50% to 55% in 1% steps. The samples were stored overnight to allow the suspension to separate into its two components.

solution for all of the cornstarch experiments described in this thesis. This solution is not a perfect density match, but does a reasonable job of slowing down the settling of the cornstarch during the time period over which experiments are completed.

In order to properly determine the density of the 51.5% cesium chloride solution, four separate solutions of 51.5% cesium chloride in distilled water were made. One milliliter of one of the solutions was measured out using a precision pipette (Biohit Corporation, Laippatie, Helsinki) and transferred to a weighing dish. The mass of the 1 mL of solution was found using a XS105 Dual Range Balance (Mettler Toledo, Greifensee, Switzerland) with an accuracy of 0.2 micrograms. As a control, one

milliliter of distilled water was measured out three separate times and weighed. The experiment was repeated a minimum of three times with each of the four separate solutions of 51.5% cesium chloride in distilled water. The results of this experiment are shown in Table 3.1. The method was validated, because the measurements of the density of water are approximately 1.0 g/mL.

	Distilled Water Mass (g)	Sample 1 Mass (g)	Sample 2 Mass (g)	Sample 3 Mass (g)	Sample 4 Mass (g)
Measurement #1	0.99628	1.62087	1.60912	1.62212	1.63186
Measurement #2	1.00000	1.62206	1.61824	1.62736	1.62871
Measurement #3	0.99784	1.62438	1.63046	1.62425	1.63329
Measurement #4	-	-	1.62470	-	-
Average	0.998 ± 0.002	1.622 ± 0.002	1.619 ± 0.011	1.625 ± 0.003	1.631 ± 0.002

TABLE 3.1: The measurements of the mass of 1 mL from a sample of distilled water and from four samples of 51.5% cesium chloride solutions.

The average of the four samples was found to be 1.624 g ± 0.005 g and thus the density of the 51.5% cesium chloride in distilled water solution was determined to be approximately 1.62 g/mL.

The ultrasonic properties of the 51.5% cesium chloride solution were measured using the techniques described in Chapters 4, 5, and 8 . Two separate samples of the solution were made and put into two of the sample molds. The ultrasonic group velocity, the ultrasonic attenuation properties, and the ultrasonic backscatter properties were all measured in the two separate samples at a temperature of approximately

21°C. The results of the ultrasonic measurements are shown in Table 3.2. The 51.5% cesium chloride solution had ultrasonic properties very close to that of water, although the density of the solution was much greater than that of water.

	Solution #1	Solution #2
Temperature °C	21.1	21.1
Group Velocity (m/s)	1483 ± 10	1483 ± 10
Slope of Attenuation (dB/cm/MHz)	∼0	∼0
Attenuation Coefficient at 5 MHz (dB/cm)	∼0	∼0
Backscatter	Essentially None	Essentially None

TABLE 3.2: Ultrasonic measurements of two separate samples of a 51.5% cesium chloride solution

3.4 Cornstarch Suspensions

The ultrasonic measurements described in this thesis were made on suspensions of 10% cornstarch in a 51.5% cesium chloride solution, 20% cornstarch in a 51.5% cesium chloride solution, 30% cornstarch in a 51.5% cesium chloride solution, and 40% cornstarch in a 51.5% cesium chloride solution. The actual amounts of cornstarch, cesium chloride, and distilled water used to make one sample of a particular solution are displayed in Table 3.3.

The process of making a suspension involves measuring out 15 mL of distilled water using a graduated cylinder and 15.9 g of cesium chloride using an Ohaus Adventurer

Pro precision balance (Ohaus Corporation, Pine Brook, New Jersey) and weighing paper. The cesium chloride is mixed into the distilled water in a 100 mL glass beaker using a metal spatula. The proper amount of cornstarch for that particular solution (see Table 3.3) is measured out using the precision balance and weighing paper. Depending upon the concentration of the solution, the cornstarch is stirred into the 51.5% cesium chloride solution with either a metal spatula or an electric hand mixer (GE Corporation, Fairfield, Connecticut). The electric mixer is especially helpful for the more concentrated solutions, although care must be taken to not spill any of the suspension and to not overheat the mixer's motor.

Mass Fraction	Distilled Water	Cesium Chloride	Cornstarch
0% Cornstarch in 51.5% CsCl	15 mL	15.9 g	0.00 g
10% Cornstarch in 51.5% CsCl	15 mL	15.9 g	3.43 g
20% Cornstarch in 51.5% CsCl	15 mL	15.9 g	7.73 g
30% Cornstarch in 51.5% CsCl	15 mL	15.9 g	13.24 g
40% Cornstarch in 51.5% CsCl	15 mL	15.9 g	20.60 g

TABLE 3.3: Ingredients required to make enough of each solution to fill a single sample mold

3.5 Sample Mold

The sample mold used for the ultrasonic measurements is made up of a plastic cylinder and two plastic rings shown disassembled in Figure 3.6. The plastic cylinder has a diameter of approximately 45 mm and a thickness of approximately 12 mm.

When the cesium chloride solution is included with the molds, the side of the plastic cylinder is coated with a thin layer of vacuum grease to decrease the loss of cesium chloride from the suspension (see Figure 3.7). A Saran Wrap^{TM}layer is laid down over this layer of vacuum grease and is sealed to the plastic cylinder using one of the plastic rings. The outer diameter of the cylinder is only slightly smaller than the inner diameter of the plastic rings so the two pieces are friction fit together. After one Saran Wrap^{TM}window has been attached to the mold, the mold is flipped over and a layer of vacuum grease is put on the upward facing surface of the plastic cylinder (in a fashion similar to the way it was applied to this same surface on the other side of the plastic cylinder). The mold is filled with the cornstarch suspension and a Saran Wrap^{TM}layer is then applied and sealed into place creating a finished sample mold, as shown in Figure 3.7.

3.6 Reproducibility

The reproducibility of the ultrasonic measurements of cornstarch suspensions in a density-matched cesium chloride solution was an important component of all of the studies in this thesis. To that end, it was important to test whether separate batches of the same concentration of cornstarch would have similar ultrasonic properties. To test the reproducibility of the ultrasonic properties from sample to sample, three suspensions of 30% cornstarch in 51.5% cesium chloride were mixed together. For one of the suspensions, double the amount of each ingredient was used to create two

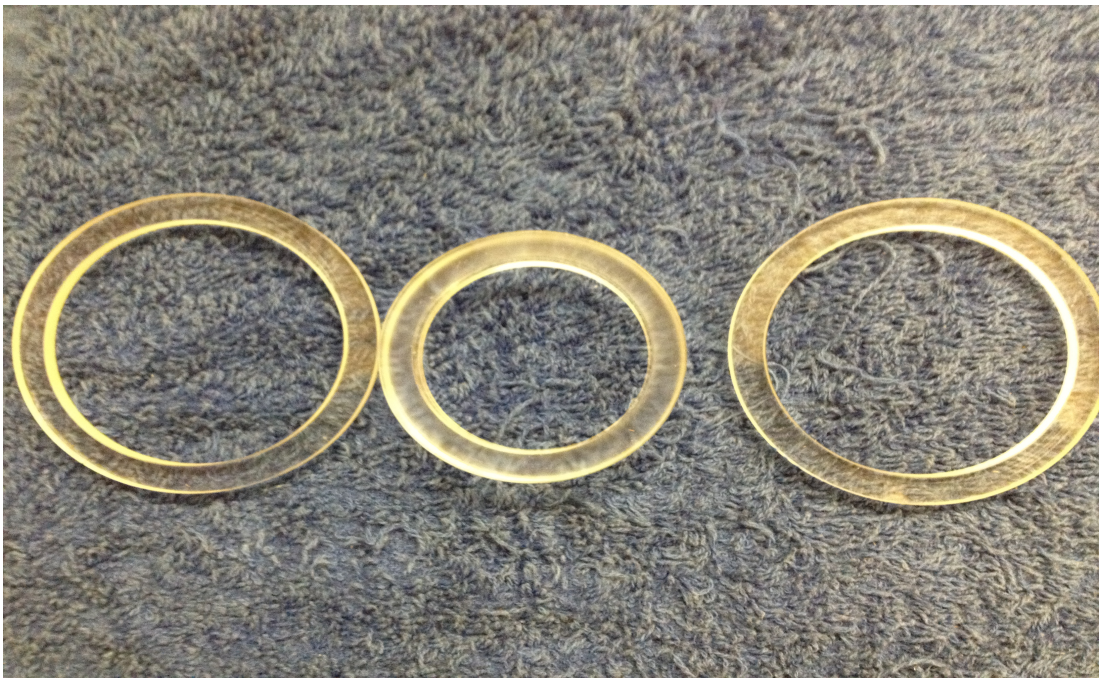

FIGURE 3.6: The disassembled sample mold showing the three main pieces. Photography by Ben Johnson.

samples from a single batch. Therefore, four total samples were created in three batches. The ultrasonic properties of each of these samples was measured using the techniques described in Chapters 4, 5, and 8. The sample thickness, ultrasonic group velocity, ultrasonic phase velocity at 5 MHz, slope of attenuation, attenuation coefficient at 5 MHz, apparent integrated backscatter, backscatter coefficient at 5 MHz, and the frequency dependence of the backscatter coefficient are all shown in Table 3.4. The quantities that are displayed in the table are described in the later chapters of this thesis. The importance of the table is to show the consistency in the four measurements.

As can be seen from the Table 3.4, both the group velocity (described in Chapter 4) and the phase velocity at 5 MHz (detailed in Chapter 6) vary only slightly among the

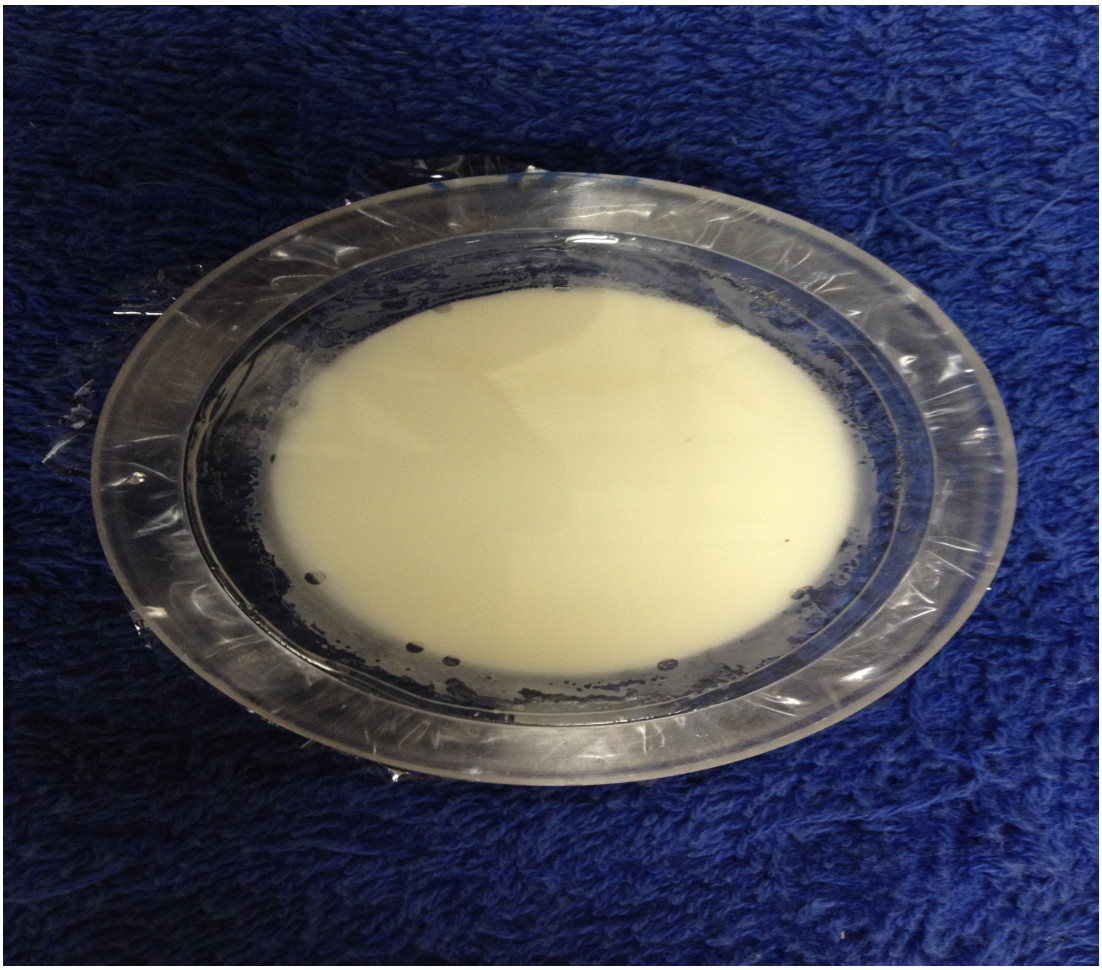

FIGURE 3.7: A completed sample mold containing a cornstarch in density-matched cesium chloride solution. The vacuum grease layer can be observed under the saran wrap window. Photography by Ben Johnson.

four suspensions. The attenuation properties (described in Chapter 5) are also seen to be very reproducible from sample to sample with both the slope of the attenuation coefficient and the attenuation coefficient at 5 MHz all showing consistency across the four measurements. The backscatter properties (described in Chapter 8) have slight differences among the four samples, but the variance in the samples is very reasonable considering the typical uncertainty of the backscatter measurement (Yang

	Solution #1	Solution#1a	Solution #2	Solution #3
Temperature (°C)	20.6	20.6	19.3	19.4
Sample Thickness (mm)	14.1 ± 0.1	14.3 ± 0.1	13.8 ± 0.1	13.8 ± 0.1
Group Velocity (m/s)	1673 ± 7	1669 ± 7	1674 ± 8	1670 ± 6
Phase Velocity at 5 MHz (m/s)	1674 ± 7	1672 ± 7	1675 ± 8	1674 ± 7
Slope of Attenuation (dB/cm/MHz)	2.1 ± 0.1	2.2 ± 0.1	2.1 ± 0.1	2.2 ± 0.1
Attenuation Coefficient at 5 MHz (dB/cm)	7.2 ± 0.1	7.3 ± 0.1	6.8 ± 0.1	7.0 ± 0.3
Apparent Integrated Backscatter (dB)	-62.1	-62.8	-63.6	-63.6
Backscatter Coefficient at 5 MHz (dB/cm)	$2.96 * 10^{-4}$	$3.13 * 10^{-4}$	$2.25 * 10^{-4}$	$2.17 * 10^{-4}$
Frequency Exponent of the Backscatter Coefficient	3.0	3.1	3.4	3.4

TABLE 3.4: Comparing the reproducibility of the ultrasonic measurements from four samples of 30% cornstarch in a 51.5% cesium chloride solution. The first two suspensions #1 and #1a were from the same batch of suspension. Suspension #2 and #3 were each made separately.

et al., 2007).

The other reproducibility question that must be answered is how much the ultrasonic properties of the sample change over time. Two 20% cornstarch in density-matched cesium chloride suspensions were made and put into two sample molds. Ultrasonic measurements were made on the two samples. The following day the measurements were repeated. The measurements were repeated again the day after that as well. The attenuation coefficient at 5 MHz measured for both suspensions on each

of the three days is displayed in Table 3.5. As can be seen from the table, the attenuation coefficient was much higher the day the suspension was made than at any point thereafter for both suspensions. Two potential causes of the higher attenuation may be air bubbles in the suspension or the gradual sedimentation of the cornstarch. If the sample was stored overnight the attenuation coefficient was found to decrease. After the initial waiting period, all of the ultrasonic measurements were determined to be reproducible as shown in Table 3.6. Because the measurements were repeatable after the first day, and because the sample was agitated before each measurement, one can conclude that the increased attenuation initially is probably the result of air bubbles rather than sedimentation.

Suspension	Attenuation Coefficient at 5 MHz (dB/cm)	Standard Deviation (dB/cm)
Suspension #1 (Day 1)	4.9	0.8
Suspension #1 (Day 2)	4.2	0.1
Suspension #1 (Day 3)	4.3	0.1
Suspension #2 (Day 1)	6.3	1.6
Suspension #2 (Day 2)	4.1	0.1
Suspension #2 (Day 3)	4.3	0.1

TABLE 3.5: Measurements of the attenuation coefficient at 5 MHz on three successive days for two different suspensions of 20% cornstarch in a 51.5% cesium chloride solution. The measurements were very reproducible after the first day.

	Solution #1 (Day 2)	Solution#1 (Day 3)	Solution #2 (Day 2)	Solution #2 (Day 3)
Temperature (°C)	20.6	20.6	20.5	20.5
Sample Thickness (mm)	13.5 ± 0.1	13.5 ± 0.1	14.2 ± 0.1	14.2 ± 0.1
Group Velocity (m/s)	1607 ± 6	1600 ± 6	1595 ± 6	1607 ± 7
Phase Velocity at 5 MHz (m/s)	1605 ± 6	1604 ± 7	1604 ± 6	1607 ± 7
Slope of Attenuation (dB/cm/MHz)	1.4 ± 0.1	1.4 ± 0.1	1.4 ± 0.1	1.4 ± 0.1
Attenuation Coefficient at 5 MHz (dB/cm)	4.2 ± 0.1	4.3 ± 0.1	4.1 ± 0.1	4.3 ± 0.1
Apparent Integrated Backscatter (dB)	-61.2	-61.3	-61.7	-62.1
Backscatter Coefficient at 5 MHz (dB/cm)	$2.15 * 10^{-4}$	$1.76 * 10^{-4}$	$1.79 * 10^{-4}$	$1.77 * 10^{-4}$
Frequency Dependence of the Backscatter Coefficient	3.6	3.4	3.5	3.6

TABLE 3.6: Comparing the reproducibility of the ultrasonic measurements in two samples of 20% cornstarch in a 51.5% cesium chloride solution from one day to the next. Each sample was measured twice approximately twenty-four hours apart.

3.7 Qualitative Rheological Measurements

The second part of this chapter discusses some preliminary rheological measurements that were made on a number of suspensions of cornstarch in various liquids. Before quantitative measurements of the rheological properties of any of the suspensions were made, a number of qualitative experiments were undertaken. The purpose of these experiments was to determine at approximately what concentration of corn-

starch that a suspension would display shear thickening behavior.

3.7.1 Cornstarch in Water

A series of suspensions of cornstarch in water were mixed together in order to determine the approximate critical concentration for the onset of shear thickening. Each suspension started with 50 g of distilled water in its own 250 mL beaker. Table 3.7 displays the amount of cornstarch and water mixed together for each of the cornstarch and water suspensions studied. The volume fractions were determined using the densities of both the distilled water (1.00 g/mL) and the cornstarch granules (1.62 g/cm^3). The two components of each suspension were mixed together and a determi-

Mass Fraction	Volume Fraction	Distilled Water (g)	Cornstarch (g)
10% Cornstarch	6.4%	50	5.56
20% Cornstarch	13.4%	50	12.50
30% Cornstarch	20.9%	50	21.43
40% Cornstarch	29.1%	50	33.33
50% Cornstarch	38.2%	50	50.00
55% Cornstarch	43.0%	50	61.11

TABLE 3.7: The amounts of cornstarch and distilled water added to each concentration of the cornstarch and water suspensions.

nation of shear thickening behavior was made qualitatively from examining the nature of the mixing behavior. At a concentration of 40% by mass, the suspension is very viscous, but does not display shear thickening behavior. At a concentration of 50% by mass, the suspension became markedly more difficult to mix and the difficulty in

mixing increased with the rate of mixing. Thus, at a concentration of 50% by mass, the suspension qualitatively displayed shear thickening behavior. The same behavior was observed at a concentration of 55% by mass as well. In order to confirm these conclusions the experiment was repeated an additional time with the same results.

3.7.2 Cornstarch in a Density-Matched Solution

The experiment was repeated for a series of suspensions of cornstarch in a 51.5% cesium chloride solution in order to determine the approximate critical concentration for the onset of shear thickening. Each suspension contained a 51.5% cesium chloride solution consisting of 10 g of distilled water and 10.62 g of cesium chloride. Table 3.8 displays the amount of cornstarch, cesium chloride, and distilled water mixed together for each of the cornstarch and 51.5% cesium chloride suspensions studied. Because the cesium chloride solution is density matched to the cornstarch, the mass fraction is the same as the particle volume fraction (Roche *et al.*, 2011). The two components of

Mass Fraction	Volume Fraction	Distilled Water (g)	Cesium Chloride (g)	Cornstarch (g)
10% Cornstarch	10%	10	10.62	2.29
20% Cornstarch	20%	10	10.62	5.16
30% Cornstarch	30%	10	10.62	8.84
40% Cornstarch	40%	10	10.62	13.75

TABLE 3.8: The amounts of cornstarch, cesium chloride and distilled water added to each concentration of suspension of cornstarch in a 51.5% cesium chloride solution.

each suspension were mixed together and a determination of shear thickening behavior was made qualitatively from examining the mixing. At a concentration of 30% by mass, the suspension is very viscous, but is not shear thickening. At a concentration of 40% by mass, the suspension displayed shear thickening behavior as it was mixed. To confirm these qualitative observations, the experiment was repeated several times with similar results.

3.7.3 Cornstarch in Olive Oil

The experiment was repeated for a series of suspensions of cornstarch in olive oil in order to determine the approximate critical concentration for the onset of shear thickening. The concentrations of the suspension were determined by mass with each suspension starting with 50 g of olive oil in its own 250 mL beaker. Each sample of olive oil was weighed in order to determine the correct amount to add to the suspension. Table 3.9 displays the amount of cornstarch and oil mixed together for each of the suspensions studied. The volume fractions were determined using the densities of the olive oil (0.91 g/mL at 23 °C) and the cornstarch granules (1.62 g/cm^3) (Weast, 1970). The two components of each suspension were mixed together and a determination of shear thickening behavior was made from examining the mixing. As the concentration increased the suspensions became more and more viscous, but shear thickening behavior was not observed in any of the suspensions up to a concentration of 65% by mass. At a mass fraction of 69.3% the suspension, when mixed completely, was no longer a liquid, but had changed phase becoming a soft solid. None of the

Mass Fraction	Volume Fraction	Olive Oil (g)	Cornstarch (g)
10% Cornstarch	5.9%	50	5.56
20% Cornstarch	12.3%	50	12.50
30% Cornstarch	19.5%	50	21.43
40% Cornstarch	27.3%	50	33.33
50% Cornstarch	36.0%	50	50.00
55% Cornstarch	40.8%	50	61.11
60% Cornstarch	45.8%	50	75.00
65% Cornstarch	51.1%	50	92.86
69.3% Cornstarch	56.0%	50	112.86

TABLE 3.9: The amounts of cornstarch and olive oil added to each concentration of the cornstarch and oil suspensions.

concentrations of cornstarch in oil appeared to display shear thickening behavior qualitatively. In order to confirm this conclusion, the experiment was repeated an additional time with the same results. This qualitative result agrees with other results from the literature that indicated that cornstarch (a hydrophilic particle) will shear thicken in water, but will not shear thicken in hydrophobic liquids such as oil (**?**).

3.8 Quantitative Viscosity Measurements

The basic rheology of cornstarch and water suspensions has been reported extensively in the literature in recent years (Brown and Jaeger, 2009; **?**; Fall *et al.*, 2008). Although the qualitative observation that cornstarch suspensions in hydrophobic materials will not shear thicken has been made in the literature, the quantitative rheo-

logical measurement of suspensions of cornstarch in oil does not appear to have been completed (Brown and Jaeger, 2009). Understanding why a suspension of cornstarch in oil does not shear thicken will add to the general understanding of shear thickening behavior. For this reason, preliminary measurements were made on the rheological properties of a number of concentrations of cornstarch in oil.

3.8.1 AR-G2 Rheometer

All of the quantitative rheological measurements described in this chapter were made on an AR-G2 rheometer. The AR-G2 is a controlled-stress/controlled-rate rotational rheometer. The lower portion of the system is fixed and consists of a temperature-controlled Peltier plate with a temperature range of -20°C to 180°C with a stated accuracy of 0.1°C. The upper portion of the system can oscillate or rotate continuously depending on the application. A parallel plate (8 to 60 mm in diameter) or cone (20 or 40 mm in diameter) geometry is attached to the top portion of the system in order to make the rheological measurements.

The system was used to make steady shear measurements where the system would rotate until a steady shear rate was reached, and would then measure the shear stress. The ratio of the stress to shear rate is the steady shear viscosity of the sample as defined in Equation 3.1.

$$\text{Apparent Viscosity (Pa*s)} = \frac{\text{Stress (Pa)}}{\text{Shear Rate } (s^{-1})} \tag{3.1}$$

In this way, the viscosity of the sample can be measured at a number of different

shear rates.

The cone attachment (also known as the cone geometry) was exclusively used for the measurements discussed in the rest of this thesis. The main advantage of the cone attachments is that the shear is constant throughout the sample as long as the angle on the cone is small (typically less than 4°). The torque and the shear rate can be found for any cone and plate setup such as this. The total torque, T, can be determined by first considering only the torque, dT, acting on an element of fluid between r=r and r=r+dr as shown in Figure 3.8 and Equation 3.2

$$dT = (2\pi r dr)\tau r \tag{3.2}$$

where r is the distance from the center of the cone to the fluid element, dr is the length of the fluid element, and τ is the shear stress on the system (Chhabra and Richardson, 2008). The total torque can be obtained with Equation 3.3

$$T = \int_0^T \mathrm{d}T = \int_0^R 2\pi r^2 \tau \mathrm{d}r \tag{3.3}$$

where R is the radius of the cone. For constant values of the shear stress, Equation 3.3 can be used to arrive at Equation 3.4 which can be re-expressed in terms of the shear stress as in Equation 3.5 (Chhabra and Richardson, 2008).

$$T = \frac{2\pi R^3 \tau}{3} \tag{3.4}$$

$$\tau = \frac{3T}{2\pi R^3} \tag{3.5}$$

The shear rate at a distance r from the center of a cone that is rotating at a angular velocity of Ω as shown in Figure 3.8 can be determined from the gradient in the

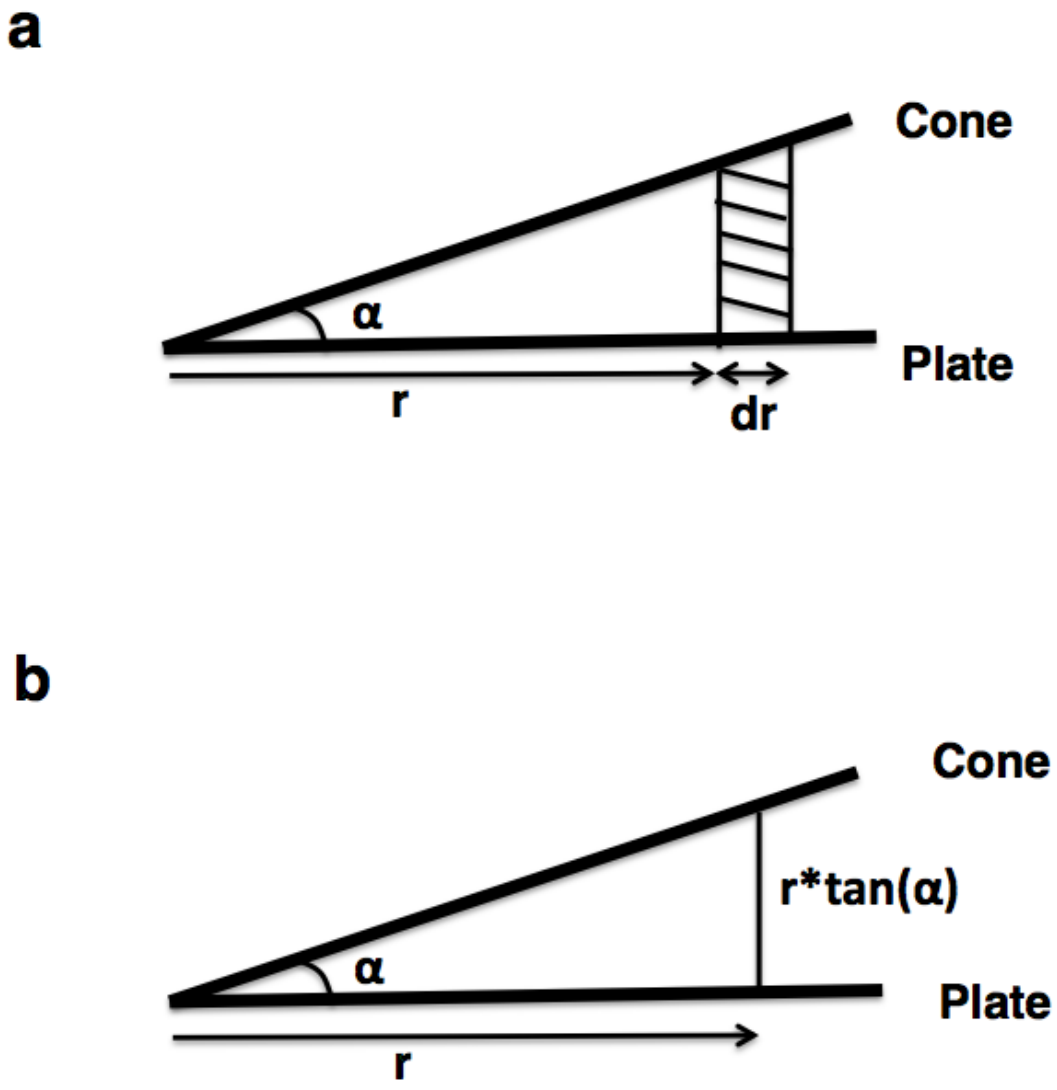

FIGURE 3.8: The setup for the cone and plate system with the relevant parameters for the shear stress shown in (a) and the relevant parameters for the shear rate shown in (b) (Chhabra and Richardson, 2008).

angular velocity (Chhabra and Richardson, 2008). At the surface of the rotating cone, the velocity is $r\Omega$, whereas at the surface of the stationary plate the velocity is 0 (Chhabra and Richardson, 2008). Equation 3.6 expresses the shear rate in terms of this velocity gradient

$$\text{Shear Rate} = \frac{r\Omega - 0}{r\tan(\alpha)} = \frac{\Omega}{\tan(\alpha)} \tag{3.6}$$

where α is the angle of the cone (Chhabra and Richardson, 2008). From Equation 3.6 one can see that the shear rate does not depend on the distance r from the center of the cone and the fluid everywhere within the rotating cone and plate system experiences the same shear rate (Chhabra and Richardson, 2008). When the angle of the cone is small, then $tan(\alpha) \approx \alpha$ and the shear rate can be expressed as shown in Equation 3.7.

$$\text{Shear Rate} = \frac{\Omega}{\alpha} \tag{3.7}$$

Thus, the shear rate in the cone and plate setup depends only on the angular velocity of the cone and the angle of the cone (Chhabra and Richardson, 2008).

The gap between the cone and the plate is fixed in the cone and plate geometry case (unlike the case of other geometries such as the parallel plate), thus the cone and plate measurements should normally only be made at a fixed temperature (TA, 2000). All of the rheological experiments described in this thesis were conducted at a fixed temperature, because thermal expansion due to temperature changes could change the gap and affect the measurement for this setup (TA, 2000). Another concern when using a cone and plate setup with suspensions of relatively large particles is particle

jamming (Chhabra and Richardson, 2008). The recommendations for the ratio of the size of the gap to the particle size range from 10 or 20 (Chhabra and Richardson, 2008) or alternatively up to 100 (Mewis and Wagner, 2012) in order to minimize effects due to jamming.

3.8.2 Cornstarch in Oil Suspensions

One experiment performed with the AR-G2 rheometer used the 40 mm diameter cone geometry with an angle of slightly less than two degrees. Measurements were made on seven different concentrations of cornstarch in oil starting from 0% (pure oil) up to 60% cornstarch by mass. In order to minimize any settling of the particles, all of the samples were mixed thoroughly using a spatula just before being placed in the rheometer. The temperature of the Peltier plate was set to 23°C which was approximately room temperature at the time of the measurements. For each experiment at each concentration, a thin layer of the suspension spilled out beyond the edges of the cone on the plate. For these initial experiments, the layer was not wiped up and stayed there throughout the measurements. In subsequent experiments, the extra suspension was cleaned up before the measurement was taken so that it would not affect the measurement.

For each of the samples, the starting shear rate for the measurements was 28.8 s^{-1}. The shear rate was increased from the starting shear rate for each sample with measurements made at at least four shear rates. The first sample measured was the 0% cornstarch suspension (100% olive oil). The pure olive oil sample was expected to

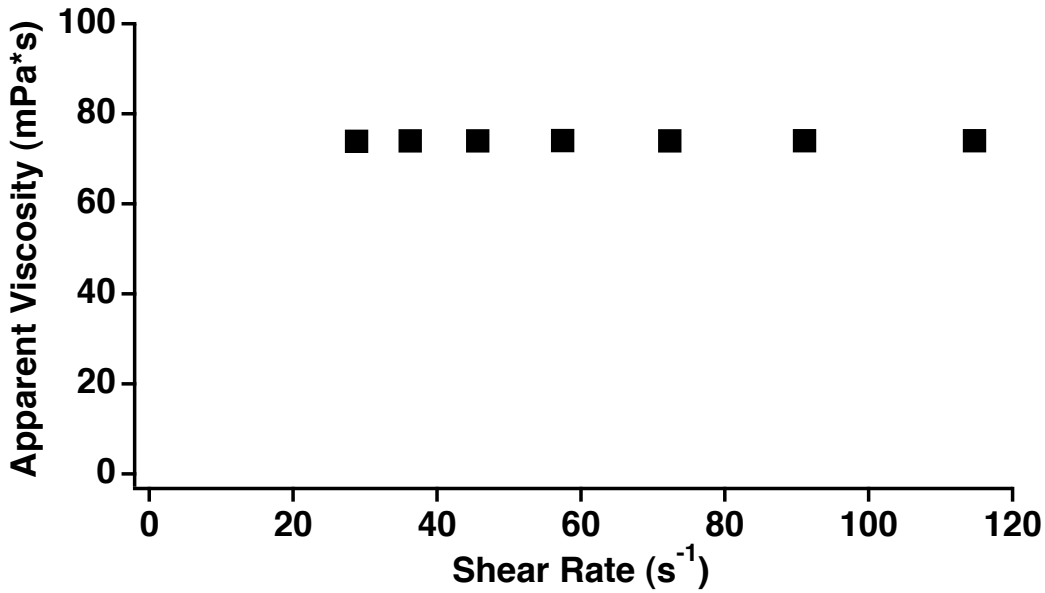

FIGURE 3.9: The apparent viscosity of the olive oil sample as a function of shear rate. Note that the units for apparent viscosity are milliPascal*seconds.

behave as a pure Newtonian fluid and therefore served as a check on the reliability of the measurements. The apparent viscosity of the 100% olive oil sample as a function of shear rate is displayed in Figure 3.9. The apparent viscosity was defined in Equation 3.1. The olive oil's viscosity is approximately 74 mPa*s independent of shear rate across this range, indicating the oil is behaving as a Newtonian fluid over this range of shear rates as expected. This value of the viscosity of olive oil at this temperature is consistent with other measurements of olive oil from the literature (Abramovic and Klofutar, 1998). The apparent viscosity measured for each suspension at a shear rate of 28.8 s^{-1} was plotted in Figure 3.10. As can be seen from the figure, the apparent viscosity increases significantly as a function of the cornstarch concentration.

The 60% suspension of cornstarch in oil was investigated over a wider range of

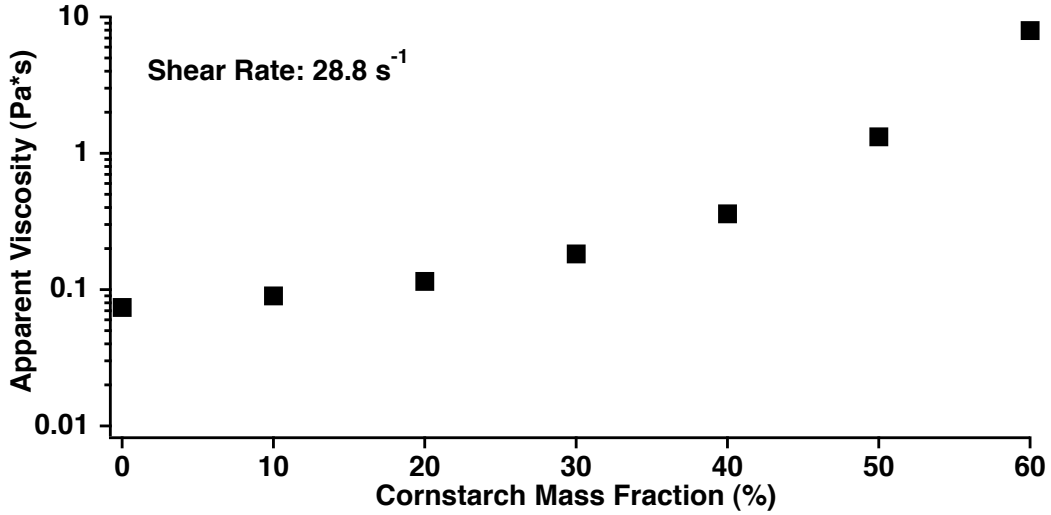

FIGURE 3.10: The apparent viscosity of the cornstarch in oil suspensions as a function of cornstarch concentration. Note that the units for apparent viscosity are Pascal*seconds.

shear rates than the other suspensions. The apparent viscosity as a function of shear rate for this suspension is plotted in Figure 3.11. The 60% cornstarch in oil suspension was seen to be displaying shear thinning behavior over this range of shear rates; that is, the apparent viscosity decreases as the shear rate increases. A power law fit to the shear stress versus shear rate data led to a dependence of the shear stress on shear rate to a power of approximately 0.55 as shown in Figure 3.12.

In order to test the reproducibility of the viscosity measurements, two additional 60% cornstarch in oil suspensions were made. The apparent viscosity of the two suspensions was measured as a function of shear rate over a range from approximately 0.1 s^{-1} to 100 s^{-1}. The results of these measurements, along with the earlier measurement of the other 60% cornstarch in oil sample, are plotted in Figure 3.13. All three of the measurements of the apparent viscosity as a function of shear rate are

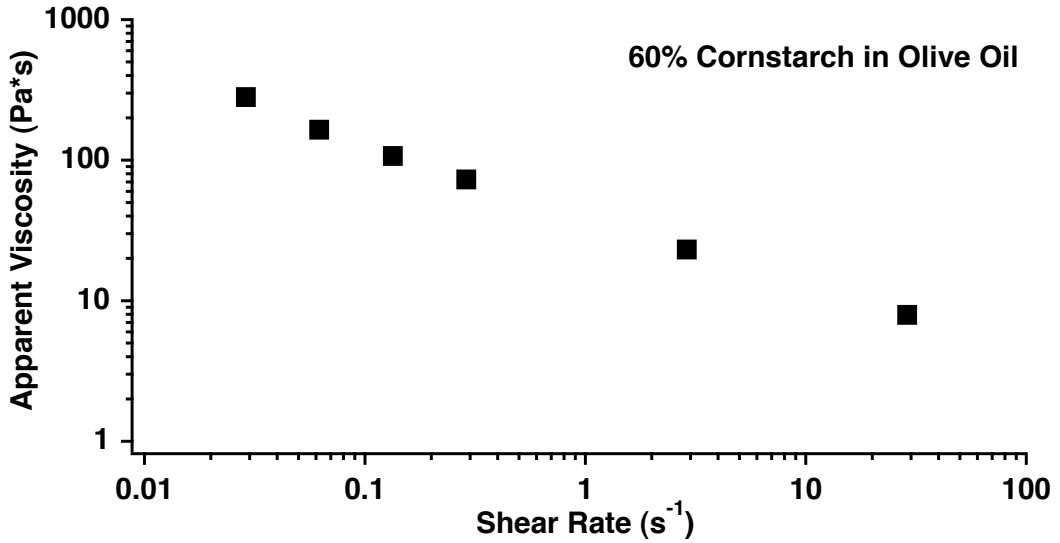

FIGURE 3.11: The apparent viscosity of the 60% cornstarch in oil suspension as a function of shear rate. Note that the units for apparent viscosity are Pascal*seconds.

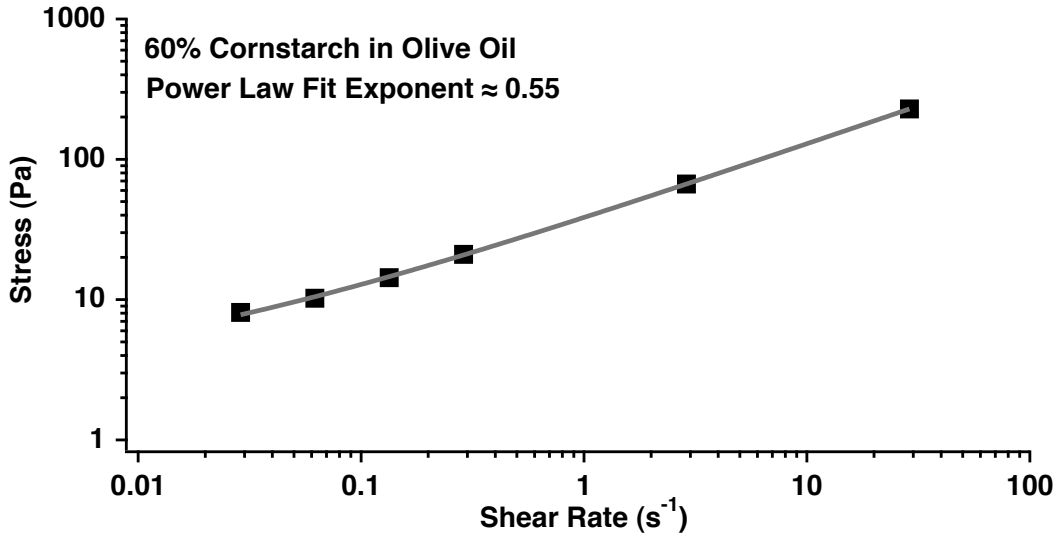

FIGURE 3.12: The shear stress as a function of shear rate for the 60% cornstarch in oil suspension on a log-log plot. The power law fit to the data is also plotted.

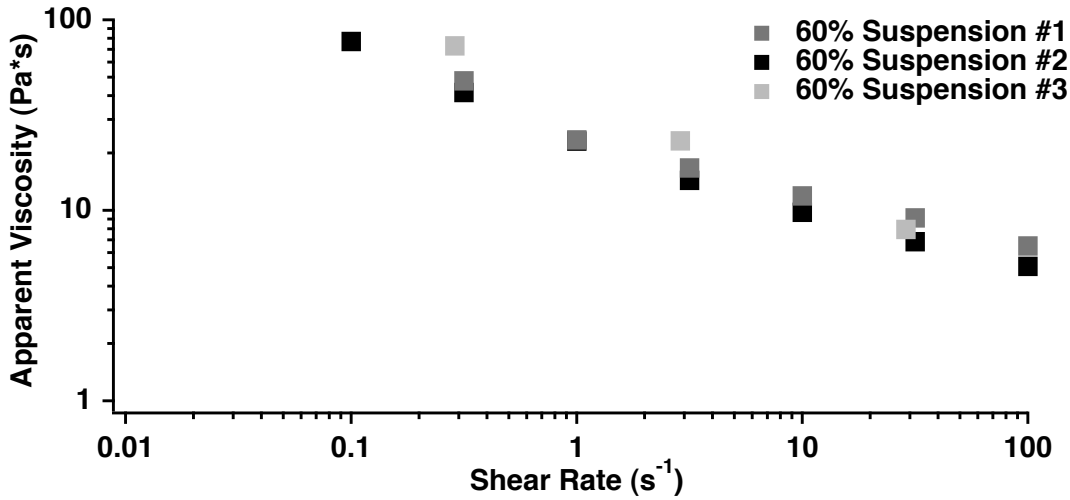

FIGURE 3.13: The apparent viscosity of three 60% cornstarch in oil suspensions as a function of shear rate on a log-log plot. Note that the units for apparent viscosity are Pascal*seconds.

mutually consistent and thus the measurements were reproducible.

3.9 Conclusion

The work described in this chapter was undertaken in order to make sure that the measurements outlined in the rest of this thesis were as reliable and accurate as possible. This chapter also detailed some preliminary work examining the rheology of suspensions of cornstarch in water, cornstarch in a density-matched solution, and cornstarch in oil. The initial rheology measurements were conducted to better understand the onset of shear thickening in each of the suspensions. The cornstarch in oil suspensions were measured quantitatively in a rotational rheometer. In contrast with the results displaying shear thickening behavior in cornstarch in water, the suspensions of cornstarch in oil showed shear thinning behavior over the range of shear rates

studied. This chapter outlined all of the experiments that were completed in order to assure that reliable ultrasonic characterization of the cornstarch in density-matched cesium chloride suspensions could be made.

Bibliography

Abramovic, H. and Klofutar, C. (**1998**). "The temperature dependence of dynamic viscosity for some vegetable oils", Acta Chim Slov **45**, 69–77.

Brown, E. and Jaeger, H. (**2009**). "A dynamic jamming point for shear thickening suspensions", Physical Review Letters **103**, 086001.

Brown, E. and Jaeger, H. (**2010**). "The role of dilation and confining stresses in shear thickening of dense suspensions", arXiv:1010.4921v1 1–43.

Chhabra, R. and Richardson, J. (**2008**). *Non-Newtonian Flow and Applied Rheology*, 2nd edition (Butterworth-Henemann).

Fall, A., Huang, N., Bertrand, F., Ovarlez, G., and Bonn, D. (**2008**). "Shear thickening of cornstarch suspensions as a reentrant jamming transition", Physical Review Letters **100**, 018301.

Merkt, F. S., Deegan, R. D., Goldman, D. I., Rericha, E. C., and Swinney, H. L. (**2004**). "Persistent holes in a fluid", Phys Rev Lett **92**, 184501.

Mewis, J. and Wagner, N. (**2012**). *Colloidal Suspension Rheology* (Cambridge).

Roche, M., Kellay, H., and Stone, H. (**2011**). "Heterogeneity and the role of normal stresses during the extensional thinning of non-brownian shear-thickening fluids", Physical Review Letters **107**, 134503.

TA (**2000**). "Ta instruments ar 500/1000 rheometer hardware manual", .

Washburn, E. (**1928**). *International Critical Tables Vol. 3* (McGraw-Hill).

Weast, R., ed. (**1970**). *CRC Handbook of Chemistry and Physics*, 51 edition (The Chemical Rubber Company).

White, E. E. B., Chellamuthu, M., and Rothstein, J. P. (**2009**). "Extensional rheology of a shear-thickening cornstarch and water suspension", Rheologica Acta **49**, 119–129.

Yang, M., Krueger, T., Holland, M., and Miller, J. (**2007**). "Anisotropy of the backscatter coefficient of formalin-fixed ovine myocardium", Journal of the Acoustical Society of America **122**, 581–586.

Chapter 4

Group Velocity Measurements of Cornstarch Suspensions

4.1 Preface

This chapter details the method and results of the group velocity measurements made on suspensions of cornstarch in density-matched solutions and in water. An approximation for the speed of sound in cornstarch granules is inferred from the measurements of the density-matched suspensions. The group velocity and sample thickness measurements are critical to the later measurements of the attenuation coefficient and the phase velocity.

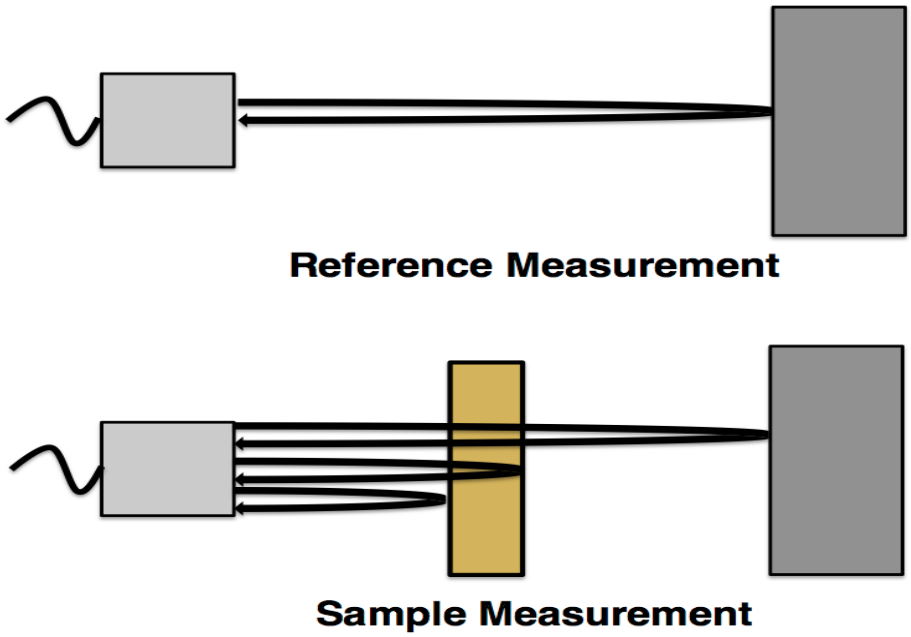

FIGURE 4.1: The shadowed reflector setup used for the measurements of the group velocity. Four timing measurements were necessary because the sample was not placed in contact with the reflector.

4.2 Experimental Setup

The group velocity of the cornstarch suspensions was measured using the Sollish method (Sollish, 1979; Trousil, 2002). The method can be used in either the shadowed reflector setup or the through transmission setup. The shadowed reflector method displayed in Figure 4.1 was exclusively employed for the group velocity measurements described in this thesis. The data was acquired using a focused piezoelectric transducer (Panametrics V309 transducer with a nominal center frequency of 5 MHz, a 0.5 inch diameter and a 2 inch point target focus; Panametrics, Waltham, MA) attached to a Panametrics 5800 Pulser/Receiver. The signal was received by the

transducer, amplified by the Pulser/Receiver, and digitized at 8 bits by the TDS5052 Digital Oscilloscope (Tektronix, Beaverton, OR)

The group velocity in the sample was determined using Equation 4.1.

$$v_s = v_h \left[1 + \frac{t_{ref} - t_{samp}}{t_{BW} - t_{FW}} \right] \tag{4.1}$$

where v_h is the velocity in the host medium, t_{ref} is the roundtrip time for the reference measurement, t_{samp} is the roundtrip time for the signal to reflect off of the steel reflector and return to the transducer with the sample interspersed, t_{FW} is the roundtrip time for the signal to reflect off of the front wall of the sample and return to the transducer, and t_{BW} is the roundtrip time for the signal to reflect off of the back wall and return to the transducer (Trousil, 2002).

An additional benefit of the Sollish method is that the sample thickness can be determined from the same timing measurements as the group velocity. The sample thickness is given by Equation 4.2

$$\ell = \frac{v_h}{2}[(t_{ref} - t_{samp}) + (t_{BW} - t_{FW})] \tag{4.2}$$

Measuring the sample thickness ultrasonically was the most accurate means of determining the thickness of a liquid in a sample holder with saran wrap windows. The host velocity is calculated using a known polynomial relationship between the temperature of water and the speed of sound in water (Marczak, 1997). The calculated speed of sound in water over a small range of temperatures typical for the experiment is shown in Table 4.1 (Marczak, 1997). The temperature of the host medium was monitored throughout all of the experiments and did not vary more than 0.2°C

Temperature (°C)	Predicted Water Velocity (m/s)
19.0	1479.3
19.1	1479.6
19.2	1479.9
19.3	1480.2
19.4	1480.5
19.5	1480.8
19.6	1481.1
19.7	1481.5
19.8	1481.8
19.9	1482.1
20.0	1482.4

TABLE 4.1: The calculated speed of sound in water as a function of temperature over a small range of temperatures (Marczak, 1997).

over the course of any of the group velocity measurements. A variation of 0.2°C is approximately equivalent to variation of 0.5 m/s in the speed of sound in the water.

The timing differences necessary for the determination of both the group velocity and sample thickness could be found with a correlation technique (Trousil, 2002). An alternative way of determining the timing differences involved calculating the time at which the maximum of the analytic signal occurs for each signal of interest. The analytic signal of some function of time $x(t)$ is defined in Equation 4.3

$$x_a(t) = x(t) + i * H[x(t)] \tag{4.3}$$

where $x_a(t)$ is the analytic signal of $x(t)$ and $H[x(t)]$ is the Hilbert transform of $x(t)$

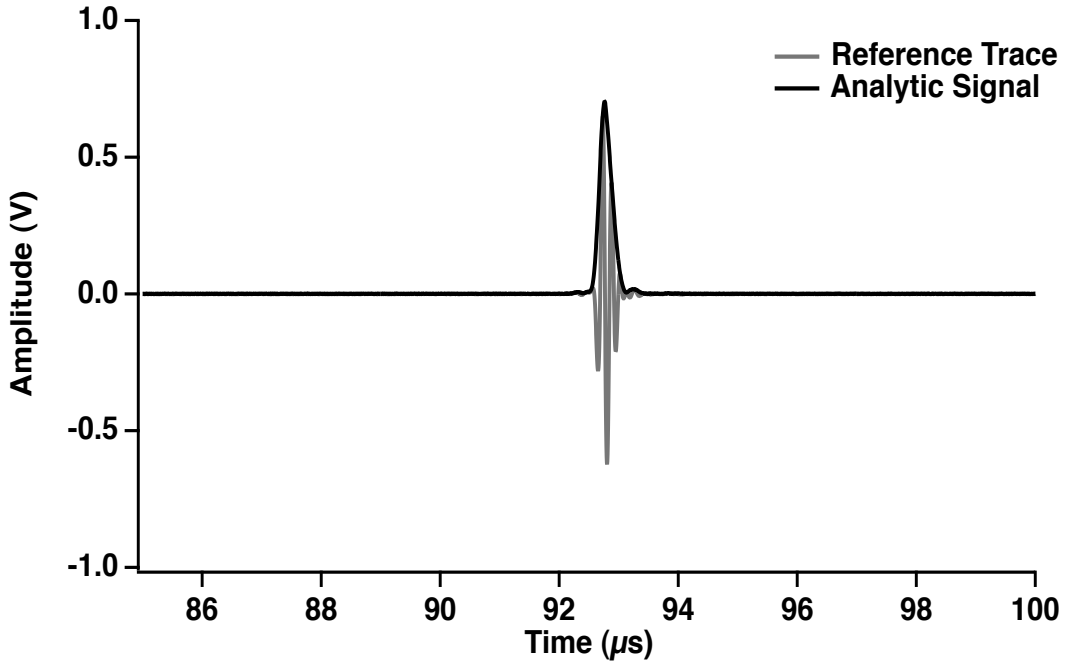

FIGURE 4.2: An example reference trace is plotted with the magnitude of its analytic signal.

(Bracewell, 2000). The magnitude of the analytic signal is defined in Equation 4.4

$$|x_a(t)| = \sqrt{x^2(t) + (H[x(t)])^2} \tag{4.4}$$

An example reference signal is plotted in Figure 4.2 along with the magnitude of its analytic signal determined using Equation 4.4. The time where the maximum of the analytic signal of the reference signal occurred was determined to be t_{ref}. The time of the corresponding maxima in the analytic signal for the front wall signal, back wall signal, and sample signal were used to find t_{FW}, t_{BW}, and t_{samp}. Figure 4.3 plots the front wall, back wall, and steel reflector signals along with their corresponding analytic signals for an example trace.

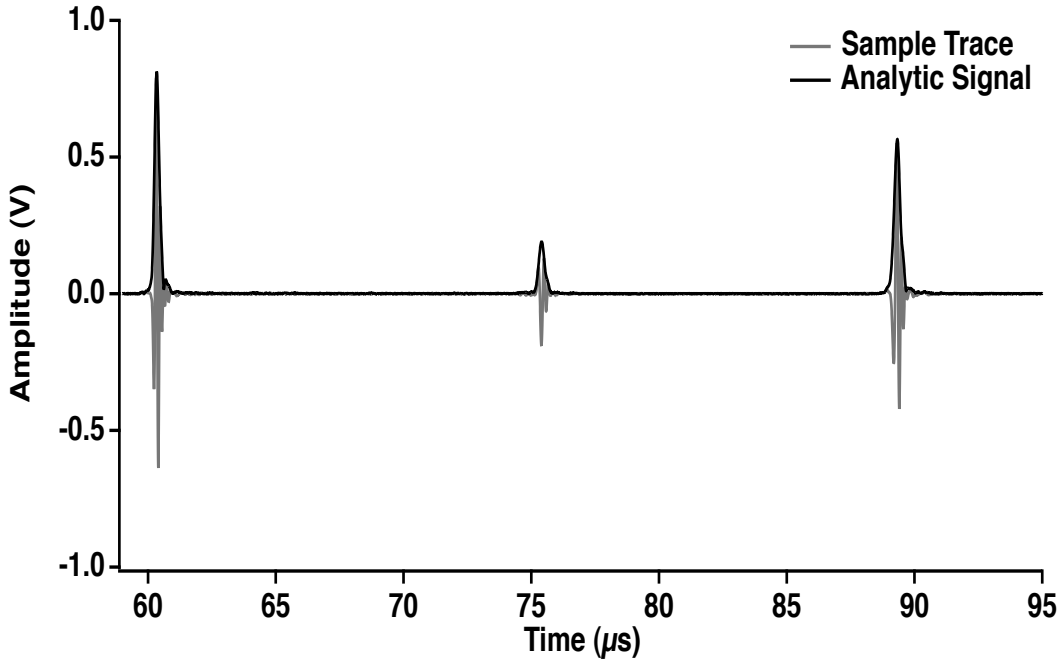

FIGURE 4.3: A sample trace containing the front wall, back wall, and sample reflector signals is plotted with the magnitudes of the corresponding analytic signals.

4.3 Cornstarch Measurements

The group velocity was measured for eight samples of cornstarch in a density-matched solution at concentrations (by mass) of 10%, 20%, 30%, and 40%. Group velocity measurements were also made of suspensions of cornstarch and water without cesium chloride. For the cornstarch suspensions in density-matched solutions, shear thickening behavior was apparent only in the 40% concentration. The samples were not sheared during measurement, so the shear thickening behavior only affected how well the samples could be mixed. Extra care was taken to mix the 40% cornstarch samples as thoroughly as possible, but keeping the sample homogeneously mixed throughout the measurements proved difficult. Despite this limitation, reasonable

group velocity measurements were made on a set of 40% cornstarch suspensions in a density-matched cesium chloride solution.

For the suspensions of cornstarch and water without the addition of cesium chloride for density matching, none of the samples were affected by shear thickening behavior. As discussed in Section 3.7.1, the shear thickening behavior was not apparent in cornstarch and water suspensions until a concentration of 50%. These samples were strongly affected by settling, because of the lack of density matching. For this reason, each sample was vigorously agitated before each individual group velocity measurement was recorded. Reasonably reliable data was acquired on all of the measured samples using this method.

4.3.1 10% Cornstarch Suspensions

The group velocity was measured for eight samples of 10% cornstarch suspended in a 51.5% cesium chloride solution using the Sollish method. The results of those measurements are presented in Table 4.2 along with the approximate temperature of the water during each measurement and the standard deviation in the measurement.

Group velocity measurements were also made on four suspensions of 10% cornstarch in water. The results are displayed in Table 4.3. The absolute magnitude of the group velocity measured in these samples was approximately 30 m/s lower the magnitude of a 10% cornstarch in density-matched cesium chloride brine. The presence of the cesium chloride partially explains this difference. Additionally, more cornstarch

	Temperature (°C)	Group Velocity (m/s)	Standard Deviation (m/s)
10% Cornstarch Suspension #1	19.3	1534	8
10% Cornstarch Suspension #2	19.1	1534	7
10% Cornstarch Suspension #3	18.6	1529	5
10% Cornstarch Suspension #4	20.0	1531	4
10% Cornstarch Suspension #5	19.2	1530	5
10% Cornstarch Suspension #6	18.7	1530	6
10% Cornstarch Suspension #7	19.2	1531	5
10% Cornstarch Suspension #8	20.0	1530	6
Average	-	1531	6

TABLE 4.2: The group velocity measured in the eight samples of the 10% cornstarch suspension in a 51.5% cesium chloride brine.

needs to be added to a 10% suspension in a 51.5% cesium chloride solution to achieve the same volume fraction than in an equivalent amount of just water. Thus, the presence of more cornstarch in the density-matched suspensions also helps to explain the difference. The effect of the faster settling rate in the cornstarch and water suspension can be seen in the higher standard deviation in these measurements than in the standard deviations of the measurements in the approximately density-matched solution.

4.3.2 20% Cornstarch Suspensions

Eight samples of 20% cornstarch suspended in a density-matched cesium chloride brine had their group velocity measured. Group velocity measurements were also

	Temperature (°C)	Group Velocity (m/s)	Standard Deviation (m/s)
10% Cornstarch in Water #1	19.2	1500	10
10% Cornstarch in Water #2	19.3	1499	11
10% Cornstarch in Water #3	19.2	1497	9
10% Cornstarch in Water #4	19.2	1499	12
Average	-	1499	10

TABLE 4.3: The group velocity measured in the eight samples of the 10% cornstarch suspension in water.

made on four samples of 20% cornstarch suspended in plain water. The results of those measurements are presented in Tables 4.4 and 4.5. These results are consistent with the 10% cornstarch measurements in that the absolute magnitude of the group velocity is higher in the density-matched suspensions, whereas the standard deviation is lower.

4.3.3 30% Cornstarch Suspensions

Group velocity measurements of eight samples of 30% cornstarch suspended in a density-matched cesium chloride solution and four samples of 30% cornstarch in water were made. The results of both of these measurements are presented in Tables 4.6 and 4.7. The magnitude of the group velocity is higher in the density-matched suspensions, whereas the standard deviation is lower consistent with the results in the other suspensions.

	Temperature (°C)	Group Velocity (m/s)	Standard Deviation (m/s)
20% Cornstarch Suspension #1	19.5	1605	5
20% Cornstarch Suspension #2	19.6	1604	7
20% Cornstarch Suspension #3	19.6	1604	5
20% Cornstarch Suspension #4	19.7	1601	6
20% Cornstarch Suspension #5	19.5	1596	4
20% Cornstarch Suspension #6	19.5	1596	7
20% Cornstarch Suspension #7	21.1	1606	6
20% Cornstarch Suspension #8	20.6	1604	7
Average	-	1602	6

TABLE 4.4: The group velocity measured in the eight samples of the 20% cornstarch suspension in density-matched cesium chloride brine.

	Temperature (°C)	Group Velocity (m/s)	Standard Deviation (m/s)
20% Cornstarch in Water #1	18.8	1525	10
20% Cornstarch in Water #2	19.2	1522	13
20% Cornstarch in Water #3	19.1	1516	11
20% Cornstarch in Water #4	19.2	1522	10
Average	-	1521	11

TABLE 4.5: The group velocity measured in the four samples of the 20% cornstarch suspension in water.

	Temperature (°C)	Group Velocity (m/s)	Standard Deviation (m/s)
30% Cornstarch Suspension #1	20.6	1673	6
30% Cornstarch Suspension #2	20.6	1672	6
30% Cornstarch Suspension #3	20.4	1677	7
30% Cornstarch Suspension #4	20.4	1666	4
30% Cornstarch Suspension #5	19.6	1673	5
30% Cornstarch Suspension #6	19.5	1673	8
30% Cornstarch Suspension #7	19.4	1663	7
30% Cornstarch Suspension #8	19.5	1669	5
Average	-	1671	6

TABLE 4.6: The group velocity measured in the eight samples of the 30% cornstarch suspension in density-matched cesium chloride brine.

	Temperature (°C)	Group Velocity (m/s)	Standard Deviation (m/s)
30% Cornstarch in Water #1	18.9	1558	12
30% Cornstarch in Water #2	18.9	1557	11
30% Cornstarch in Water #3	18.9	1543	11
30% Cornstarch in Water #4	18.9	1549	8
Average	-	1552	11

TABLE 4.7: The group velocity measured in the four samples of the 30% cornstarch suspension in water.

	Temperature (°C)	Group Velocity (m/s)	Standard Deviation (m/s)
40% Cornstarch Suspension #1	18.7	1763	9
40% Cornstarch Suspension #2	18.6	1772	10
40% Cornstarch Suspension #3	19.8	1758	8
40% Cornstarch Suspension #4	19.8	1758	9
40% Cornstarch Suspension #5	20.8	1753	9
40% Cornstarch Suspension #6	20.8	1764	10
40% Cornstarch Suspension #7	20.6	1770	8
40% Cornstarch Suspension #8	18.5	1778	9
Average	-	1765	9

TABLE 4.8: The group velocity measured in the eight samples of the 40% cornstarch suspension in density-matched cesium chloride brine.

4.3.4 40% Cornstarch Suspensions

Group velocity measurements of eight samples of 40% cornstarch suspended in a density-matched cesium chloride solution and four samples of 40% cornstarch in water were made. The results of these measurements are presented in Tables 4.8 and 4.9. Unlike the measurements at the lower concentrations of cornstarch, the standard deviation in the measurement was approximately the same between the samples that were density-matched and those that were not. This is a reflection of the difficulty of creating a homogeneous solution when trying to mix a shear thickening fluid. The magnitude of the group velocity is still much higher in the suspensions with the cesium chloride brine than in the suspensions in water.

	Temperature (°C)	Group Velocity (m/s)	Standard Deviation (m/s)
40% Cornstarch in Water #1	19.1	1586	10
40% Cornstarch in Water #2	19.1	1587	9
40% Cornstarch in Water #3	19.2	1599	12
40% Cornstarch in Water #4	19.0	1585	11
40% Cornstarch in Water #3	19.1	1598	10
40% Cornstarch in Water #4	18.9	1603	11
Average	-	1593	11

TABLE 4.9: The group velocity measured in the four samples of the 40% cornstarch suspension in water.

4.3.5 Summary of Group Velocity Measurements

The group velocity in the cornstarch suspensions in 51.5% cesium chloride solutions was plotted as a function of cornstarch concentration in Figure 4.4. The group velocity in the cornstarch suspensions increases fairly systematically from 0% to 30% cornstarch. The 0% cornstarch measurements were of a 51.5% cesium chloride in water solution described in Section 3.3. The increase in the group velocity between 30% and 40% is higher than the increase seen between the lower concentrations.

The group velocity in the cornstarch in water suspensions as a function of cornstarch concentration is plotted in Figure 4.5. The group velocity is seen to increase rather systematically with concentration. The group velocity measurements for both sets of cornstarch suspensions are plotted in Figure 4.6 as a function of cornstarch concentration. One should note that the amount of cornstarch in the density-matched

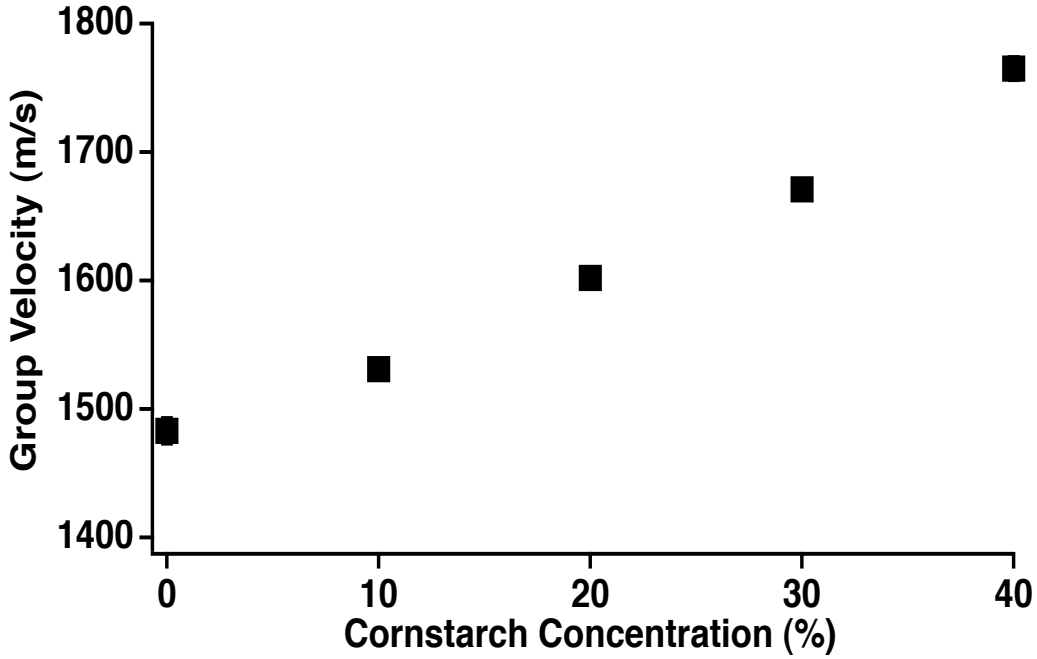

FIGURE 4.4: The group velocity of the cornstarch in cesium chloride suspensions plotted as a function of cornstarch concentration. The 0% cornstarch concentration is a solution 51.5% cesium chloride. The mean ± the standard deviation is plotted although the error bars are too small to be visible.

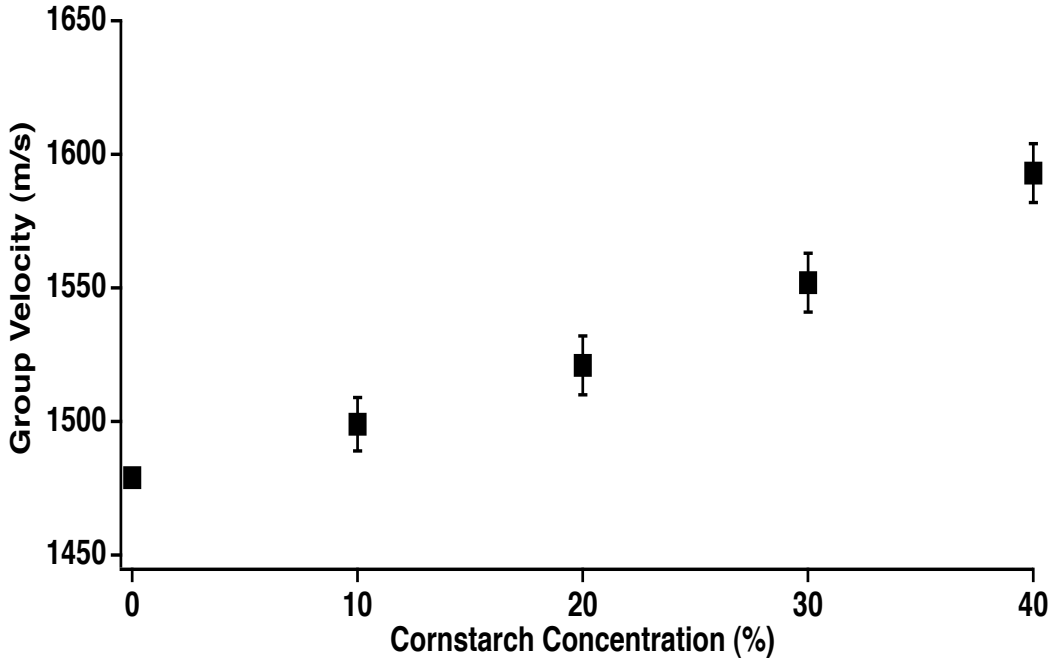

FIGURE 4.5: The group velocity of the cornstarch in water suspensions plotted as a function of cornstarch concentration. The 0% cornstarch concentration is the speed of sound in water calculated at 19.0°C.

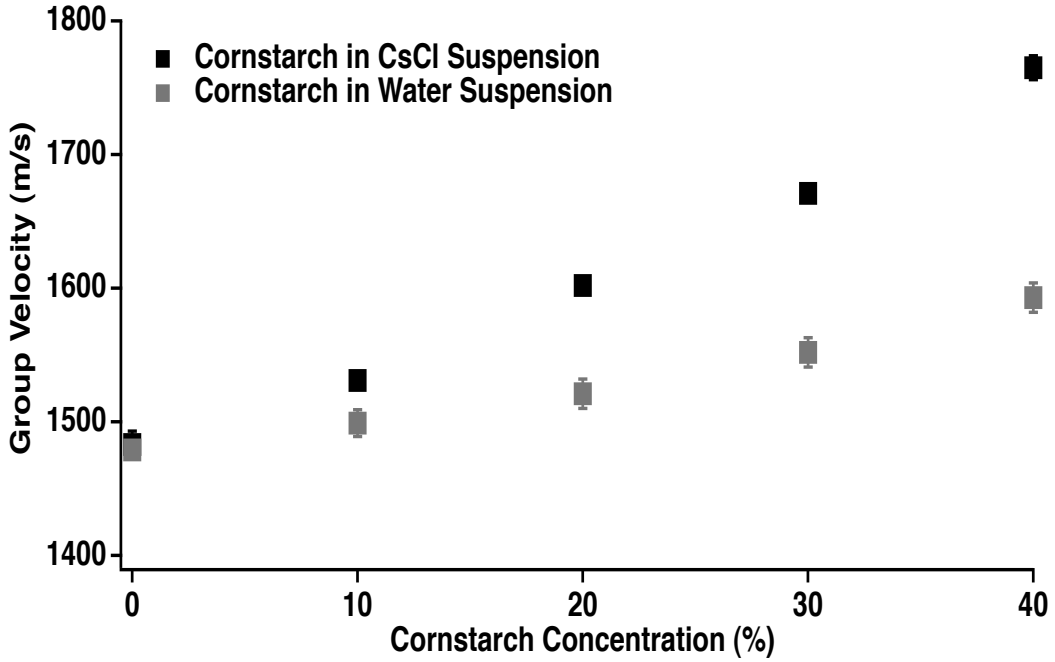

FIGURE 4.6: A comparison between the group velocity of cornstarch in cesium chloride suspensions and cornstarch in water suspensions.

suspensions is larger than in the cornstarch in water suspensions even at the same concentration.

4.4 Conclusion

Group velocity and sample thickness measurements were made on a number of concentrations of cornstarch suspensions in both a density-matched brine and in plain water. While interesting in their own right, these measurements are also critical to the measurement of the attenuation, the phase velocity, and the backscatter coefficient described in the next several chapters.

Bibliography

Bracewell, R. (**2000**). *The Fourier Transform and its Applications*, 3rd edition (McGraw-Hill).

Marczak, W. (**1997**). "Water as a standard in the measurements of speed of sound in liquids", J Acoust Soc Am **102**, 2776–2779.

Sollish, B. (**1979**). "A device for measuring ultrasonic propagation velocity in tissue", National Bureau of Standards, Spec. Publ. 525: Ultrasonic Tissue Charaterization II .

Trousil, R. (**2002**). "Ultrasonic propagation in inhomogeneous media: toward quantitative ultrasonic imaging", Ph.D. thesis, Washington University in St. Louis.

Chapter 5

Attenuation Measurements of Cornstarch Suspensions

5.1 Preface

This chapter outlines the methods and results of the attenuation measurements in the cornstarch suspensions. The first section discusses the experimental methods involved with the measurement. The next section details a study looking into an experimental diffraction correction. The last section describes the measurement of the attenuation coefficient as a function of frequency for each of the concentrations of the cornstarch suspensions.

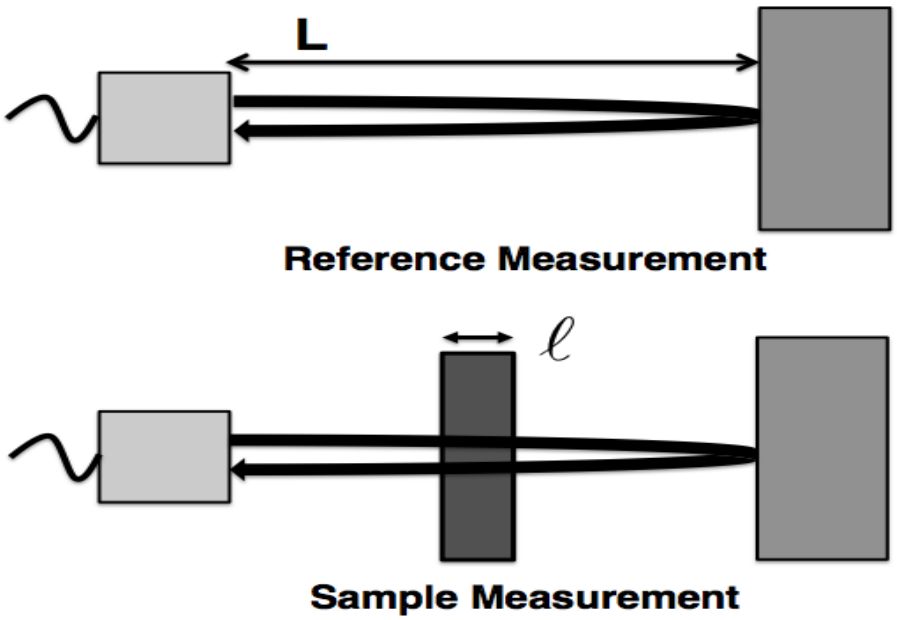

FIGURE 5.1: The shadowed reflector experimental setup for the measurement of the attenuation coefficient as a function of frequency.

5.2 Experimental Methods

The attenuation properties of the cornstarch suspensions were measured using the shadowed reflector method shown in Figure 5.1. The frequency dependent attenuation coefficient was determined using the log-spectral subtraction method (Ophir *et al.*, 1984; Trousil, 2002). The reference measurement was made by recording the reflection of a signal off of a steel reflector placed at the focus of the transducer (the distance "L" in Figure 5.1). The sample measurement was also made with the focus of the transducer on the steel reflector but with a sample of thickness ℓ placed in between the transducer and the reflector.

The reference power spectrum, $|\tilde{V}_{ref}|^2$, is given by Equation 5.1.

$$|\tilde{V}_{ref}|^2 = |\tilde{E}_0(f)|^2 * [e^{-\alpha_w(f)*(2L)}]^2 * (\mathrm{R}^I_{w\to r}) \tag{5.1}$$

where $|\tilde{E}_0(f)|^2$ represents the frequency responses of the transducer and the electronics, $\alpha_w(f)$ is the amplitude attenuation coefficient in the water, and $\mathrm{R}^I_{w\to r}$ is the intensity reflection coefficient at the boundary between the water and the steel reflector (Trousil, 2002). The intensity reflection coefficient due to the interface between the water and the steel reflector can be determined using Equation 5.2

$$\mathrm{R}^I_{w\to r} = \frac{|\tilde{Z}_r - \tilde{Z}_w|^2}{|\tilde{Z}_r + \tilde{Z}_w|^2} \tag{5.2}$$

where $\tilde{Z}_r$ is the complex acoustic impedance of the steel reflector and $\tilde{Z}_w$ is the complex acoustic impedance of the water (Trousil, 2002). Although the complex acoustic impedances are shown in Equation 5.2, the acoustic impedance can be approximated as real because the attenuation coefficient is very small compared to the wavenumber in both water and steel. The power spectrum of the sample, $|\tilde{V}_{samp}|^2$, can be determined using Equation 5.3

$$|\tilde{V}_{samp}|^2 = |\tilde{E}_0(f)|^2 * [e^{-\alpha_w(f)*(2(L-\ell))}]^2 * [e^{-\alpha_s(f)*(2\ell)}]^2 * (\mathrm{R}^I_{w\to r}) * (\mathrm{T}^I_{w\to s\to c}(f))^2 * (\mathrm{T}^I_{c\to s\to w}(f))^2 \tag{5.3}$$

where α_s is the amplitude attenuation coefficient in the sample, and $\mathrm{T}^I_{w\to s\to c}$ and $\mathrm{T}^I_{c\to s\to w}$ are the frequency-dependent intensity transmission coefficients at the interface between the water, the thin saran wrap window, and the cornstarch suspension (Trousil, 2002). The duration of the pulses used in this thesis are on the order of mi-

croseconds, whereas the round trip travel time in the saran wrap windows is approximately two orders of magnitude smaller (Trousil, 2002). Therefore, the transmission coefficients can be expressed in their steady state form (Trousil, 2002; Wear *et al.*, 2005; Ford, 1970). The steady-state form of the intensity transmission coefficients between the water, saran wrap, and cornstarch suspension interface is expressed in Equation 5.4

$$\mathrm{T}^{I}_{w\to s\to c}(f) = \mathrm{T}^{I}_{c\to s\to w}(f) = \frac{4\tilde{Z}_w\tilde{Z}_c}{(\tilde{Z}_w+\tilde{Z}_c)^2 * \cos^2(k_s h) + [\tilde{Z}_s + \tilde{Z}_w * \tilde{Z}_c/\tilde{Z}_s]^2 * \sin^2(k_s h)} \tag{5.4}$$

where $\tilde{Z}_c$ is the complex acoustic impedance of the cornstarch suspension and $\tilde{Z}_s$ is the complex acoustic impedance of the saran wrap, k_s is the wavenumber in the saran wrap, and h is the thickness of the saran wrap (Trousil, 2002). The thin saran wrap layer at the interface causes the intensity transmission coefficients to have a slight frequency dependence. An example intensity transmission coefficient calculated for a 10% cornstarch suspension in a 51.5% cesium chloride solution is plotted in Figure 5.2.

The reference power spectrum provides a means for compensating for the system dependent effects. In order to do this compensation, the signal loss in the system is determined by dividing the reference power spectrum by the sample power spectrum as shown in Equation 5.5

$$\frac{|\tilde{V}_{ref}|^2}{|\tilde{V}_{samp}|^2} = \frac{e^{4*(\alpha_s(f)-\alpha_w(f))*\ell}}{(\mathrm{T}^{I}_{w\to s\to c}(f))^2 * (\mathrm{T}^{I}_{c\to s\to w}(f))^2} \tag{5.5}$$

The factor of four in the exponent of the numerator comes from a factor of two because

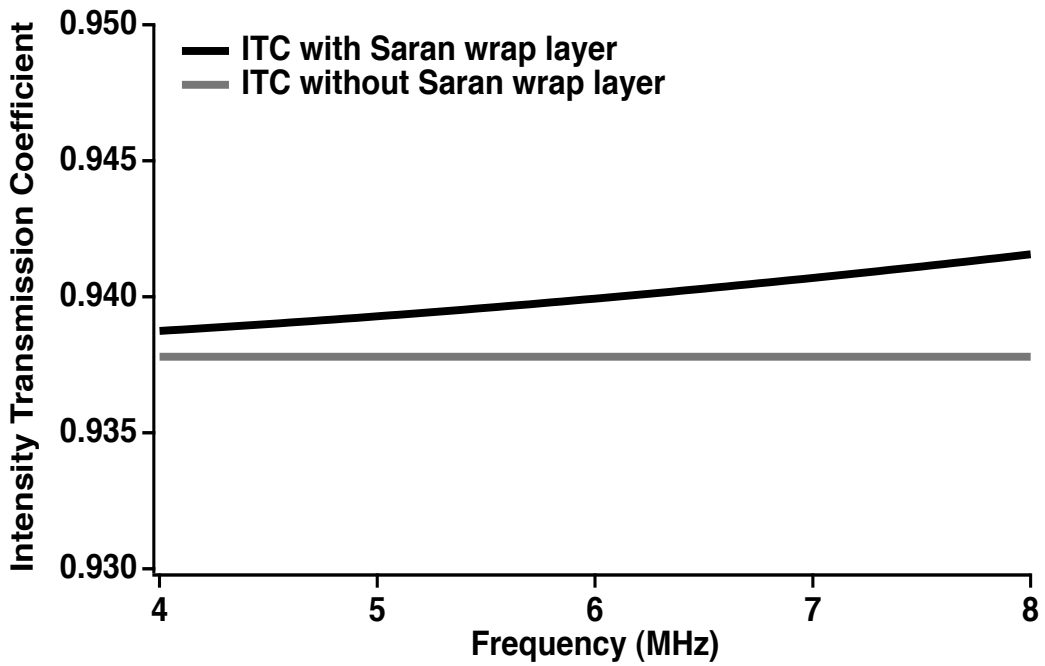

FIGURE 5.2: An example frequency-dependent intensity transmission coefficient calculated at the interface between the water, the very thin saran wrap window, and a 10% cornstarch suspension in 51.5% cesium chloride solution. The intensity transmission coefficient between the water and a 10% cornstarch suspension in 51.5% cesium chloride solution is also plotted for comparison.

of considering the power, and another factor of two due to traversing the sample twice in the shadowed reflector setup. At the frequencies studied in this thesis (between 1 and 10 MHz) the attenuation coefficient in the sample, $\alpha_s(f)$, is several orders of magnitude larger than the attenuation coefficient in the water, α_w. The attenuation coefficient in the cornstarch samples is at minimum on the order of 0.1 Np/cm at 5 MHz, while the attenuation coefficient in water is on the order of 10^{-3} Np/cm at 5 MHz (Markham *et al.*, 1951; Trousil, 2002). Thus for these measurements, the attenuation coefficient in the water was considered negligible and the signal loss could be re-expressed in Equation 5.6

$$\frac{|\tilde{V}_{ref}|^2}{|\tilde{V}_{samp}|^2} = \frac{e^{4*\alpha_s(f)*\ell}}{(\mathrm{T}^I_{w\to s\to c}(f))^2 * (\mathrm{T}^I_{c\to s\to w}(f))^2}. \tag{5.6}$$

The signal loss is converted into the logarithmic (base ten) domain in Equation 5.7 using the standard rules of logarithms

$$10*\log(|\tilde{V}_{ref}|^2) - 10*\log(|\tilde{V}_{samp}|^2) = \frac{20}{\ln(10)} * [\alpha_s(f)*2\ell] - 10*\log[(\mathrm{T}^I_{w\to s\to c}(f))^2 * (\mathrm{T}^I_{c\to s\to w}(f))^2]. \tag{5.7}$$

The units of the attenuation coefficient as expressed are Np/m, but the factor $\frac{20}{\ln(10)}$ is a conversion between Nepers and decibels. The name of the log spectral subtraction technique arises as a result of the expression in Equation 5.7. Because the attenuation coefficient in the sample is the experimental parameter of interest, Equation 5.7 can be rearranged to arrive at Equation 5.8 (Trousil, 2002).

$$\alpha_s^{dB}(f) = \frac{1}{2\ell} * [10*\log(|\tilde{V}_{ref}|^2) - 10*\log(|\tilde{V}_{samp}|^2)] + \frac{1}{2\ell} * 10*\log[(\mathrm{T}^I_{w\to s\to c}(f))^2 * (\mathrm{T}^I_{c\to s\to w}(f))^2]. \tag{5.8}$$

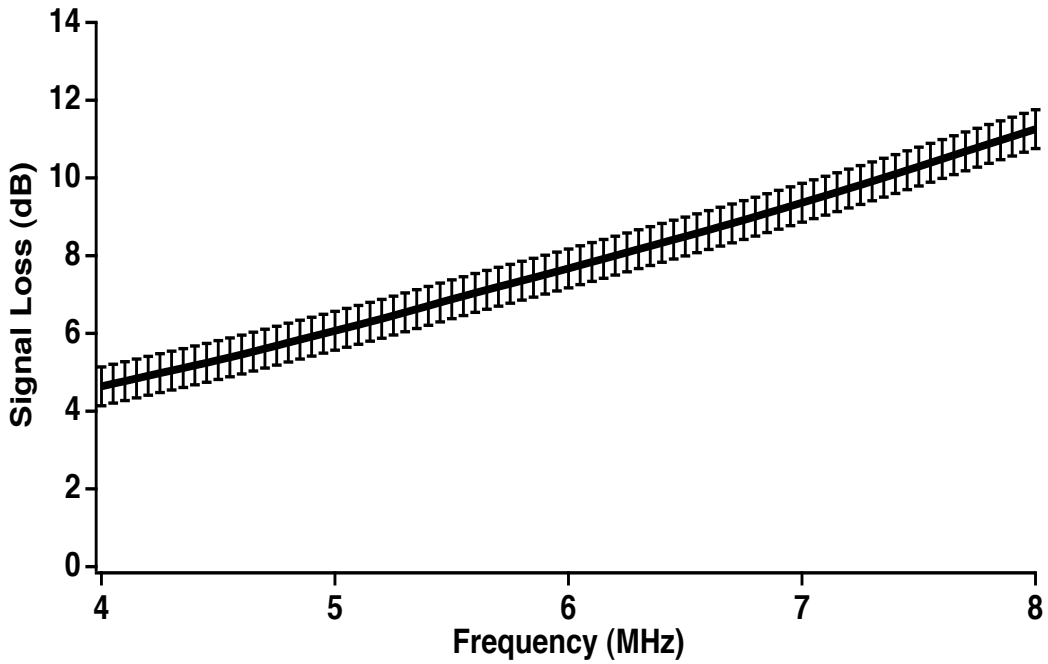

FIGURE 5.3: The signal loss for an example 10% cornstarch suspension in a 51.5% cesium chloride solution. The signal loss is the logarithm of the reference power spectrum minus the logarithm of the sample power spectrum. The error bars are ± one standard deviation in the measurement.

The reference and sample power spectra are determined from the experimental measurements of the reference and sample signals. The log spectral subtraction of the two power spectra detailed in first term on the right hand side of Equation 5.8 results in the signal loss as displayed in Figure 5.3. The signal loss is then compensated by the intensity transmission coefficients and the sample thickness in order to arrive at the experimentally measured attenuation coefficient. The attenuation coefficient for an example 10% cornstarch suspension in Figure 5.4 (Trousil, 2002).

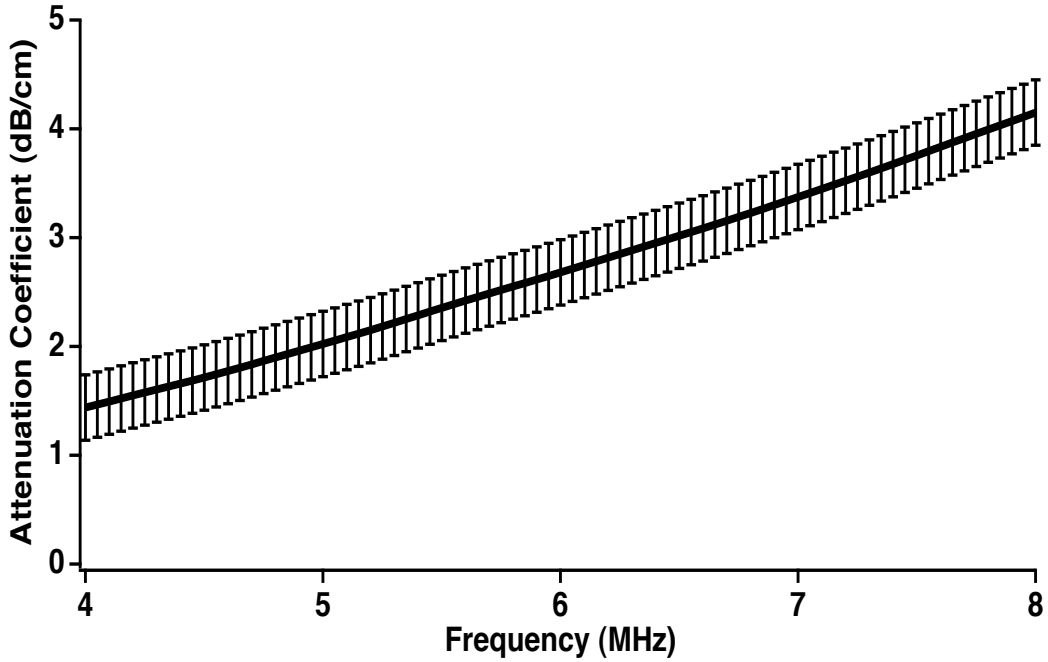

FIGURE 5.4: The attenuation coefficient plotted in dB/cm for an example 10% cornstarch suspension in a 51.5% cesium chloride solution. The attenuation coefficient is the signal loss compensated by the intensity transmission coefficients and the sample thickness. The error bars are ± one standard deviation in the measurement.

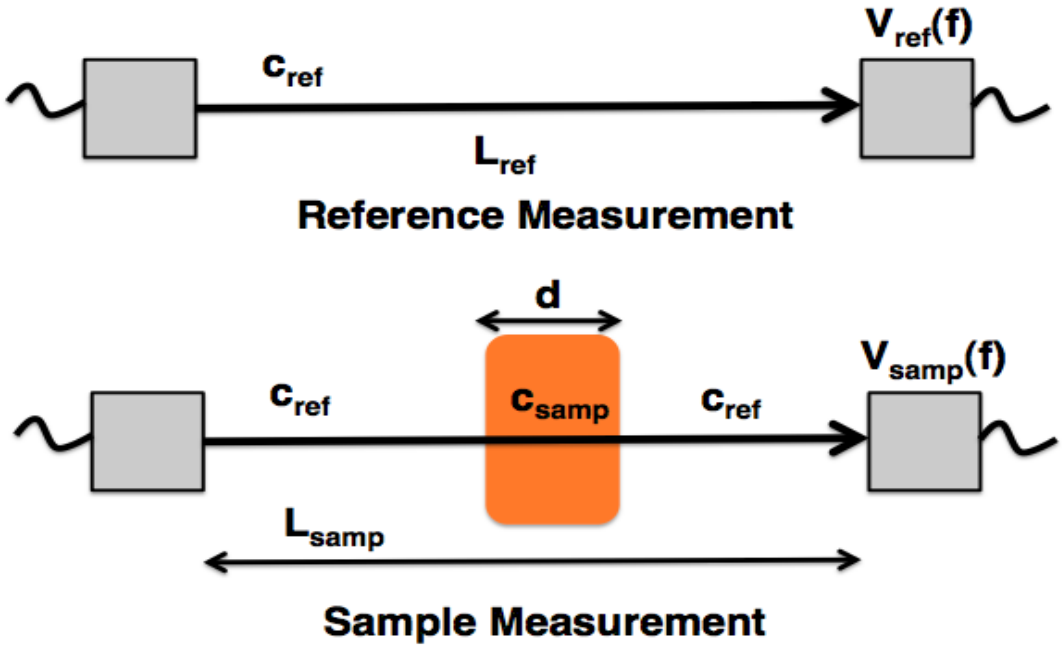

FIGURE 5.5: The experimental setup for the measurement of the attenuation coefficient of the cornstarch suspensions used for exploring the diffraction correction.

5.3 Diffraction Correction

The effect of diffraction on the measurement of the attenuation coefficient as a function of frequency was a concern with all of the measurements of the cornstarch. An experimental diffraction correction had been developed by Wu and Kaufman and independently derived by Laboratory for Ultrasonics alumnus Chris Lloyd (Xu and Kaufman, 1993; Lloyd, 2010). The Lloyd formalism will be followed throughout this section (Lloyd, 2010). Figure 5.5 displays the experimental setup and necessary parameters.

The near field distance for a single frequency of a planar transducer can be calcu-

lated using Equation 5.9

$$N = \frac{a^2}{\lambda} * [1 - (\frac{\lambda}{2a})^2] \tag{5.9}$$

where a is the radius of the transducer and λ is the wavelength of the ultrasonic signal. For all the measurements in this thesis the transducer had a center frequency of 5 MHz and a radius of one half inch. For these parameters and a typical ultrasonic sound speed in water (approximately 1500 m/s), $\lambda/a^2 \ll 1$ and thus the near field distance can be approximated using Equation 5.10

$$N \approx \frac{a^2}{\lambda} = \frac{a^2 f}{c} \tag{5.10}$$

where f is the frequency of interest and c is the ultrasonic speed of sound. For a particular experimental setup, the transmitting transducer radius and the frequency of interest does not change, and thus the near field distance and the speed of sound are inversely related. An equivalent statement would be for a particular experimental setup, the product of the propagation distance, L_{ref}, and the speed of sound in the host medium, c_{ref}, is fixed. The equivalent expression for the sample measurement shown in Equation 5.11 can be found from examining Figure 5.5.

$$L_{ref}c_{ref} = constant = (L_{samp} - d)c_{ref} + dc_{ref}. \tag{5.11}$$

Rearranging the terms in Equation 5.11 and solving for L_{samp} results in Equation 5.12

$$L_{samp} = L_{ref} + d(1 - c_{samp}/c_{ref}) \tag{5.12}$$

The receiving transducer can thus be moved closer or further away from the transmitting transducer for the sample measurement depending on the sample thickness

Cornstarch Concentration	Sample Thickness	Group Velocity	Diffraction Correction
0% Cornstarch (c_{ref})	∼13 mm	1483 m/s ± 10 m/s	0.0000 m
10% Cornstarch	∼13 mm	1531 m/s ± 6 m/s	-0.0004 m
20% Cornstarch	∼13 mm	1602 m/s ± 6 m/s	-0.0010 m
30% Cornstarch	∼13 mm	1671 m/s ± 6 m/s	-0.0016 m
40% Cornstarch	∼13 mm	1765 m/s ± 9 m/s	-0.0026 m

TABLE 5.1: The approximate sample thickness and the average group velocity measurements for each concentration of cornstarch in a 51.5% cesium chloride suspension. The diffraction correction calculated for each concentration is also displayed.

and the ratio of the sample speed of sound to the reference speed of sound. The group velocities and approximate sample thicknesses for each concentration of cornstarch in a density-matched cesium chloride solution are shown in Table 5.1.

Using the values from Table 5.1 and Equation 5.12, the experimental diffraction correction was calculated for each concentration of cornstarch in suspension with a 51.5% cesium chloride solution. The experimental diffraction corrections were also displayed in Table 5.1 with a negative correction indicating that the receiving transducer must be moved that distance closer to the transmitting transducer.

Attenuation measurements were made on a 30% cornstarch suspension in 51.5% cesium chloride solution to test whether the experimental diffraction correction needed to be used for all of the attenuation measurements. The 30% cornstarch suspension was chosen, because this concentration displayed the highest speed of sound of the concentrations examined without displaying shear thickening which would make the

	Slope of Attenuation (dB/cm/MHz)	Attenuation Coefficient at 5 MHz (dB/cm)
Not Diffraction Corrected	2.09 ± 0.01	6.5 ± 0.1
Diffraction Corrected	2.12 ± 0.02	6.4 ± 0.1

TABLE 5.2: The slope of the attenuation coefficient and the attenuation coefficient at 5 MHz for a 30% cornstarch suspension in a 51.5% cesium chloride solution for a normal measurement and a measurement that has been corrected for diffraction.

measurement more difficult. A through transmission measurement of the attenuation coefficient was made in which the distance between the transducers was kept the same for both the reference and the sample measurement (the normal procedure). The through transmission attenuation coefficient measurement was then repeated on the same sample except for this time the receiving transducer was moved 1.6 mm closer to the transmitting transducer for the sample measurement in order to experimentally correct for diffraction. The data was analyzed and the results of the attenuation coefficient measurement are shown in Figure 5.6. The slope of the attenuation coefficient and the attenuation coefficient at 5 MHz for both measurements are displayed in Table 5.2.

The difference between the diffraction-corrected attenuation coefficient and the attenuation coefficient that was not diffraction corrected was negligible for this particular sample. From examining the results of this investigation of one of the 30% cornstarch suspensions, it was concluded that diffraction was having a small effect on the attenuation results and thus would not be compensated for in the experimental

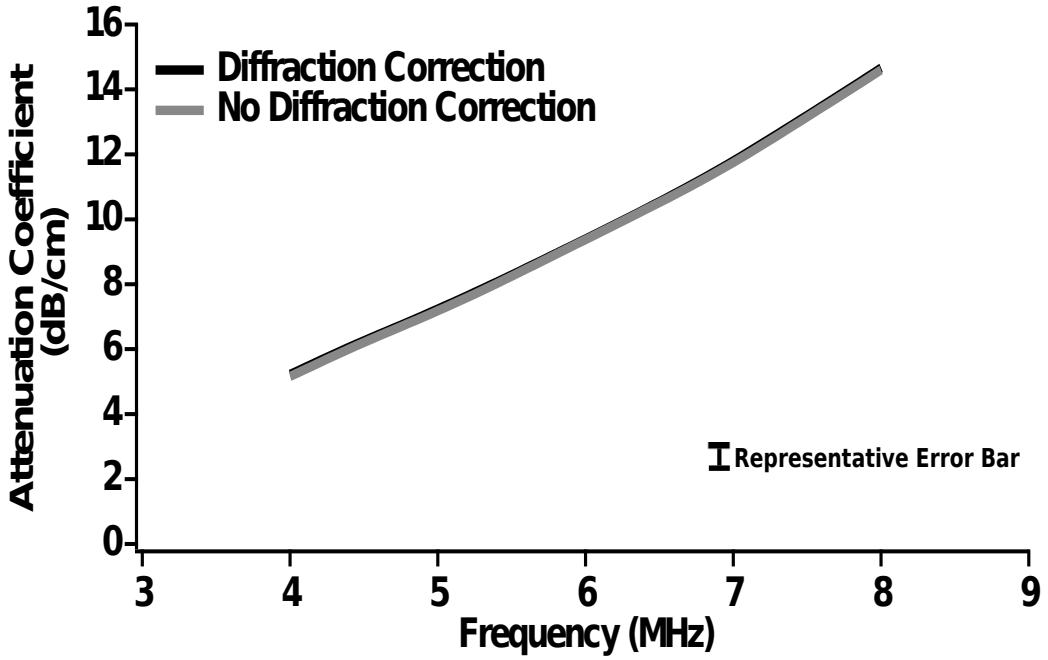

FIGURE 5.6: The attenuation coefficient plotted as a function of frequency for a sample of 30% cornstarch in a 51.5% cesium chloride brine. One of the measurements has been corrected for diffraction and one has not been corrected for diffraction. A representative error bar is shown for ± one standard deviation.

studies described in this thesis. Effects of variations in diffraction arising from imperfect alignment of the transducer, specimen, and reference reflector appear to be small or negligible based on the reproducibility of the results, which are consistent among a significant number of runs for which the experimental configuration was reassembled.

5.4 Attenuation Measurements of Cornstarch Suspensions

Using the methods outlined in Section 5.2, measurements of the attenuation properties of several concentrations of cornstarch suspensions in a 51.5% cesium chloride solution were made. Attenuation measurements were also made on a number of suspensions of cornstarch and water without the addition of the cesium chloride.

5.4.1 10% Cornstarch Suspensions

The frequency-dependent attenuation coefficient of eight 10% cornstarch in 51.5% cesium chlorine brine suspensions was measured and displayed in Figure 5.7. The representative error bar plotted in the figure shows plus or minus one standard deviation for a typical measurement determined from the variability between the individual measurements of each sample. The slope of the attenuation coefficient was determined by a linear fit to the attenuation coefficient data. The attenuation coefficient at 5 MHz and the slope of the attenuation coefficient for each of the eight samples is given in Table 5.3. Both the slope of the attenuation coefficient and the attenuation

coefficient at 5 MHz were consistent over the eight samples measured. The average slope of the attenuation coefficient for the 10% cornstarch suspensions in a 51.5% cesium chloride brine was 0.71 dB/cm/MHz ± 0.02 dB/cm/MHz. The average attenuation coefficient at 5 MHz was 2.04 dB/cm ± 0.05 dB/cm. The small differences observed in the two attenuation parameters are partly due to slight inhomogeneities in the sample due to incomplete mixing. Another potential cause for the difference between the measurements was settling of the cornstarch particles. Although the 51.5% cesium chloride solution is a good match for the density of the cornstarch, some slight settling may occur over the time period of the experiment.

The attenuation coefficient as a function of frequency was measured for two 10% cornstarch in water suspensions and displayed in Figure 5.7. The slope of the attenuation coefficient and the attenuation coefficient at 5 MHz are displayed in Table 5.3. The slope of the attenuation coefficient was approximately 0.3 dB/cm/MHz and the attenuation coefficient at 5 MHz was approximately 0.9 dB/cm in the two samples.

5.4.2 20% Cornstarch Suspensions

The attenuation coefficient as a function of frequency measured in eight 20% cornstarch suspensions in a 51.5% cesium chlorine solution is plotted in Figure 5.8. The slope of the attenuation coefficient was determined by a linear fit to the attenuation coefficient data. Table 5.4 displays the attenuation coefficient at 5 MHz and the slope of the attenuation coefficient for each of the eight samples. Both the slope of the attenuation coefficient and the attenuation coefficient at 5 MHz were consistent

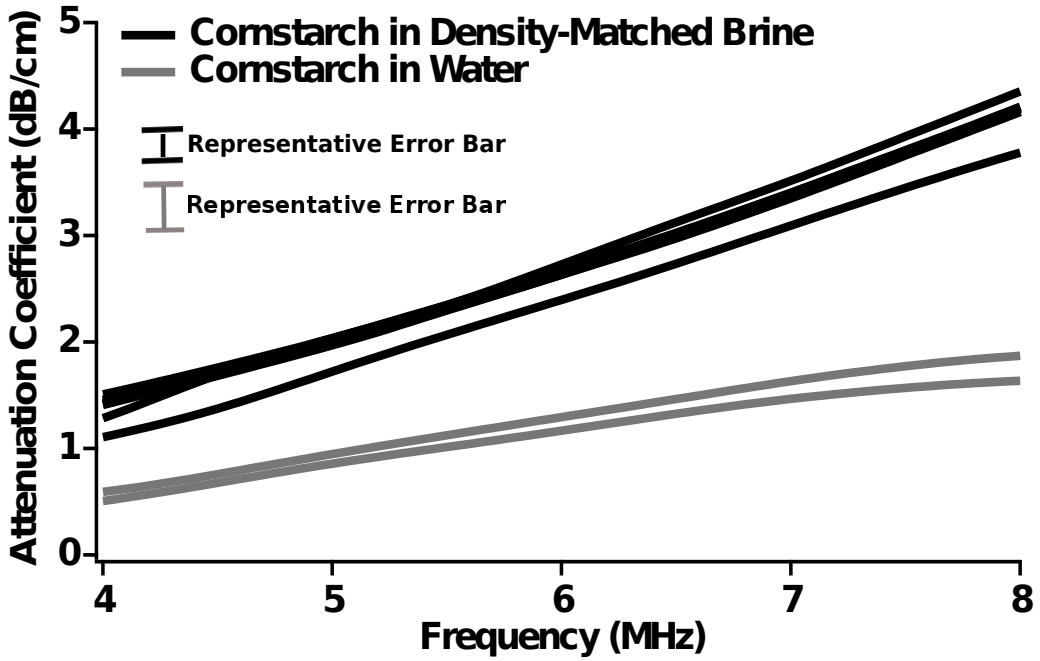

FIGURE 5.7: The attenuation coefficient plotted as a function of frequency for the 10% cornstarch suspensions in density-matched cesium chloride brine. The attenuation coefficient for the 10% cornstarch suspensions in water is plotted as well. A representative error bar displaying plus or minus one standard deviation in the measurement is displayed in the figure for both the density-matched suspensions and the cornstarch in water suspensions.

	Slope of Attenuation (dB/cm/MHz)	Attenuation Coefficient at 5 MHz (dB/cm)
10% Cornstarch Suspension #1	0.71 ± 0.01	2.00 ± 0.05
10% Cornstarch Suspension #2	0.68 ± 0.02	2.03 ± 0.06
10% Cornstarch Suspension #3	0.69 ± 0.01	1.99 ± 0.04
10% Cornstarch Suspension #4	0.71 ± 0.01	2.01 ± 0.05
10% Cornstarch Suspension #5	0.71 ± 0.02	1.97 ± 0.05
10% Cornstarch Suspension #6	0.70 ± 0.01	2.02 ± 0.06
10% Cornstarch Suspension #7	0.69 ± 0.01	1.72 ± 0.07
10% Cornstarch Suspension #8	0.75 ± 0.02	2.04 ± 0.05
Average	0.71 ± 0.02	1.97 ± 0.10
10% Cornstarch in Water #1	0.32 ± 0.09	0.94 ± 0.10
10% Cornstarch in Water #2	0.28 ± 0.11	0.86 ± 0.12

TABLE 5.3: The slope of the attenuation coefficient and the attenuation coefficient at 5 MHz measured in the eight samples of the 10% cornstarch suspension in a 51.5% cesium chloride brine and two samples of a 10% cornstarch in water suspensions.

over the eight samples measured with the average slope of the attenuation coefficient determined to be 1.41 dB/cm/MHz ± 0.05 dB/cm/MHz and the average attenuation coefficient at 5 MHz determined to be 4.32 dB/cm ± 0.22 dB/cm. The small differences observed in the two attenuation parameters across the eight samples are primarily due to slight inhomogeneities in the sample due to incomplete mixing.

The frequency-dependent attenuation coefficient was measured for two 20% cornstarch in water suspensions and displayed in Figure 5.8. The slope of the attenuation coefficient and the attenuation coefficient at 5 MHz are displayed in Table 5.4. The slope of the attenuation coefficient was approximately 0.55 dB/cm/MHz and the attenuation coefficient at 5 MHz was approximately 2 to 3 dB/cm in the two samples.

5.4.3 30% Cornstarch Suspensions

The attenuation coefficient of eight 30% cornstarch suspensions in a 51.5% cesium chlorine solution were measured. The results of those measurements are plotted in Figure 5.9. The slope of the attenuation coefficient was determined by a linear fit to the attenuation coefficient data. Table 5.5 displays the attenuation coefficient at 5 MHz and the slope of the attenuation coefficient for each of the eight samples. Both the slope of the attenuation coefficient and the attenuation coefficient at 5 MHz were consistent over the eight samples measured with the average slope of the attenuation coefficient determined to be 2.12 dB/cm/MHz ± 0.11 dB/cm/MHz and the average attenuation coefficient at 5 MHz determined to be 6.71 dB/cm ± 0.45 dB/cm. The

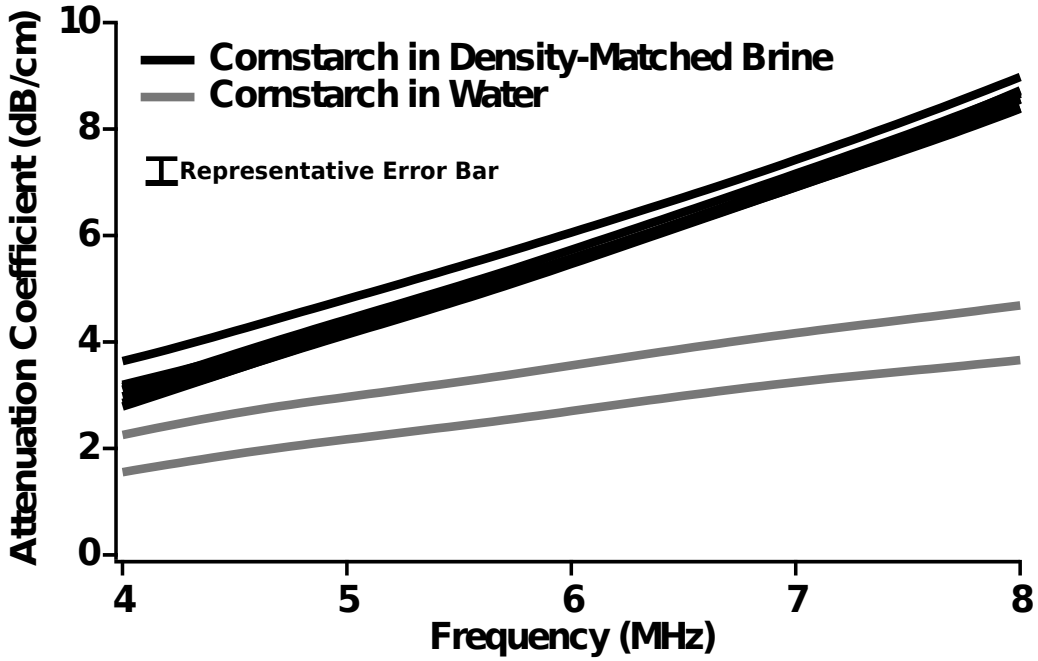

FIGURE 5.8: The attenuation coefficient plotted as a function of frequency for the 20% cornstarch suspensions in density-matched cesium chloride brine. The attenuation coefficient for the 20% cornstarch suspensions in water is plotted as well. A representative error bar displaying plus or minus one standard deviation in the measurement is displayed in the figure that approximately represents the error in both the density-matched suspension measurement and the cornstarch in water measurement.

	Slope of Attenuation (dB/cm/MHz)	Attenuation Coefficient at 5 MHz (dB/cm)
20% Cornstarch Suspension #1	1.42 ± 0.04	4.43 ± 0.19
20% Cornstarch Suspension #2	1.36 ± 0.03	4.81 ± 0.25
20% Cornstarch Suspension #3	1.41 ± 0.08	4.14 ± 0.11
20% Cornstarch Suspension #4	1.38 ± 0.06	4.22 ± 0.19
20% Cornstarch Suspension #5	1.45 ± 0.06	4.16 ± 0.06
20% Cornstarch Suspension #6	1.39 ± 0.01	4.26 ± 0.09
20% Cornstarch Suspension #7	1.41 ± 0.01	4.27 ± 0.04
20% Cornstarch Suspension #8	1.42 ± 0.02	4.30 ± 0.05
Average	1.41 ± 0.05	4.32 ± 0.22
20% Cornstarch in Water #1	0.58 ± 0.07	2.97 ± 0.14
20% Cornstarch in Water #2	0.51 ± 0.04	2.17 ± 0.31

TABLE 5.4: The slope of the attenuation coefficient and the attenuation coefficient at 5 MHz measured in the eight samples of the 20% cornstarch suspension in a 51.5% cesium chloride brine and two samples of a 20% cornstarch in water suspensions.

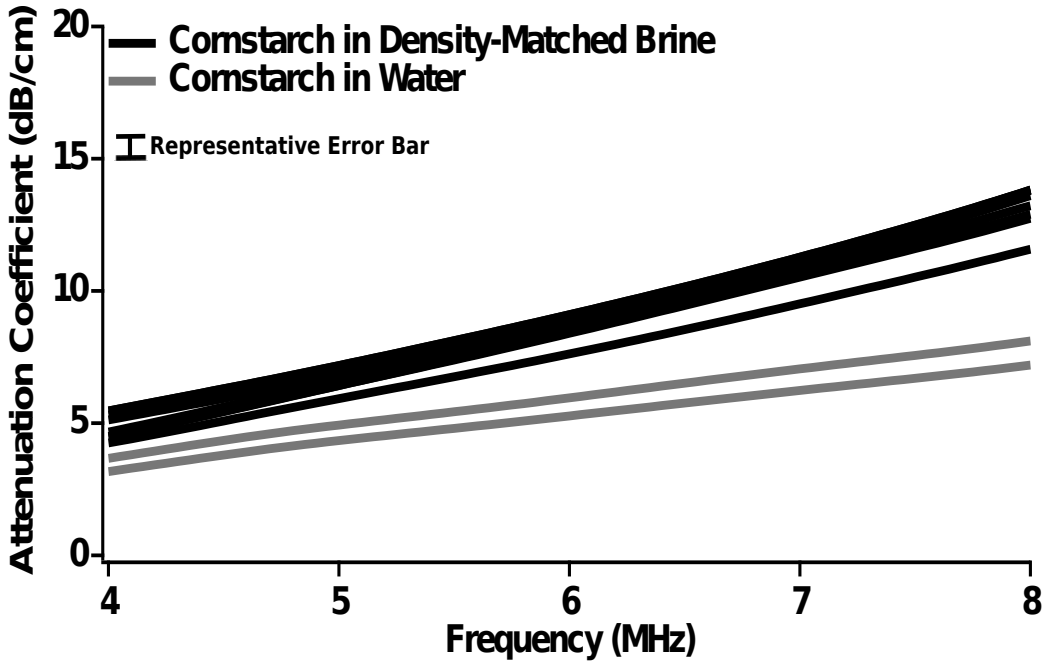

FIGURE 5.9: The attenuation coefficient plotted as a function of frequency for the 30% cornstarch suspensions in density-matched cesium chloride brine. The attenuation coefficient for the 30% cornstarch suspensions in water is plotted as well. A representative error bar displaying plus or minus one standard deviation in the measurement is displayed in the figure that approximately represents the error in both the density-matched suspension measurement and the cornstarch in water measurement.

small differences observed in the two attenuation parameters across the eight samples are primarily due to slight inhomogeneities in the sample due to incomplete mixing.

The frequency-dependent attenuation coefficient was measured for two 30% cornstarch in water suspensions and displayed in Figure 5.9. The slope of the attenuation coefficient and the attenuation coefficient at 5 MHz are displayed in Table 5.5. The slope of the attenuation coefficient was approximately 1.0 dB/cm/MHz and the attenuation coefficient at 5 MHz was approximately 4.5 dB/cm in the two samples.

	Slope of Attenuation (dB/cm/MHz)	Attenuation Coefficient at 5 MHz (dB/cm)
30% Cornstarch Suspension #1	2.14 ± 0.04	7.18 ± 0.16
30% Cornstarch Suspension #2	2.20 ± 0.04	7.28 ± 0.20
30% Cornstarch Suspension #3	2.14 ± 0.02	6.84 ± 0.19
30% Cornstarch Suspension #4	2.16 ± 0.03	7.02 ± 0.25
30% Cornstarch Suspension #5	2.14 ± 0.03	6.42 ± 0.08
30% Cornstarch Suspension #6	2.09 ± 0.11	6.43 ± 0.15
30% Cornstarch Suspension #7	1.87 ± 0.04	5.93 ± 0.11
30% Cornstarch Suspension #8	2.20 ± 0.02	6.61 ± 0.15
Average	2.12 ± 0.11	6.71 ± 0.45
30% Cornstarch in Water #1	0.96 ± 0.02	4.34 ± 0.27
30% Cornstarch in Water #2	1.07 ± 0.10	4.93 ± 0.35

TABLE 5.5: The slope of the attenuation coefficient and the attenuation coefficient at 5 MHz measured in the eight samples of the 30% cornstarch suspension in a 51.5% cesium chloride brine and two samples of a 30% cornstarch in water suspensions.

5.4.4 40% Cornstarch Suspensions

Eight 40% cornstarch suspensions in a 51.5% cesium chlorine solution had their attenuation coefficient as a function of frequency measured and displayed in Figure 5.10. The 40% cornstarch suspensions were the first set of suspensions at a concentration high enough to display shear thickening behavior. The shear thickening behavior made the suspensions difficult to mix which resulted in a greater variability in the ultrasonic measurements. Table 5.6 displays the attenuation coefficient at 5 MHz and the slope of the attenuation coefficient for each of the eight samples. The slope of the attenuation coefficient determined by a linear fit to the data was 3.41 dB/cm/MHz $\pm$ 0.20 dB/cm/MHz. The average attenuation coefficient at 5 MHz was determined to be 11.98 dB/cm $\pm$ 1.23 dB/cm.

The frequency-dependent attenuation coefficient was measured for two 40% cornstarch in water suspensions and displayed in Figure 5.10. The slope of the attenuation coefficient and the attenuation coefficient at 5 MHz are displayed in Table 5.6. The slope of the attenuation coefficient was approximately 1.75 dB/cm/MHz. The attenuation coefficient at 5 MHz was measured to be approximately 7 to 8 dB/cm.

5.4.5 Summary of Measurements

The measurements of the attenuation coefficient as a function of frequency are summarized in Figure 5.11. The figure displays the individual measurements of the

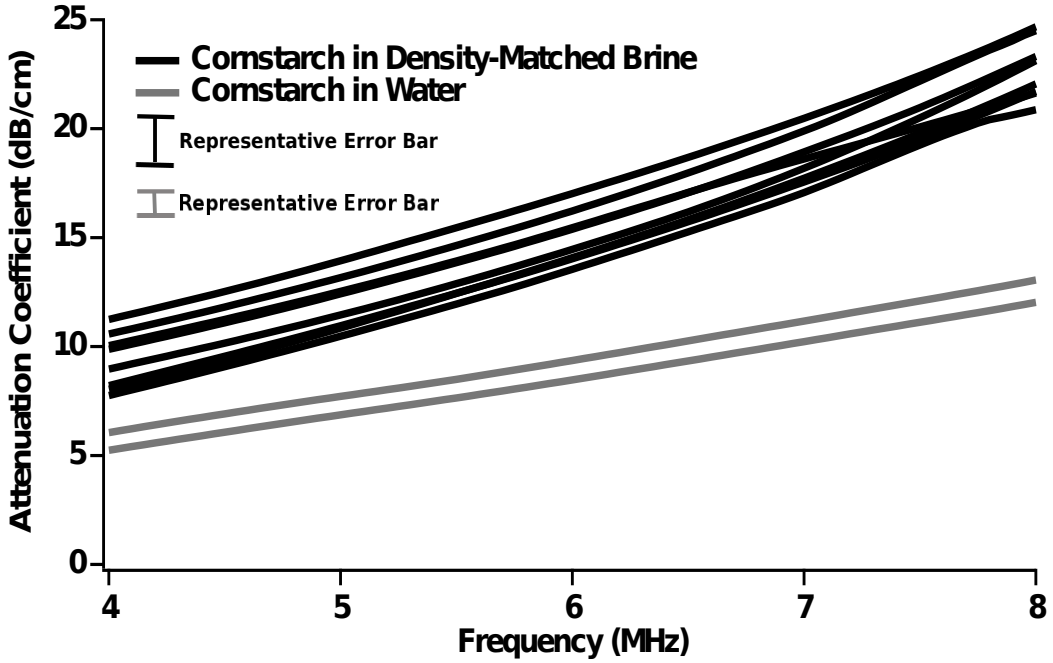

FIGURE 5.10: The attenuation coefficient plotted as a function of frequency for the 40% cornstarch suspensions in density-matched cesium chloride brine. The attenuation coefficient for the 40% cornstarch suspensions in water is plotted as well. A representative error bar displaying plus or minus one standard deviation in the measurement is displayed in the figure for both the density-matched suspensions and the cornstarch in water suspensions.

	Slope of Attenuation (dB/cm/MHz)	Attenuation Coefficient at 5 MHz (dB/cm)
40% Cornstarch Suspension #1	3.62 ± 0.13	11.45 ± 0.61
40% Cornstarch Suspension #2	3.31 ± 0.26	10.48 ± 0.14
40% Cornstarch Suspension #3	3.41 ± 0.18	12.42 ± 0.64
40% Cornstarch Suspension #4	3.50 ± 0.22	13.17 ± 0.38
40% Cornstarch Suspension #5	2.97 ± 0.41	12.53 ± 1.09
40% Cornstarch Suspension #6	3.42 ± 0.08	13.94 ± 0.24
40% Cornstarch Suspension #7	3.44 ± 0.21	10.96 ± 0.76
40% Cornstarch Suspension #8	3.57 ± 0.14	10.85 ± 0.25
Average	3.41 ± 0.20	11.98 ± 1.23
40% Cornstarch in Water #1	1.72 ± 0.04	6.87 ± 0.38
40% Cornstarch in Water #2	1.77 ± 0.11	7.71 ± 0.77

TABLE 5.6: The slope of the attenuation coefficient and the attenuation coefficient at 5 MHz measured in the eight samples of the 40% cornstarch suspension in a 51.5% cesium chloride brine and two samples of a 40% cornstarch in water suspensions.

	Slope of Attenuation (dB/cm/MHz)	Attenuation Coefficient at 5 MHz (dB/cm)
10% Cornstarch Suspensions	0.71 ± 0.02	1.97 ± 0.10
20% Cornstarch Suspensions	1.41 ± 0.05	4.32 ± 0.22
30% Cornstarch Suspensions	2.12 ± 0.11	6.71 ± 0.45
40% Cornstarch Suspensions	3.41 ± 0.20	11.98 ± 1.23

TABLE 5.7: The average slope of the attenuation coefficient and the average attenuation coefficient at 5 MHz for each of the concentrations of cornstarch suspended in a 51.5% cesium chloride solution.

attenuation coefficient for each of the samples at each concentration. Both the magnitude of the attenuation coefficient and the slope of the attenuation coefficient can be seen to increase relatively systematically as the concentration of cornstarch in the suspension increases. To further illustrate the changes in the attenuation properties with increasing concentration Table 5.7 displays the average slope of the attenuation coefficient and the average attenuation coefficient at 5 MHz for each of the concentrations of cornstarch. Both parameters of attenuation are seen to increase systematically from a concentration of 10% to 20% to 30% before a larger increase to 40%. The variability in the measurements can also be seen to increase as the concentration increases, reflecting the increasing difficulty of the measurement as the suspension became more viscous. Table 5.8 and Figure 5.8 display a summary of the attenuation measurements for the cornstarch and water suspensions for comparison purposes. A further comparison can be seen in Figure 5.13 of the attenuation coefficient at 5 MHz for the two different types of suspensions.

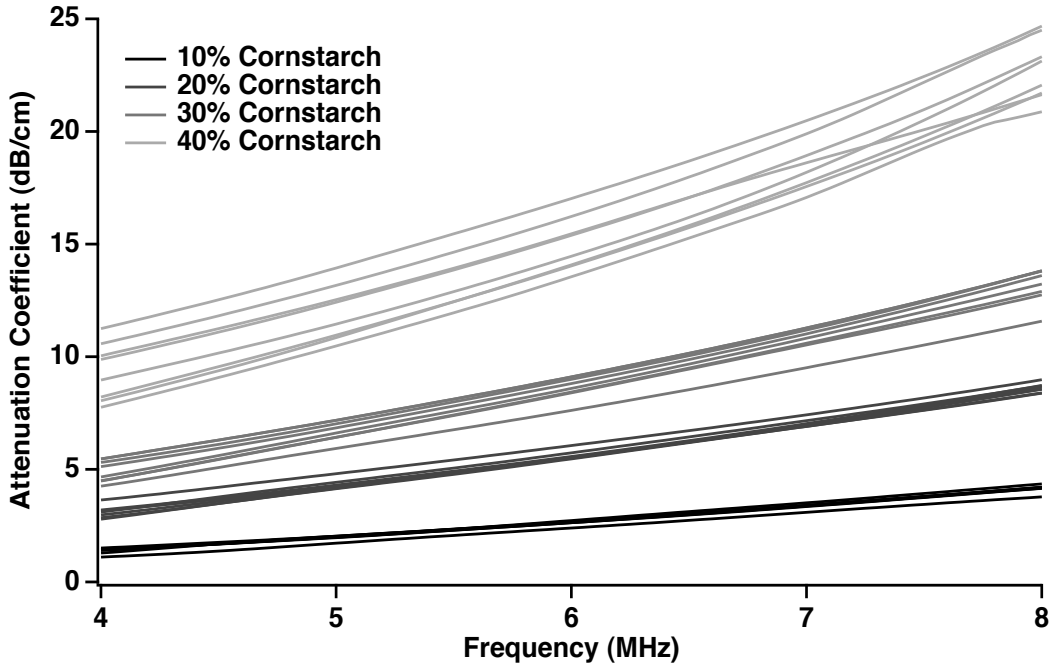

FIGURE 5.11: The attenuation coefficient plotted as a function of frequency for each of the individual measurements at each of the concentrations of cornstarch suspended in a 51.5% cesium chloride solution. The error bars are not plotted but representative error bars for each of the different concentrations of cornstarch can be seen in the earlier figures.

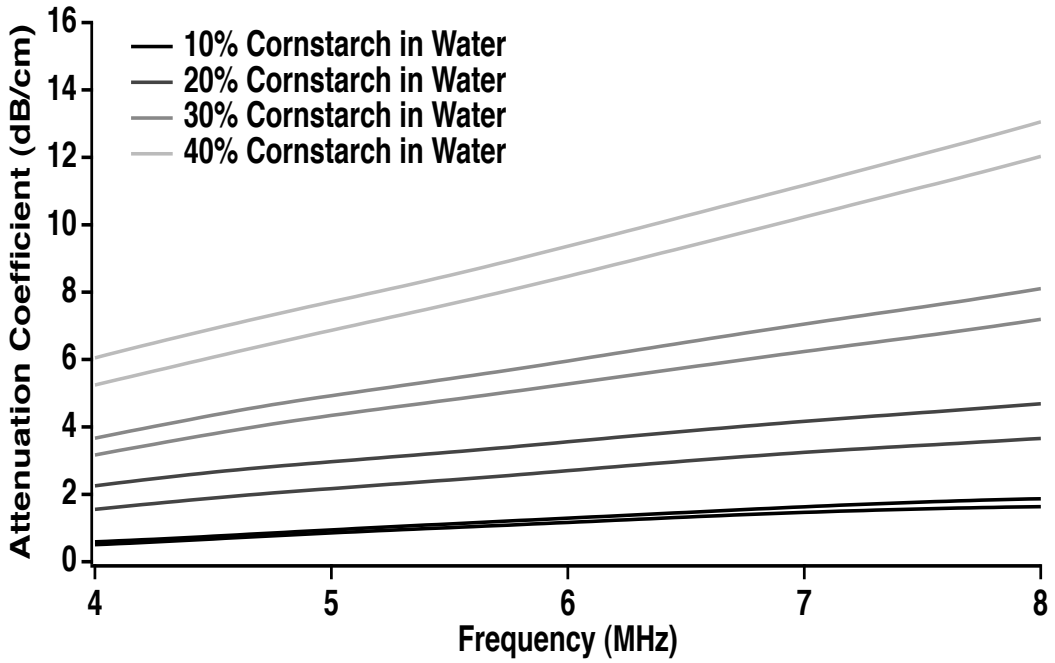

FIGURE 5.12: The attenuation coefficient plotted as a function of frequency for each of the cornstarch in water suspensions. The error bars are not plotted but representative error bars for each of the different concentrations of cornstarch can be seen in the earlier figures.

	Slope of Attenuation (dB/cm/MHz)	Attenuation Coefficient at 5 MHz (dB/cm)
10% Cornstarch Suspensions #1	0.32 ± 0.09	0.94 ± 0.10
10% Cornstarch Suspensions #2	0.28 ± 0.11	0.86 ± 0.12
20% Cornstarch Suspensions #1	0.58 ± 0.07	2.97 ± 0.14
20% Cornstarch Suspensions #2	0.51 ± 0.04	2.17 ± 0.31
30% Cornstarch Suspensions #1	0.96 ± 0.02	4.34 ± 0.27
30% Cornstarch Suspensions #2	1.07 ± 0.10	4.93 ± 0.35
40% Cornstarch Suspensions #1	1.72 ± 0.04	6.71 ± 0.45
40% Cornstarch Suspensions #2	1.77 ± 0.11	7.71 ± 0.77

TABLE 5.8: The slope of the attenuation coefficient and the attenuation coefficient at 5 MHz for each of the cornstarch in water suspensions

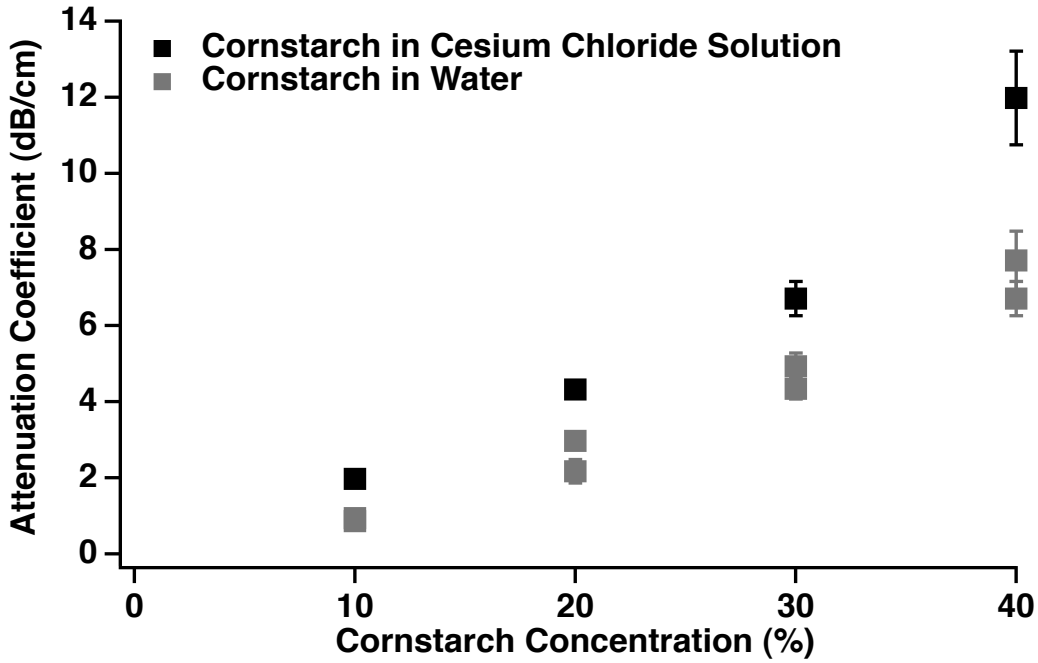

FIGURE 5.13: The average attenuation coefficient at 5 MHz plotted for each concentration of the cornstarch suspensions in a 51.5% cesium chloride solution. The error bars are plotted as ± one standard deviation. The attenuation coefficient at 5 MHz for each of the measurements of samples of cornstarch in water suspensions is also plotted.

5.5 Conclusion

This chapter described the experimental method for measuring the attenuation coefficient as a function of frequency in the cornstarch suspensions. A method for the diffraction correction was described, studied and ultimately determined to be unnecessary for the attenuation measurements, because the speed of sound in the sample was not different enough from the speed of sound in water. The rest of the chapter presented the results of the measurement of the attenuation coefficient for each of the concentrations of cornstarch in suspension with a 51.5% cesium chloride solution. Measuring the attenuation coefficient of the cornstarch suspensions in a 51.5% cesium chloride solution is an important step toward determining the feasibility and design of future ultrasonic experiments probing the cornstarch suspensions' shear thickening behavior.

Bibliography

Ford, R. (**1970**). *Introduction to Acoustics*, volume 77 (Amsterdam, the Netherlands).

Lloyd, C. (**2010**). "Enhancing nonlinear ultrasonic methods for laboratory and clinical applications", Ph.D. thesis, Washington University in St. Louis.

Markham, J., Beyer, R., and Lindsay, R. (**1951**). "Absorption of sound in fluids", Reviews of Modern Physics **23**, 353–411.

Ophir, J., Shawker, T., Maklad, H., Miller, J., Flax, S., Narayana, P., and Jones, J. (**1984**). "Attenuation estimation in reflection: progress and prospects", Ultrasonic Imaging **6**, 349–395.

Trousil, R. (**2002**). "Ultrasonic propagation in inhomogeneous media: toward quantitative ultrasonic imaging", Ph.D. thesis, Washington University in St. Louis.

Wear, K., Stiles, T., Frank, G., Madsen, E., Cheng, F., Feleppa, E., Hall, C., Kim, B. S., Lee, P., O'Brien, W., Oelze, M., Raju, B., Shung, K., Wilson, T., and Yuan, J. (**2005**). "Interlaboratory comparison of ultrasonic backscatter coefficient measurements from 2 to 9 mhz", J Ultrasound Med **24**, 1235–1250.

Xu, W. and Kaufman, J. (**1993**). "Diffraction correction methods for insertion ultrasound attenuation estimation", IEEE Transactions on Biomedical Engineering **40**, 563–570.

Chapter 6

Phase Velocity Measurements of Cornstarch Suspensions

6.1 Preface

This chapter begins with a brief review of phase that is used to help explain the broadband phase spectroscopy method employed for some of the experimental measurements. The chapter continues with an explanation of the narrowband phase velocity technique followed by a discussion of the Kramers-Kronig relations. The last section of the chapter presents the phase velocity measurements of four different concentrations of cornstarch in a density-matched cesium chloride solution and highlights a surprising result.

6.2 A Brief Review of Phase

To better understand the phase velocity measurements, a short review of phase is in order. The Fourier Shift Theorem shown in Equation 6.1 demonstrates how a shift in the time domain is equivalent to a shift in phase in the frequency domain (Bracewell, 2000).

$$\mathcal{F}[f(t-a)] = e^{-ia\omega}\tilde{F}(\omega) \tag{6.1}$$

where a is the shift in the time domain, $\mathcal{F}$ indicates a Fourier transform, and $\tilde{F}(\omega)$ is the Fourier transform of $f(t)$. The Fourier shift theorem shows that as a signal propagates in time, the Fourier transform of that signal accumulates phase. One important insight gained from examination of Equation 6.1 is that higher frequencies experience larger phase shifts for the same shift in the time domain. Although most of the experimental work was completed using the shadowed reflector setup shown in Figure 6.1, this discussion of the phase will center around the through transmission setup displayed in Figure 6.2.

The key component of the phase velocity measurement is determining the difference in the accumulated phase between the reference signal and sample signal over the entire distance between the transducers. In order to visualize this phase accumulation, a through transmission experiment involving a host medium with a phase velocity of 1480 m/s and a sample with a phase velocity of 1530 m/s can be considered. The phase accumulation at a certain frequency per distance the signal travels can be calculated from the knowledge of the phase velocities. The wavenumber in the

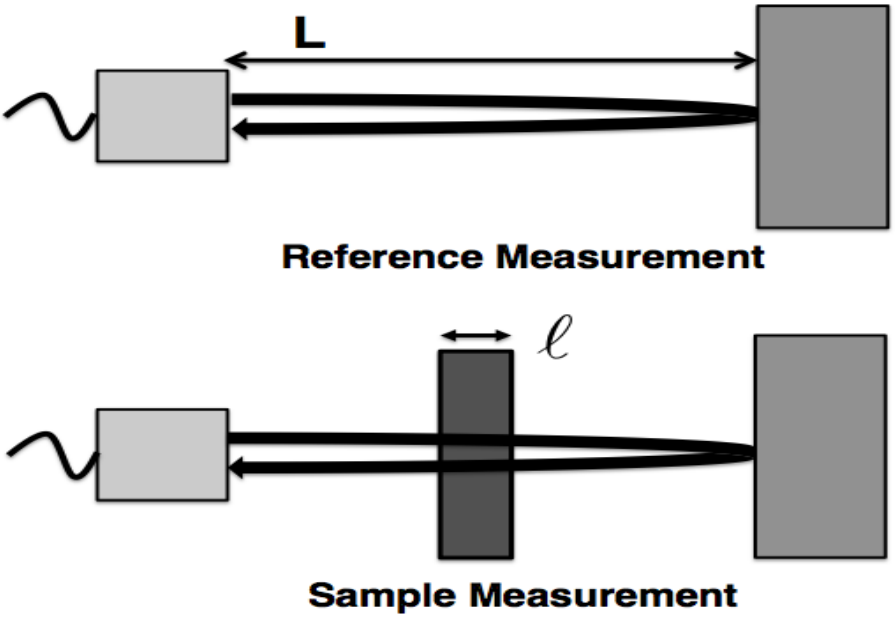

FIGURE 6.1: Shadowed reflector setup for the broadband phase velocity measurements. The transducer is aligned with the steel reflector. The sample is placed in between the transducer and the reflector but in this case is not touching the reflector.

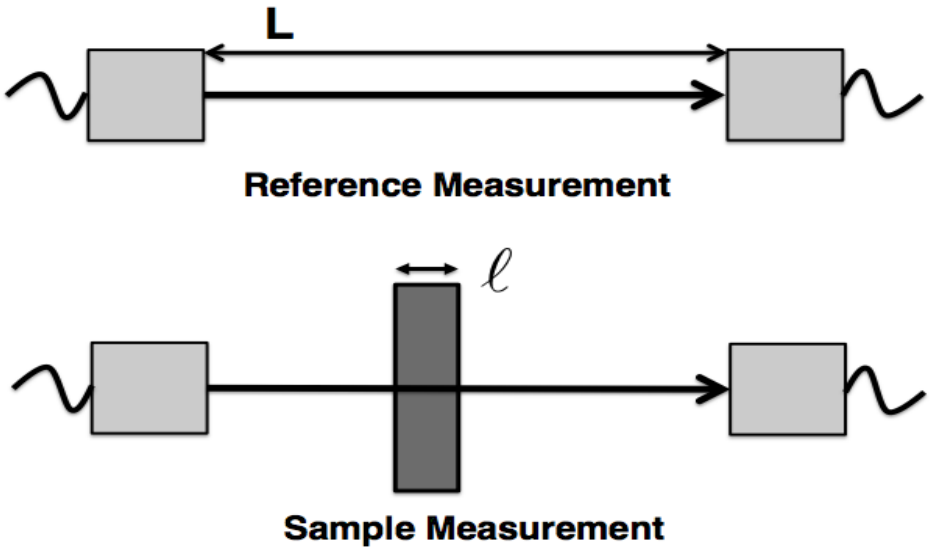

FIGURE 6.2: Through transmission setup for the broadband phase velocity measurements. The two transducers are aligned with each other. The sample is placed between the two transducers for the sample measurement.

host medium and in the sample is calculated in Equations 6.2 and 6.3 respectively at a frequency of 4 MHz. If a frequency higher than 4 MHz was considered, both the Fourier Shift theorem and the equation for the wavenumber indicate that the phase would accumulate more quickly with distance.

$$k_{ref}(\omega) = \frac{\omega}{v_{ref}} \approx \frac{2\pi(4 * 10^6 \text{ Hz})}{1480 \text{ m/s}} = 16,982 \text{ rad/m} \tag{6.2}$$

$$k_{samp}(\omega) = \frac{\omega}{v_{samp}} \approx \frac{2\pi(4 * 10^6 \text{ Hz})}{1530 \text{ m/s}} = 16,426 \text{ rad/m} \tag{6.3}$$

The calculations in Equations 6.2 and 6.3 indicate that the phase accumulates faster in the medium with the lower phase velocity. From these calculated wavenumbers, the accumulated phase as a function of distance can be plotted for both the reference signal and the sample signal. Figure 6.3 plots the accumulated phase for both the reference signal and the sample signal as a function of distance up until the point that the sample signal reaches the sample. In this figure both signals are propagating through the host medium so they accumulate phase at the rate given by Equation 6.2. Figure 6.4 displays the accumulated phase from the transmitting transducer through the point where the sample signal has traversed the entire sample. The reference signal travels the same distance but entirely through the host medium. Figure 6.5 shows a magnified version of the difference in phase accumulation over the thickness of the sample. The reference phase accumulates more quickly over this distance because the phase velocity in the host medium is less than the phase velocity in the sample.

Figure 6.6 shows the phase that accumulates throughout the entire experiment for the both the reference and the sample signal plotted as a function of distance. Once

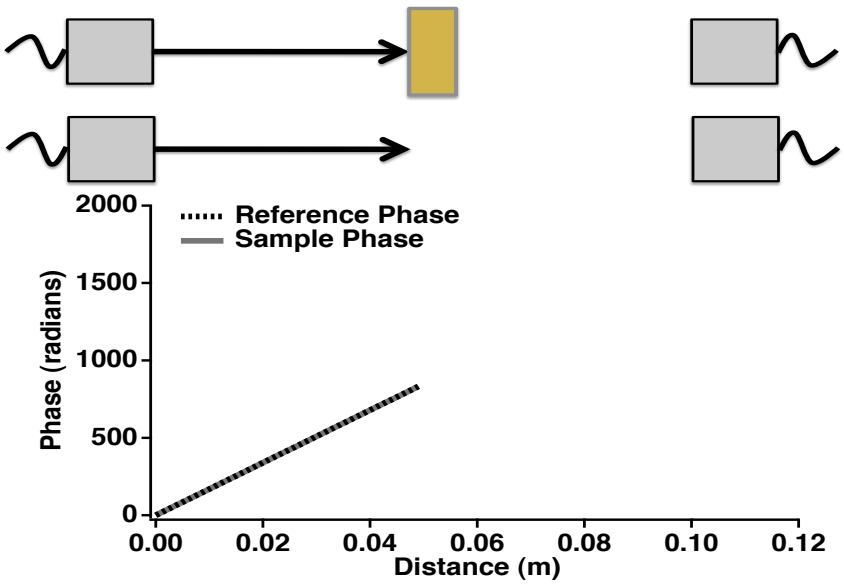

FIGURE 6.3: The comparison of the accumulation of phase for both reference and sample measurement as a function of distance. The transmitting and receiving transducer are shown in the figure to help connect the phase accumulation with the physical measurement.

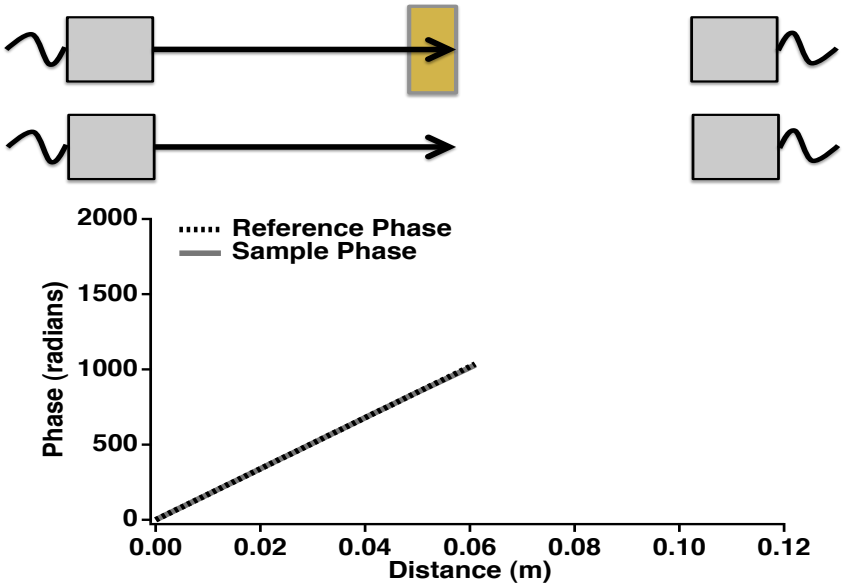

FIGURE 6.4: The comparison of the accumulation of phase for both the reference and sample measurements as a function of distance up until the back wall of the sample.

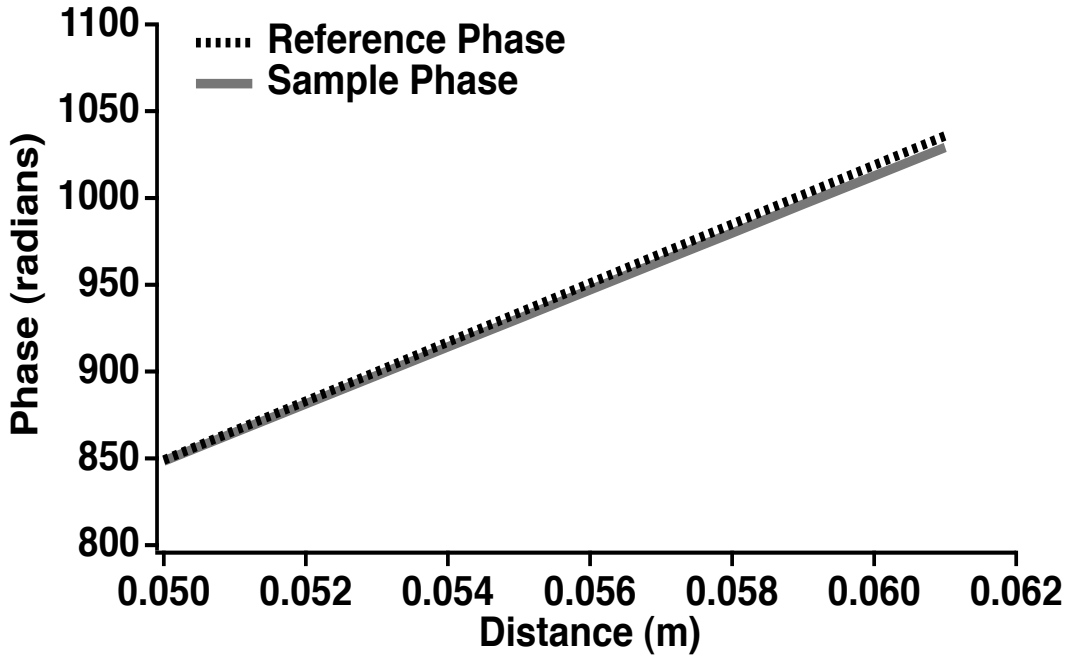

FIGURE 6.5: A magnified portion of Figure 6.4 to highlight the difference in the accumulation of phase between the reference and sample signal over the sample thickness.

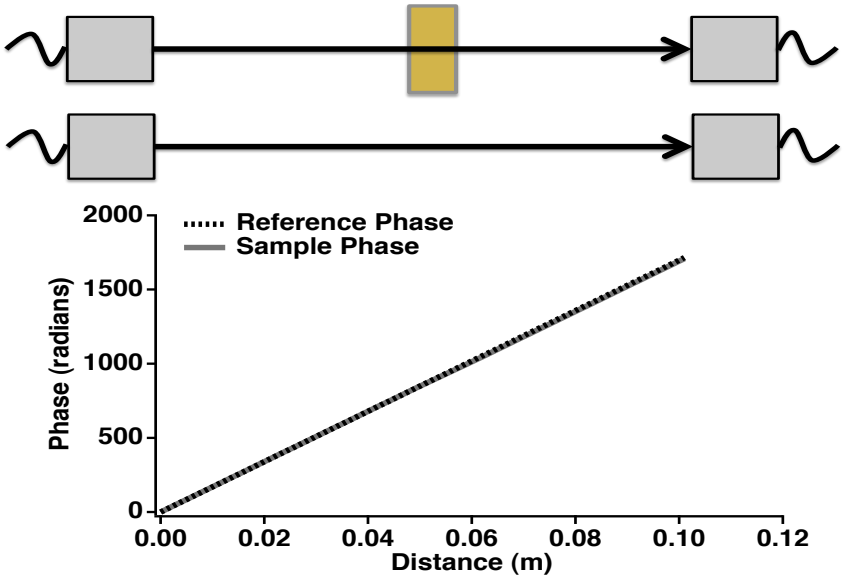

FIGURE 6.6: The comparison of the accumulation of phase for both the reference and sample measurements as a function of distance from the transmitting transducer to the receiving transducer

the sample signal has made it through the sample it travels through the host medium until it reaches the receiving transducer. Thus, the two signals accumulate phase at the same rate over this distance and the phase difference does not change. Figure 6.7 highlights this point by plotting the phase for both signals over the distance from the back wall of the sample until the receiving transducer.

The previous set of figures highlighted the difference between the phase accumulated by the reference signal and the phase accumulated by the sample signal as a function of distance. However, this discussion assumed a knowledge of the phase velocity to determine the phase difference. In the actual measurement, the phase difference is used to calculate the phase velocity.

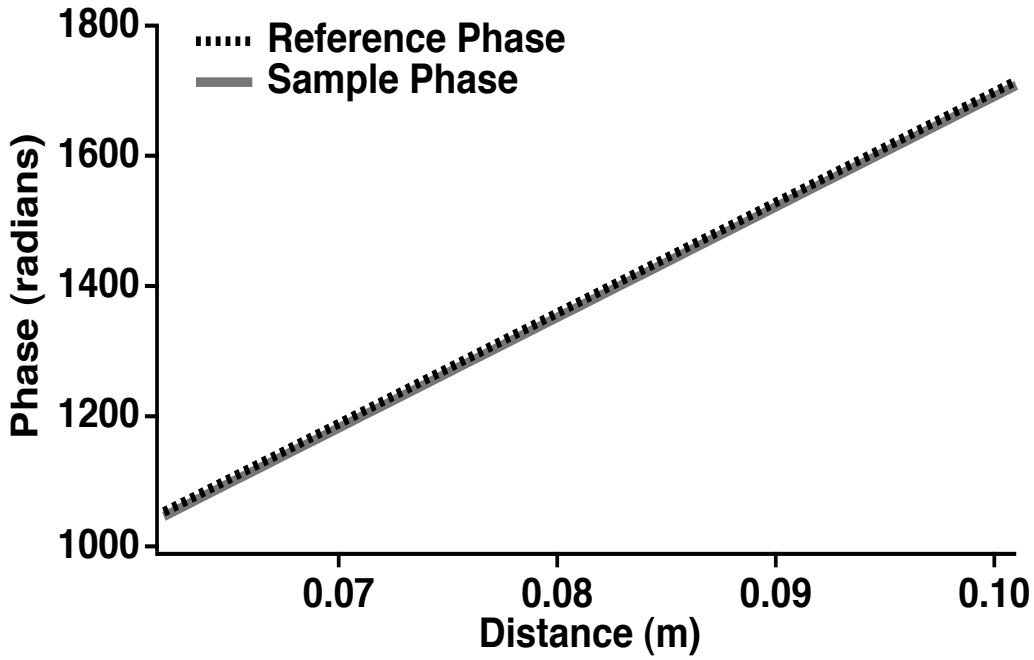

FIGURE 6.7: A magnified portion of Figure 6.6 to highlight that both signals accumulate phase at the same rate once the sample signal has moved through the sample.

A different but equally valid way of visualizing the phase difference would be to look at the accumulation on a phase plot as shown in Figures 6.8, 6.9, 6.10, and 6.11. In the first figure, both the reference phase and sample phase start at an arbitrary phase dependent on the phase at the face of the transmitting transducer when the signals are transmitted (Trousil *et al.*, 2001) . In the second figure, both the reference and sample phase accumulate at the same rate until the signal reaches the front wall of the sample, because they are both moving through the same distance of the host medium. Each revolution around the phase plot would indicate the accumulation of 2π radians of phase. Figure 6.4 shows that the actual accumulated phase up until the signal reaches the front wall of the sample is much larger than 2π. The "paths" shown in Figure 6.9 are merely meant to indicate the many revolutions about the

phase plot this accumulated phase would require.

Figure 6.10 shows the apparent phase difference after the sample signal has traveled through the sample and the reference signal has traveled an equivalent distance. The actual phase difference may be larger than what the figure at first seems to be indicating. The reference phase may have accumulated much more quickly than the sample phase (or vice versa) and may have "lapped" the sample phase many times. The actual phase difference is the angle between the two phases shown in the figure plus some integer multiple of 2π. This ambiguity in the phase angle to integer multiples of 2π is known as the phase sheet ambiguity and is an important component of the phase velocity calculation discussed later in the chapter.

Figure 6.11 shows both phases after both signals have traversed the rest of the distance from the back wall of the sample to the receiving transducer. Because both signals travel through the host medium for this entire period, the phase difference between them does not change (as was the case in Figure 6.6). The "paths" shown in Figure 6.9 are not displayed, although both phases went through many revolutions around the phase plot between the back wall of the sample and the receiving transducer.

The ideas of the phase difference and the phase sheet ambiguity are central to the measurement of the phase velocity using the broadband phase spectroscopy technique. Building on the ideas explained in this section, the experimental method for broadband phase spectroscopy will be discussed in detail in the next section.

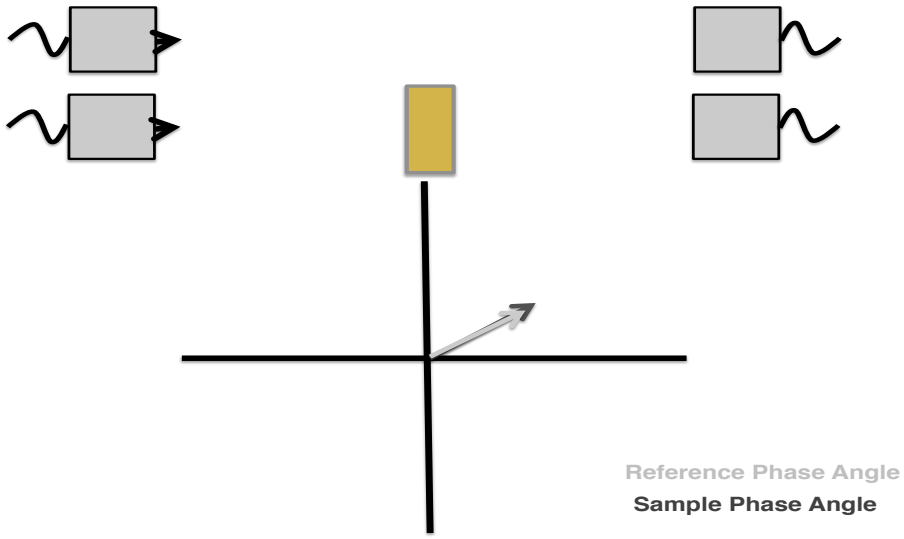

t

FIGURE 6.8: Both the sample and reference phase start at an arbitrary phase dependent on the experimental setup. This figure shows the starting point of the phase accumulation.

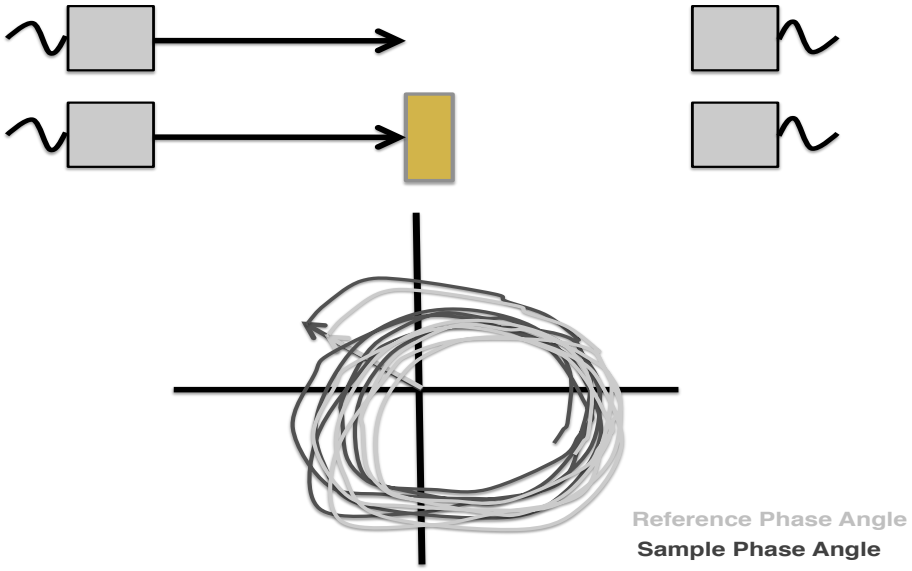

FIGURE 6.9: This phase plot shows the accumulation of the sample and reference phase in the host medium before reaching the sample. They both travel the same path up to this point so they accumulate phase at the same rate. The "paths" shown are meant only to indicate that the phase accumulated thus far would require many revolutions around the phase plot.

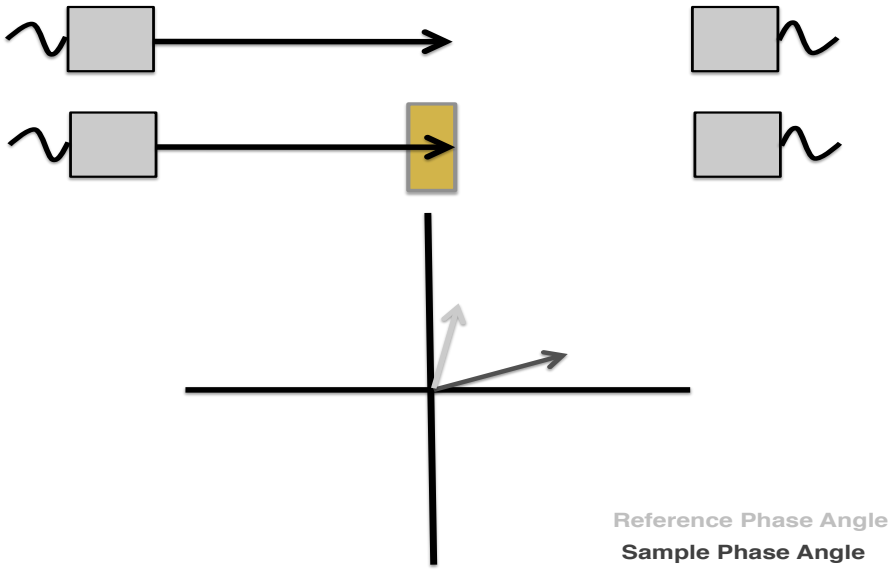

FIGURE 6.10: The accumulation of phase as the sample signal goes through the sample and the reference signal continues to travel through the host medium. In this example, the sample phase velocity is assumed to be greater than the host medium's phase velocity so the reference phase accumulates more quickly over this distance.

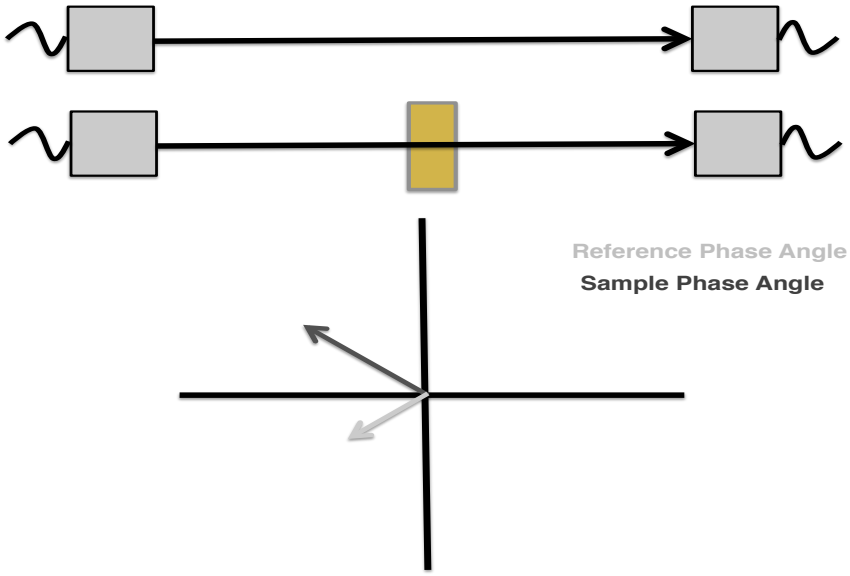

FIGURE 6.11: The accumulation of phase after the sample signal has passed through the sample. At this point both the reference and the sample signal traverse the same distance in the host medium so the phase difference does not change over this region.

6.3 Broadband Phase Spectroscopy

The formalism followed in this thesis for the explanation of phase spectroscopy was laid out by Laboratory for Ultrasonics alumnus Rebecca Trousil in her Ph.D. dissertation (Trousil, 2002). Trousil's formalism is based on that of Sachse and Pao who first introduced the broadband phase spectroscopy technique (Sachse and Pao, 1978). One notable exception to the formalism will be a difference in the labeling of one of the steps in the broadband phase spectroscopy analysis. Most of the broadband phase velocity measurements discussed in this thesis were made using the shadowed reflector method, so the discussion of the method will be based on this technique.

Figure 6.1 displays the two measurements that are made for the broadband phase spectroscopy technique using the shadowed reflector method. The general complex frequency response received at the transducer is expressed in Equation 6.4.

$$\tilde{U}(x,\omega) = A(\omega)e^{i[(k(\omega)+i\alpha(\omega))x+\gamma(\omega)]} \tag{6.4}$$

where $\tilde{U}$ is the complex frequency response received, $A(\omega)$ is the frequency dependent amplitude, $k(\omega)$ is the wavenumber, α is the amplitude attenuation coefficient, x is the propagation distance, and ζ is some initial arbitrary phase that depends on the experimental setup (Trousil, 2002). The complex frequency response for the reference measurement is shown in Equation 6.5.

$$\tilde{U}_{ref}(x,\omega) = |\tilde{U}_{ref}(x=2L,\omega)|e^{i\phi_{ref}(\omega)} \tag{6.5}$$

where $\tilde{U}_{ref}$ is the complex frequency response of the reference measurement, $|\tilde{U}_{ref}| =$

$A(\omega)e^{-2\alpha_{ref}(\omega)L}$ is the magnitude of the complex frequency response with L being the distance between the transducer and the steel reflector, and $\phi_{ref}(\omega) = 2k_{ref}(\omega)L + \zeta(\omega)$ is the phase of the complex frequency response of the reference measurement.

The complex frequency response for the sample measurement is displayed in Equation 6.6

$$\tilde{U}_{samp}(x,\omega) = |\tilde{U}_{samp}(x = 2L,\omega)|e^{i\phi_{samp}(\omega)} \tag{6.6}$$

where $\tilde{U}_{samp}$ is the complex frequency response of the sample measurement, $|\tilde{U}_{samp}| = (\tilde{T}^p_{h\to s}\tilde{R}^p_{s\to r}\tilde{T}^p_{s\to h})A(\omega)e^{-\alpha_{ref}(\omega)2(L-\ell)-\alpha_s(\omega)2\ell}$ is the magnitude of the complex frequency response, $\tilde{T}^p_{s\to h}$ and $\tilde{T}^p_{h\to s}$ are the pressure amplitude transmission coefficients between the host medium and the sample, $\tilde{R}^p_{s\to r}$ is the pressure amplitude reflection coefficient between the host medium and the reflector, ℓ is the sample thickness, and $\phi_{samp}(\omega) = 2k_{ref}(\omega)(L-\ell) + 2k_s(\omega)\ell + \zeta(\omega)$ is the phase of the complex frequency response of the sample measurement (Trousil, 2002).

The complex transmission and reflection coefficients are defined in terms of the complex acoustic impedance. The attenuation coefficient in all of the media studied in this thesis is small compared to the rest of the complex wavenumber (Trousil, 2002). For this reason, the complex acoustic impedance (and thus the transmission and reflection coefficients) was approximated as a real quantity (Trousil, 2002).

The phase velocity is determined from the phase difference between the reference measurement and the sample measurement. The phase difference between the sample and reference signals is defined in Equation 6.7 (Trousil, 2002). The phase velocity

in the host medium is known to be approximately independent of frequency.

$$\text{Phase Difference} \equiv \phi_{samp}(\omega) - \phi_{ref}(\omega) = 2\omega\ell \left(\frac{1}{v_s(\omega)} - \frac{1}{v_h} \right) \tag{6.7}$$

The phase velocity in the sample can be found by rearranging Equation 6.7 to arrive at Equation 6.8.

$$v_s(\omega) = v_h \left(\frac{2\omega\ell}{2\omega\ell + v_h \Delta\phi(\omega)} \right) \tag{6.8}$$

The thickness of the sample is measured ultrasonically as described in Section 4.2 and the phase velocity of the host medium (typically water) is calculated from inputting the temperature of the water into a fifth degree polynomial (Marczak, 1997). As discussed in the previous section, the key component to determining the phase velocity experimentally is finding the phase difference.

6.4 Experimental Phase Difference

The phase difference is defined as the difference between the sample phase and the reference phase. The experimental reference phase is shown by Equation 6.9 and the experimental sample phase is shown by Equation 6.10.

$$\phi_{ref}(\omega) = (\phi^{ref}_{shift}(\omega) + 2\pi m) + \omega\tau^{ref}_{delay} + \omega\tau^{ref}_{shift} \tag{6.9}$$

$$\phi_{samp}(\omega) = (\phi^{samp}_{shift}(\omega) + 2\pi n) + \omega\tau^{samp}_{delay} + \omega\tau^{samp}_{shift} \tag{6.10}$$

where ϕ_{shift} is the phase of the shifted signal, m and n are integers indicating the ambiguity in the phase sheet, τ_{delay} is the b-delay time, and τ_{shift} is the amount in time that the signal is shifted. Note that the difference between Trousil's formalism and

the formalism in this thesis comes from the labeling and explanation of the "shift". Both methods shift the signal but Trousil's formalism emphasizes the symmetrization of the signal. The formalism established in this thesis treats the shift in a similar way to the shift due to the b-delay. Although the labeling of this step has been changed, the analysis itself stays exactly the same. Using Equations 6.9 and 6.10, Equation 6.7 can be re-expressed in Equation 6.11

$$\text{Phase Difference} = [(\phi_{shift}^{samp}(\omega) - \phi_{shift}^{ref}(\omega)) + 2\pi(m-n))] + \omega(\tau_{delay}^{samp} - \tau_{delay}^{ref}) + \omega(\tau_{shift}^{samp} - \tau_{shift}^{ref}) \tag{6.11}$$

where the difference $(m-n)$ is known as the phase sheet offset. This description of the phase breaks up the components in a slightly different way than the earlier discussion of phase. The different parts are due to the way the experimental data is analyzed. Figure 6.12 displays a reference signal labeling some of the terms of Equation 6.11. The trigger delay (b-delay) tells the oscilloscope to wait a certain amount of time after the trigger before beginning to acquire data. Because the time the signal takes to propagate from one transducer to the other is many tens of microseconds, the b-delay allows the oscilloscope window to be centered around the received signal on a much shorter time base than would otherwise be possible.

The phase angles for both the reference and sample signal are found using a four quadrant inverse tangent function. This function is ambiguous to integer multiples of 2π. One revolution around the phase plot shown in Figure 6.9 would be equivalent to accumulating 2π in phase. The four quadrant inverse tangent is only capable of determining a phase angle between -π and π. Thus, no matter how much phase a

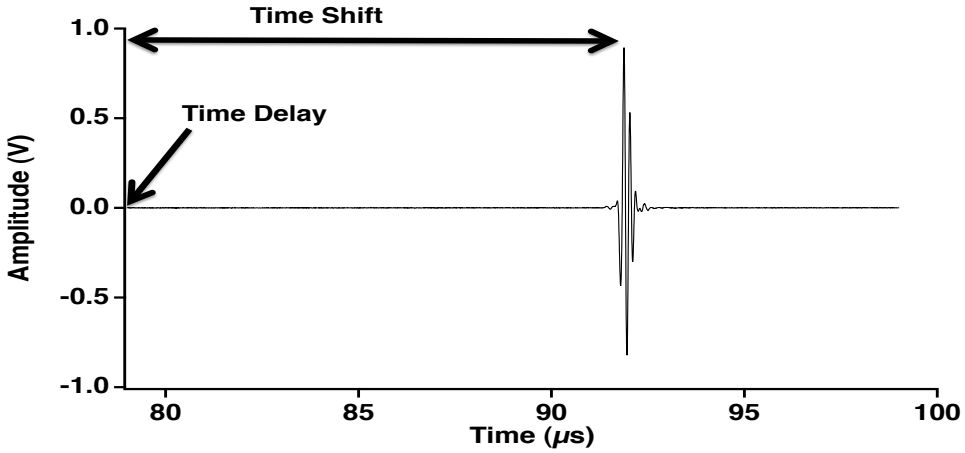

FIGURE 6.12: An example reference signal is shown. Both the reference b-delay time and the time shift are labeled.

signal has accumulated, the phase found using the four quadrant inverse tangent will be between -π and π radians.

The term ϕ_{shift} from Equation 6.11 is the portion of the phase difference calculated using the four quadrant inverse tangent function. The other components of the phase in the equation are found from multiplying the angular frequency by the time shift inherent in each component. The τ_{delay} term is due to the time from the point when the transmitting transducer emits the signal until the beginning of the oscilloscope window as shown in Figure 6.12.

In order to put the reference and the sample trace on even more equal footing before the calculation of the four quadrant inverse tangent, both signals are shifted to the beginning of the trace. This process (referred to as "symmetrization" in Trousil's

formalism) reduces the amount of phase wrapping that will occur when the phase angle shifts from π to -π (Trousil, 2002). Phase wrapping occurs when the phase angle appears to undergo an abrupt discontinuity from π to -π as shown in Figure 6.13. The figure illustrates how a small actual accumulation in phase results in jump from π to -π in the phase angle because of the way it is determined. Minimizing the number of times the phase angle wraps in this way is the main reason for this shifting of the signal in time. Figure 6.14 plots the phase for the reference signal shown in Figure 6.12 when the signal is unshifted and when the signal has been shifted so that the peak positive voltage is at the beginning of the trace. The figure demonstrates the benefit of shifting the trace before calculating the phase angle in order to cut down on the rapid phase wrapping evident across the bandwidth in the unshifted signal. A number of different methods for shifting the trace have been proposed including shifting the peak intensity of the signal, the positive peak of the signal, and the centroid of the signal (Trousil, 2002; He, 1999). When the time domain signal is shifted in this way, the portion of the signal that would lie to the left of zero appears at the far right of the time record. For the work in this thesis, the peak positive voltage was shifted to the start of the record, because this technique is particularly effective at reducing any additional discontinuities in the phase spectrum (Trousil, 2002).

After both the reference and sample signals have been shifted to the start of the window the four quadrant inverse tangent can be used to determine the phase across the bandwidth of interest. At this point all of the components of Equation 6.11

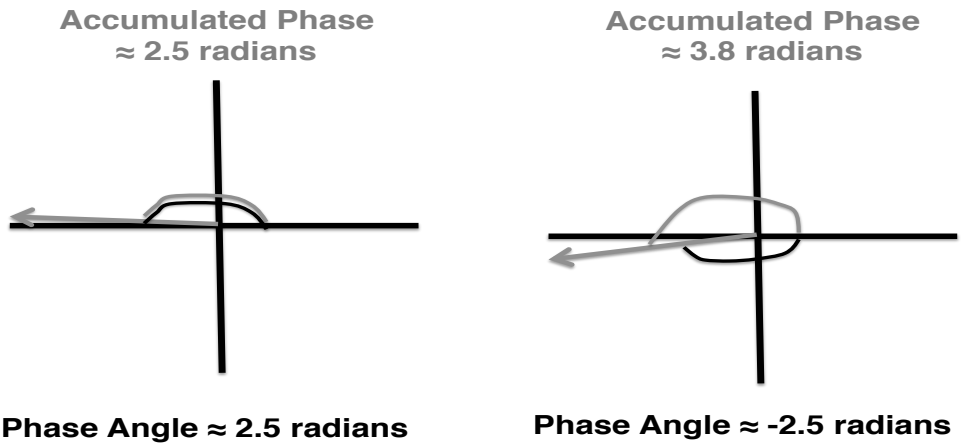

FIGURE 6.13: A visual explanation of phase wrapping demonstrating how a small change in phase leads to a large jump in the phase angle because of how the phase angle is found. The accumulated phase is shown in grey and the phase angle is shown in black.

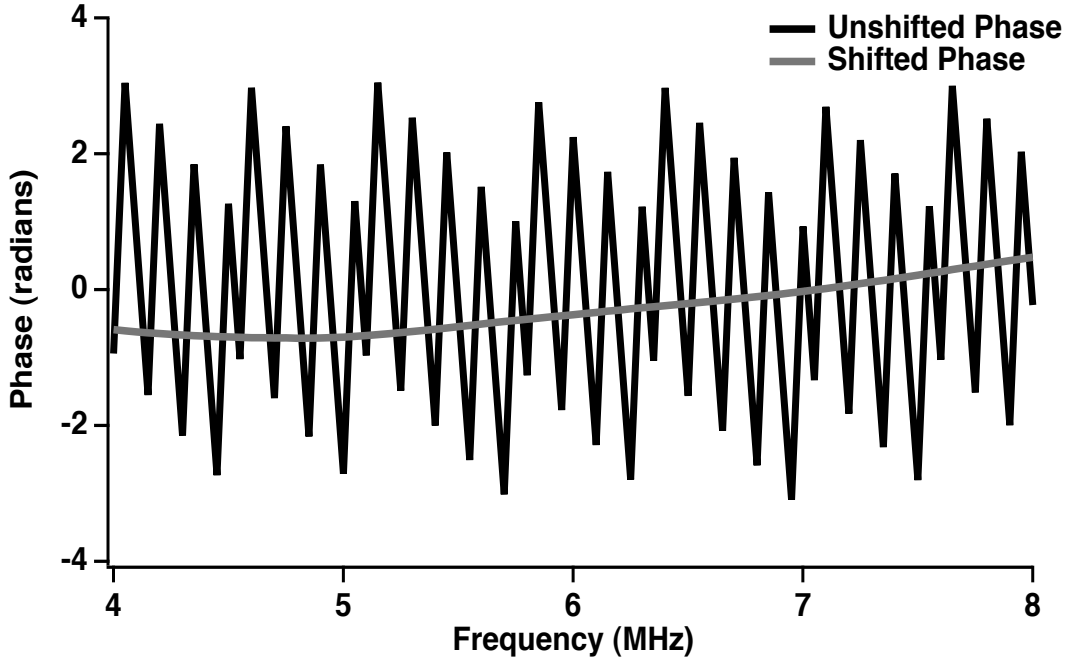

FIGURE 6.14: The phase angle is plotted for a signal that has been shifted to the beginning of the trace and the same signal unshifted. The rapid phase wrapping evident in the bandwidth if the signal is not shifted is readily apparent.

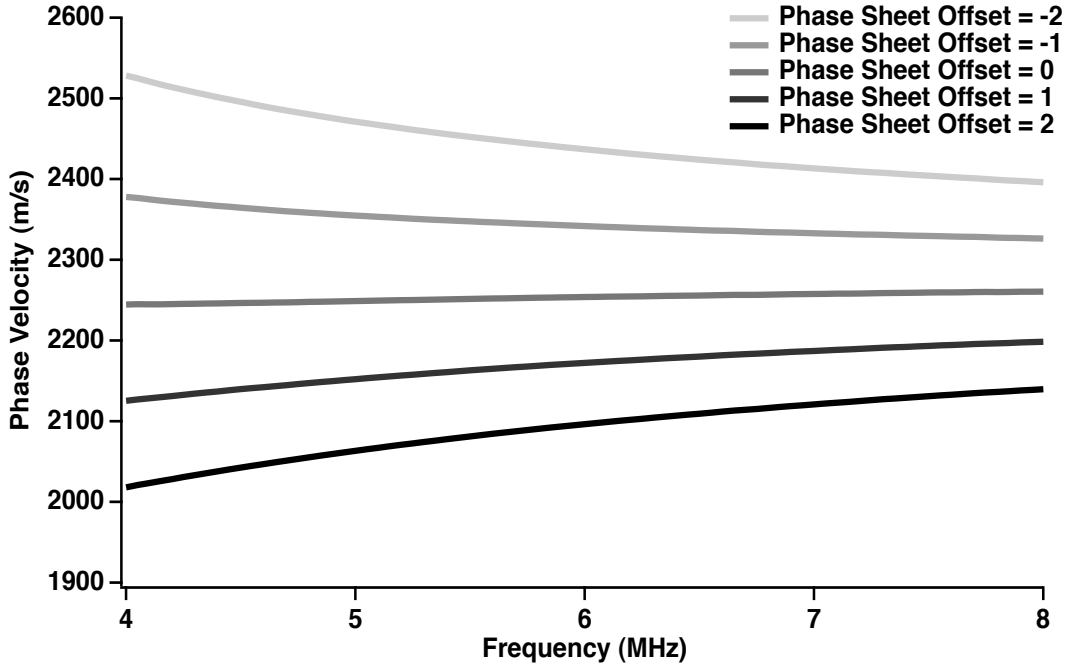

FIGURE 6.15: The phase velocity calculated using five different phase sheet offsets. The large variation in the phase velocity with the phase sheet offset is apparent. The error bars (±3 m/s) were not plotted on the figure because they were too small to be seen on this scale.

have been determined other than the phase sheet ambiguity. The phase difference is calculated for a number of different phase sheet ambiguities and these values are used to calculate the phase velocity using Equation 6.8. An example phase velocity with several different phase sheet offsets is shown in Figure 6.15. The significant effect the phase sheet offset can have on the phase velocity is apparent from the figure. A number of different methods have been proposed for eliminating the phase sheet ambiguity including measuring the narrowband phase velocity or using the Kramers-Kronig relations (Trousil *et al.*, 2001). For this thesis, the phase sheet ambiguity was resolved using both of these methods where appropriate.

6.4.1 Saran Wrap Window Compensation

The sample molds used for the phase velocity measurements contained very thin saran wrap windows. The calculation for the sample phase must take into account the effect of the saran wrap windows. The best estimates of the physical and ultrasonic properties of Saran Wrap^{TM} were made by an alumnus of the Laboratory for Ultrasonics Chris Lloyd (Lloyd, 2009). The density of Saran Wrap^{TM} was reported at 921 kg/m^3, the speed of sound in Saran^{TM} wrap was estimated to be 2400 m/s, and the thickness of the Saran Wrap^{TM} was estimated to be 15 μm. In the shadowed reflector setup, the ultrasonic signal passes through the Saran Wrap^{TM} windows four times (into the front wall of the sample, out of the back wall of the sample and then into the back wall and out of the front wall after the reflection of the signal off of the steel reflector). Mobley et al. utilizes a slightly modified version of Equation 6.8 given in Equation 6.12 that includes a compensation for the Saran Wrap^{TM} layer (Mobley *et al.*, 1999).

$$v_s(\omega) = v_h \left(\frac{2\omega\ell}{2\omega\ell + v_h(\Delta\phi(\omega) + \phi_c(\omega, h))} \right) \tag{6.12}$$

where $\phi_c = 2\omega \mathrm{h}(1/c_p(\omega) - 1/c_w)$ is the phase accumulation due to the saran wrap windows, h is the thickness of the saran wrap, and c_p is the speed of sound in the saran wrap. Because the saran wrap windows are so thin, the contribution to the overall phase velocity from the ϕ_c term is negligible and thus the compensation was not used in this thesis.

The measurements discussed in Section 6.7.1 that compare the through transmis-

sion and shadowed reflector method provide experimental evidence of the insignificance of this compensation. In the shadowed reflector method, the ultrasonic signal travels through the saran wrap window four times as opposed to two times for the through transmission method. Despite a doubling in the influence of the saran wrap between the two methods, essentially no difference is found in the resulting measurements of the phase velocity displayed in Figure 6.27.

6.5 Narrowband Phase Velocity Measurements

Narrowband phase velocity measurements were made in order to determine unambiguously the proper phase sheet offset for the broadband phase velocity measurements (Trousil *et al.*, 2001). These measurements also provided an independent check on the dispersion of the phase velocity.

The Sollish method described in Section 4.2 for the shadowed reflector setup in the context of measuring the group velocity was used to find the narrowband phase velocity. The experimental setup is shown in Figure 6.16. The Sollish method relies on time differences between signals that were determined with a correlation technique. The equation for the phase velocity determined with the measurements is given in Section 4.2 by Equation 4.1. The relative timing differences necessary for the measurement are found using Equation 6.13.

$$t_i - t_j = [(\tau_{delay})_i - (\tau_{delay})_j] + T * (n_i - n_j) \tag{6.13}$$

where τ_{delay} is the b-delay for signal of interest, T is the time spacing between each

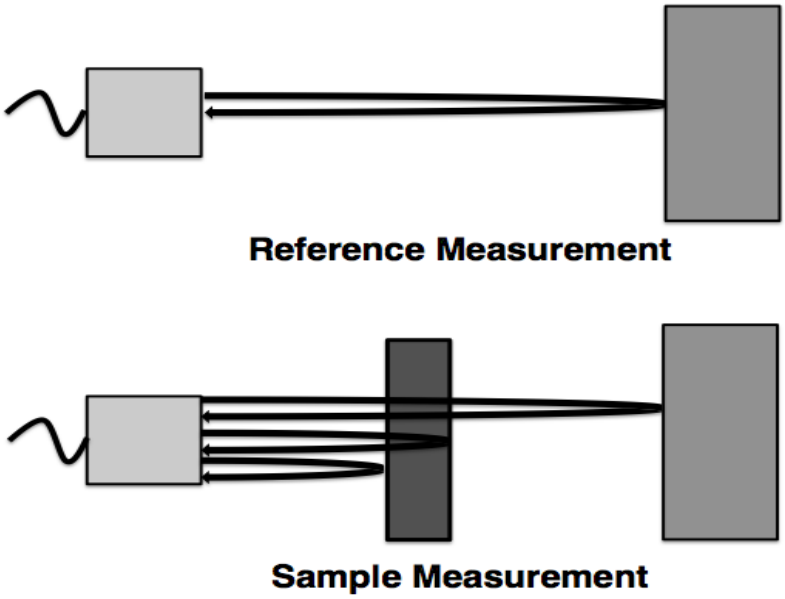

FIGURE 6.16: Shadowed reflector setup for the narrowband phase velocity measurements. The transducer is aligned with the steel reflector. The sample is placed in between the transducer and the reflector but in this case is not touching the reflector. For the sample measurement, the reflection off of the steel reflector through the sample, the reflection off of the back wall of the sample, and the reflection off of the front wall of the sample are all signals of interest. The reference measurement involves the reflection off the steel reflector in the absence of a sample.

point, and $(n_i - n_j)$ is the maximum of the correlation between signal i and signal j (Trousil *et al.*, 2001).

In order to do the correlation in time correctly, phase shifts that occur during reflection due to impedance differences between media must be taken into account. The reflected wave of an ultrasonic signal moving from a lower acoustic impedance medium into a higher acoustic impedance medium experiences a 180 degree phase shift (Bushberg *et al.*, 2002). For the narrowband measurements, that phase shift occurs for the reference signal, the sample signal, and the front wall signal because the host medium has a lower acoustic impedance than the sample and the steel reflector. The back wall signal is the only signal that does not experience this phase shift. Thus, the correlation between the front wall and the back wall signals must take into account the effect of the shift.

The electronics necessary for the narrowband setup were different than those used in the broadband setup and are shown in Figure 6.17. The pulse is generated using the 8116A Function Generator. After a number of calibration tests, it was determined that using a sine wave pulse in "I Burst" mode with an input peak-to-peak amplitude of 250 mV, a repeat interval of 10 ms, and a duty cycle of 50% produced a reasonable signal. The frequency and number of cycles were varied depending on the measurement. The function generator's sync out went to the Tektronix TDS5052B oscilloscope's trigger, while the function generator's output went to the ENI Power Amplifier. The power amplifier has a constant gain of approximately 50 dB.

The Ritec Diplexer permits shadowed reflector data to be taken with this system.

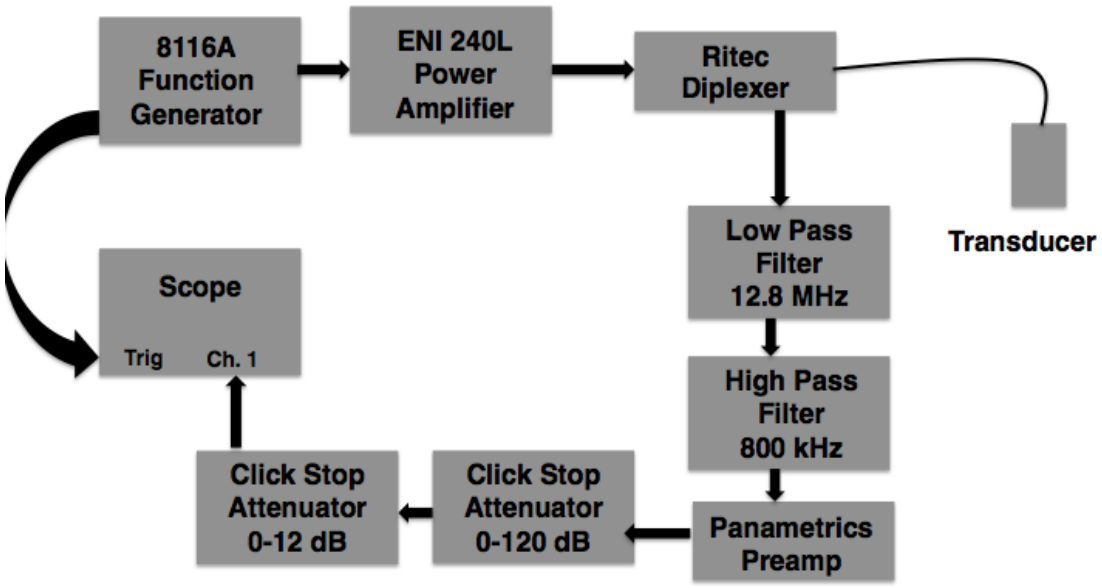

FIGURE 6.17: The electronic setup for the narrowband phase velocity shadowed reflector measurement.

The Diplexer's diode expander setting was on "In" and the two attenuators were set to "1 dB" and "0 dB". The Low Frequency Cutoff was set at 3 kHz (setting "A") and the damping resistor was set to 10 ohms (setting "8"). The diplexer was attached to a Panametrics V309 transducer with a nominal center frequency of 5 MHz, a 0.5 inch diameter, and a nominal 2 inch point target focus. The output of the diplexer was connected to two custom built filters (a 12.8 MHz low pass filter and an 800 kHz high pass filter) that were attached to a Panametrics Pre-Amplifier with a fixed 40 dB gain. Two click stop attenuators were included in the system, although initially both were set to 0 dB. The output of the click stop attenuators was connected to the oscilloscope.

For each narrowband measurement, the phase velocity was measured every half

Frequency (MHz)	Phase Velocity (m/s) (Variable Number of Cycles)	Phase Velocity (m/s) (40 Cycles)
4.0	1532.3 ± 0.2	1532.3 ± 0.4
5.0	1531.8 ± 0.2	1532.0 ± 0.1
6.0	1532.2 ± 0.1	1532.2 ± 0.2
7.0	1531.5 ± 0.2	1531.4 ± 0.2

TABLE 6.1: A comparison between the narrowband phase velocity measured with a variable number of cycles and the narrowband phase velocity measured keeping the number of cycles constant. For the most part good agreement can be seen between the two measurements. Measurements are reported as mean ± standard deviation of the six measurements taken at each frequency for each number of cycles to illustrate the precision. The actual uncertainty reflecting the accuracy of the narrowband measurements was estimated to be ±2 m/s.

megahertz across the bandwidth from 4 MHz to 7 MHz. The number of cycles per pulse determines the bandwidth of the pulse. In order to determine a reasonable number of cycles for each pulse, two separate narrowband measurements were made at 4.0 MHz, 5.0 MHz, 6.0 MHz, and 7.0 MHz. In the first experiment, the number of cycles increased as the frequency increased. The number of cycles was set to 12 at 4.0 MHz and increased by 4 cycles for every MHz of frequency to 24 cycles at 7.0 MHz. For the second experiment, the number of cycles was kept at a constant 40 for each frequency. The phase velocity was measured at each frequency using both methods and the results are shown in Table 6.1. Reasonable agreement is seen between the two measurements. For the measurements detailed in this thesis, the number of cycles was increased as the frequency of the input signal was increased resulting in a bandwidth of approximately 0.5 MHz for the narrowband output at each frequency.

6.6 The Kramers-Kronig Relations

The Kramers-Kronig relations were used as another way of unambiguously determining the correct phase sheet offset for the broadband measurement (Trousil *et al.*, 2001). The relations also served as a theoretical check on the measured dispersion in the phase velocity. The nearly local Kramers-Kronig relations with one subtraction were used to calculate the predicted dispersion in the phase velocity for media with a linear-with-frequency amplitude attenuation coefficient (Waters *et al.*, 2005, 2003; Trousil, 2002). The nearly local Kramers-Kronig relations with two subtractions were used to determine the dispersion in the phase velocity for media whose amplitude attenuation coefficient obeys a frequency power law with an exponent between 1 and 2 (Waters *et al.*, 2000; Trousil, 2002).

6.6.1 Nearly Local Kramers-Kronig Relations with One Subtraction

For media with a linear-with-frequency dependence of the amplitude attenuation coefficient the nearly local Kramers-Kronig relations with one subtraction are used to predict the dispersion in the phase velocity (Waters *et al.*, 2005, 2003; Trousil, 2002). These media have attenuation of the form expressed in Equation 6.14

$$\alpha(\omega) = \alpha(\omega_c) + \frac{\beta}{2\pi}(\omega - \omega_c) \tag{6.14}$$

where β is the slope of the amplitude attenuation coefficient in Np/m/Hz and ω_c is the angular frequency at band center. A linear fit to the attenuation coefficient data

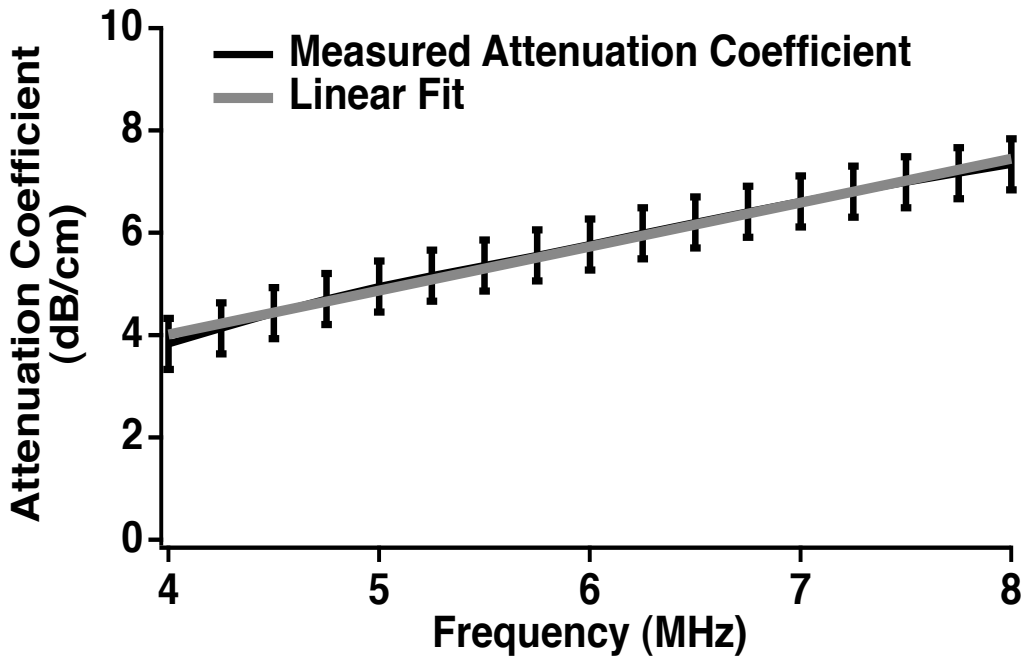

FIGURE 6.18: The experimentally measured attenuation coefficient for Lucite^{TM} a medium with approximately linear with frequency dependence. The linear fit line is displayed to show the reasonableness of the fit. The slope from this fit will be in units of dB/cm/MHz and must be converted to the proper units before the Kramers-Kronig prediction can be made. The error bars are the experimentally measured standard deviation in the data. The error bars are only plotted at a few frequencies across the bandwidth.

as a function of frequency leads to the determination of β as shown in Figure 6.18 for an example data set (Lucite^{TM}). The attenuation coefficient fit in the example has the units of decibels/centimeter and thus the slope of the attenuation coefficient (β) determined from the fit must be converted into the proper units before the Kramers-Kronig prediction can be calculated. The dispersion in the phase velocity is approximated by the nearly local Kramers-Kronig relations with one subtraction shown in Equation 6.15 (Waters *et al.*, 2005, 2003; Trousil, 2002).

$$\frac{1}{v(\omega)} - \frac{1}{v(\omega_0)} = -\frac{2}{\pi}\frac{\beta}{2\pi}\ln(\omega/\omega_0) \tag{6.15}$$

where v(ω) is the phase velocity as a function of frequency and ω_0 is a frequency within the usable bandwidth. When the dispersion in the phase velocity is small, then Equation 6.15 can be expanded to first order in the dispersion as displayed in Equation 6.16 (Waters *et al.*, 2005, 2003; Trousil, 2002). Equation 6.16 was used to predict the dispersion in the phase velocity measured in the lucite sample.

$$v(\omega) \cong v(\omega_0) + v^2(\omega_0)\frac{\beta}{\pi^2}\ln(\omega/\omega_0) \tag{6.16}$$

The Kramers-Kronig relations can only predict relative changes in phase velocity. In order to compare the experimentally-measured broadband phase velocity to the Kramers-Kronig prediction, the experimental phase velocity at approximately the center of the bandwidth (6 MHz in this case) was used for $v(\omega_0)$ (Waters *et al.*, 2005, 2003; Trousil, 2002). The measured broadband phase velocity at a phase sheet offset (m-n) of zero and the predicted dispersion are displayed in Figure 6.19. Good agreement can be seen between the measured dispersion in the broadband phase velocity and the predicted dispersion from the nearly local Kramers-Kronig relations with one subtraction. As stated before, an additional benefit of the Kramers-Kronig relations is that they provide a method of determining the proper phase sheet offset for the broadband measurement (Trousil, 2002).

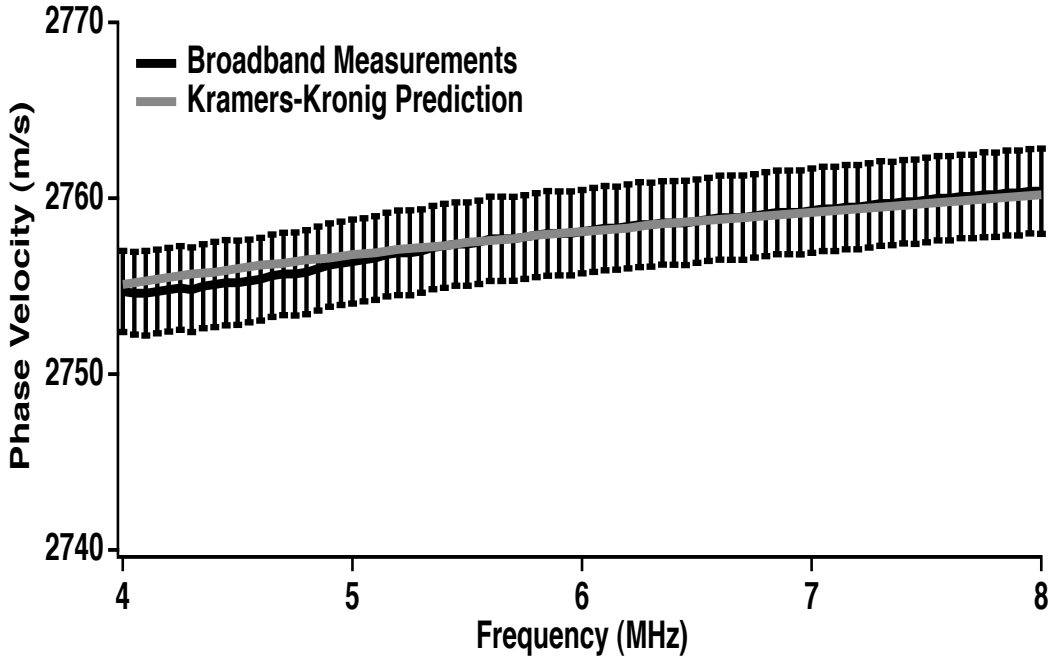

FIGURE 6.19: The experimentally measured phase velocity for a media (Lucite^{TM}) with approximately linear with frequency amplitude attenuation coefficient is displayed along with the predicted dispersion from the nearly local Kramers-Kronig relations with one subtraction.

6.6.2 Nearly Local Kramers-Kronig Relations with Two Subtractions

For media with a power law frequency dependence of the amplitude attenuation coefficient with an exponent between one and two, the nearly local Kramers-Kronig relations with two subtractions is used to predict the dispersion in the phase velocity (Waters *et al.*, 2000). An example of this type of media is castor oil that has attenuation of the form shown in Equation 6.17

$$\alpha(\omega) = \alpha_0 \omega^y \tag{6.17}$$

Equation 6.17 can be re-expressed in Equation 6.18 in terms of the frequency for clarity.

$$\alpha(\omega) = \alpha_0^{'} f^y \tag{6.18}$$

A power law fit to the attenuation coefficient data as a function of frequency leads to the determination of $\alpha_0^{'}$ and y as shown in Figure 6.20 for example data from castor oil that display an attenuation coefficient that increases with frequency as a power law.

Theoretically, the form of the attenuation expressed in Equation 6.17 is correct, but, in actuality, experimental measurements of the attenuation coefficient sometimes appear to have an attenuation coefficient that does not extrapolate to zero at zero frequency. The possible consequences of this are not germane to the work presented in this thesis

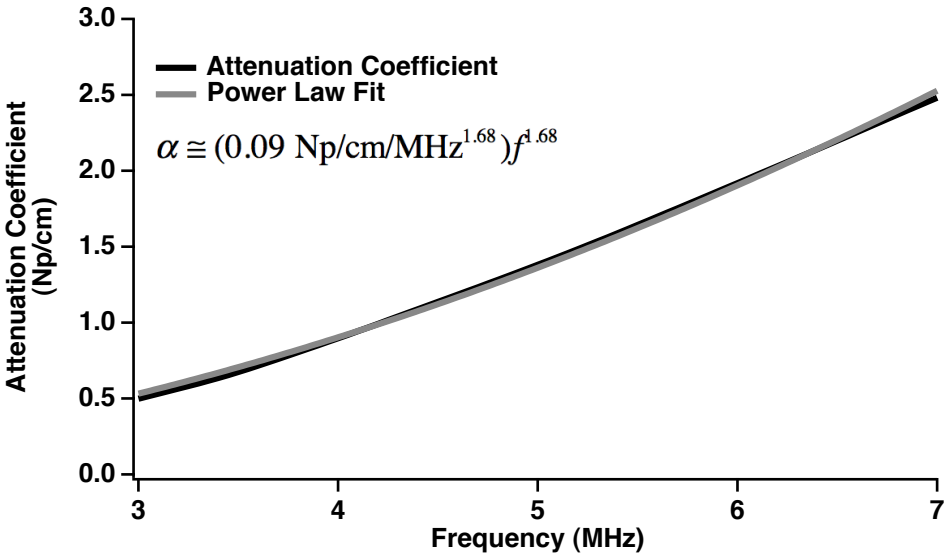

FIGURE 6.20: The experimentally measured attenuation coefficient in Np/cm for a media (castor oil) with frequency dependence greater than linear with frequency. The power law fit is of the form expressed in Equation 6.18.

The dispersion in the phase velocity is approximated by the nearly local Kramers-Kronig relations with two subtractions shown in Equation 6.19 (Waters *et al.*, 2000).

$$\frac{1}{v(\omega)} - \frac{1}{v(\omega_0)} = \alpha_0 \tan\left(\frac{\pi y}{2}\right)\left(\omega^{y-1} - \omega_0^{y-1}\right) \tag{6.19}$$

As in the case of the Kramers-Kronig relations with one subtraction, if the dispersion in the phase velocity is small, Equation 6.19 can be expanded to arrive at an expression for the Kramers-Kronig prediction of the phase velocity shown in Equation 6.19. Equation 6.20 was used to predict the dispersion in the phase velocity measured in the example medium (castor oil).

$$v(\omega) \cong v(\omega_0) - v^2(\omega_0)\alpha_0 \tan\left(\frac{\pi y}{2}\right)\left(\omega^{y-1} - \omega_0^{y-1}\right) \tag{6.20}$$

In order to compare the experimentally-measured broadband phase velocity and the Kramers-Kronig prediction, the experimentally-measured phase velocity at approximately the center of the bandwidth (6 MHz in this case) was used for $v(\omega_0)$ (Waters *et al.*, 2000; Trousil, 2002).

The measured broadband phase velocity and the predicted dispersion for the power law fit expressed in Equation 6.17 are displayed in Figure 6.21. Good agreement can be seen between the measured dispersion in the broadband phase velocity and the predicted dispersion from the nearly local Kramers-Kronig relations with two subtractions.

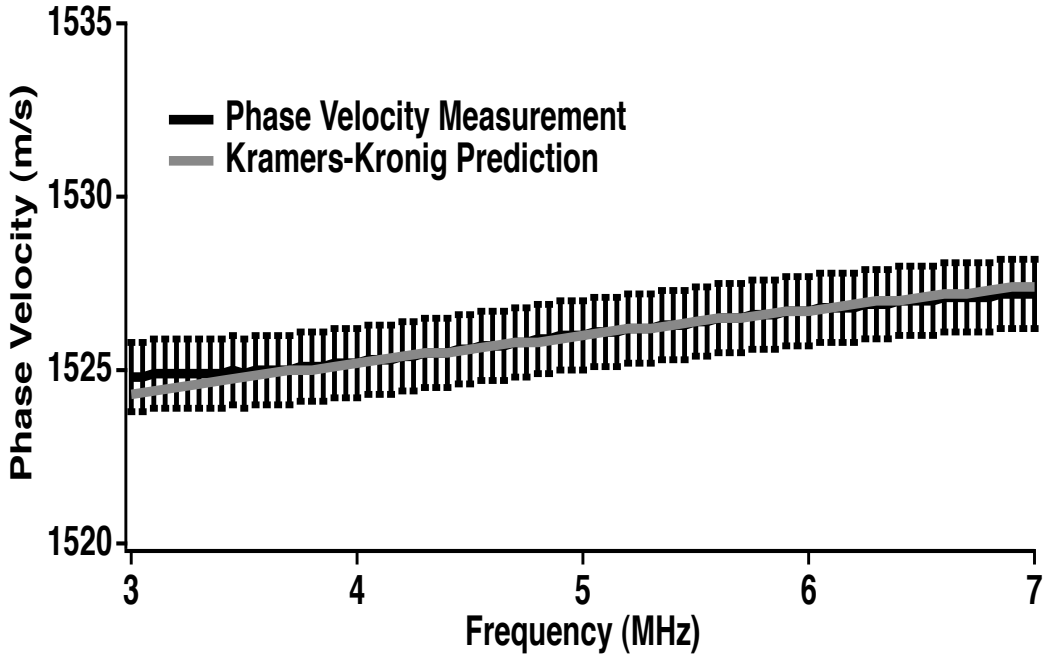

FIGURE 6.21: The experimentally measured phase velocity for a media with amplitude attenuation coefficient with a power law dependence on frequency is displayed along with the predicted dispersion from the nearly local Kramers-Kronig relations with two subtractions for the power law fit expressed in Equation 6.18.

6.7 Phase Velocity Measurements of Cornstarch Suspensions

The broadband phase spectroscopy technique detailed in Section 6.3 was used to measure the phase velocity of cornstarch suspensions in 51.5% cesium chloride solutions for several different concentrations of cornstarch. The narrowband phase velocity measurement technique discussed in Section 6.5 was employed for several of the concentrations. The theoretical dispersion in the phase velocity was predicted using the nearly local Kramers-Kronig relations with one subtraction from Section 6.6.1, because the suspensions displayed an approximately linear with frequency amplitude attenuation coefficient.

6.7.1 10% Cornstarch Suspensions

Broadband phase velocity measurements of eight different samples of a 10% cornstarch suspension in a 51.5% cesium chloride solution were made. The results of these measurements are displayed in Figures 6.22 and 6.23. The magnitude of the phase velocity at the center of the bandwidth (6 MHz) is displayed in Figure 6.22. The absolute magnitude of the phase velocity is consistent with the group velocity measurement of the 10% cornstarch suspensions discussed in Section 4.3.1. The group velocity of the 10% cornstarch suspensions in a 51.5% cesium chloride brine was 1531 m/s $\pm$ 6 m/s. Small differences in the absolute level of the phase velocity arose as a result of a slight inhomogeneity in the samples due to incomplete mixing. Differences

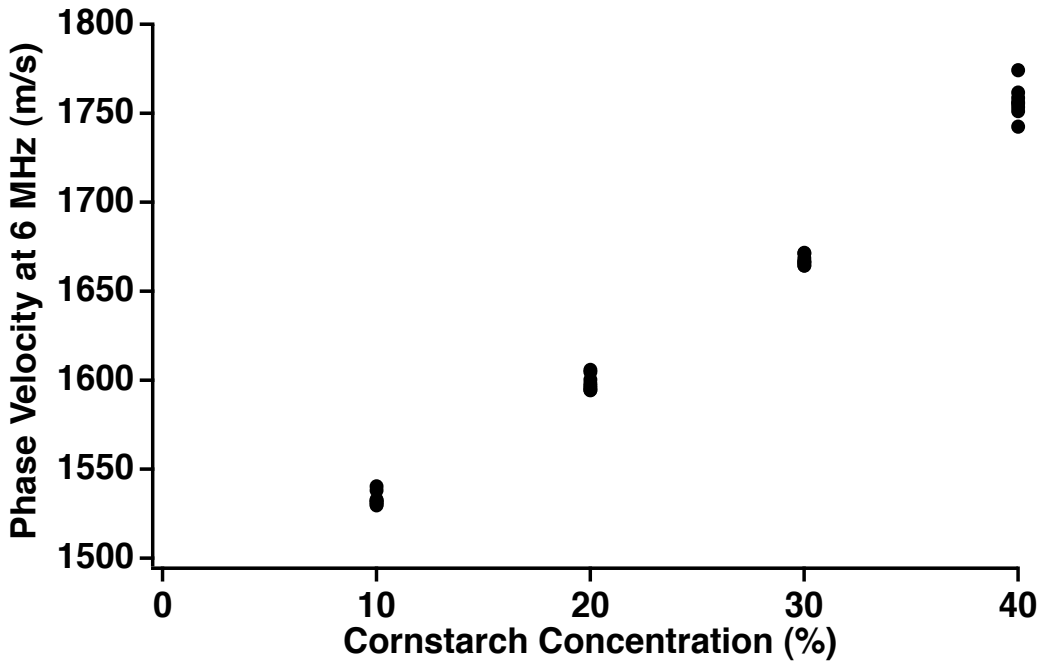

FIGURE 6.22: The broadband phase velocity at the center of the bandwidth (6 MHz) for each of the cornstarch suspensions in 51.5% cesium chloride solution at every concentration studied.

in the temperature of the suspension during the time of measurement (the temperatures at measurement ranged from approximately 18.5°C to 21.5°C) also contributed to the slight differences in the magnitude observed.

The dispersion in the broadband phase velocity of the 10% cornstarch suspensions in 51.5% cesium chloride brine is plotted in Figure 6.23. Each of the eight measurements of the phase velocity has been normalized by the magnitude of the phase velocity at the center of the bandwidth (6 MHz). Based on Kramers-Kronig, considerations the phase velocity is expected to increase with frequency, but the experimental phase velocity decreases with frequency for each sample.

From the attenuation coefficient measurements from Section 5.4.1, the slope of

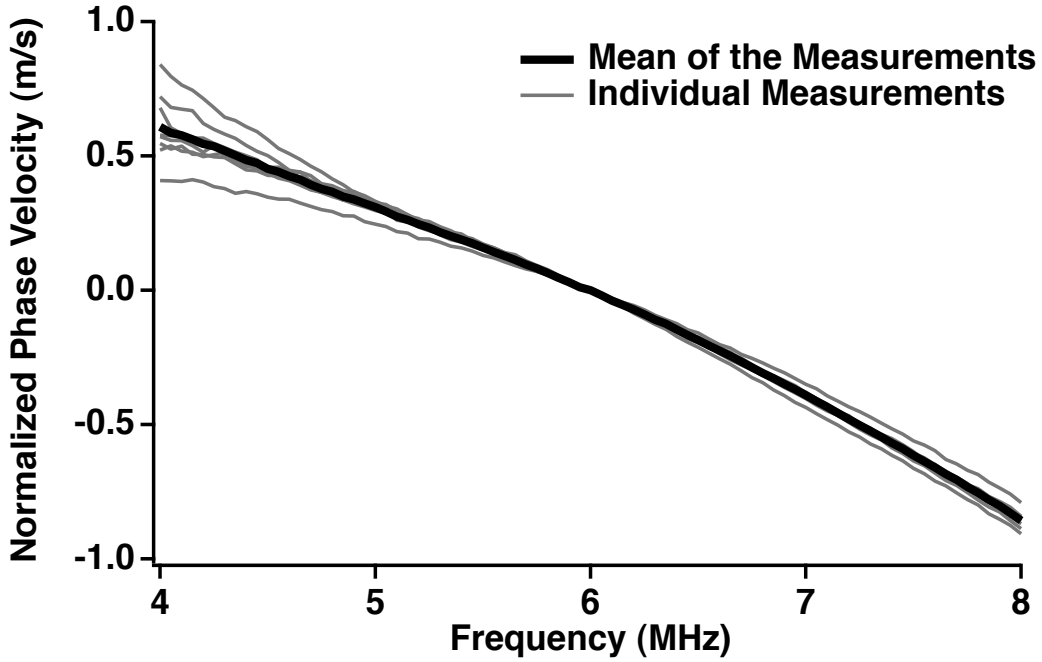

FIGURE 6.23: The broadband phase velocity of eight different samples of 10% cornstarch suspensions in a density-matched cesium chloride brine. Each individual phase velocity measurement is normalized to its value at the center of the bandwidth (6 MHz). To better compare the results the error bars are not displayed on the graph. A typical standard deviation in the measurement was approximately ± 1 m/s.

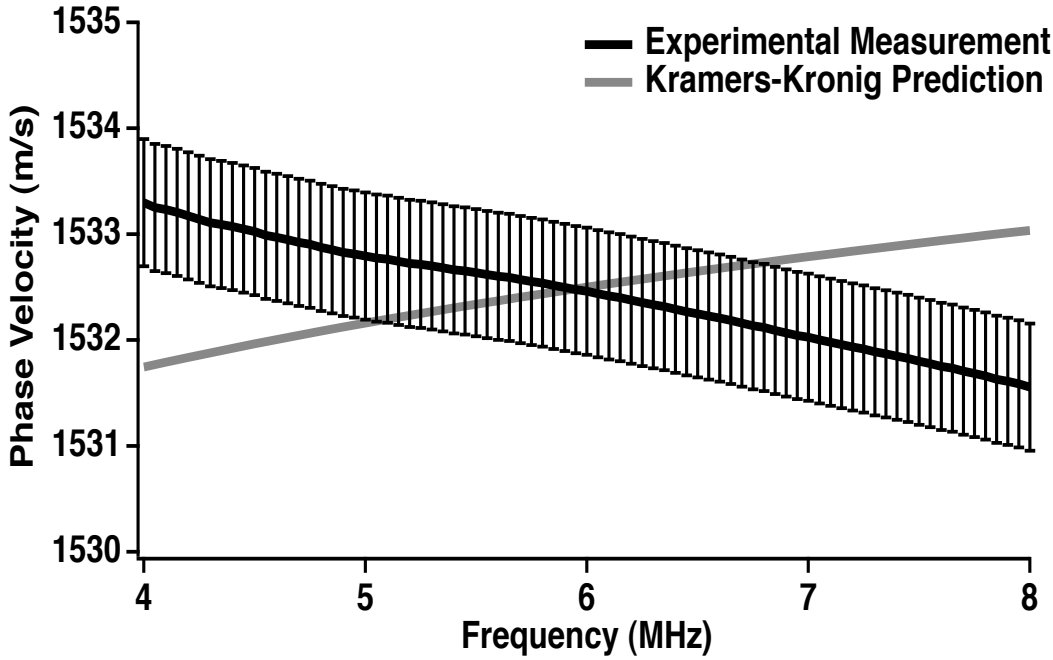

FIGURE 6.24: The broadband phase velocity of a single sample of a 10% cornstarch suspension in a density-matched cesium chloride brine compared to the Kramers-Kronig prediction. The experimental measurement is plotted as the mean ± the standard deviation in the measurement.

the attenuation coefficient for one of the samples was found. The Kramers-Kronig relations with one subtraction were used to predict the dispersion in the phase velocity for this sample. The broadband measurement of phase velocity at 6 MHz (the approximate center of the bandwidth) was used to set the absolute level of the Kramers-Kronig prediction of the phase velocity. Figure 6.24 displays the experimentally measured phase velocity compared to the Kramers-Kronig prediction. As stated earlier, the Kramers-Kronig relations predict a positive dispersion in contrast to the negative dispersion in the experimental measurements.

To further check the experimental result, the narrowband phase velocity technique described in Section 6.5 was employed. For one sample of the 10% cornstarch suspen-

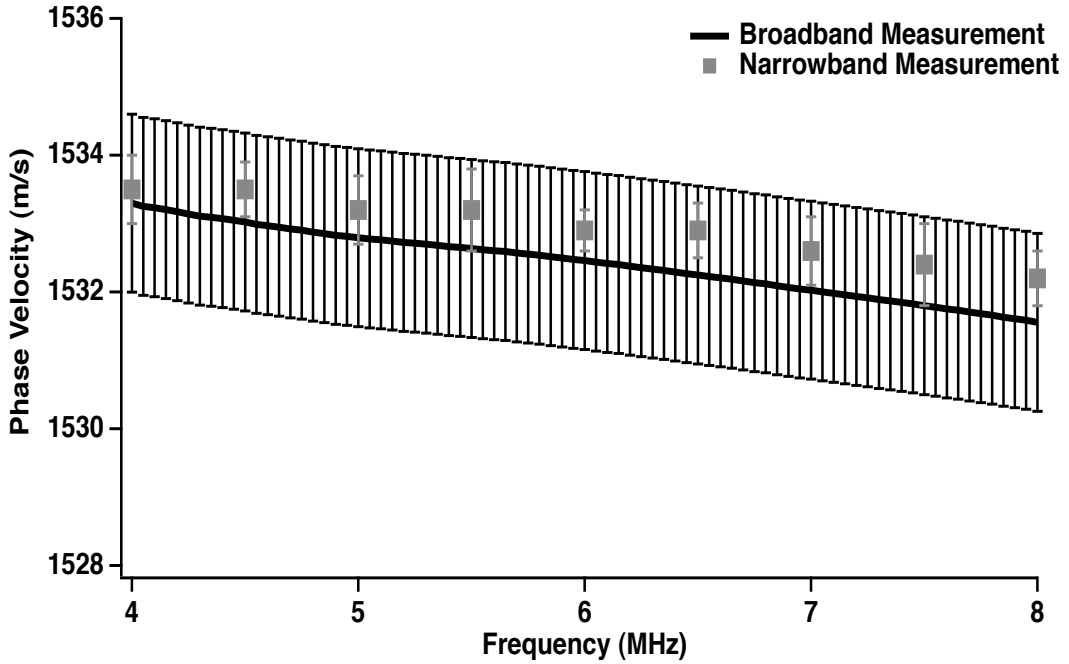

FIGURE 6.25: The broadband phase velocity of a single sample of a 10% cornstarch suspension in a density-matched cesium chloride brine compared to the narrowband phase velocity measurement.

sion in a 51.5% cesium chloride solution, the phase velocity was measured using both the broadband phase spectroscopy and the narrowband phase velocity technique. The results of this measurement are shown in Figure 6.25. The narrowband phase velocity results mirror the broadband phase velocity measurements providing an initial check on the accuracy of the measurements even though both display the unexpected negative dispersion.

The broadband phase velocity was also measured for two samples of a 10% suspension of cornstarch and water without the cesium chloride added. The measurements were made more difficult without the density-matching because the particles settled more quickly and thus greater variability was seen in the measurements. To combat

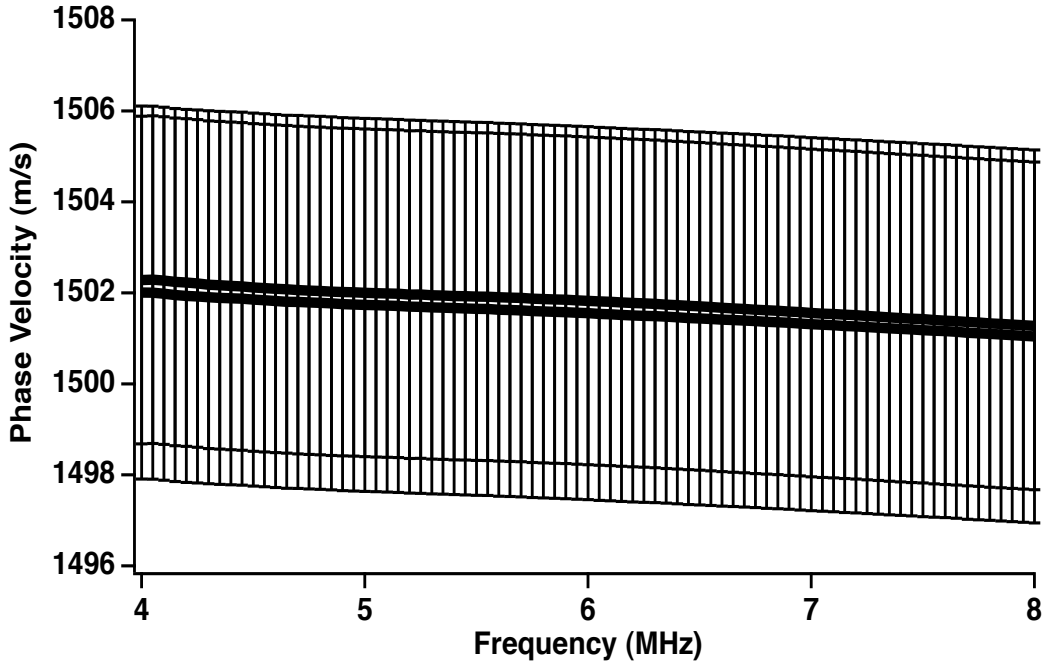

FIGURE 6.26: The two broadband phase velocity samples of a 10% cornstarch suspension in water without cesium chloride added. The measurements are plotted as the mean ± the standard deviation of the measurement.

settling, the sample mold was agitated before each individual phase velocity measurement was taken. The results of the measurement are shown in Figure 6.26. The negative dispersion is also apparent in the samples containing only cornstarch in water. The absolute magnitude of the phase velocity is much lower than the magnitude measured for the samples in a density-matched brine, but is reasonably consistent with the group velocity measurement made on the cornstarch and water samples discussed in 4.3.1. The group velocity reported in the earlier chapter in the 10% cornstarch suspensions with water was 1499 m/s ± 10 m/s.

As another check on the data, the broadband phase velocity was measured on a sample using both the shadowed reflector method and the through transmission

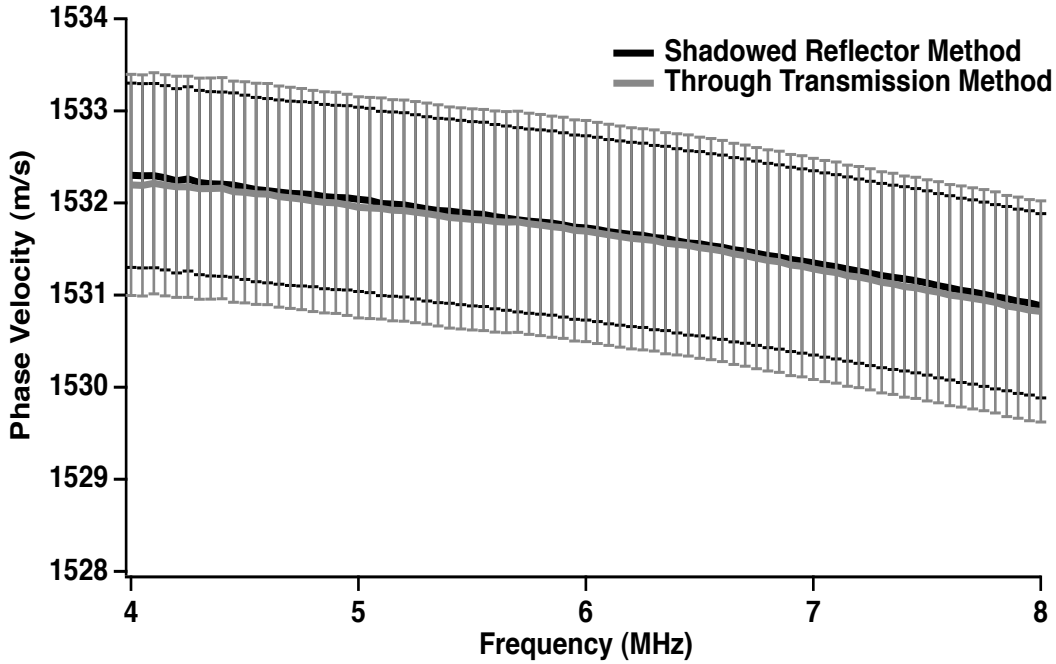

FIGURE 6.27: A comparison between the shadowed reflector method and the through transmission method for measuring the phase velocity showing the mean of the measurements from one sample. The error bars are the standard deviation of the measurement.

method. The results are shown in Figure 6.27 for the mean of the measurement and the standard deviation in the measurements. Figure 6.28 plots individual phase velocity traces that were averaged together in Figure 6.27 for both the through transmission and shadowed reflector method. All of the phase velocity traces plotted show that not only does the mean of the measurement display the negative dispersion, but each individual measurement does as well. These measurements are typical of all of the measurements of the phase velocity shown in the this thesis. Good agreement can be seen in both figures between the two different methods for measuring the phase velocity.

The magnitude of dispersion over the bandwidth (4 MHz to 8 MHz) was measured

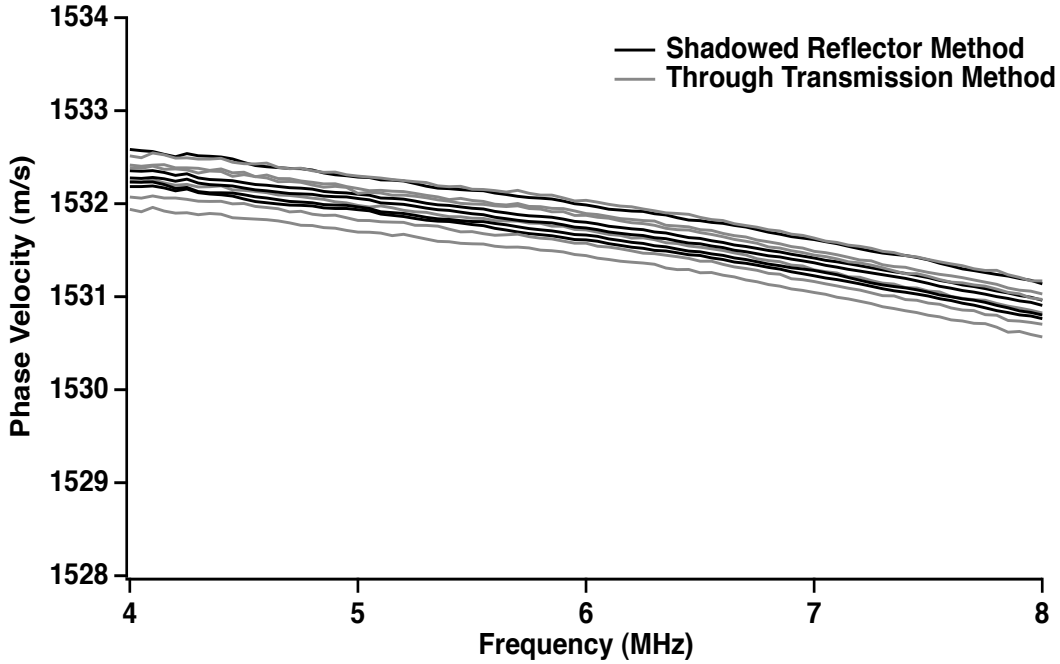

FIGURE 6.28: A comparison between the shadowed reflector method and the through transmission method for measuring the phase velocity. The individual traces are plotted for both sets of measurements.

Sample	Dispersion Magnitude (m/s/MHz)
10% Cornstarch in CsCl #1	-0.35
10% Cornstarch in CsCl #2	-0.35
10% Cornstarch in CsCl #3	-0.35
10% Cornstarch in CsCl #4	-0.43
10% Cornstarch in CsCl #5	-0.40
10% Cornstarch in CsCl #6	-0.43
10% Cornstarch in CsCl #7	-0.43
10% Cornstarch in CsCl #8	-0.35
Average	-0.39 ± 0.04
10% Cornstarch in Water #1	-0.25
10% Cornstarch in Water #2	-0.25

TABLE 6.2: The magnitude of dispersion in the phase velocity measured for each of the 10% cornstarch in density-matched cesium chloride brine samples compared to the magnitude of dispersion for the two 10% cornstarch in water samples.

for each of the eight samples of cornstarch in a density-matched cesium chloride solution and for the two cornstarch in water samples and displayed in Table 6.2. The average magnitude of dispersion in the cornstarch suspensions in a 51.5% cesium chloride solution was determined to be approximately -0.39 m/s/MHz ± 0.04 m/s/MHz and the magnitude of dispersion in the cornstarch suspensions in water was approximately -0.25 m/s/MHz.

6.7.2 20% Cornstarch Suspensions

Broadband phase velocity measurements of eight different samples of a 20% cornstarch suspension in a 51.5% cesium chloride solution were made. The magnitude of

the phase velocity at the center of the bandwidth is plotted in Figure 6.22. The overall level of the phase velocity is consistent with the group velocity measured to be 1602 m/s ± 6 m/s. The small differences observed in the absolute magnitude of the phase velocity between the eight samples are probably due to slight inhomogeneities in the samples due to incomplete mixing. Another contributing factor is the differences in the temperature of the suspension during the time of measurement (the temperatures at measurement ranged from approximately 19.0°C to 21.5°C).

The broadband phase velocity of each of the eight samples normalized by the phase velocity at 6 MHz in order to highlight the dispersion across the bandwidth is plotted in Figure 6.29. The phase velocity once again decreases with frequency for each sample.

The slope of the attenuation coefficient for these samples had been measured as discussed in Section 5.4.2. The Kramers-Kronig relations with one subtraction were used to predict the dispersion in the phase velocity for this sample using the measured slope of the attenuation coefficient. The broadband measurement of phase velocity at 6 MHz (the approximate center of the bandwidth) was used to set the absolute level of the Kramers-Kronig prediction. Figure 6.30 displays the experimentally measured phase velocity compared to the Kramers-Kronig prediction. The Kramers-Kronig relations predict positive dispersion whereas the experimental measurement displays negative dispersion.

For one sample of the 20% cornstarch suspension in a 51.5% cesium chloride solution the phase velocity was measured using both the broadband phase spectroscopy

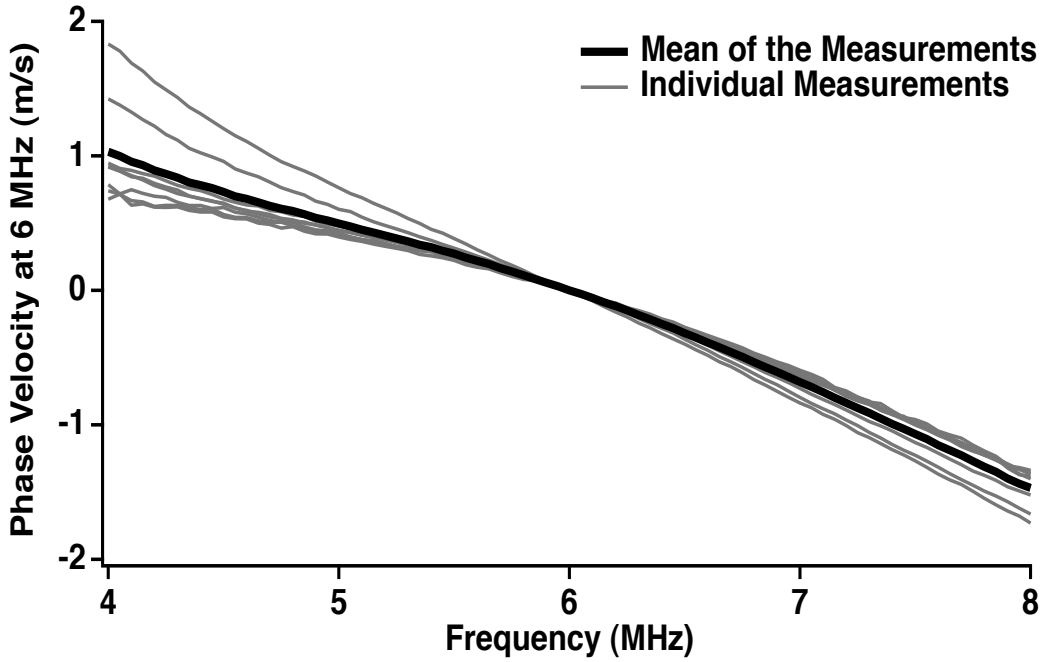

FIGURE 6.29: The broadband phase velocity of eight different samples of 20% cornstarch suspensions in a density-matched cesium chloride brine normalized to the magnitude of the phase velocity at 6 MHz. To better compare the results the error bars are not displayed on the graph. A typical standard deviation for the measurement would be approximately ± 2 m/s.

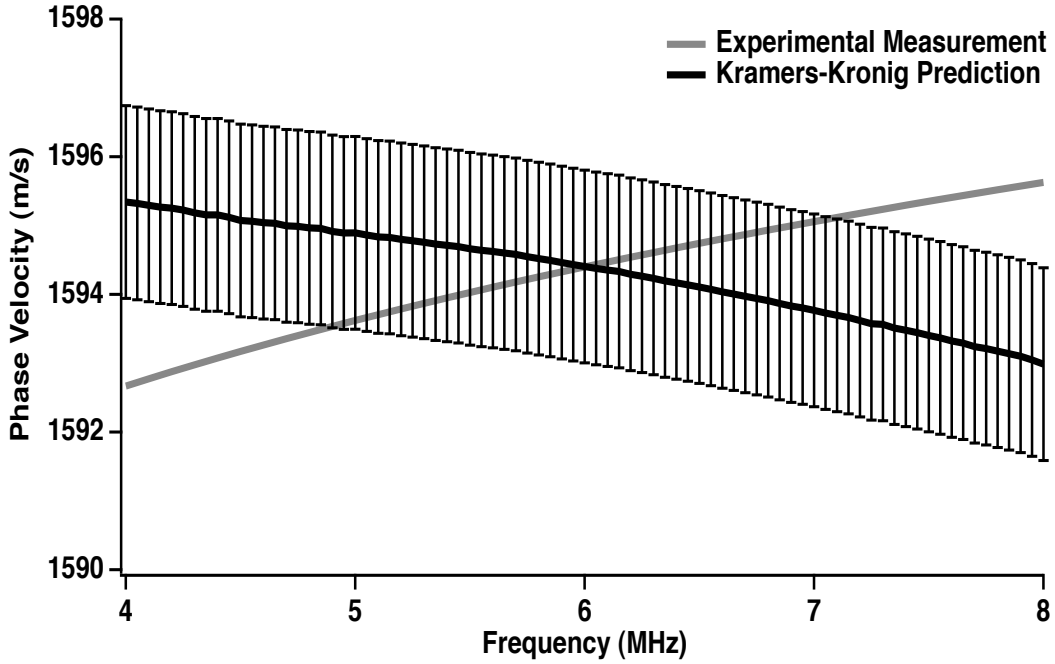

FIGURE 6.30: The broadband phase velocity of a single sample of a 20% cornstarch suspension in a density-matched cesium chloride brine compared to the Kramers-Kronig prediction.

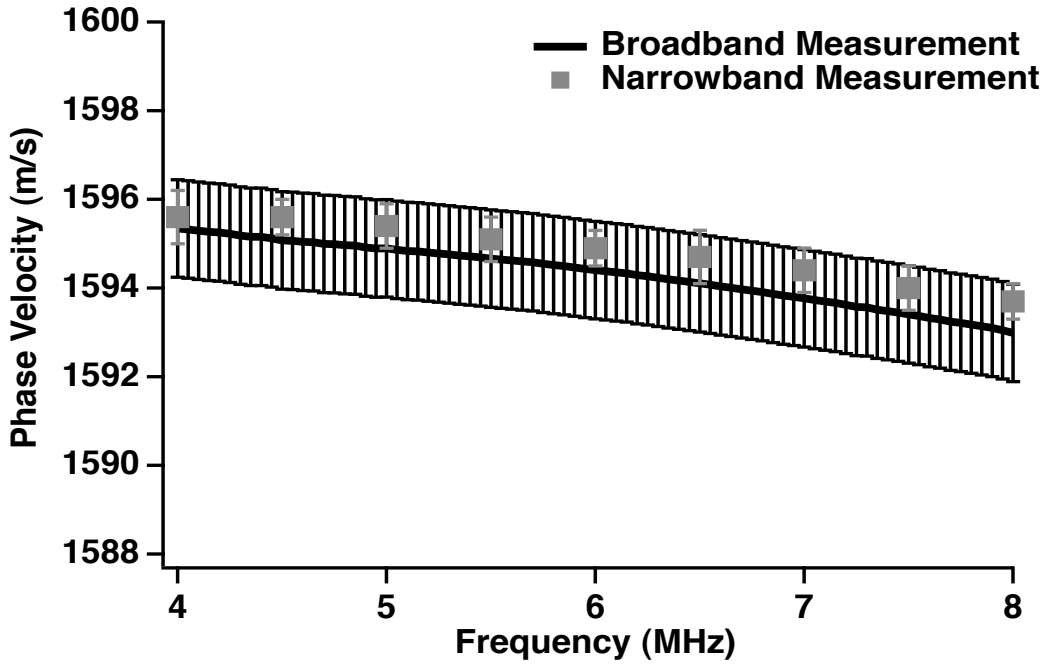

FIGURE 6.31: The broadband phase velocity of a single sample of a 20% cornstarch suspension in a density-matched cesium chloride brine compared to the narrowband phase velocity measurement.

and the narrowband phase velocity techniques. The results of this measurement are shown in Figure 6.31. Once again, the narrowband measurements are consistent with the broadband phase velocity measurements providing at least a basic check on the validity of the data.

The broadband phase velocity was also measured in two samples of a 20% suspension of cornstarch and water without the cesium chloride added. The results of the measurement are shown in Figure 6.32. The negative dispersion is also apparent in the samples containing only cornstarch in water. The absolute magnitude of the phase velocity is consistent with the group velocity measurement made on the cornstarch and water samples discussed in Section 4.3.2 that measured the group velocity

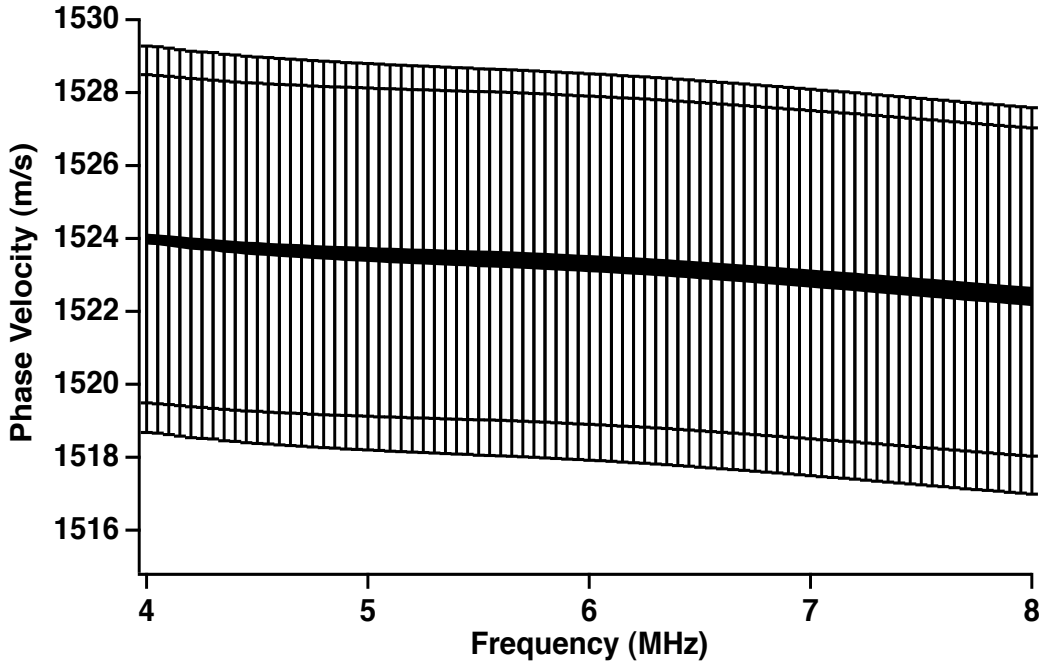

FIGURE 6.32: The broadband phase velocity of two samples of a 20% cornstarch suspension in water without cesium chloride added. The measurements are plotted as the mean ± the standard deviation of the measurement.

in the 20% cornstarch suspensions with water to be 1521 m/s ± 11 m/s.

The magnitude of dispersion over the bandwidth (4 MHz to 8 MHz) measured for all of the 20% cornstarch suspensions was displayed in Table 6.3. The average magnitude of dispersion in the density-matched samples was -0.64 m/s/MHz ± 0.13 m/s/MHz. The magnitude of dispersion in the cornstarch in water suspensions was approximately -0.4 m/s/MHz. Comparing Tables 6.2 and 6.3, the average magnitude of dispersion was seen to be higher in the 20% cornstarch suspension in the density-matched brine than in the 10% cornstarch suspensions.

Sample	Dispersion Magnitude (m/s/MHz)
20% Cornstarch in CsCl #1	-0.73
20% Cornstarch in CsCl #2	-0.58
20% Cornstarch in CsCl #3	-0.63
20% Cornstarch in CsCl #4	-0.90
20% Cornstarch in CsCl #5	-0.53
20% Cornstarch in CsCl #6	-0.73
20% Cornstarch in CsCl #7	-0.55
20% Cornstarch in CsCl #8	-0.5
Average	-0.64 ± 0.13
20% Cornstarch in Water #1	-0.38
20% Cornstarch in Water #2	-0.43

TABLE 6.3: The magnitude of dispersion in the phase velocity measured for each of the 20% cornstarch in density-matched cesium chloride brine samples compared to the magnitude of dispersion for the two 20% cornstarch in water samples.

6.7.3 30% Cornstarch Suspensions

The magnitude of the broadband phase velocity at 6 MHz measured for eight different samples of a 30% cornstarch suspension in a 51.5% cesium chloride solution is displayed in Figure 6.22. The group velocity measured for this concentration of cornstarch in a 51.5% cesium chloride solution was 1671 m/s ± 6 m/s as reported in Section 4.3.3. The small differences in the absolute level of the phase velocity are due to either slight inhomogeneities in the sample due to incomplete mixing or differences in the temperature of the suspension during the time of measurement (the temperatures at measurement ranged from approximately 19.0°C to 20.5°C).

The dispersion in the broadband phase velocity is displayed in Figure 6.33 in which each of the phase velocity measurements has been normalized by the magnitude of the phase velocity at the center of the bandwidth. The negative dispersion seen in the other concentrations of cornstarch is also found in these samples.

The Kramers-Kronig relations with one subtraction were used to predict the dispersion in the phase velocity for one of the samples using that sample's measured slope of the attenuation coefficient. The broadband measurement of phase velocity at 6 MHz (the approximate center of the bandwidth) was used to set the absolute level of the Kramers-Kronig prediction. Figure 6.34 displays the experimentally measured phase velocity compared to the Kramers-Kronig prediction.

A comparison between the narrowband phase velocity and the broadband phase velocity measured for one sample of the 30% cornstarch suspension in 51.5% cesium

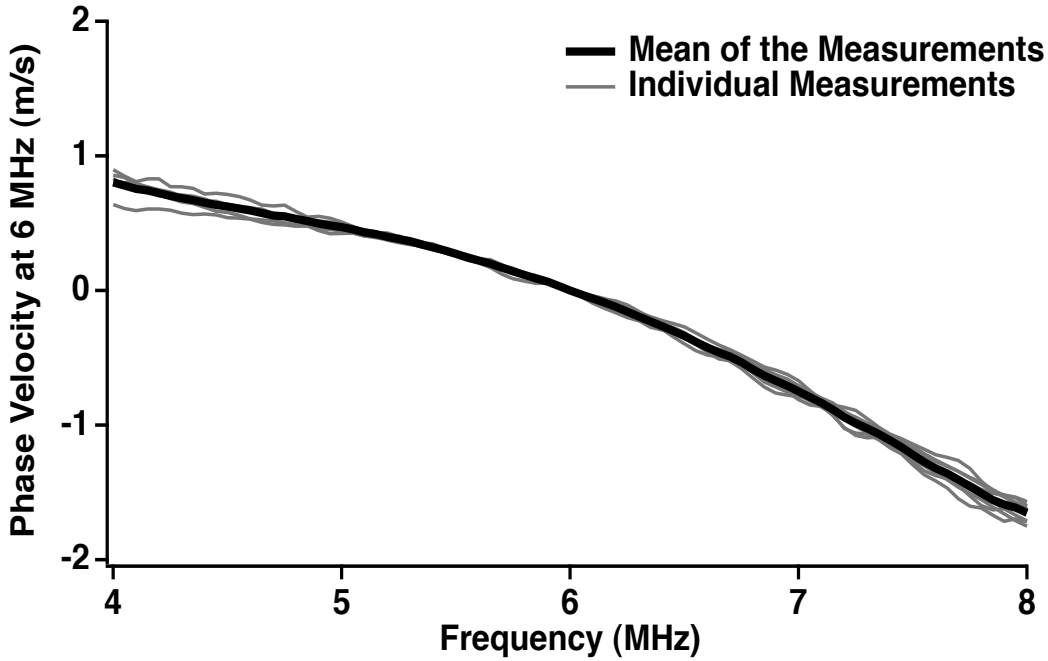

FIGURE 6.33: The broadband phase velocity of eight different samples of 30% cornstarch suspensions in a density-matched cesium chloride brine normalized to the magnitude at the center of the bandwidth. To permit a better comparison of the results the error bars are not displayed on the graph. A typical standard deviation for the measurement would be approximately ± 2 m/s

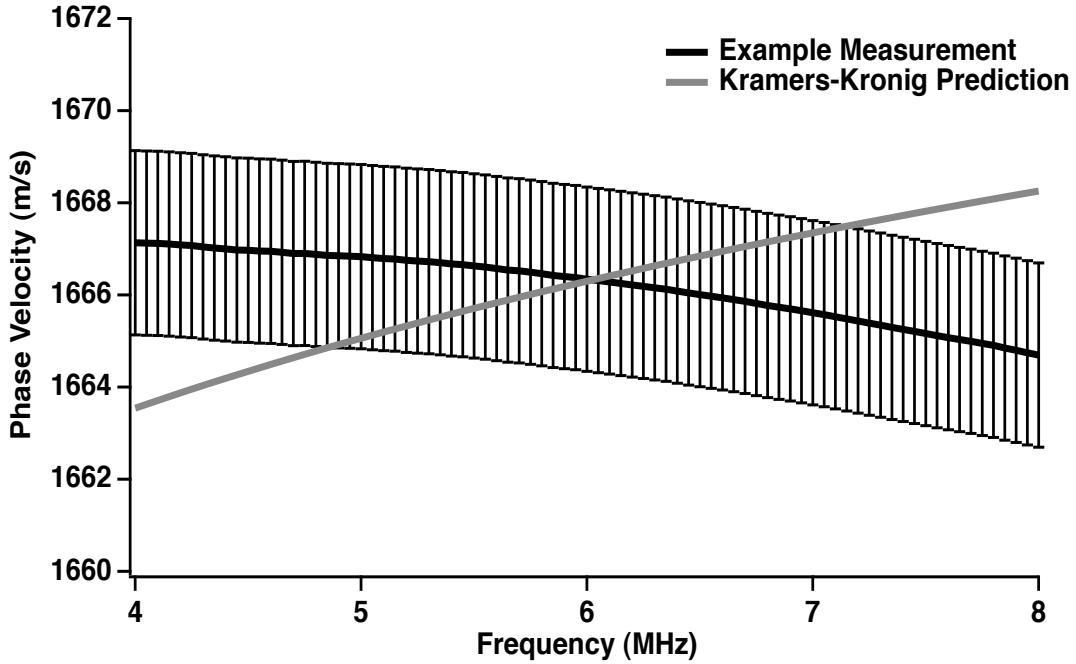

FIGURE 6.34: The broadband phase velocity of a single sample of a 30% cornstarch suspension in a 51.5% cesium chloride brine compared to the Kramers-Kronig prediction.

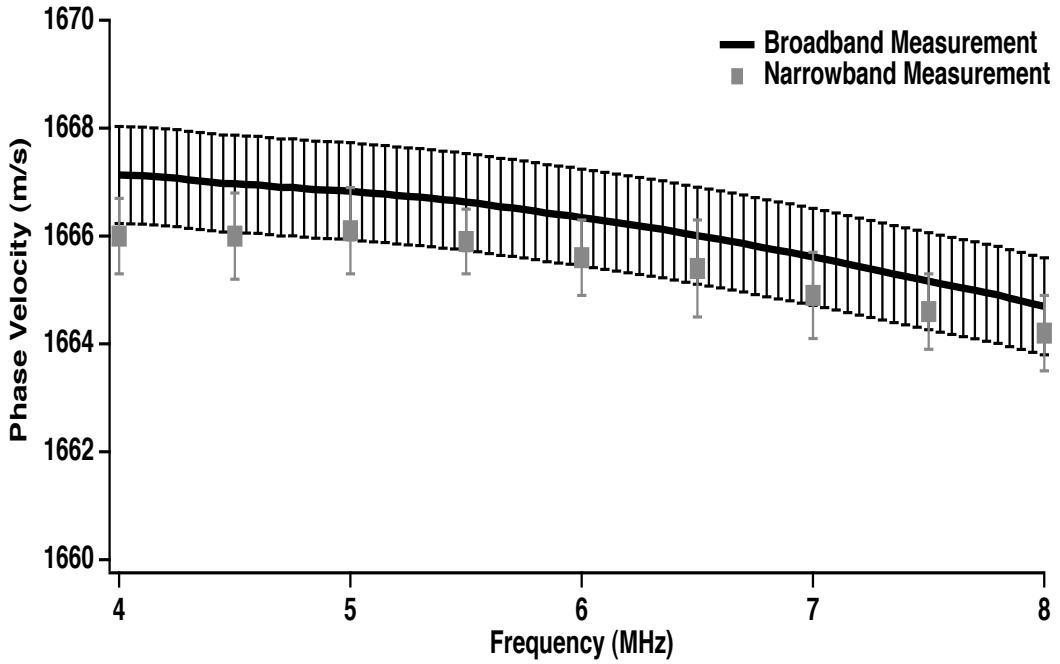

FIGURE 6.35: The broadband phase velocity of a single sample of a 30% cornstarch suspension in a density-matched cesium chloride brine compared to the narrowband phase velocity measurement.

chloride is displayed in Figure 6.35. The two different methods for measuring the phase velocity in the samples at least appear consistent with each other.

The results of the measurement of the broadband phase velocity in two suspensions of 30% cornstarch in water are shown in Figure 6.36. The negative dispersion is also apparent in the samples containing only cornstarch in water. As expected, the absolute magnitude of the phase velocity is much lower than the magnitude measured for the samples in the 51.5% cesium chloride solution, but is reasonably consistent with the group velocity of 1552 m/s $\pm$ 11 m/s of these cornstarch and water samples measured in Section 4.3.3.

The magnitude of dispersion over the bandwidth (4 MHz to 8 MHz) was deter-

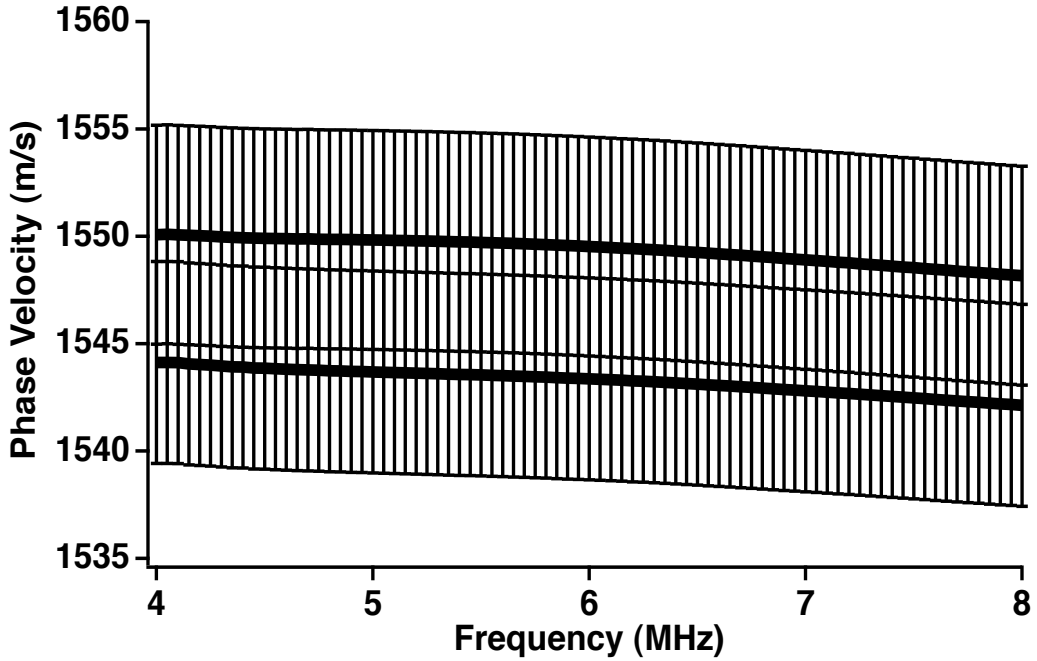

FIGURE 6.36: The broadband phase velocity of two samples of a 30% cornstarch suspension in water without cesium chloride added. The measurements are plotted as the mean ± the standard deviation of the measurement.

Sample	Dispersion Magnitude (m/s/MHz)
30% Cornstarch in CsCl #1	-0.60
30% Cornstarch in CsCl #2	-0.68
30% Cornstarch in CsCl #3	-0.55
30% Cornstarch in CsCl #4	-0.65
30% Cornstarch in CsCl #5	-0.78
30% Cornstarch in CsCl #6	-0.73
30% Cornstarch in CsCl #7	-0.63
30% Cornstarch in CsCl #8	-0.55
Average	-0.64 ± 0.08
30% Cornstarch in Water #1	-0.48
30% Cornstarch in Water #2	-0.50

TABLE 6.4: The magnitude of dispersion in the phase velocity measured for each of the 30% cornstarch in density-matched cesium chloride brine samples compared to the magnitude of dispersion for the two 30% cornstarch in water samples.

mined from the phase velocity measurements for each of the suspensions and displayed in Table 6.4. The average magnitude of dispersion in the density-matched samples was -0.64 m/s/MHz ± 0.08 m/s/MHz and the magnitude of dispersion in the samples of cornstarch and water was approximately -0.5 m/s/MHz. The average magnitude of dispersion in the 30% cornstarch suspensions was approximately the same as the average magnitude of dispersion measured in the 20% cornstarch suspensions, although the variability in the magnitude for the 30% suspensions was smaller than that for the 20% cornstarch suspensions. The magnitude of dispersion in the suspensions of just cornstarch and water was slightly higher in the 30% cornstarch suspensions than in the 20% cornstarch suspensions.

6.7.4 40% Cornstarch Suspensions

Broadband phase velocity measurements of eight different samples of a 40% cornstarch suspension in a 51.5% cesium chloride solution were made. The 40% cornstarch suspensions were the first set of suspensions at a concentration high enough to display shear thickening behavior. Because of this, the suspensions were difficult to mix which resulted in more variability in the ultrasonic measurements. Despite these potential issues, the results shown in Figure 6.37 still consistently show negative dispersion. The absolute magnitude of the phase velocities plotted in Figure 6.22 is relatively consistent with the average group velocity of 1765 m/s $\pm$ 9 m/s of the 40% cornstarch suspensions.

The attenuation in the 40% cornstarch suspensions was high enough that the usable bandwidth was determined to only be between 4 MHz and 7 MHz for these measurements. All of the 40% cornstarch results are thus only plotted from 4 MHz to 7 MHz. The variability in the absolute level of the phase velocity and in the magnitude of the dispersion in this case are primarily due to difficulties in keeping the sample homogeneously mixed. Temperature variations also played a role in the differences seen as the range of temperatures at measurement was approximately 19.0°C to 21.0°C.

The Kramers-Kronig relations were used to predict the dispersion expected in the phase velocity using the measured slope of the attenuation coefficient for one of the samples. Figure 6.38 displays the experimentally measured phase velocity compared

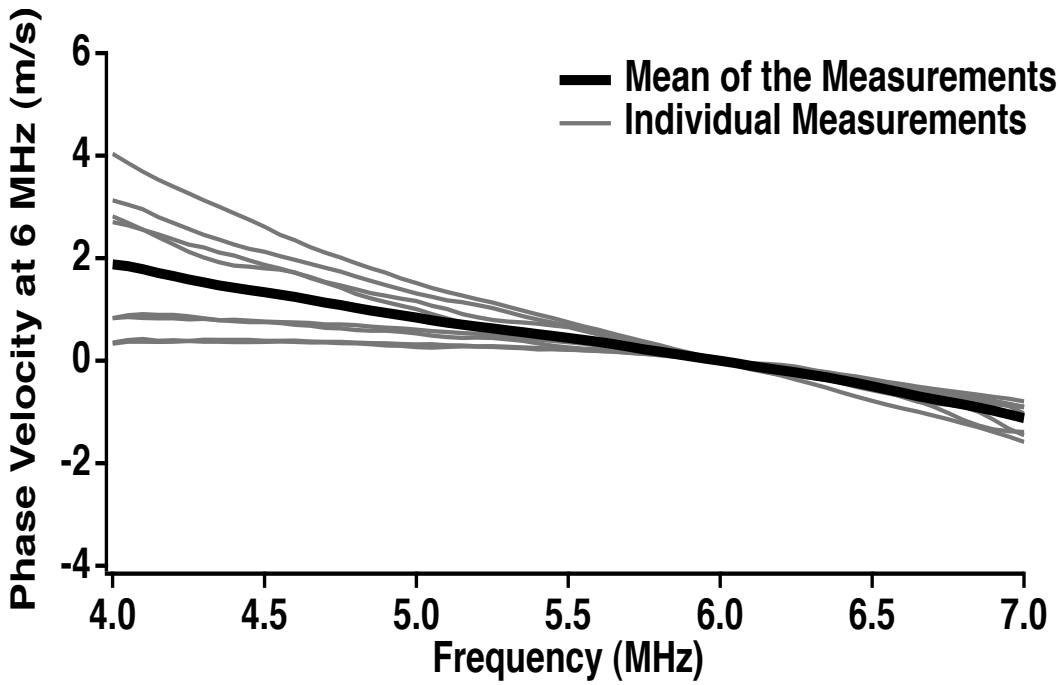

FIGURE 6.37: The broadband phase velocity of eight different samples of 40% cornstarch suspensions in a 51.5% cesium chloride brine normalized to the magnitude of the phase velocity at the center of the bandwidth. To permit a better comparison of the results, the error bars are not displayed on the graph. A typical standard deviation for the measurement would be approximately ±5 m/s.

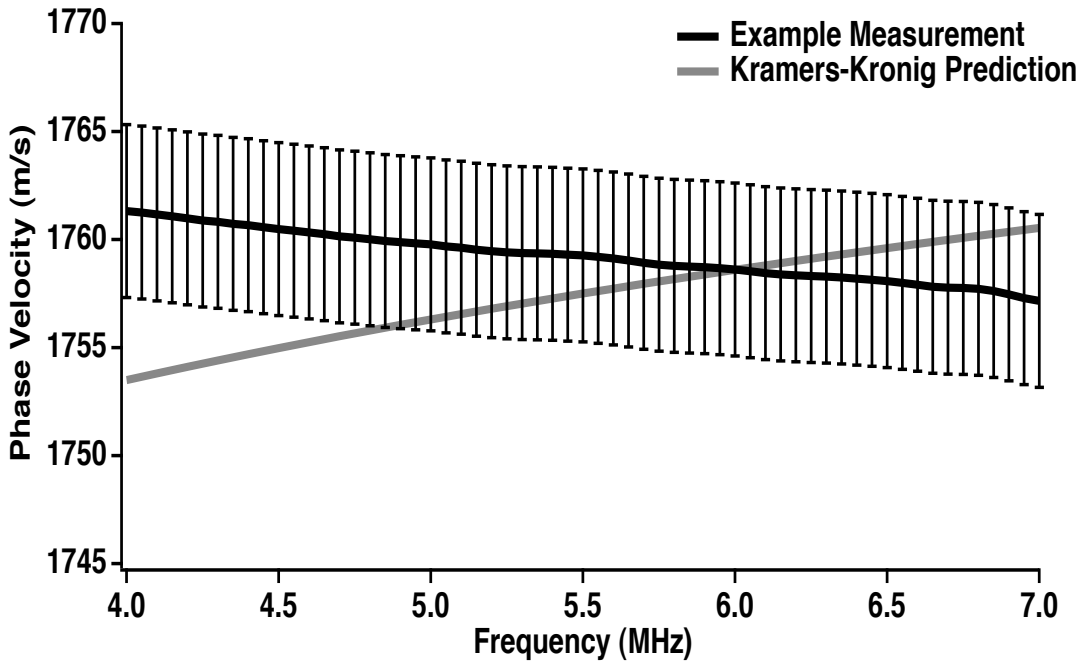

FIGURE 6.38: The broadband phase velocity of a single sample of a 40% cornstarch suspension in a density-matched cesium chloride brine compared to the Kramers-Kronig prediction.

to the Kramers-Kronig prediction. The negative dispersion measured in the samples is in contrast to the positive dispersion predicted by the Kramers-Kronig relations.

Narrowband phase velocity measurements were not made on any of the 40% cornstarch suspensions because of the consistency between the broadband and narrowband results found at the other concentrations. The broadband phase velocity of two samples of a 40% suspension of cornstarch and water without the cesium chloride added was measured. The results of the measurement are shown in Figure 6.39. Consistent with the earlier measurements negative dispersion is apparent in both samples. The absolute magnitude of the phase velocity is much lower than the magnitude measured for the samples in the 51.5% cesium chloride solution, but is reasonably consistent

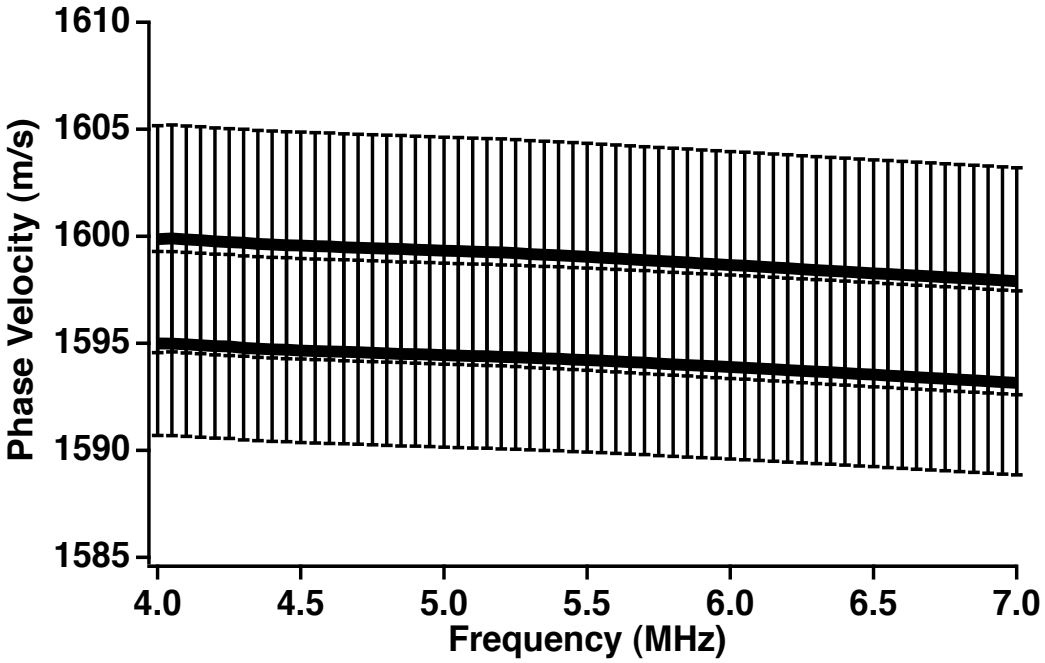

FIGURE 6.39: The broadband phase velocity of two samples of a 40% cornstarch suspension in water without cesium chloride added. The measurements are plotted as the mean ± the standard deviation of the measurement.

with the group velocity measurement made on the cornstarch and water samples discussed in Section 4.3.4 that measured the group velocity in the 40% cornstarch suspensions with water to be 1593 m/s ± 11 m/s.

The magnitude of dispersion over the bandwidth (4 MHz to 8 MHz) was measured for each of the eight cornstarch in cesium chloride solution samples and for the two cornstarch in water samples and displayed in Table 6.5. The average magnitude of dispersion in the 40% cornstarch suspensions was higher than that measured in any of the other concentrations of cornstarch at -0.74 m/s/MHz ± 0.43 m/s/MHz. However, the variability in the dispersion measurements was high probably for reasons discussed at the beginning of the section. The average magnitude of dispersion can

Sample	Dispersion Magnitude (m/s/MHz)
40% Cornstarch in CsCl #1	-0.33
40% Cornstarch in CsCl #2	-0.93
40% Cornstarch in CsCl #3	-1.03
40% Cornstarch in CsCl #4	-1.13
40% Cornstarch in CsCl #5	-0.40
40% Cornstarch in CsCl #6	-1.40
40% Cornstarch in CsCl #7	-0.28
40% Cornstarch in CsCl #8	-0.43
Average	-0.74 ± 0.43
40% Cornstarch in Water #1	-0.50
40% Cornstarch in Water #2	-0.45

TABLE 6.5: The magnitude of dispersion in the phase velocity measured for each of the 40% cornstarch in density-matched cesium chloride brine samples compared to the magnitude of dispersion for the two 40% cornstarch in water samples.

only be viewed as a very rough approximation of the dispersion in the samples at this concentration. The change in the phase velocity over the bandwidth found in the samples containing only cornstarch and water was approximately -0.5 m/s/MHz about the same as that measured in the 30% cornstarch samples.

To better compare all of the measurements, the phase velocity measured in each sample was plotted in Figure 6.40. The phase velocity appears to increase relatively consistently with concentration for the 10%, 20% and 30% concentration before a larger increase between 30% and 40%. These results mirror the group velocity measurements made and discussed in Chapter 4. All of the samples at all of the concentrations display negative dispersion over this bandwidth.

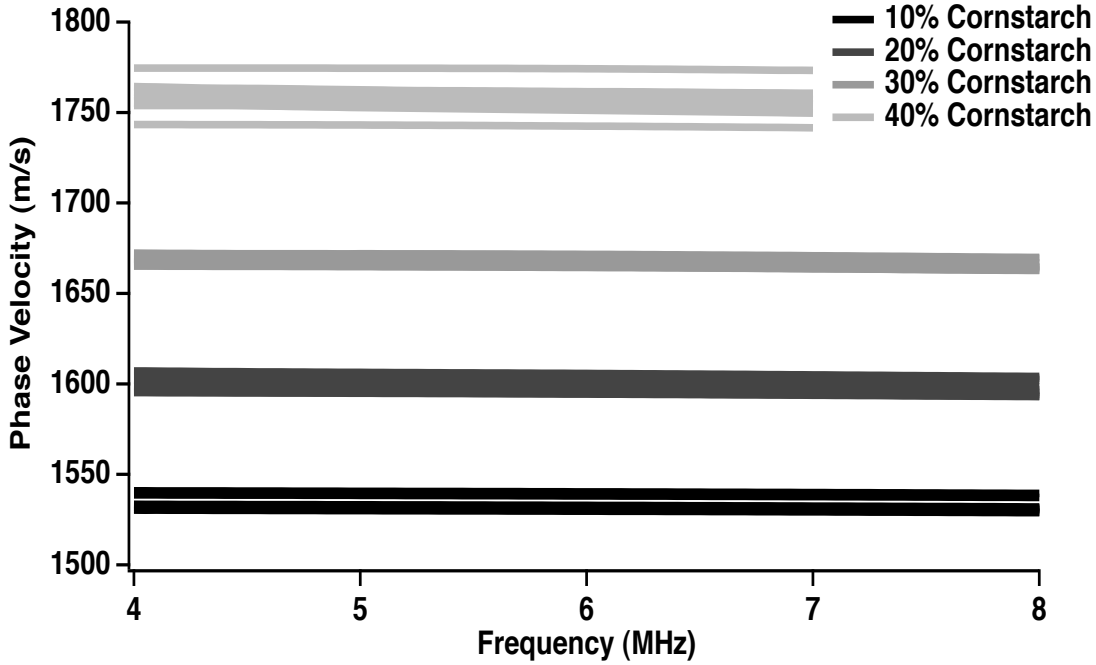

FIGURE 6.40: The broadband phase velocity measurements for each of the samples at all four of the concentrations. No error bars are plotted but the maximum standard deviation measured in any of the samples was approximately 5 m/s.

6.7.5 The Phase Velocity of Cornstarch

The speed of sound in a granule of cornstarch can be inferred from the measurements of the phase velocity of the suspension (Katz, 2012; Wood, 1930). Equation 6.21 is provided by Wood for the speed of sound in a suspension of two liquids that do not chemically react with each other,

$$c = \sqrt{\frac{K_1 K_2}{[f_1 K_2 + (1 - f_1)K_1][f_1 \rho_1 + (1 - f_1)\rho_2]}} \tag{6.21}$$

where ρ_1 is the density of the suspending medium (51.5% cesium chloride solution), ρ_2 is the density of the granule of cornstarch, K_1 is the bulk modulus of the suspending medium, K_2 is the bulk modulus of the granule of cornstarch, c is the speed of sound in the suspension, f_1 is the volume fraction of the suspending medium, and f_2 is the volume fraction of the cornstarch particles (Wood, 1930). This derivation ignores any shear stiffness in the grains, but this assumption is probably valid because the grains are small compared to the acoustic wavelength, so in this limit they will be isotropically compressed. The speed of sound in a liquid is defined by Equation 6.22

$$c_x = \sqrt{\frac{K_x}{\rho_x}}. \tag{6.22}$$

With this knowledge of the definition of the speed of sound in a liquid, Equation 6.21 can be re-expressed as Equation 6.23

$$c = \sqrt{\frac{c_1^2 c_2^2 \rho_1 \rho_2}{[f_1 \rho_1 + (1 - f_1)\rho_2][f_1 \rho_2 c_2^2 + (1 - f_1)\rho_1 c_1^2]}} \tag{6.23}$$

where c_1 is the phase velocity in the suspending medium and c_2 is the phase velocity in the cornstarch granule (Wood, 1930).

Equation 6.23 can be simplified to Equation 6.24 in the case of the density-matched suspension because $\rho_1 = \rho_2$ (Katz, 2012).

$$c = \frac{c_1^2 c_2^2}{f_1 c_2^2 + (1 - f_1) c_1^2} \tag{6.24}$$

Solving Equation 6.24 for the speed of sound in the cornstarch results in Equation 6.25.

$$c_2 = \sqrt{\frac{c^2 c_1^2 (1 - f_1)}{c_1^2 - c^2 f_1}} \tag{6.25}$$

This equation can be used to infer a speed of sound in the cornstarch particles from the phase velocity measurements of the suspension (Wood, 1930). Table 6.6 shows the necessary parameters for the calculation and the calculated phase velocity in the cornstarch particles at suspension concentrations of 20%, 30%, and 40%. For each concentration, the phase velocity at 6 MHz (the approximate center of the bandwidth) was averaged across the eight samples to find the value reported in the table. The speed of sound in the suspending medium (51.5% cesium chloride solution) for the calculation was taken to be the 1483 m/s measured in Section 3.3. An estimate of the bulk modulus in the cornstarch granules was inferred from the calculated speed of sound at each concentration using Equation 6.22 and a density of 1.62 g/cm^3.

The speed of sound in the cornstarch inferred from the phase velocity measurements of the suspension is reasonably consistent for the 20% and the 30% concentrations and slightly higher for the 40% concentration. The estimates of the bulk moduli are slightly higher than reported values ($\sim$5*10^9 Pa) in the literature for extruded starches (Lionetto *et al.*, 2006). The sources of error include uncertainty in the exact

Cornstarch Concentration	Suspension Phase Velocity at 6 MHz (m/s)	Cornstarch Phase Velocity (m/s)	Bulk Modulus (Pa)
20%	1599	2704	$1.18*10^{10}$
30%	1667	2686	$1.17*10^{10}$
40%	1757	2797	$1.27*10^{10}$

TABLE 6.6: An approximate determination of the speed of sound in cornstarch particles inferred from the phase velocity data. The bulk modulus inferred from the determined speed of sound was also reported.

volume fraction for each suspension as well as all of the uncertainties related to the phase velocity measurement itself (uncertainty in the sample thickness, uncertainty in the temperature, uncertainty in the timing measurements, etc.).

6.8 Conclusion

This chapter laid out both the experimental techniques for measuring the phase velocity and the theoretical calculations necessary to check those measurements. The experimental phase velocity results for four different concentrations of cornstarch in a density-matched cesium chloride solution were presented. Although both the broadband and narrowband measurements of the phase velocity agreed for all of the concentrations studied, the predictions of the Kramers-Kronig relations applied over the 4 MHz to 8 MHz frequency range showed a marked disagreement with experiment. The negative dispersion measured at all concentrations is not accounted for by the band-limited Kramers-Kronig formulae, and thus the experimental methods must

be checked very closely. The next chapter focuses on the search for a potential explanation.

Bibliography

Bracewell, R. (**2000**). *The Fourier Transform and its Applications*, 3rd edition edition (McGraw-Hill).

Bushberg, J., Seibert, J., EM Leidholdt, J., and Boone, J. (**2002**). *The essential physics of medical imaging*, second edition (Lippincott Williams and Wilkins).

He, P. (**1999**). "Experimental verification of models for determining dispersion from attenuation", IEEE Transactions on Ultrasonics, Ferroelectrics, and Frequency Control **46**, 706–714.

Katz, J. (**2012**). "Private communication", .

Lionetto, F., Maffezzoli, A., Ottenhof, M., Farhat, I., and Mitchell, J. (**2006**). "Ultrasonic investigation of wheat starch retrogradation", Journal of Food Engineering **75**, 258–266.

Lloyd, C. (**2009**). "Private communication", .

Marczak, W. (**1997**). "Water as a standard in the measurements of speed of sound in liquids", J Acoust Soc Am **102**, 2776–2779.

Mobley, J., Waters, K., Hall, C., Marsh, J., Hughes, M., Brandenburger, G., and Miller, J. (**1999**). "Measurements and predictions of the phase velocity and attenuation coefficient in suspensions of elastic microspheres", J Acoust Soc Am **106**, 652–659.

Sachse, W. and Pao, Y. (**1978**). "On the determination of phase and group velocities of dispersive waves in solids", Journal of Applied Physics **49**.

Trousil, R. (**2002**). "Ultrasonic propagation in inhomogeneous media: toward quantitative ultrasonic imaging", Ph.D. dissertation (Washington University in St. Louis, MO) .

Trousil, R., Waters, K., and Miller, J. (**2001**). "Experimental validation of the use of the kramers-kronig relations to eliminate the phase sheet ambiguity in broadband phase spectroscopy", J Acoust Soc Am **109**, 2236–2243.

Waters, K., Hughes, M., Mobley, J., Brandenburger, G., and Miller, J. (**2000**). "On the applicability of kramers-kronig relations for ultrasonic attenuation obeying a frequency power law", J Acoust Soc Am **108**, 556–563.

Waters, K., Hughes, M., Mobley, J., and Miller, J. (**2003**). "Differential forms of the kramers-kronig dispersion relations", IEEE Transactions on Ultrasonics, Ferroelectrics, and Frequency Control **50**, 68–76.

Waters, K., Mobley, J., and Miller, J. (**2005**). "Causality-imposed (kramers-kronig) relationships between attenuation and dispersion", IEEE Transactions on Ultrasonics, Ferroelectrics, and Frequency Control **52**, 822–833.

Wood, A. (**1930**). *A textbook of sound* (The MacMillan Company).

Chapter 7

Accounting for the Observed Negative Dispersion

7.1 Preface

This chapter outlines the work completed to attempt to explain the negative dispersion in the phase velocity measured in the cornstarch suspensions. The chapter begins with descriptions of phase velocity measurements made on two different types of plastic and on a sample of castor oil. The chapter continues with a summary of a study looking into possible nonlinear effects on the phase velocity measurement. The chapter concludes by putting forth an explanation that large resonances outside of the measured bandwidth provide a potential explanation for the negative dispersion.

7.2 Phase Velocity in Plastics

In order validate the broadband and the narrowband methods to be employed, the phase velocity of two plastics (Lucite^{TM}and Lexan^{TM}) was measured. Lucite^{TM} and Lexan^{TM} are both materials that this laboratory has previously measured.

7.2.1 Lexan

The group velocity, sample thickness, and attenuation properties of Lexan^{TM} were determined using the methods outlined in Sections 4.2 and 5.2 respectively. The results of these measurements are displayed in Table 7.1. The ultrasonic thickness agreed with thickness measurements made with digital calipers and the group velocity measurement was consistent with earlier phase velocity measurements made by this group (Bauer *et al.*, 2007). The attenuation coefficient as a function of frequency is shown in Figure 7.1. The slope of the attenuation coefficient and the attenuation coefficient at 5 MHz were also consistent with earlier measurements (Bauer *et al.*, 2007).

The broadband phase velocity displayed in Figure 7.2 was measured using the broadband phase velocity technique described in Section 6.3. A comparison between these broadband measurements and narrowband phase velocity measurements made at every half-megahertz across the bandwidth is displayed in Figure 7.3. Reasonably good agreement can be seen between the two measurements, especially in terms of the magnitude of dispersion across the bandwidth. Differences in the absolute magnitude

Sample	Thickness (mm)	Group Velocity (m/s)	Slope of Attenuation (dB/cm/MHz)	Attenuation Coefficient at 5 MHz (dB/cm)
Lexan	5.0 ± 0.1	2295 ± 4 m/s	4.5 ± 0.1	20.5 ± 0.5
Lucite	11.9 ± 0.1	2768 ± 5 m/s	0.8 ± 0.1	5.3 ± 0.4

TABLE 7.1: The results of the ultrasonic measurements of the group velocity, thickness, and attenuation properties of the two plastics investigated. Measurements are reported as mean ± standard deviation.

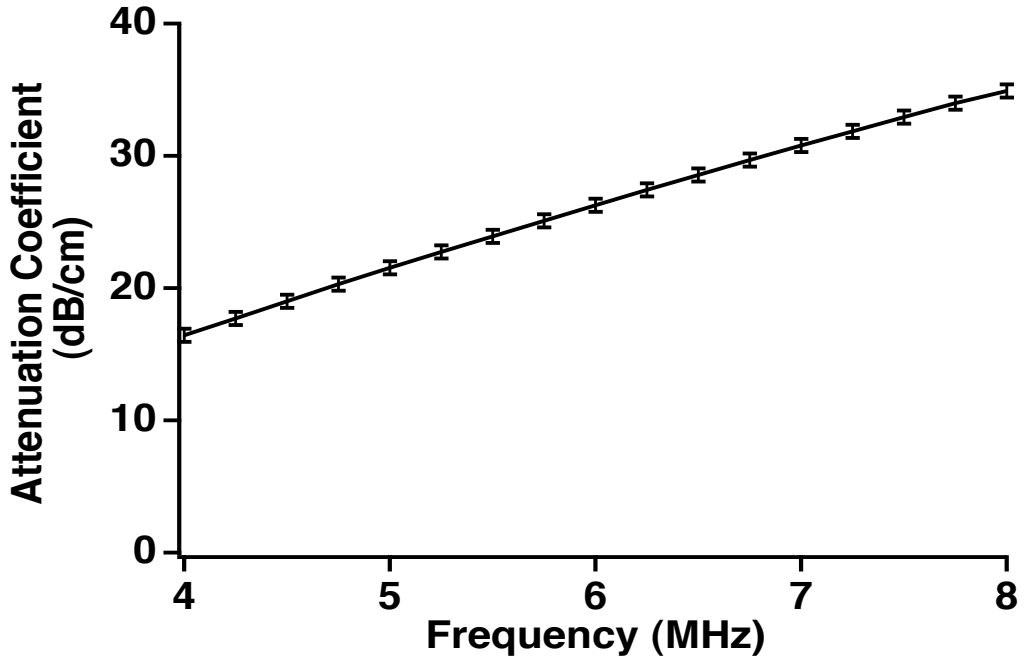

FIGURE 7.1: The attenuation coefficient as a function of frequency for the 5 mm thick Lexan^{TM} sample. Error bars are plus or minus one standard deviation and are only plotted at a few frequencies.

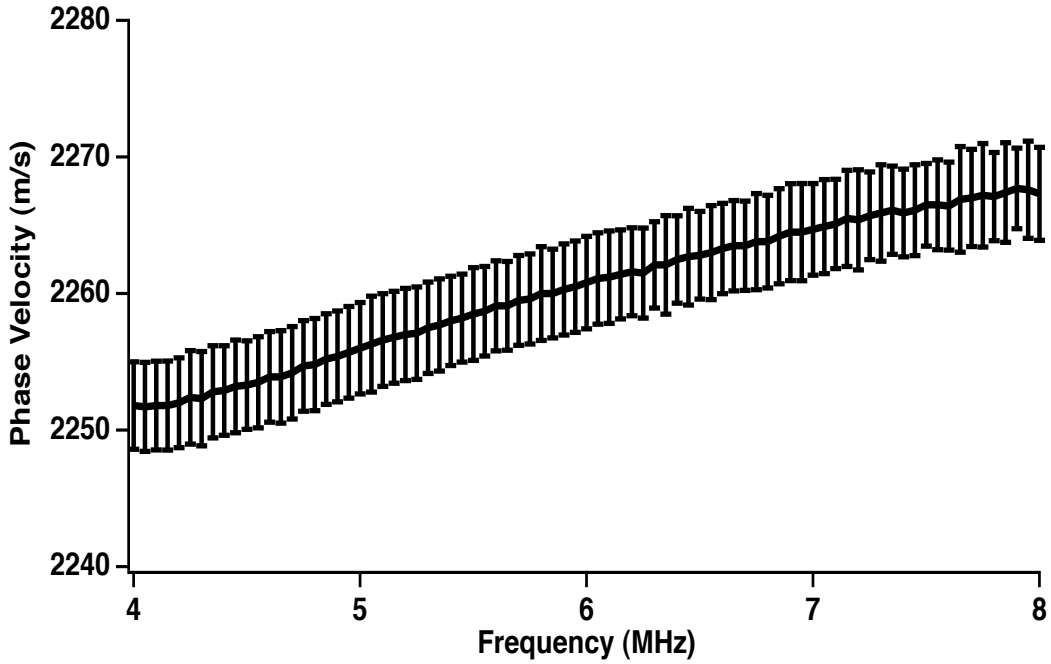

FIGURE 7.2: The broadband phase velocity as a function of frequency for the 5 mm thick Lexan^{TM} sample. Error bars are plus or minus one standard deviation.

of the phase velocity are most likely due to differences in temperature in the samples and water during the measurement and slight differences in the alignment of the plastic sample during measurement. The broadband phase velocity had a magnitude of dispersion from 4 MHz to 8 MHz of 3.9 m/s/MHz and the narrowband phase velocity had a magnitude of dispersion of 4.2 m/s/MHz.

To further validate the measurements, a Kramers-Kronig prediction of the dispersion in the phase velocity was made using the nearly local Kramers-Kronig relation with one subtraction (Waters *et al.*, 2003). The method for the Kramers-Kronig prediction is described in Section 6.6. The experimentally measured phase velocity at the approximate center of the bandwidth was used in the Kramers-Kronig formula to set the absolute level of the predicted phase velocity. The agreement between the

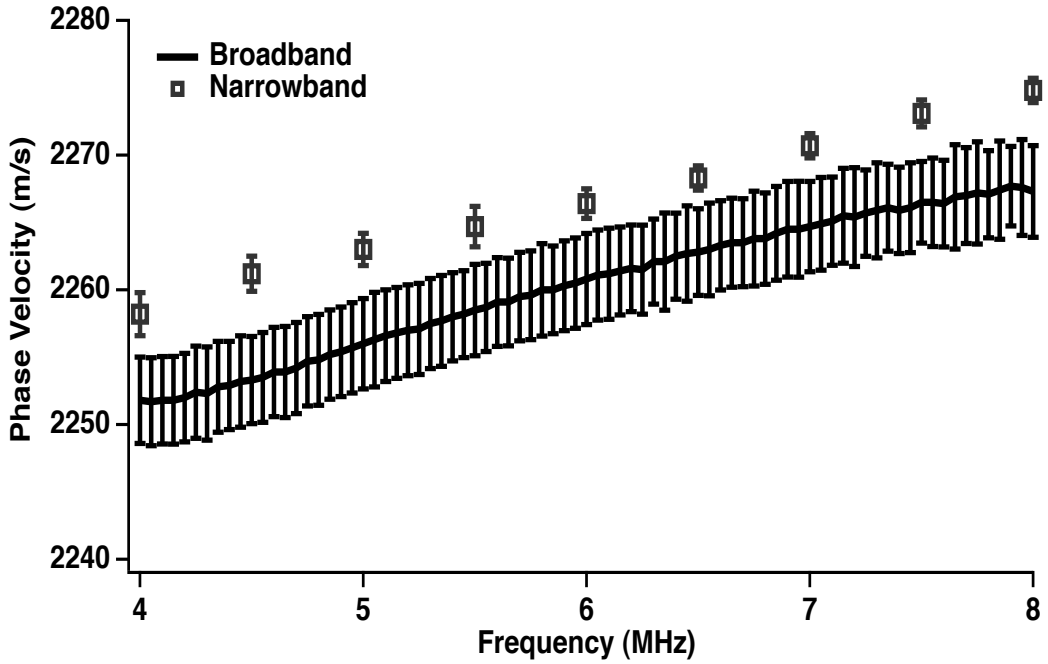

FIGURE 7.3: Both the narrowband phase velocity and the broadband phase velocity are plotted as a function of frequency for the 5 mm thick Lexan^{TM} sample. Error bars are plus or minus one standard deviation.

Kramers-Kronig prediction and the broadband phase velocity can be seen in Figure 7.4.

7.2.2 Lucite

The group velocity, sample thickness, and attenuation properties of a block of Lucite^{TM} were determined ultrasonically and displayed in Table 7.1. The findings were consistent with previously published results from this group (Bauer *et al.*, 2007). The attenuation coefficient plotted as a function of frequency is shown in Figure 7.5. The broadband phase velocity was measured and compared to narrowband phase velocity measurements as shown in Figure 7.6 and a comparison of both results is

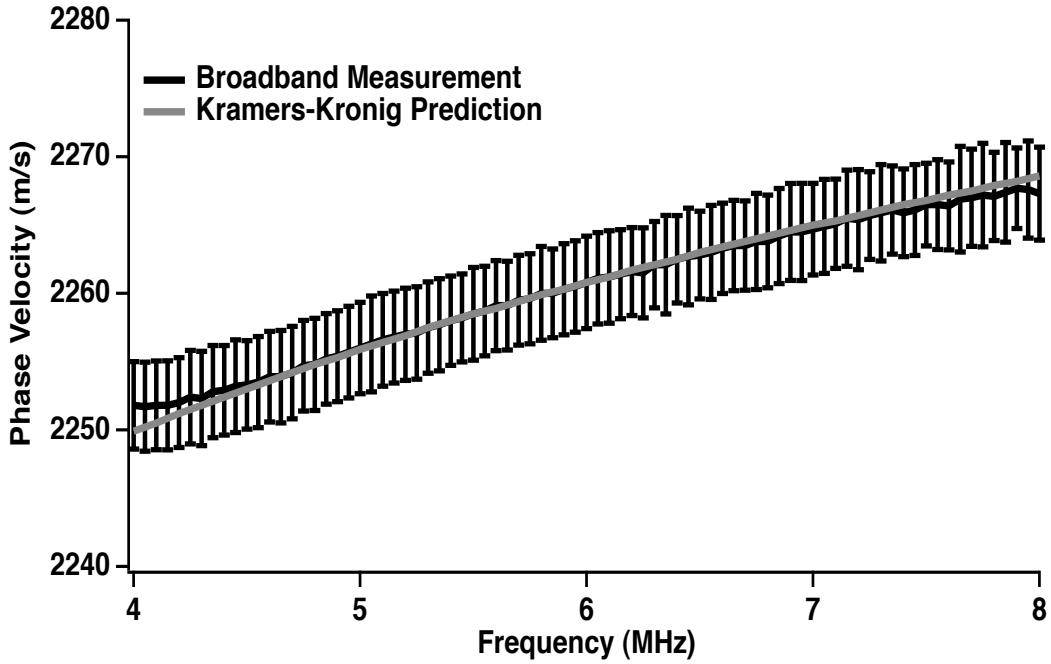

FIGURE 7.4: The Kramers-Kronig prediction for the dispersion in the phase velocity is plotted with the broadband phase velocity measurement for the 5 mm thick lexan sample.

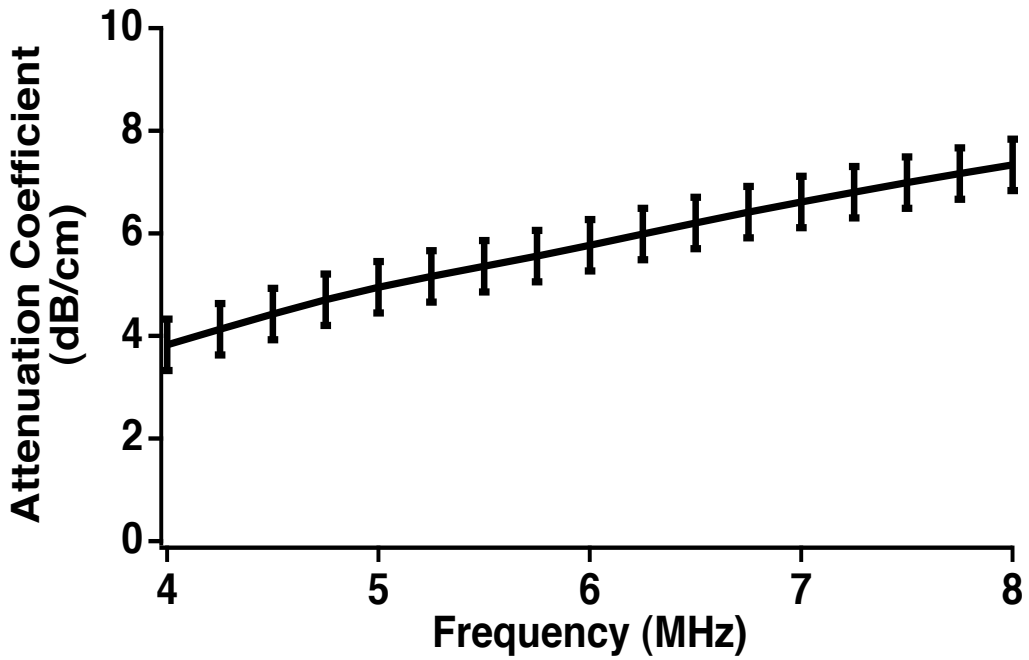

FIGURE 7.5: The attenuation coefficient as a function of frequency for the 12 mm thick Lucite^{TM} sample. Error bars are plus or minus one standard deviation and are plotted at only a couple of frequencies.

shown in Figure 7.7. The Kramers-Kronig prediction for the dispersion in the phase velocity was determined using the slope of the attenuation coefficient and the phase velocity at the approximate center of the bandwidth and displayed in Figure 7.8. The comparison of the Kramers-Kronig prediction to the broadband phase velocity results demonstrates good agreement.

The phase velocity measurements in the Lucite^{TM} and Lexan^{TM} samples served to validate the experimental methods, the phase spectroscopy and narrowband phase velocity analysis, and the linear with attenuation Kramers-Kronig predictions. The only remaining aspect of the experimental apparatus that was not incorporated into these measurements, and thus still needed to be validated, was the sample mold used

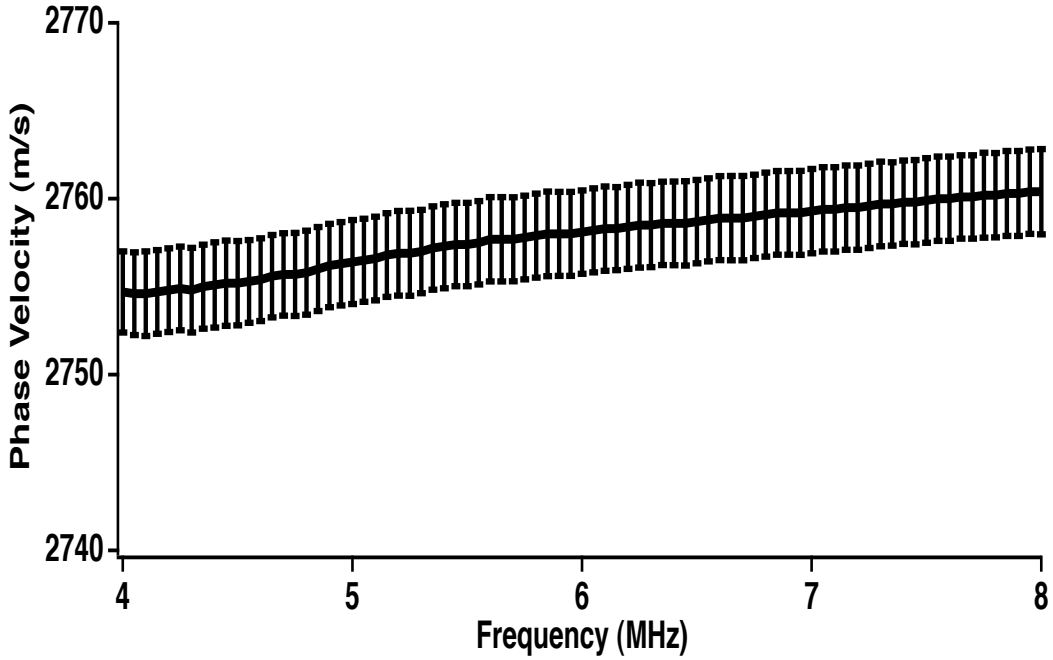

FIGURE 7.6: The broadband phase velocity as a function of frequency for the 12 mm thick Lucite^{TM} sample. Error bars are plus or minus one standard deviation.

for the cornstarch suspensions.

7.3 Castor Oil

The cornstarch phase velocity measurements were made with the sample contained in a plastic sample mold with Saran Wrap^{TM}windows. Making the phase velocity measurements and Kramers-Kronig predictions on a viscous liquid in the sample mold served to validate the experimental technique. Castor oil has traditionally served as a standard for ultrasonic measurements (Waters *et al.*, 2003).

The group velocity, sample thickness, and attenuation properties were measured in the standard shadowed reflector setup shown in Figure 7.9. The sample thickness was

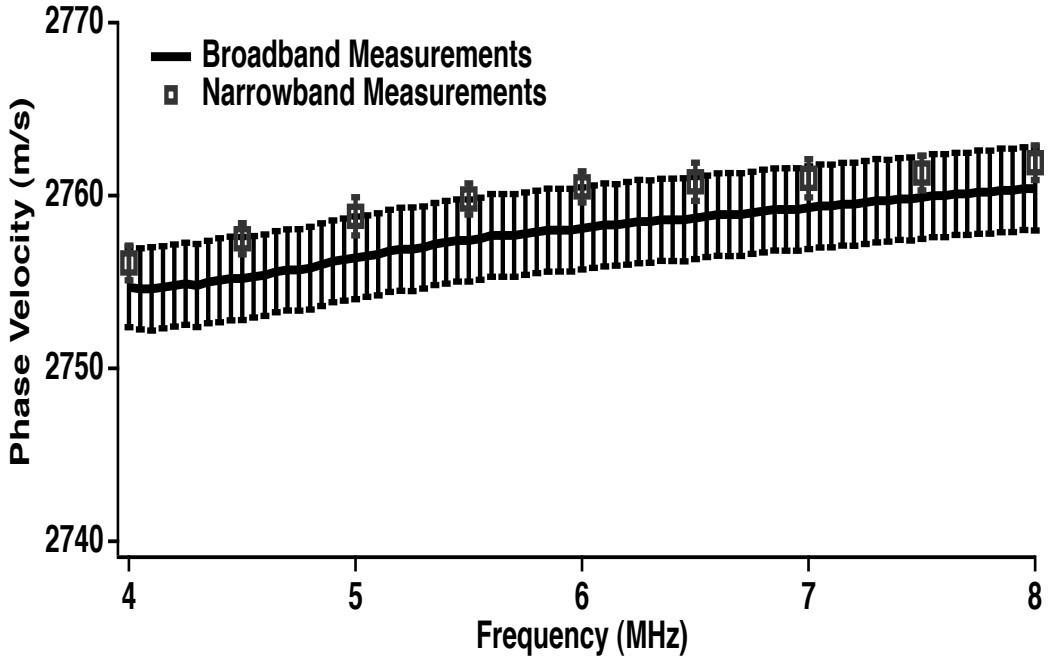

FIGURE 7.7: Both the narrowband phase velocity and the broadband phase velocity are plotted as a function of frequency for the 12 mm thick Lucite^{TM} sample. Error bars are plus or minus one standard deviation.

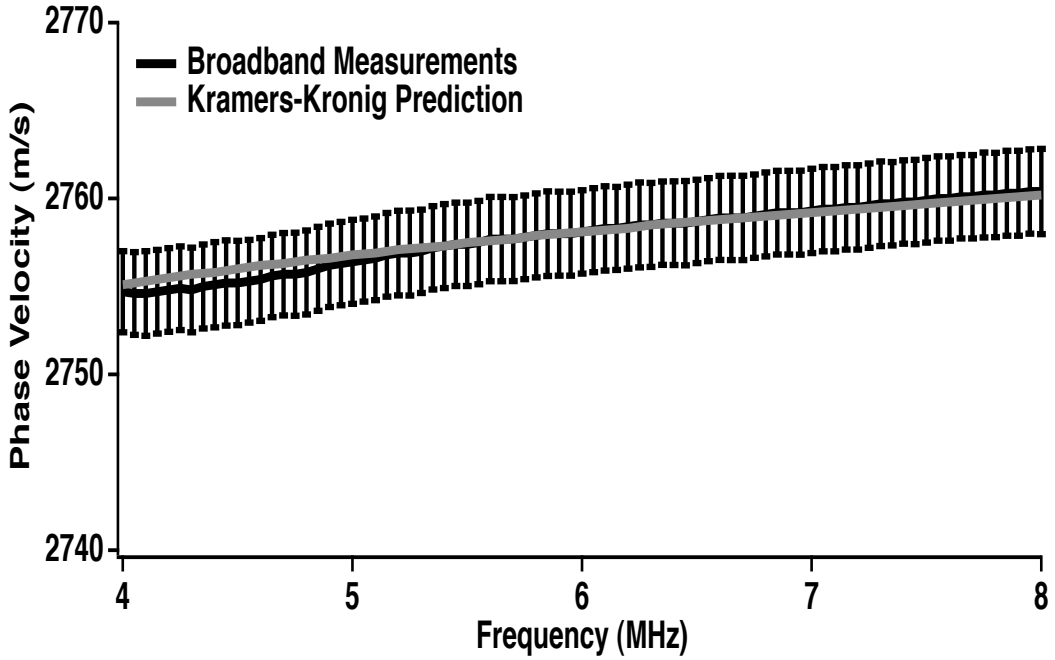

FIGURE 7.8: The Kramers-Kronig prediction for the dispersion in the phase velocity is plotted with the broadband phase velocity measurement for the 12 mm thick Lucite^{TM} sample.

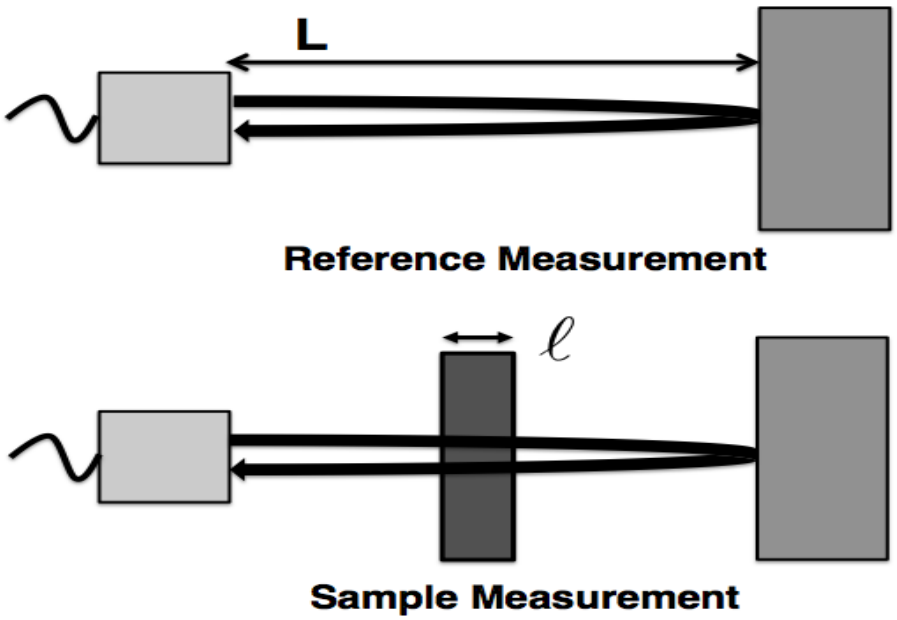

FIGURE 7.9: Shadowed reflector setup for the broadband measurements made on the castor oil sample. The two transducers are aligned with each other. The sample is placed in between the two transducers.

ultrasonically found to be 12.3 mm $\pm$ 0.1 mm and the group velocity was measured to be 1538 m/s $\pm$ 5 m/s at a temperature of approximately 18.7°C. From the attenuation coefficient measurement it was determined that the signal was dropping into the noise at the higher end of the bandwidth. Therefore, a through transmission measurement was made of the attenuation properties using the experimental setup shown in Figure 7.10.

The attenuation coefficient as a function of frequency measured using the through transmission setup is displayed in Figure 7.11. Because castor oil is a liquid, the castor oil's attenuation coefficient is expected to have a power law frequency dependence. The attenuation coefficient was converted into Np/cm and then fit with a power law

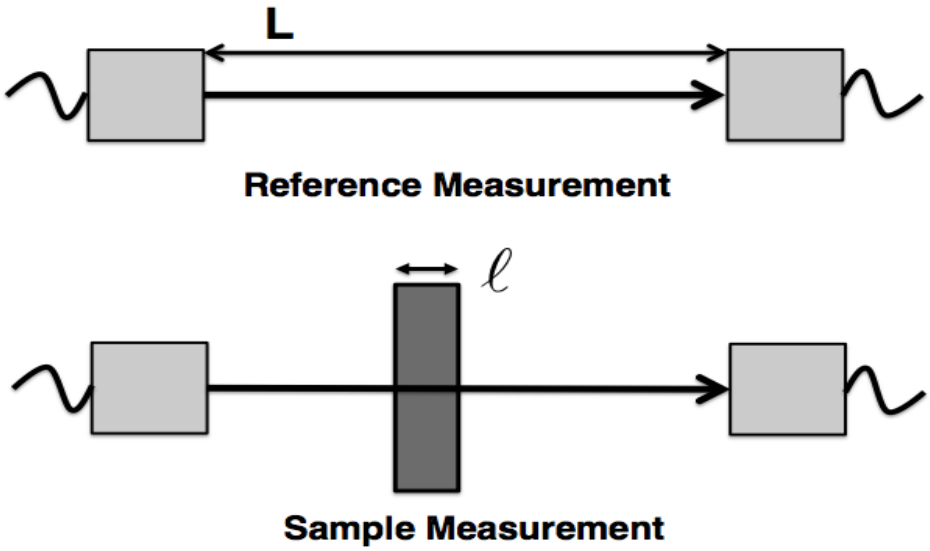

FIGURE 7.10: Through transmission setup for the broadband measurements made on the castor oil sample. The two transducers are aligned with each other. The sample is placed in between the two transducers.

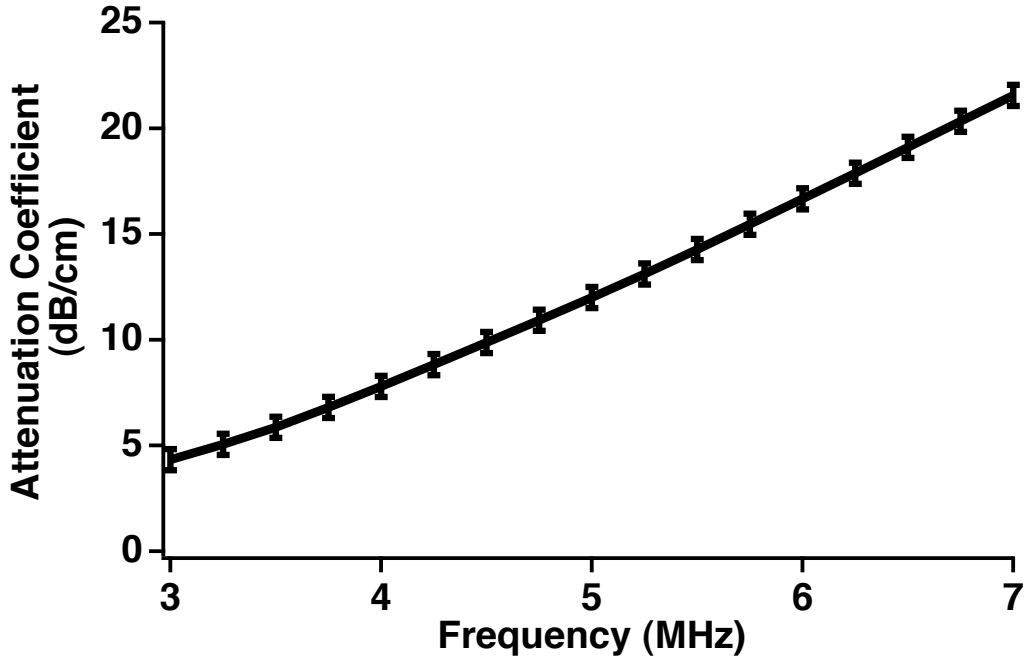

FIGURE 7.11: Through transmission measurement of the attenuation coefficient of a sample of castor oil. Note that the through transmission setup results in a slightly lower bandwidth than the shadowed reflector measurements. Error bars are plus or minus one standard deviation and are plotted at only a couple of frequencies.

of the functional form displayed in Equation 7.1. The attenuation coefficient and power law fit are shown in Figure 7.12.

$$\alpha(f) = \alpha_0^{'} * f^n \tag{7.1}$$

The fit parameters were determined to be $\alpha_0^{'} = 0.0924$ Np/cm/MHz$^{1.68}$ and n = 1.68. The power law exponent agrees well with earlier measurements from this group (Waters *et al.*, 2003).

The broadband phase velocity of the castor oil sample was measured using the through transmission setup. The broadband phase velocity is displayed in Figure 7.13. The power law form of the Kramers-Kronig relations shown in Equation 6.19 from Sec-

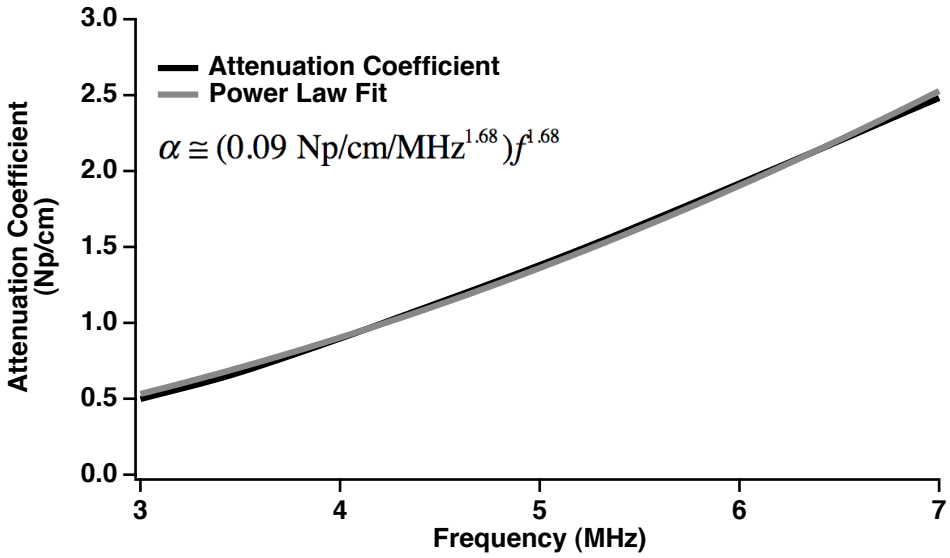

FIGURE 7.12: Comparison of the attenuation coefficient of castor oil and a power law fit of the form shown in Equation 7.1.

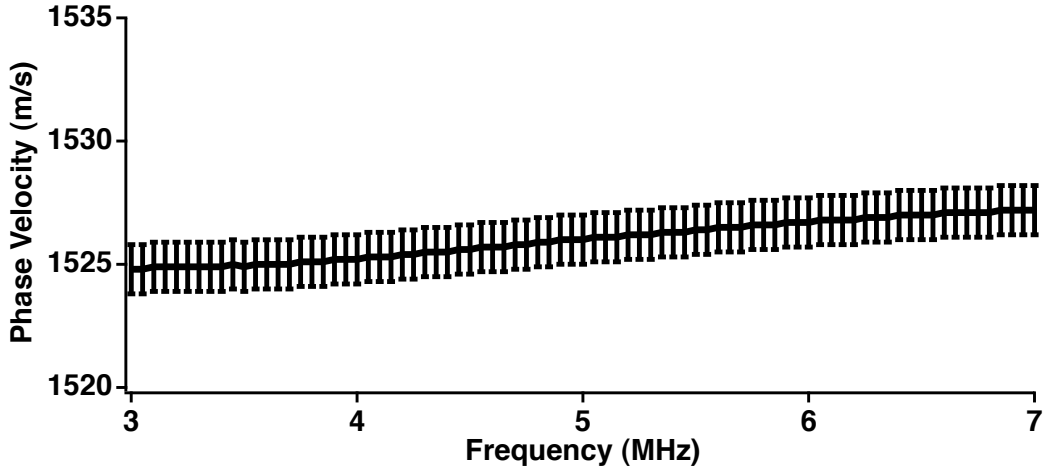

FIGURE 7.13: The broadband phase velocity as a function of frequency for the castor oil sample. Error bars are plus or minus one standard deviation.

tion 6.6.2 was used for the Kramers-Kronig prediction of the dispersion in the phase velocity. The phase velocity measured at 5 MHz was used for $v(\omega_0)$ with the power law fit parameters determined from the attenuation coefficient. The Kramers-Kronig prediction is plotted in comparison with the broadband phase velocity measurement in Figure 7.14. Good agreement is seen between the measured and predicted dispersion. The experimental methods have been further validated and the sample mold with Saran^{TM}windows has been shown to not have a significant effect on the measurement. Therefore, the negative dispersion measured in cornstarch suspensions must arise from some other cause.

7.4 Nonlinear Effects

Acoustic contrast agents have been shown to be affected by the acoustic radiation force produced by the nonlinear propagation of sound (Dayton *et al.*, 1996). Corn-

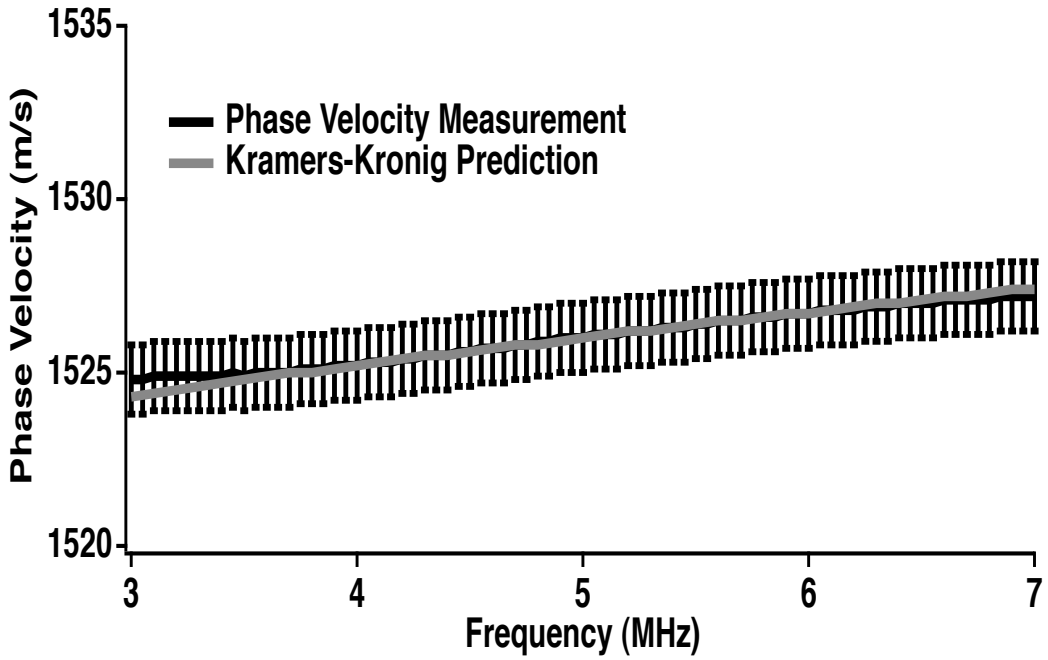

FIGURE 7.14: The Kramers-Kronig prediction for the dispersion in the phase velocity is plotted with the broadband phase velocity measurement for the castor oil sample.

starch particles are approximately the same size as some acoustic contrast agents, and thus if the acoustic radiation force is large enough then the phase velocity measurement may be affected. Nonlinear effects are amplitude dependent and thus any possible effect on the phase velocity measurement was checked by measuring the phase velocity at four different input amplitudes.

The Panametrics 5800 Pulser/Receiver permitted four different settings for the input energy that led to four different amplitudes for the reference signal. The peak-to-peak amplitudes of the reference signal for each of the four Pulser/Receiver energy settings are displayed in Table 7.2. Phase velocity measurements on two 20% cornstarch and two 30% cornstarch suspensions both in a 51.5% cesium chloride brine were made in the shadowed reflector setup at each of the different input amplitudes. The

Pulser/Receiver Energy Setting (μJ)	Peak-to-Peak Reference Pulse Amplitude (V)	Lower End of the Bandwidth (MHz)	Upper End of the Bandwidth (MHz)
12.5	0.412	4.35	8.45
25	0.785	4.45	8.50
50	1.276	4.40	8.25
100	1.715	4.25	7.90

TABLE 7.2: The peak-to-peak reference pulse amplitude in Volts at each energy setting on the pulser/receiver is displayed in the second column. The third and fourth column display the lower and upper end of the -6 dB bandwidth of the reference power spectrum for each energy.

change in the input energy affected the pulse itself, so the transducer was realigned each time the settings were varied. The reference power spectra were also affected by the shift in the input energy. The -6 dB bandwidth of each reference power spectrum was measured and the lower and upper ends of the bandwidth are also displayed in Table 7.2.

The magnitude of dispersion across the bandwidth for each of the four samples at each of the input amplitudes are displayed in Table 7.3 and Table 7.4. As shown in Table 7.2 the bandwidth was slightly different for each of the energy settings. For both of the 20% cornstarch samples and for both of the 30% cornstarch samples the magnitude of dispersion did not depend in any systematic way on the input amplitude. This provides evidence that the dispersion in the phase velocity was not affected by nonlinear effects.

Pulser/Receiver Energy Setting (μJ)	20% Cornstarch #1 Dispersion Magnitude (m/s/MHz)	20% Cornstarch #2 Dispersion Magnitude (m/s/MHz)
12.5	-0.50	-0.50
25	-0.53	-0.50
50	-0.58	-0.53
100	-0.55	-0.53

TABLE 7.3: The magnitude of dispersion across the bandwidth for the two 20% cornstarch samples for the four different input amplitudes.

Pulser/Receiver Energy Setting (μJ)	30% Cornstarch #1 Dispersion Magnitude (m/s/MHz)	30% Cornstarch #2 Dispersion Magnitude (m/s/MHz)
12.5	-0.63	-0.60
25	-0.63	-0.58
50	-0.60	-0.60
100	-0.60	-0.63

TABLE 7.4: The magnitude of dispersion across the bandwidth for the two 30% cornstarch samples for the four different input amplitudes.

7.5 A Potential Explanation for the Negative Dispersion

One possible explanation for the negative dispersion in the phase velocity measurements of the cornstarch suspensions would be some type of resonance phenomena that occurs outside of the experimental bandwidth. Looking at Figures 7.19 and 7.20 it would appear that the attenuation coefficient rises with frequency, whereas the phase velocity decreases with frequency. The Kramers-Kronig relations show that this negative dispersion is not consistent with an attenuation coefficient that rises with frequency. However, if there is a resonance outside the bandwidth that is sufficiently large, the phase velocity could behave in the manner observed. Earlier work by this laboratory showed such behavior in distributions of polystyrene microspheres (Mobley *et al.*, 1999). Large resonances were observed in the attenuation and phase velocity data (see Figures 7.15 and 7.16) that caused the phase velocity to decrease with frequency over portions of the bandwidth where the attenuation coefficient rose as function of frequency (see Figures 7.19 and 7.20).

7.5.1 Theoretical Derivation

For a suspension of particles, the phase velocity and attenuation coefficient can be connected to the scattering properties of individual particles using the Waterman

and Truell dispersion relation shown in Equation 7.2

$$K_s = k_w \sqrt{\left(1 + \frac{2\pi\eta}{k_w^2} f(0)\right)^2 - \left(\frac{2\pi\eta}{k_w^2} f(\pi)\right)^2} \tag{7.2}$$

where $K_s = \omega/c_s(\omega) - i\alpha_s(\omega)$ is the complex wavenumber of the suspension, $k_w = \omega/c_w$ is the wavenumber of the host medium, η is the number density of the particles, $f(0)$ is the forward scattering amplitude, and $f(\pi)$ is the back scattering amplitude (Mobley *et al.*, 1999; Waterman and Truell, 1961). The Waterman and Truell dispersion relation is based on the assumptions that a number of elastic spheres are uniformly distributed in a random way in a plane (Waterman and Truell, 1961). The scattering amplitude depends on the radius of the particle, the density of the particle, the longitudinal and shear speed of sound in the particle, the density and speed of sound in the fluid, and the frequency of the incident pressure wave (Mobley *et al.*, 1999). Practically, these scattering amplitudes can be calculated using the theory of Faran for elastic scattering from a solid sphere (Faran, 1951).

Faran used a matched boundary condition solution for the scattering from a solid sphere in a fluid (Faran, 1951). Expressions were derived for the pressure and particle displacement in the fluid and the stress and particle displacement in the solid sphere (Faran, 1951). At the boundary between the sphere and the surrounding fluid, the pressure in the fluid and the stress in the solid must be equal, the normal component of the displacement in the fluid must equal the normal component of the displacement in the solid, and the tangential components of the shearing stress in the solid must be equal to zero (Faran, 1951). Ultimately, Faran was determining the scattered pressure

from the solid sphere in the fluid expressed in Equation 7.3

$$p_s = \sum_{n=0}^{\infty} c_n[j_n(k_3 r) - in_n(k_3 r)]cos(n\theta) \tag{7.3}$$

where j_n is the spherical Bessel function of the first kind, n_n is the spherical Bessel function of the second kind, and θ is the scattered angle (0 meaning forward scattering and π meaning backward scattering).

Using the boundary conditions discussed above, Faran was able to solve for the expansion coefficients (labeled c_n in Equation 7.3). The expression for the solved expansion coefficients is given by Equation 28 in Faran's paper (Faran, 1951). Mobley et al. also refer to expansion coefficients (labeled D_n) that are defined in terms of the Faran expansion coefficients (Mobley *et al.*, 1999). These expansion coefficients depend on the same physical parameters as the scattering amplitudes and can be related to the scattering amplitude using Equation 7.4

$$f(\theta) = \frac{i}{k_w} \sum_{n=0}^{\infty} (2n+1) D_n P_n(cos(\theta)) \tag{7.4}$$

where $P_n(cos(\theta))$ are the Legendre polynomials (Mobley *et al.*, 1999).

For the polystyrene microsphere suspensions investigated in the Mobley et al. work, the scattering amplitude can be constrained as expressed in Equation 7.5.

$$\frac{2\pi\eta}{k_w^2} |f(\theta)| \ll 1, (\theta = 0 \; or \; \pi) \tag{7.5}$$

This constraint can arise from a number of different factors including weak scattering amplitude, small number density of scatterers, and high frequency (Mobley *et al.*, 1999). Using Equation 7.5 to simplify the Waterman and Truell dispersion relation

from Equation 7.2 leads to Equation 7.6

$$\frac{\omega}{c_s(\omega)} - i\alpha_s(\omega) \cong \frac{\omega}{c_w} + \frac{2\pi\eta c_w}{\omega} f(0) \tag{7.6}$$

The real plus imaginary nature of the right hand side of the equation is implicit in the scattering amplitude. Using Equation 7.4 and equating the real and imaginary parts of Equation 7.6 leads to expressions for the theoretical attenuation coefficient and phase velocity for a suspension of spheres. These two derived relations are shown in Equations 7.7 and 7.8.

$$\alpha_s(\omega) = -\frac{2\pi\eta c_w^2}{\omega^2} \sum_{n=0}^{\infty} (2n+1) Re[D_n(\omega)] \tag{7.7}$$

$$c_s(\omega) = c_w \left[1 - \frac{2\pi\eta c_w^3}{\omega^3} \sum_{n=0}^{\infty} (2n+1) Im(D_n(\omega)) \right]^{-1} \tag{7.8}$$

Equations 7.7 and 7.8 in combination with the information from Table 7.5 was used to reproduce the 40 μm and 50 μm theoretical phase velocity and attenuation coefficient shown in Figures 4 and 5 of the Mobley et al. paper (Mobley *et al.*, 1999). The calculated phase velocity and attenuation coefficient for an approximately 40 μm suspension of polystyrene microspheres are shown in Figures 7.16 and 7.15. The same figures for the 50 μm polystyrene microspheres are shown in Figures 7.18 and 7.17. Overall, good agreement was found between the calculated parameters shown in the figures and the same parameters plotted in Figures 4 and 5 of the Mobley et al. paper (Mobley *et al.*, 1999).

There are some slight differences between the calculations in this thesis and those seen in the Mobley et al. paper. The Mobley et al. paper used an adjustable parameter to match the absolute magnitude of the phase velocity to the experimentally

Theoretical Parameters	Value of Parameter
Phase Velocity of Host Medium (c_w)	1480 m/s
Phase Velocity of Microspheres (c_s)	2380 m/s
Density of Host Medium (ρ_w)	1000 kg/m^3
Density of Microspheres (ρ_s)	1060 kg/m^3
Poisson Ratio of Microspheres	0.34
Mean Microsphere Radius	40.4 μm 50.6 μm
Number Density of Microspheres	$1.4 * 10^{11}$ spheres/m^3 (40 μm) $1.3 * 10^{11}$ spheres/m^3 (50 μm)

TABLE 7.5: The parameters necessary for the theoretical calculation of the phase velocity and the attenuation coefficient of a distribution of microspheres in Isoton. (Mobley *et al.*, 1999; Hall *et al.*, 1997)

measured phase velocity (Mobley *et al.*, 1999). The calculations shown in this thesis did not use this adjustable parameter, so the magnitudes of the two calculations do not match perfectly. The Mobley results were calculated for a distribution of microsphere sizes close to the mean size, whereas the calculations in this thesis assumed that the distribution could be characterized by assuming all of the spheres had the mean diameter given in Table 7.5 (Mobley *et al.*, 1999). In the previous work, the distributions in size for both the 40 μm and 50 μm microspheres were small (standard deviations of 4.0 and 6.4 μm) and thus this difference did not have a large effect on the calculation (Hall *et al.*, 1997).

The attenuation coefficient and the phase velocity for the 50 μm diameter microspheres is plotted over a more limited bandwidth from 4 to 8 MHz used in the current experimental measurements in Figures 7.19 and 7.20. What can be seen from the figures is that over this limited bandwidth the attenuation coefficient increases with frequency, whereas the phase velocity decreases with frequency. The seemingly negative dispersion may arise over this limited bandwidth because of the resonances far outside the bandwidth. If measurements were only made over this limited portion of the bandwidth, then the results would also appear to violate the band-limited Kramers-Kronig relations.

In order to do the calculation with cornstarch in density-matched cesium chloride the relevant physical and ultrasonic parameters displayed in Table 7.6 had to be determined. The calculation was done for a 20% cornstarch suspension in a 51.5% cesium chloride solution. The phase velocity and density of the host medium (51.5%

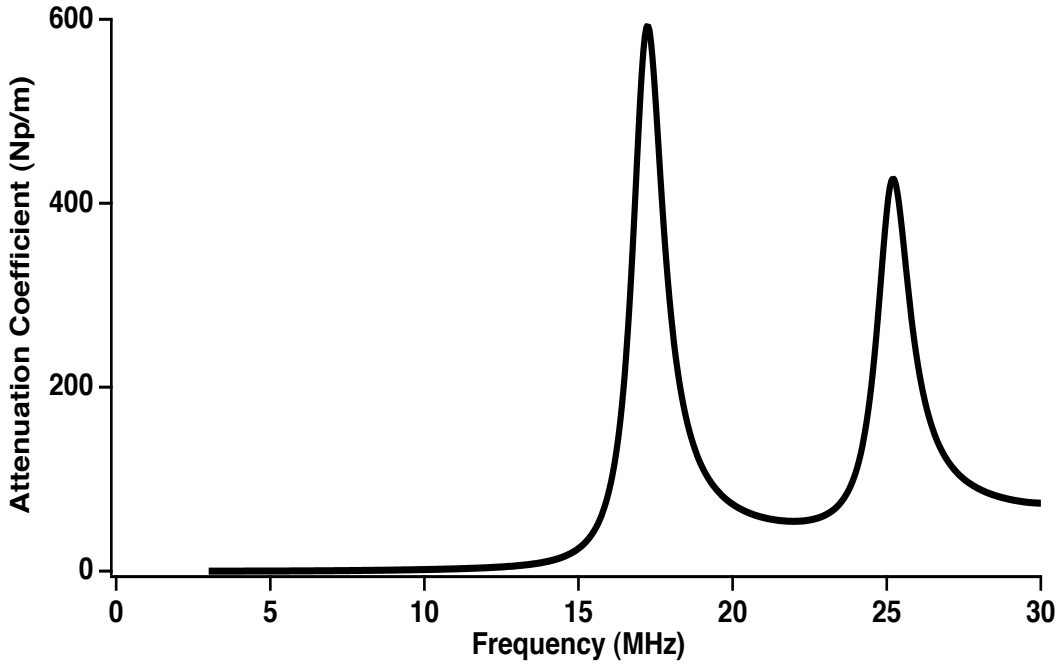

FIGURE 7.15: The theoretical attenuation coefficient calculated for 40 μm diameter polystyrene microspheres in a liquid.

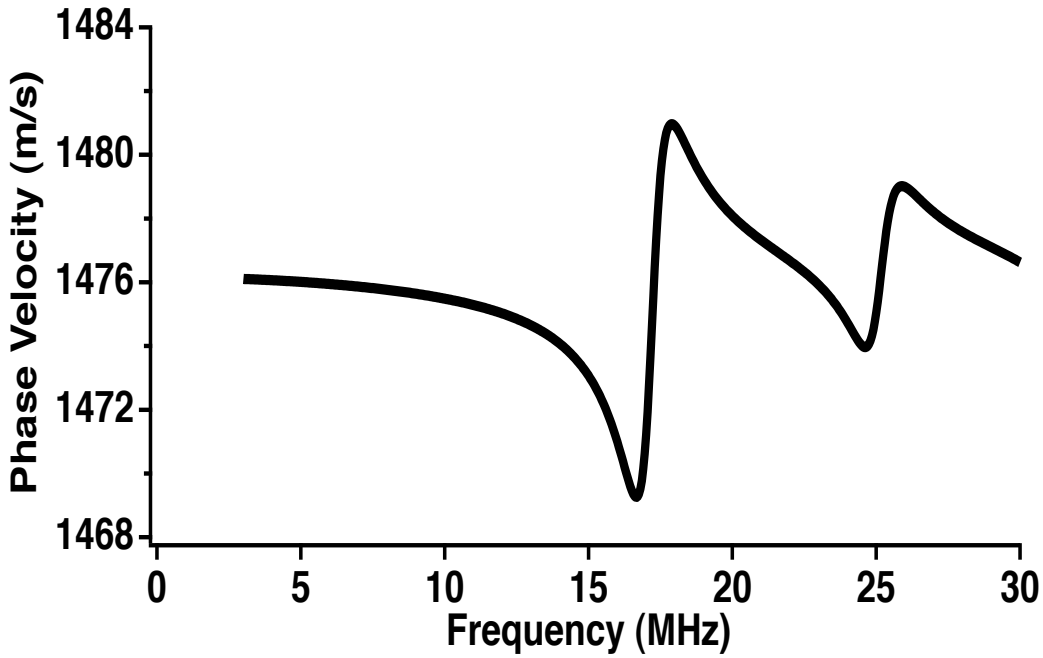

FIGURE 7.16: The theoretical phase velocity calculated for 40 μm diameter polystyrene microspheres in a liquid.

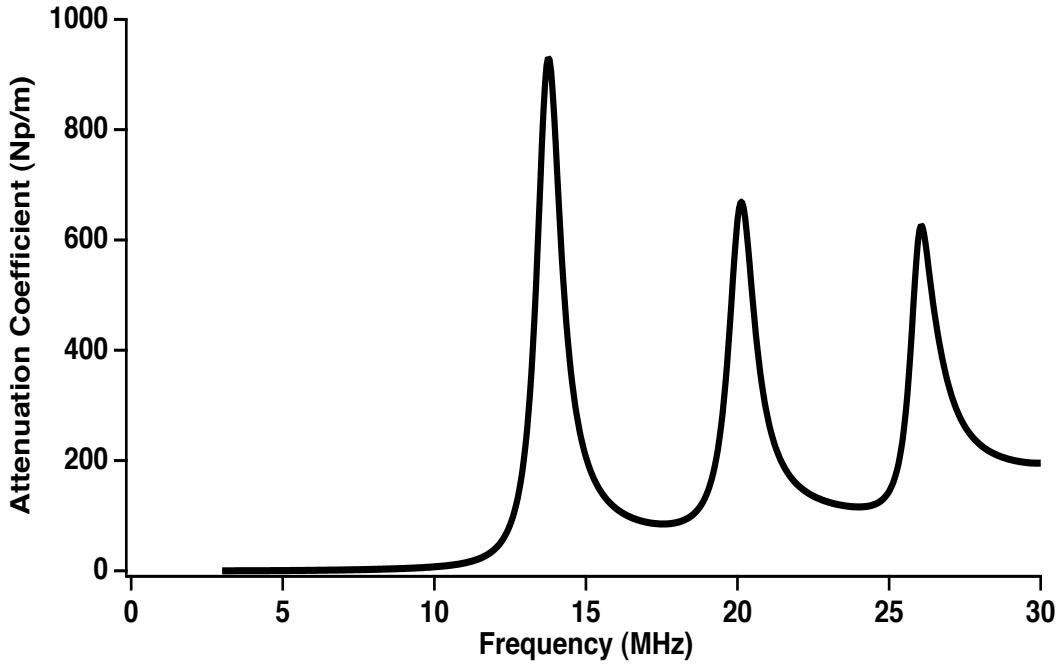

FIGURE 7.17: The theoretical attenuation coefficient calculated for 50 μm diameter polystyrene microspheres in a liquid.

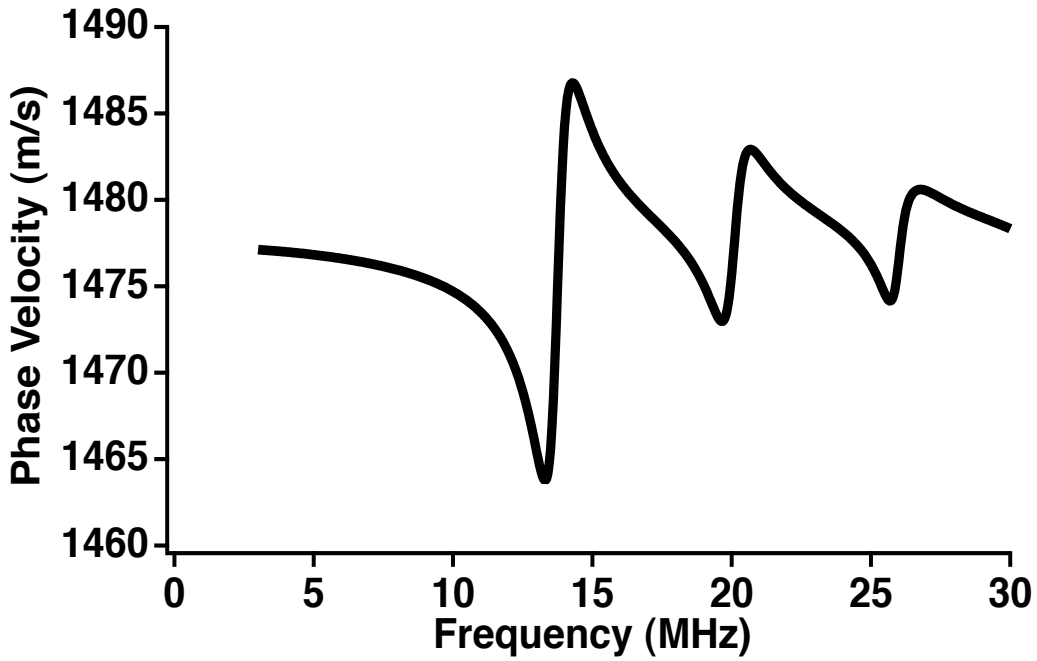

FIGURE 7.18: The theoretical phase velocity calculated for 50 μm diameter polystyrene microspheres in a liquid.

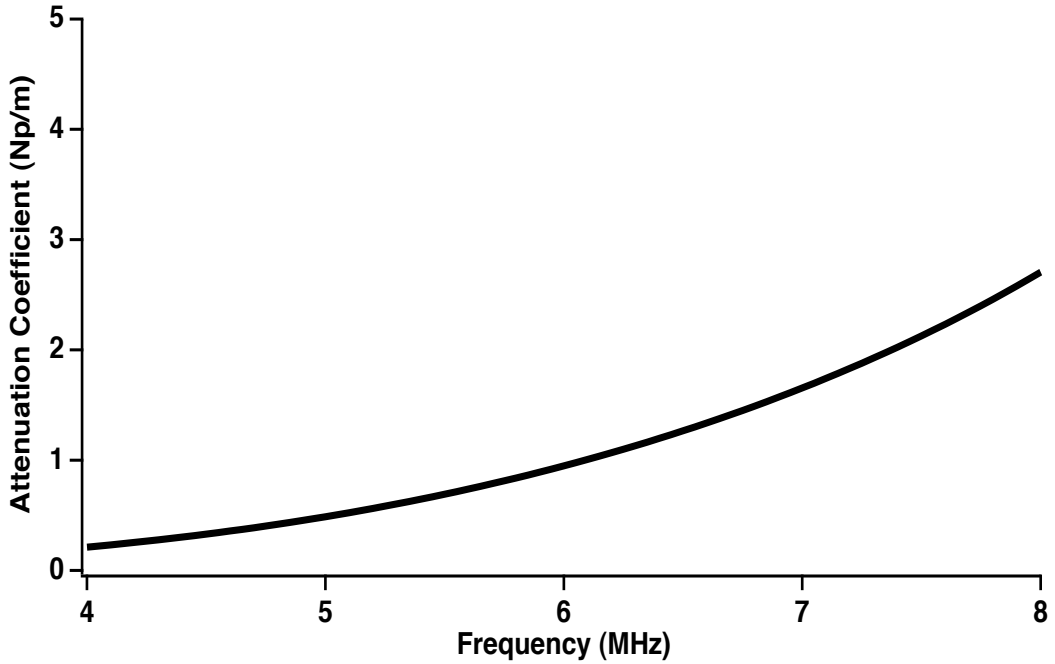

FIGURE 7.19: The theoretical attenuation coefficient calculated for 50 μm diameter polystyrene microspheres in a liquid over a bandwidth from 4 to 8 MHz.

cesium chloride in distilled water) were measured experimentally as described in Section 3.3. The density of a cornstarch granule and poisson ratio of a cornstarch granule were determined from the literature (Flores *et al.*, 2007; Fall *et al.*, 2008). The mean cornstarch radius was measured as described in Section 3.2. The group velocity measurements of the cornstarch suspension discussed in Chapter 4 were necessary for the determination of the phase velocity in cornstarch,. With this group velocity data, Dr. Jonathan Katz inferred the phase velocity in the cornstarch particles using an approach described in Section 6.7.5 (Katz, 2012). The number density of the cornstarch particles was determined from assuming that all of the cornstarch particles had a diameter of 13 μm and calculating the volume of one particle. The total volume of

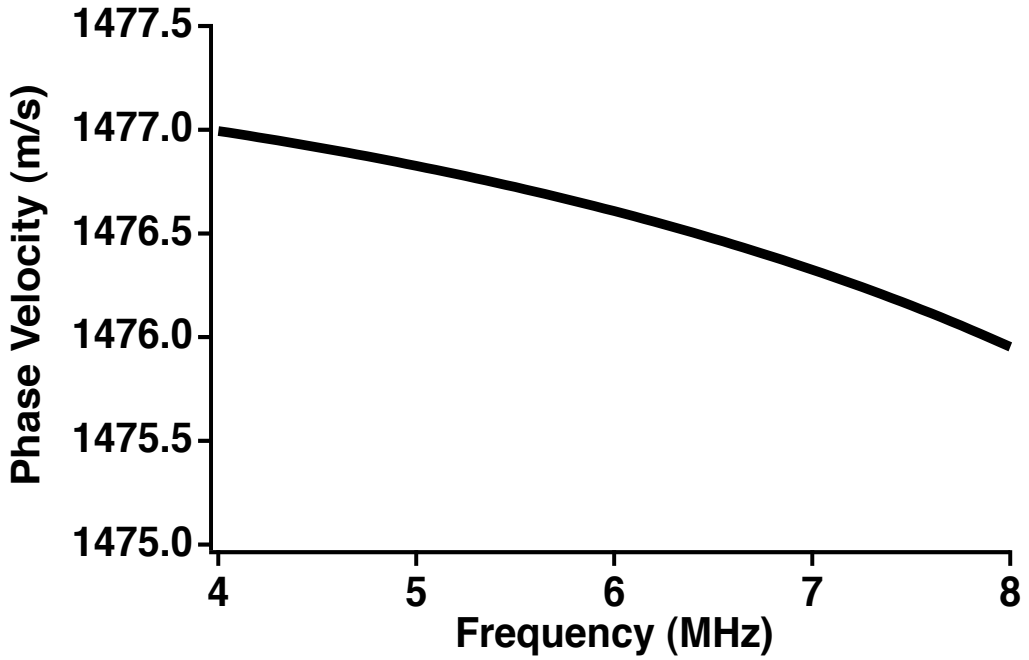

FIGURE 7.20: The theoretical phase velocity calculated for 50 μm diameter polystyrene microspheres in a liquid over a bandwidth from 4 to 8 MHz. Negative dispersion is observed over this limited bandwidth.

cornstarch added to the suspension was found and from the knowledge of the volume of one cornstarch particle and the total volume in the solution the number density of the particles was calculated. Of the parameters shown in Table 7.6, the phase velocity in the cornstarch, the poisson ratio of the cornstarch and the number density of the cornstarch granules are the three parameters that have the most potential for variability. These three parameters are estimated as accurately as possible, but are not as well known as the other parameters that were either experimentally measured or well established in the literature.

In comparing the calculated number density of the cornstarch particles to the number density of the polystyrene microspheres a number of factors must be taken into account. The volume concentration of the cornstarch suspension was 20% while the volume concentration of the microspheres was 1%. The cornstarch particles are also more than a factor of three smaller in diameter than the smallest microsphere and thus many more cornstarch particles could fit into the volume. After considering these differences, one finds that the calculated number density seems relatively reasonable for the calculation.

The results of the theoretical calculation of the attenuation coefficient and phase velocity in the 20% cornstarch suspensions in 51.5% cesium chloride brine are shown in Figures 7.21 and 7.22. In order to observe the resonance, the calculation was extended over a wider frequency range than the microsphere calculation. Figures 7.15 and 7.17 show that the first resonance peak in the attenuation coefficient moves higher in frequency as the diameter of the spheres in the suspension get smaller.

Theoretical Parameters	Value of Parameter	Source
Phase Velocity of Host Medium (c_w)	1483 m/s	Experimentally Measured
Phase Velocity of Cornstarch (c_s)	2700 m/s	Inferred from Measurement
Density of Host Medium (ρ_w)	1620 kg/m^3	Experimentally Measured
Density of Cornstarch (ρ_s)	1620 kg/m^3	(Fall *et al.*, 2008)
Poisson Ratio of Cornstarch	0.3	(Flores *et al.*, 2007)
Mean Cornstarch Radius	7 μm	Experimentally Measured
Number Density of Cornstarch	$1.8 * 10^{14}$ particles/m^3	Calculated

TABLE 7.6: The parameters necessary for the theoretical calculation of the phase velocity and the attenuation coefficient of the cornstarch in density-matched cesium chloride brine.

From this evidence, the even higher frequency peak calculated for the cornstarch particles should be expected. For the 40 μm diameter polystyrene microspheres the first resonance peak is at approximately 18 MHz, while for the cornstarch particles (13 μm diameter) the first resonance peak occurs at about 65 MHz. The calculation was also repeated with the density of the cornstarch granules set to 1.62 g/cm^3 (the density measured for the cornstarch granules in Section 3.3). The results of that calculation were consistent with the results shown in this thesis.

In order to see whether a large resonance predicted by the theory could lead to the negative dispersion seen in the experimental data, the theoretical attenuation coefficient and phase velocity were plotted over the same bandwidth as the experimental measurements (4 to 8 MHz) in Figures 7.23 and 7.24. The large resonance

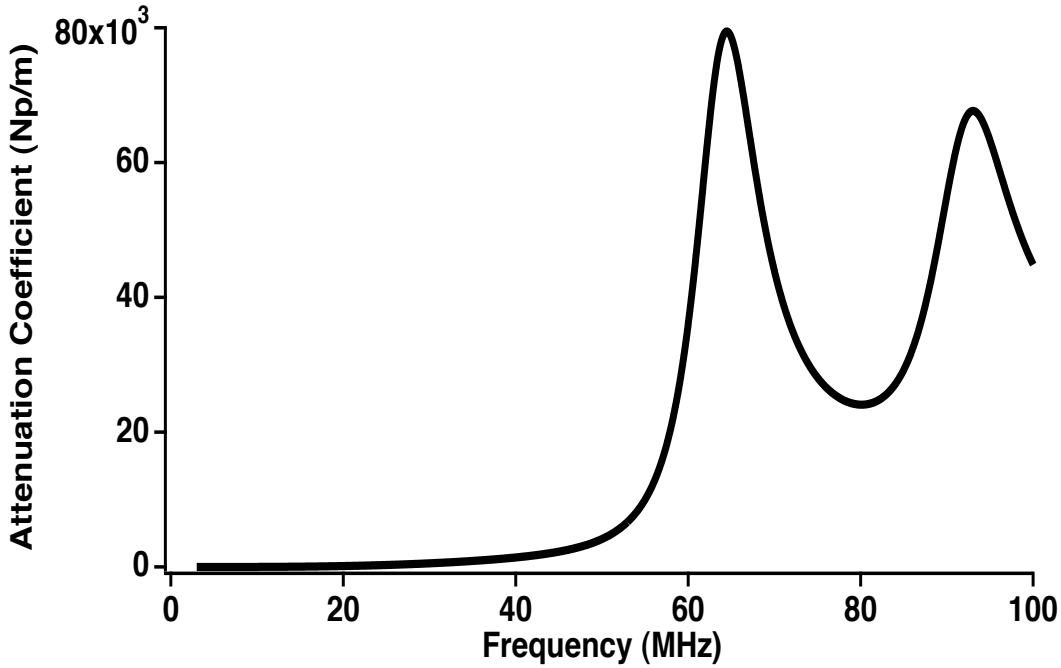

FIGURE 7.21: The theoretical attenuation coefficient calculated for a 20% cornstarch suspension in 51.5% cesium chloride brine over a range of frequency from 3 to 100 MHz.

peak predicted by the theory for the cornstarch suspension could lead to the observed negative dispersion in the data. Experimental measurements of the attenuation coefficient and phase velocity for a 20% cornstarch suspension in 51.5% cesium chloride solution are plotted in Figures 7.25 and 7.26 to permit a comparison between the theory and experiment. The point of this comparison is not to compare the detailed magnitudes of the theory and the experiment but to look at the overall trends. Considering the limitations discussed for the calculation of the theoretical attenuation coefficient and phase velocity in the cornstarch suspension, reasonable agreement can be seen between the theory and the experimental measurements.

The resonances in the attenuation coefficient and phase velocity predicted by the

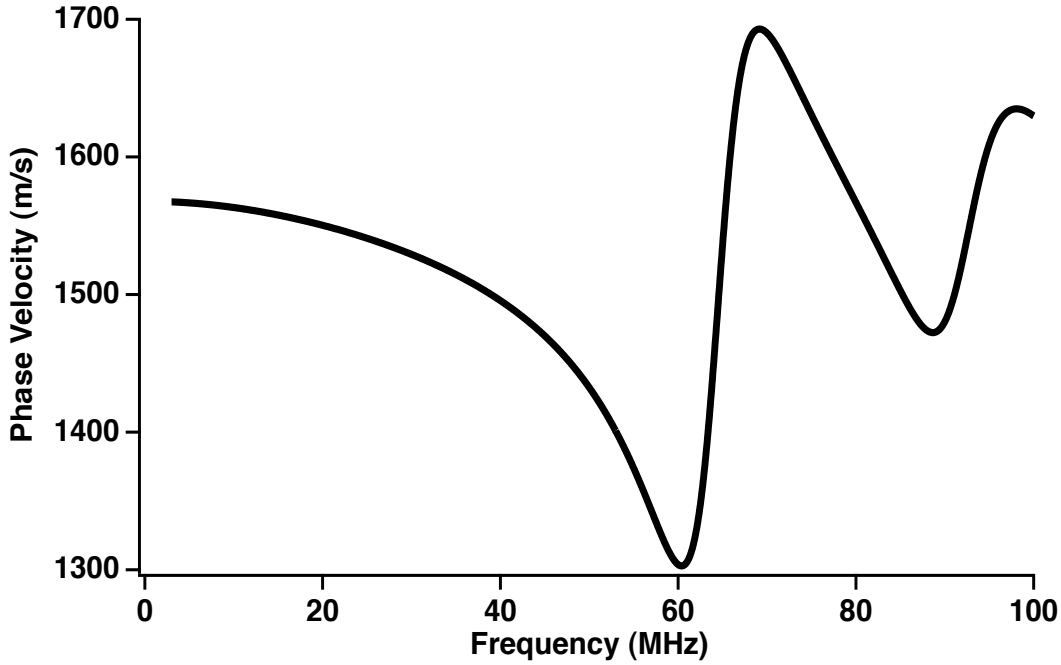

FIGURE 7.22: The theoretical phase velocity calculated for a 20% cornstarch suspension in 51.5% cesium chloride brine over a range of frequency from 3 to 100 MHz.

theory are due to surface waves specific to the interface between a solid and liquid (Mobley, 1998; Hay and Schaafsma, 1989). One paper in the literature looked at these resonances in both polystyrene microspheres and glass microspheres (Hay and Schaafsma, 1989). This study found that while large resonances exist for both types of microspheres, these resonances are much more pronounced in the plastic than in the glass (Hay and Schaafsma, 1989). The prevailing hypothesis is that the key element resulting in these large resonances is that the shear wave speed in the scatterer is lower than the speed of sound in water (Hay and Schaafsma, 1989; Mobley, 1998). The shear wave speed of plastic is less than the speed of sound in water, whereas the shear wave speed in glass is approximately twice the speed of sound in water (Hay and Schaafsma, 1989; Mobley, 1998). These measurements have also been made on

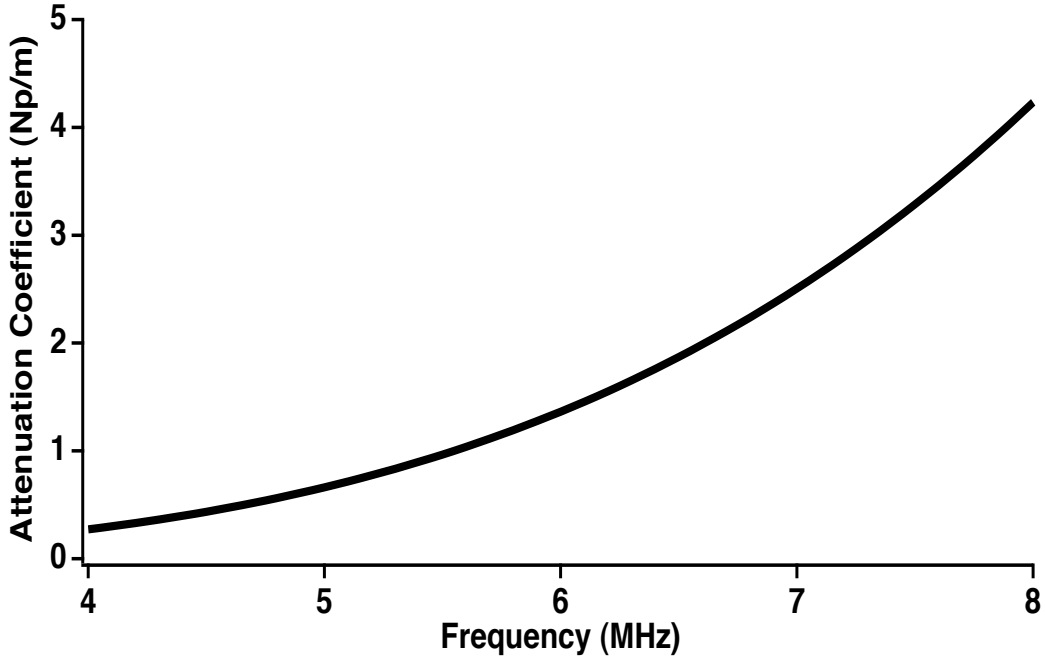

FIGURE 7.23: The theoretical attenuation coefficient calculated for a 20% cornstarch suspension in 51.5% cesium chloride brine over the experimental bandwidth from 4 to 8 MHz.

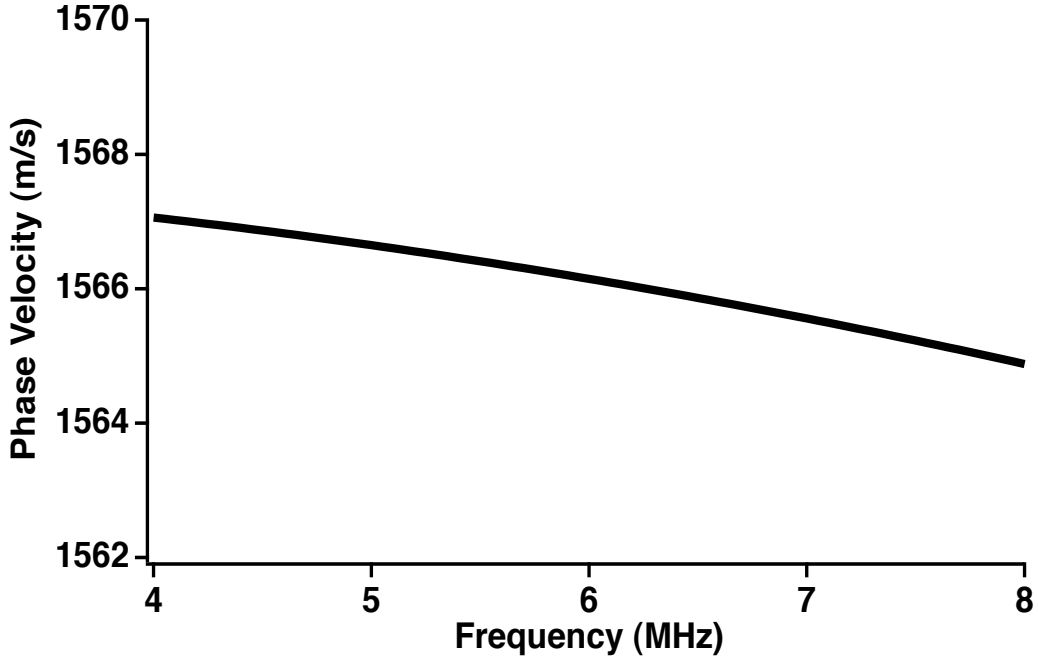

FIGURE 7.24: The theoretical phase velocity calculated for a 20% cornstarch suspension in 51.5% cesium chloride brine over over the experimental bandwidth from 4 to 8 MHz.

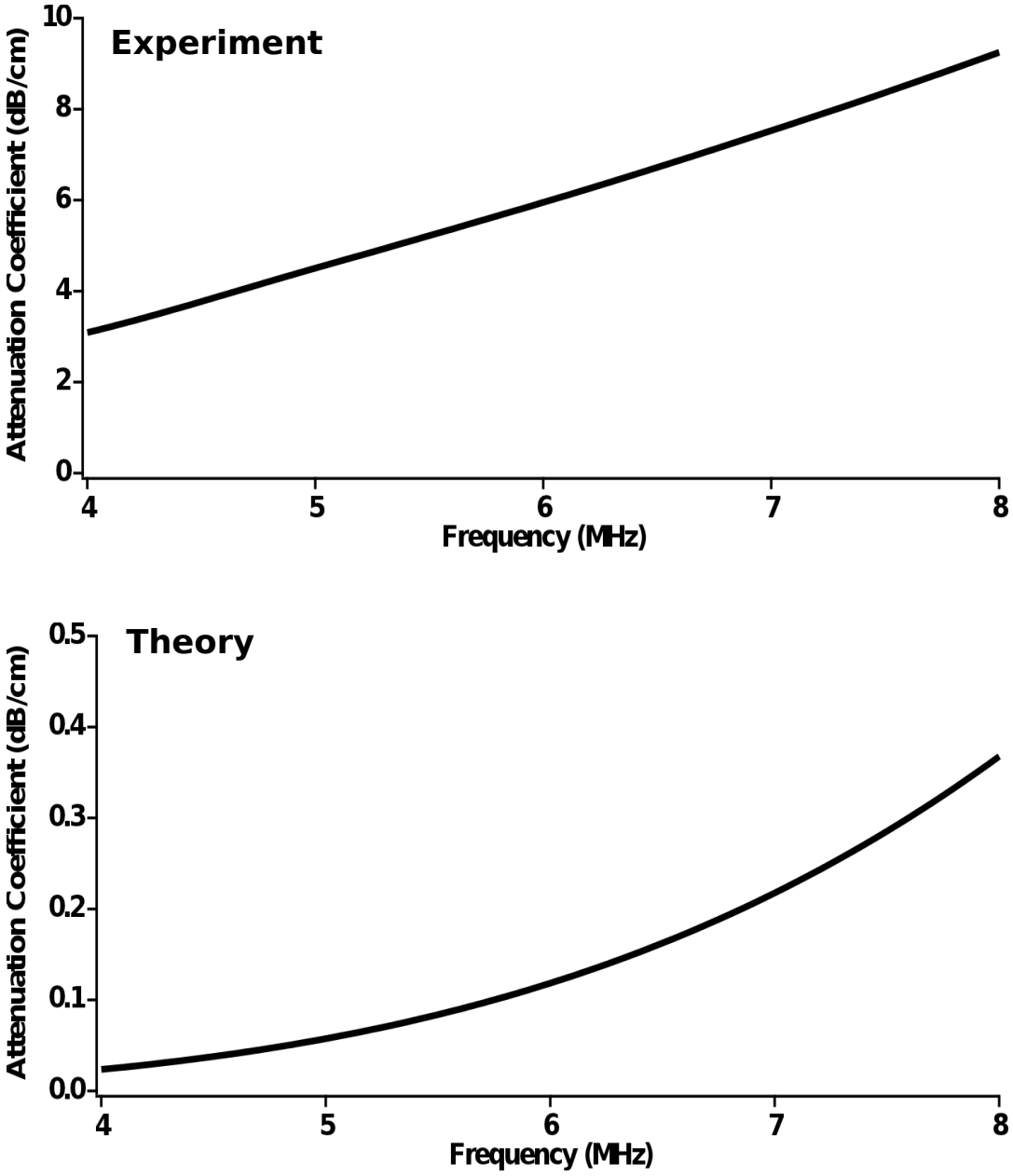

FIGURE 7.25: A comparison between the experimentally measured attenuation coefficient and the theoretically calculated attenuation coefficient for a 20% cornstarch in 51.5% cesium chloride brine over the experimental bandwidth from 4 to 8 MHz.

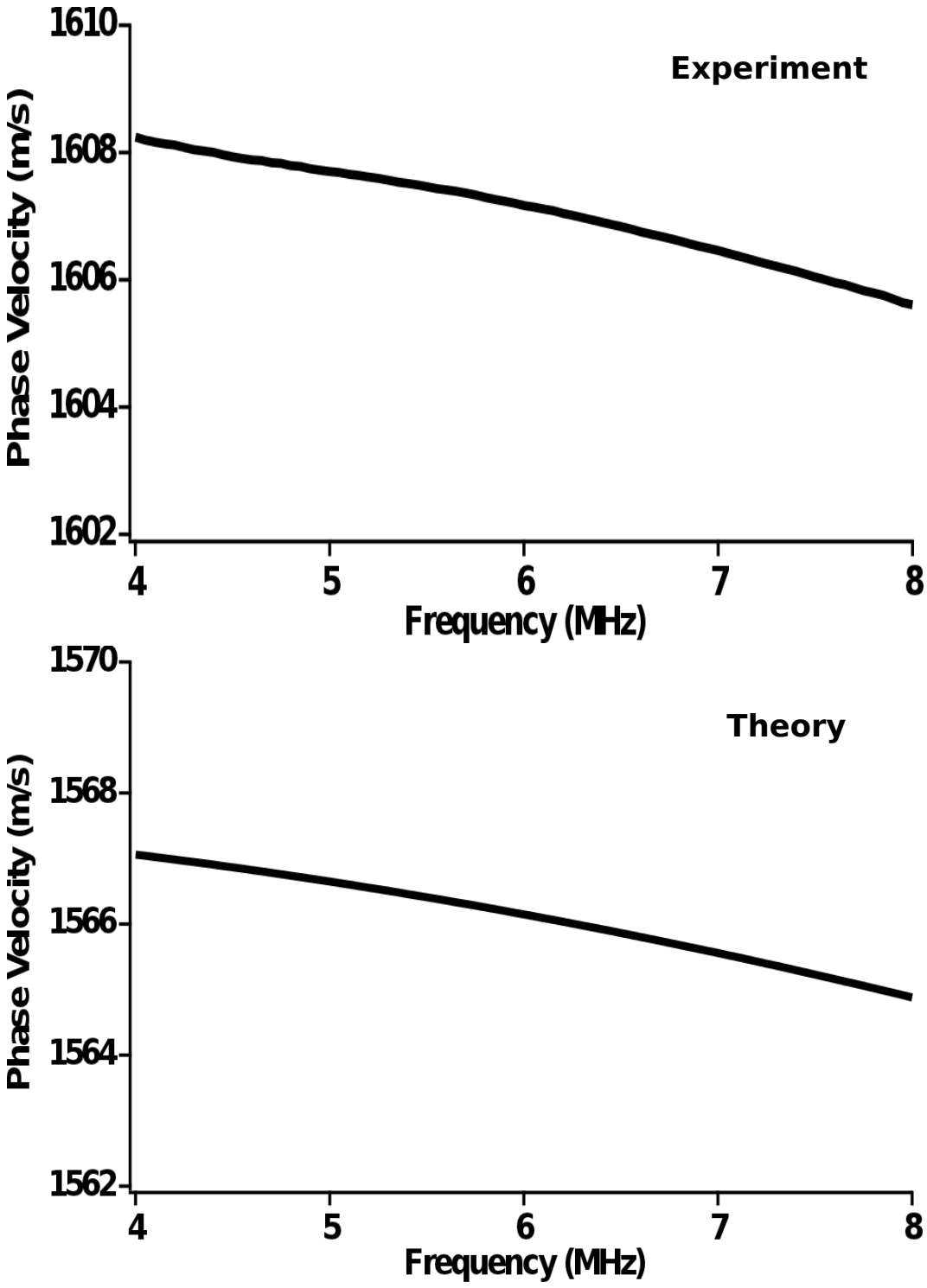

FIGURE 7.26: A comparison between the experimentally measured phase velocity and the theoretically calculated phase velocity for a 20% cornstarch in 51.5% cesium chloride brine over the experimental bandwidth from 4 to 8 MHz.

porous particles of titania aggregate of several different diameters (Richter *et al.*, 2006). This work also found resonances in the attenuation data that moved higher in frequency as the diameter of the particles decreased (Richter *et al.*, 2006).

7.5.2 Dielectric Relaxations

An analogous example of negative dispersion explained by large resonances has been reported in optical measurements of the index of refraction as a function of wavelength. In optics, the phase velocity in a medium can be defined using Equation 7.9

$$v = \frac{c}{n} \tag{7.9}$$

where c is the speed of light in a vacuum and n is the index of refraction for that particular medium (Guenther, 1990) . "Normal" optical dispersion occurs when the index of refraction decreases for increasing wavelength (Guenther, 1990). This is equivalent to stating that for typical optical media the phase velocity decreases for increasing frequency ("Anomalous dispersion" in optics occurs when the phase velocity increases for increasing frequency. As a consequence, the word "anomalous" is used differently in the optical literature than it is in this thesis and in earlier reports from our laboratory (Anderson *et al.*, 2008; Bauer *et al.*, 2008; Marutyan *et al.*, 2006)).

The Sellmeier equation is used in optics to connect the index of refraction and wavelength for a particular medium (Guenther, 1990). The most common form of the Sellmeier Equation for glasses is of the form of Equation 7.10, because glasses are

known to have three large resonances

$$n^2(\lambda) = 1 + \frac{B_1\lambda^2}{\lambda^2 - C_1} + \frac{B_2\lambda^2}{\lambda^2 - C_2} + \frac{B_3\lambda^2}{\lambda^2 - C_3} \tag{7.10}$$

where $B_{1,2,3}$ are the strengths of the absorption resonances and $\sqrt{C_{1,2,3}}$ is the wavelength of that resonances (Guenther, 1990). The actual values of $B_{1,2,3}$ and $\sqrt{C_{1,2,3}}$ are found from fitting the Sellmeier equation to the experimental data. The index of refraction is related to the dielectric constant of the medium by Equation 7.11

$$n = \frac{c}{v} = \sqrt{\frac{\epsilon\mu}{\epsilon_0\mu_0}} \approx \sqrt{\frac{\epsilon}{\epsilon_0}} \tag{7.11}$$

where ϵ is the dielectric constant in the medium, μ is permeability of the medium, ϵ_0 is the permittivity of free space and μ_0 is the permeability of free space (Guenther, 1990). The index of refraction can be approximated as the square root of the dielectric constant as long as magnetic materials are not considered (Guenther, 1990). In the case of glasses, large dielectric relaxations explain the negative dispersion found in the optical spectrum (Guenther, 1990).

Interestingly, cornstarch suspensions may also display large dielectric relaxations at frequencies well outside the bandwidth of the ultrasonic measurement. At least three dielectric relaxations have been measured in wheat starch slurries of similar concentrations to the ones examined in this thesis in a bandwidth between 0.2 and 20 GHz (Motwani *et al.*, 2012). One of these resonances is due to the bulk water in the system and the other two resonances are attributed to confined water molecules in the starch-water system due to the porosity of the starch (Motwani *et al.*, 2012). Wheat starch and corn starch are similar starches and thus it seems reasonable to

expect that the results extend to corn starch particles.

7.6 Conclusion

The negative dispersion in the cornstarch suspensions initially appeared to be inconsistent with the band-limited Kramers-Kronig relations. To rule out experimental artifacts, a series of controlled studies were carried out. Careful measurements were taken of the phase velocity in two types of plastic with different attenuation properties and in a viscous liquid. The data were shown to be consistent with the Kramers-Kronig predictions. Then nonlinear effects were explored as a possible explanation for the negative dispersion. Careful measurements showed that the negative dispersion was not dependent on the input pulse amplitude. Subsequently, a theory explaining resonances found in suspensions of plastic microspheres was evaluated. The theoretical attenuation coefficient and phase velocity were calculated for an example cornstarch suspension. The theory predicted large resonances outside of the measured bandwidth that would result in an attenuation coefficient that rises with frequency and a phase velocity that decreases with frequency. The explanation is analogous to that given for explaining the effect that large dielectric relaxations have on optical dispersion. The theoretical explanations of the negative dispersion discussed in this chapter provides some insight into the initially surprising results of the phase velocity measurements.

Bibliography

Anderson, C., Marutyan, K., Holland, M., Wear, K., and Miller, J. (**2008**). "Interference between wave modes may contribute to the apparent negative dispersion observed in cancellous bone", Journal of the Acoustical Society of America **124**, 1781–1789.

Bauer, A., Marutyan, K., Holland, M., and Miller, J. (**2008**). "Negative dispersion in bone: the role of interference in measurements of the apparent phase velocity of two temporally overlapping signals", Journal of the Acoustical Society of America **123**, 2407–2414.

Bauer, A. Q., Marutyan, K. R., Holland, M. R., and Miller, J. G. (**2007**). "Is the kramers-kronig relationship between ultrasonic attenuation and dispersion maintained in the presence of apparent losses due to phase cancellation?", J Acoust Soc Am **122**, 222–8.

Dayton, P., Goode, A., Morgan, K., Klibanov, S., Brandenburger, G., and Ferrara, K. (**1996**). "Action of microbubbles when insonified: experimental evidence", in *IEEE Ultrasonics Symposium Proceedings*, volume 2, 1131–1134.

Fall, A., Huang, N., Bertrand, F., Ovarlez, G., and Bonn, D. (**2008**). "Shear thickening of cornstarch suspensions as a reentrant jamming transition", Physical Review Letters **100**.

Faran, J. (**1951**). "Sound scattering by solid cylinders and spheres", JASA **23**, 405–418.

Flores, A., Bayer, R., Krawietz, K., and Calleja, F. B. (**2007**). "Elastoplastic properties of starch-based materials as revealed by microindentation measurements", Journal of Macromolecular Science, Part B: Physics **39**, 749–759.

Guenther, R. (**1990**). *Modern optics* (John Wiley and Sons).

Hall, C., Marsh, J., Hughes, M., Mobley, J., Wallace, K., Miller, J., and Brandenburger, G. (**1997**). "Broadband measurements of the attenuation coefficient and backscatter coefficient for suspensions: A potential calibration tool", JASA **101**, 1162–1171.

Hay, A. and Schaafsma, A. (**1989**). "Resonance scattering in suspensions", Journal of Acoustical Society of America **85**, 1124–1138.

Katz, J. (**2012**). "Private communication", .

Marutyan, K., Holland, M., and Miller, J. (**2006**). "Anomalous negative dispersion in bone can result from the interference of fast and slow waves", Journal of the Acoustical Society of America **120**, EL55–EL61.

Mobley, J. (**1998**). "Ultrasonic dispersion in suspensions and solids: A study of fundamental dynamics and the kramers-kronig relations", Ph.D. dissertation (Washington University in St. Louis, MO) .

Mobley, J., Water, K., Hall, C., Marsh, J., Hughes, M., Brandenburger, G., and Miller, J. (**1999**). "Measurements and predictions of the phase velocity and attenuation coefficient in suspensions of elastic microspheres", JASA .

Motwani, T., Lanagan, M., and Anantheswaran, R. (**2012**). "State of water in starch-water systems in the gelatization temperature range as investigated using dielectric relaxation spectroscopy", Carboyhydrate Polymers **87**, 24–31.

Richter, A., Babick, F., and Stintz, M. (**2006**). "Polydisperse particle size characterization by ultrasonic attenuation spectroscopy in the micrometer range", Ultrasonics **44**, e483–e490.

Waterman, P. and Truell, R. (**1961**). "Multiple scattering of waves", Journal of Mathematical Physics **2**, 512–537.

Waters, K. R., Hughes, M. S., Mobley, J., and Miller, J. G. (**2003**). "Differential forms of the kramers-krönig dispersion relations", IEEE Trans Ultrason Ferroelectr Freq Control **50**, 68–76.

Chapter 8

Backscatter Measurements of Cornstarch Suspensions

8.1 Preface

This chapter describes the backscatter measurements made on suspensions of cornstarch in a density-matched cesium chloride and water solution. The chapter begins by describing the experimental technique necessary to make the backscatter measurements. The analysis methods required to determine the fully-reduced, frequency dependent backscatter coefficient are discussed in detail. The results of the backscatter measurements on 10%, 20%, 30%, and 40% concentrations of cornstarch suspensions in a 51.5% cesium chloride in water solution are reported. The experimental results are explained with a theory that has been used to explain the concentration

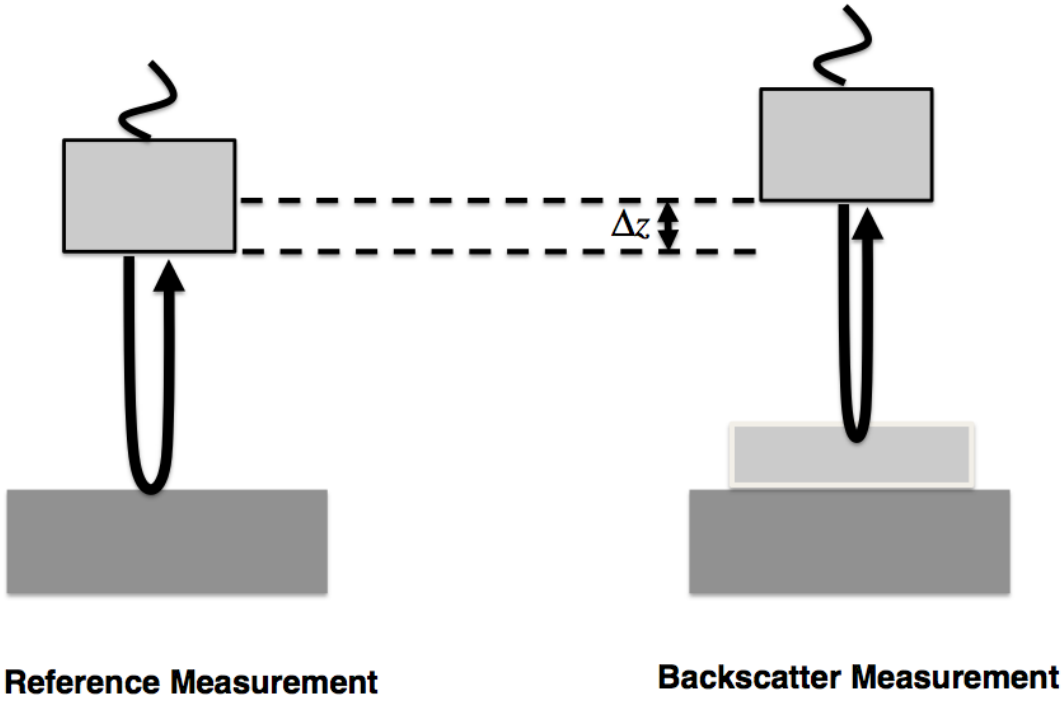

FIGURE 8.1: The experimental setup for the backscatter measurement. The transducer is aligned with the steel reflector for the reference measurement. For the backscatter measurement, the transducer is translated back a known distance, so that the focus of the transducer is just inside the front wall of the sample.

dependence of the backscatter coefficient of red blood cells.

8.2 Backscatter Methods

The backscatter measurements of the cornstarch suspensions were made using a slightly modified version of the typical technique (Yang *et al.*, 2007). The experimental setup is shown in Figure 8.1. For the reference measurement, the transducer is aligned with the steel reflector and a single trace is saved. An example reference trace is shown in Figure 8.2. The transducer is then moved back a known distance

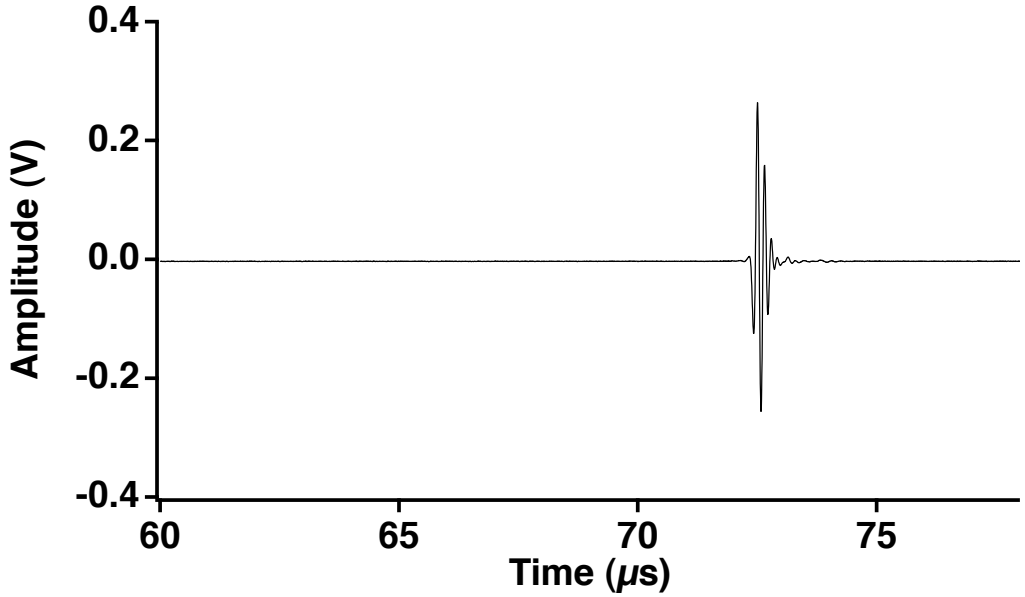

FIGURE 8.2: An example reference trace for the backscatter measurement is plotted.

(slightly less than the sample thickness), so that the focus of the transducer is just inside the front wall of the sample. Before the backscatter traces were acquired, the sample was agitated in order to make the suspension as homogeneous as possible for the measurement. No spatial averaging or time averaging was used for the backscatter measurement, because of the motion of the liquid suspension within the sample mold. For each sample, at least 150 backscatter traces were acquired in quick succession (all traces were acquired within 5 minutes of the beginning of data acquisition). For the backscatter acquisitions, the input attenuation into the system was set to 40 dB lower than for the acquisition of the reference trace in order to accommodate the weaker signals associated with the backscatter measurements. An example backscatter trace is displayed in Figure 8.3.

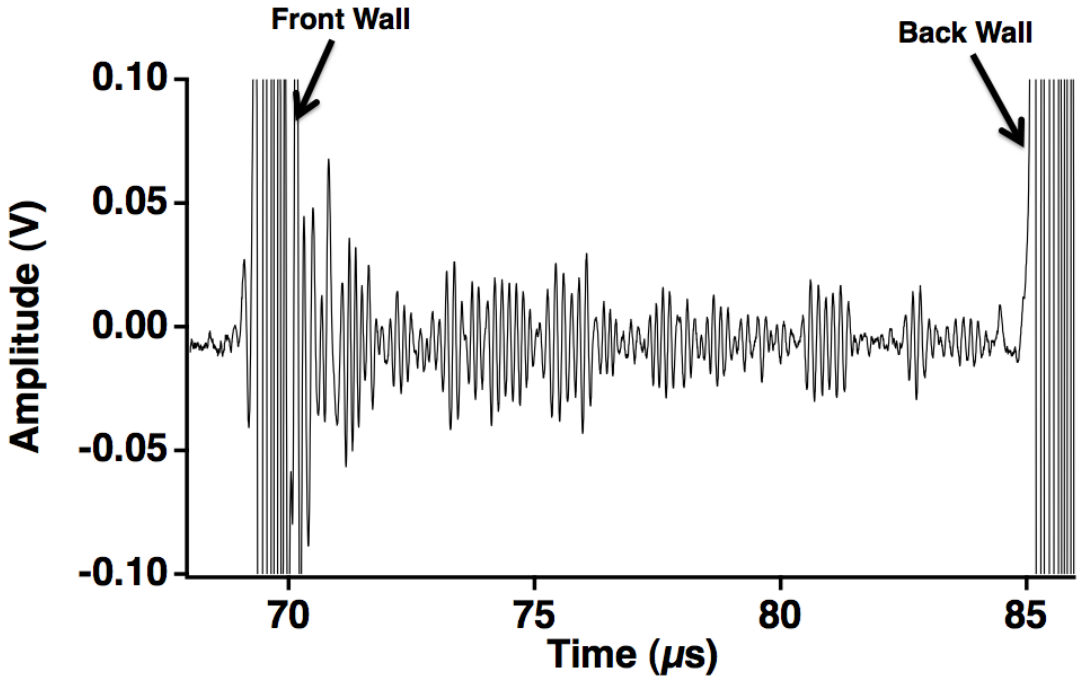

FIGURE 8.3: An example backscatter trace is shown. The front wall signal and back wall signal of the sample are labeled.

8.3 Backscatter Analysis

The backscatter coefficient is the parameter of interest for the backscatter measurements. The fully-reduced backscatter coefficient is expressed in Equation 8.1

$$\text{Backscatter Coefficient} = \text{ABTF}(f)*(\text{Atten Comp})*(\text{Diffract Comp})*(\text{Reflect and Trans Loss Com} \tag{8.1}$$

where ABTF(f) is the apparent backscatter transfer function, "Atten Comp" is the attenuation compensation function, "Diffract Comp" is the diffraction compensation function, and "Reflect and Trans Loss Comp" is the reflection and transmission loss compensation function (Yang *et al.*, 2007). Each component of the backscatter coefficient will be discussed separately in the next several sections.

8.3.1 Apparent Backscatter Transfer Function

The apparent backscatter transfer function is defined as the power spectrum of the backscattered signal from the sample normalized by the power spectrum of the signal from the steel reflector as displayed in Equation 8.2

$$\text{Apparent Backscatter Transfer Function} = \frac{P_{samp}(f)}{P_{ref}(f)} \tag{8.2}$$

where $P_{samp}(f)$ is the power spectrum of the backscattered signal from the sample and $P_{ref}(f)$ is the power spectrum of the signal from the steel reflector. The reference power spectrum is determined by first windowing the reference trace using an appropriate windowing function (Hanning function) before applying a Fast Fourier

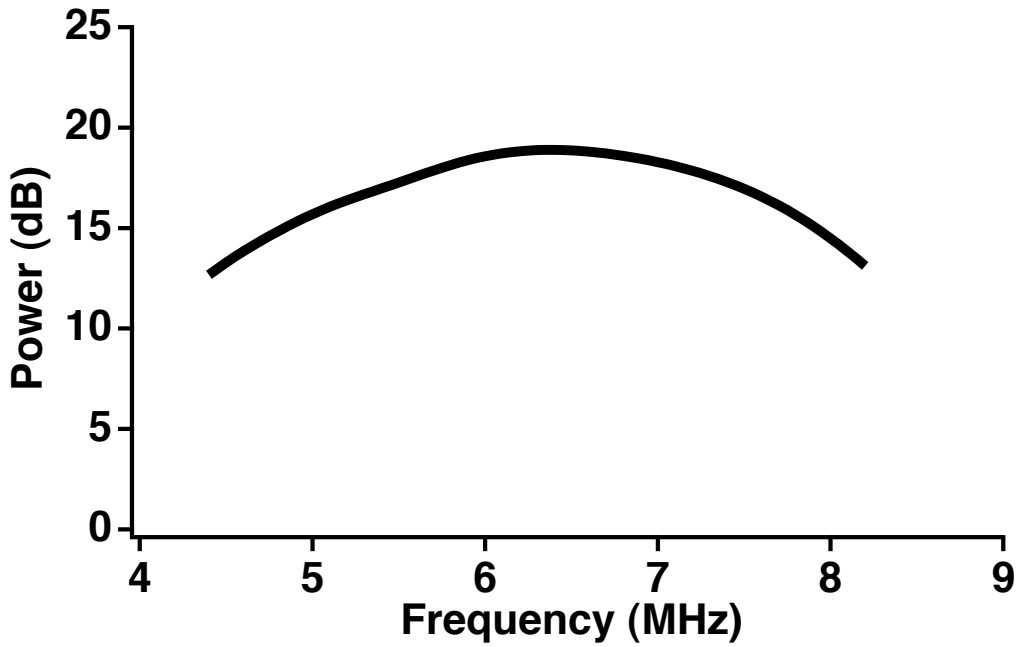

FIGURE 8.4: An example reference power spectrum is plotted as a function of frequency

transform and determining the squared magnitude. An example reference power spectrum is plotted in Figure 8.4. The sample power spectrum is determined in a similar way by first windowing a portion of the backscatter signal before finding the squared magnitude of the Fourier Transform of the windowed signal. An example sample power spectrum is plotted in Figure 8.5. For the backscatter measurements in this thesis, the time window was chosen to be 4 μs in length and begins 3 μs after the start of the front wall signal. The length of the time window for the backscattered signal was picked in order to balance the need to have a long enough window to allow for as much data as possible, while at the same time not choosing too long a window, in which case the effects of attenuation would be apparent over the length of the window (Trousil, 2002). The sample power spectra are determined for each acquired back-

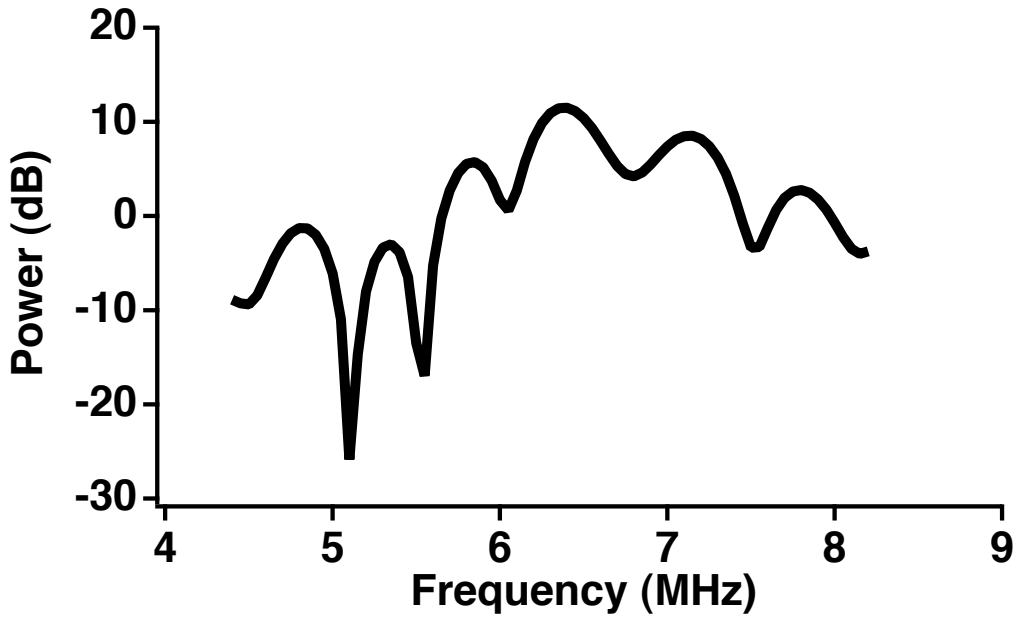

FIGURE 8.5: An example backscattered sample power spectrum from a cornstarch suspension is plotted as function of frequency. The variability in the power as a function of frequency is typical of backscatter measurements.

scatter trace and then averaged together in the linear domain. An example average sample power spectrum is plotted in Figure 8.6.

The apparent backscatter transfer function was determined with Equation 8.2 plotted in Figure 8.7. In order to provide a single value to summarize the apparent backscatter transfer function, the apparent integrated backscatter can be determined by averaging over the useful bandwidth as displayed in Equation 8.3

$$\mathrm{AIB}_{dB} = \frac{1}{\Delta f} \int_{f_L}^{f_H} \mathrm{ABTF}_{dB}(f)\, \mathrm{d}f. \tag{8.3}$$

where $\Delta f = f_H - f_L$ (Hoffman, 2010). The apparent integrated backscatter of the example apparent backscatter transfer function was calculated and displayed in Figure 8.8.

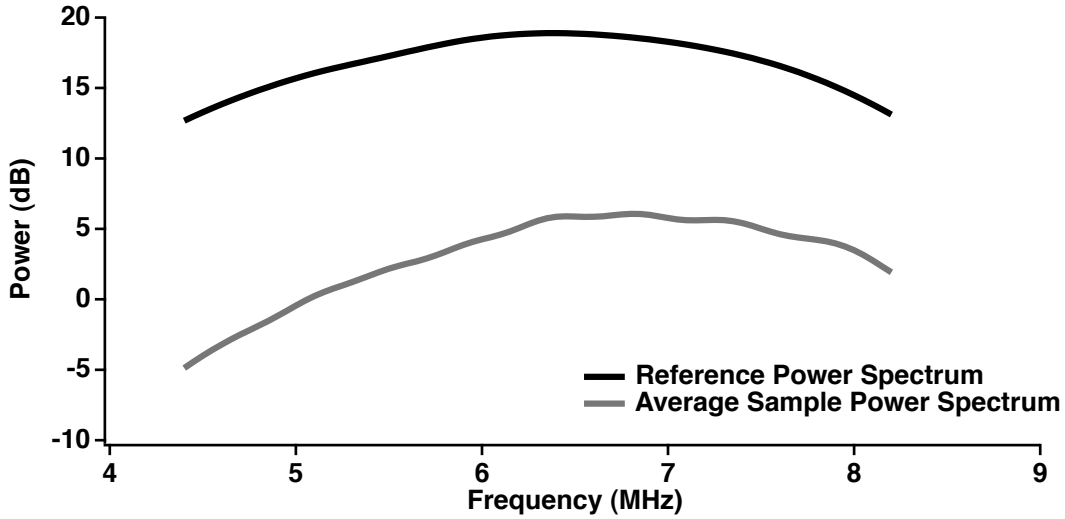

FIGURE 8.6: The average sample power spectrum from 150 backscatter measurements of a cornstarch suspension in a density-matched cesium chloride solution is plotted. The reference power spectrum is also plotted.

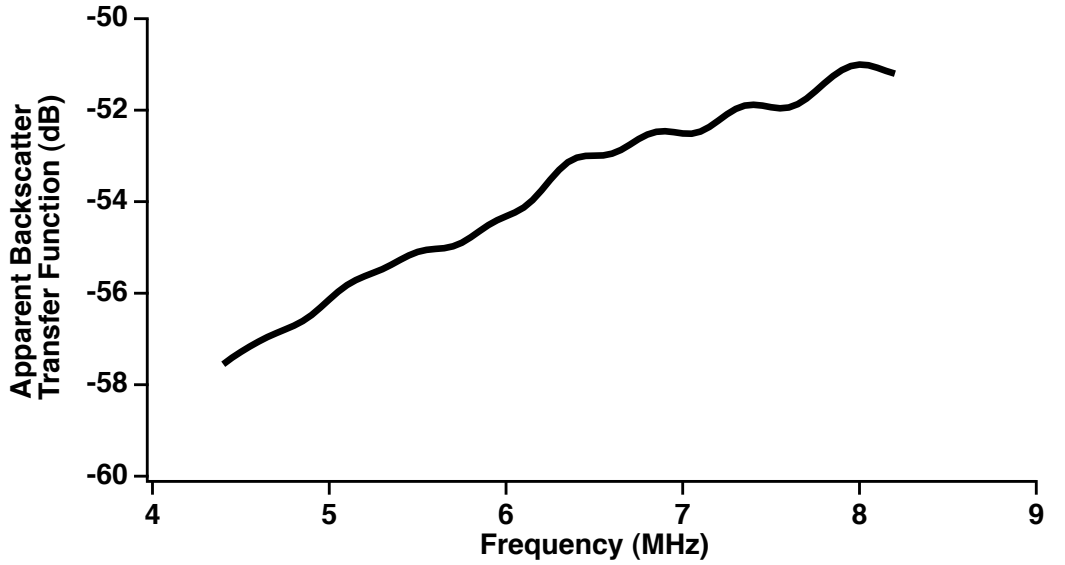

FIGURE 8.7: An example apparent backscatter transfer function is plotted as a function of frequency.

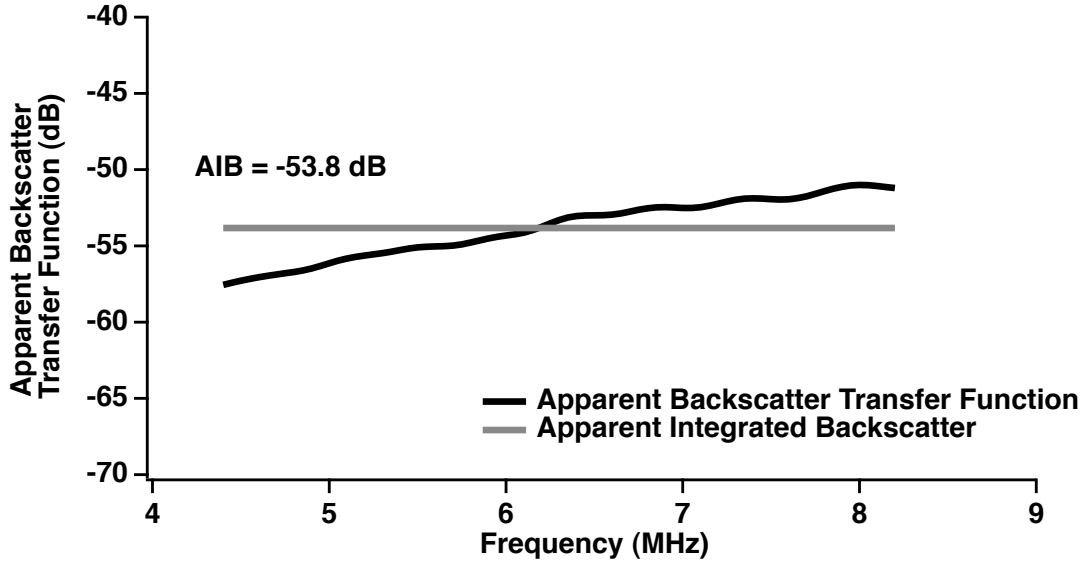

FIGURE 8.8: An example apparent backscatter transfer function is plotted as a function of frequency. The apparent integrated backscatter is also plotted.

8.3.2 Attenuation Compensation

The attenuation compensation function used for the backscatter measurements in this thesis was first proposed by Sigelmann and Reid, and then extended to broadband measurements by O'Donnell and Miller (Sigelmann and Reid, 1972; O'Donnell and Miller, 1981). At the frequencies used for the backscatter measurements in this thesis, the attenuation due to water is considered negligible (Trousil, 2002). Thus, the attenuation compensation function must take into account the attenuation that occurs immediately after the beginning of the front wall signal to the beginning of the time gate of the backscattered signal, as well as the attenuation within the time gate itself (O'Donnell and Miller, 1981). The attenuation compensation function is

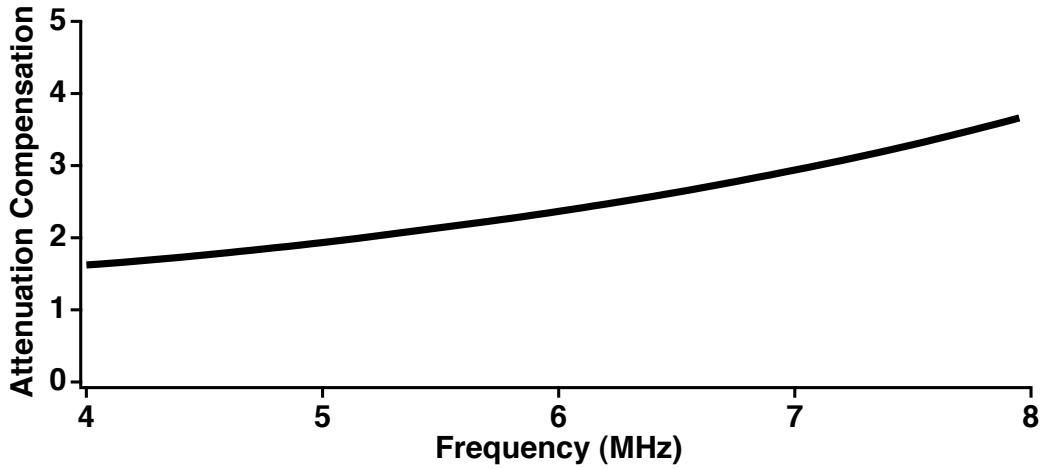

FIGURE 8.9: An example of the (dimensionless) attenuation compensation function for a 20% cornstarch in 51.5% cesium chloride solution is plotted as a function of frequency.

given by Equation 8.4

$$\text{Attenuation Compensation} = e^{4\alpha x_0} \frac{2\alpha v \tau e^{2\alpha v \tau}}{e^{\alpha v \tau} - e^{-\alpha v \tau}} \tag{8.4}$$

where α is the frequency-dependent attenuation coefficient in the sample, x_0 is the distance from the front wall of the sample to the beginning of the time gate, v is the speed of sound in the sample, and τ is the time gate duration (O'Donnell and Miller, 1981; Yang *et al.*, 2007). The first term in Equation 8.4 compensates for the attenuation effects due to the region of the sample between the front wall and the start of the time gate, whereas the second term in the equation compensates for the attenuation within the gated region. An example attenuation compensation function for a 20% cornstarch in a 51.5% cesium chloride solution was plotted in Figure 8.9.

8.3.3 Diffraction Compensation

The diffraction effects compensation technique employed in this thesis was first laid out by Chen et al. (Chen *et al.*, 1997). The compensation is valid under the following conditions: The reference measurement is made using a perfectly reflecting steel plate placed in the focal plane of the transducer. The time window for the backscatter signal must be placed so the focus of the transducer falls within or very close to it. The pressure gain factor, G_p, given by Equation 8.5 must be larger than pi for the experimental setup used

$$G_p = \frac{ka^2}{2r_0} \tag{8.5}$$

where k is the wavenumber, a is the radius of the transducer, and r_0 is the focal length of the transducer (Chen *et al.*, 1997). For the half inch diameter transducer with a focal length of approximately two inches and a usable bandwidth of about 4 MHz to 8 MHz used in the backscatter measurements described in this thesis, the pressure gain factor ranges from a little more than 2π at 4 MHz up to just over 4π at 8 MHz. Thus, for all of the backscatter measurements made in this thesis, the diffraction effects compensation was of the form given in Equation 8.6

$$\text{Diffraction Compensation} = \frac{r_0^2}{(v\tau/2)\pi a^2 E_\infty} e^{-(2/\pi)(G_p/\pi)^{-1/2}} \tag{8.6}$$

where v is the speed of sound in the medium, τ is the duration of the time gate, and E_∞ is a dimensionless constant equal to 0.46 for the experiments in this thesis (Chen *et al.*, 1997; Yang *et al.*, 2007). A typical diffraction compensation function

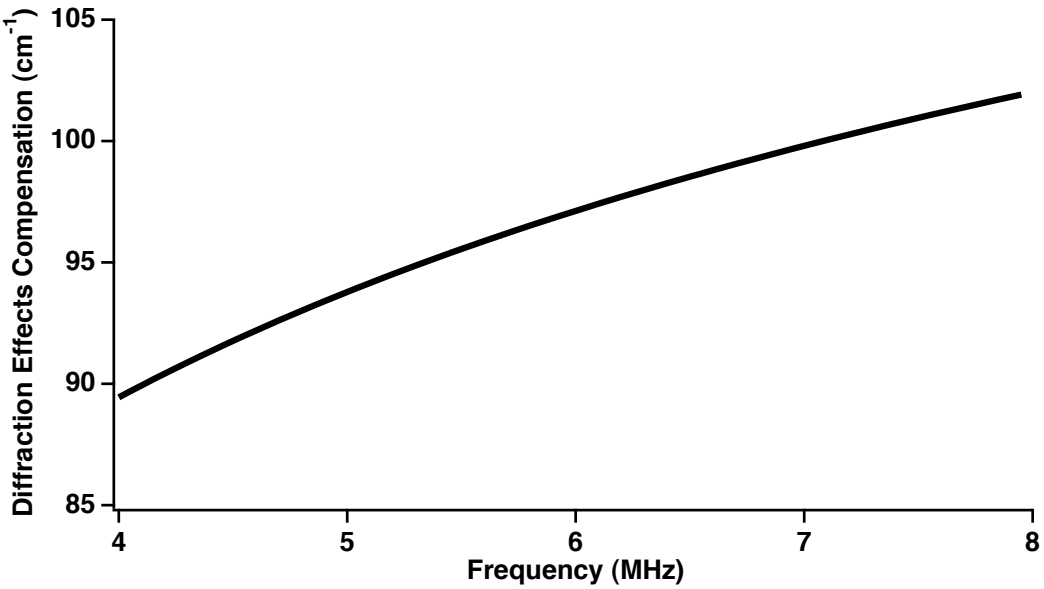

FIGURE 8.10: An example of the diffraction effects compensation function is plotted as a function of frequency.

for the measurements in this thesis is plotted as a function of frequency in Figure 8.10. The diffraction compensation function employed in this thesis contains factor compensating for the length of the time gate ($v\tau/2$). Thus, the diffraction compensation function has units of inverse distance. This form of the diffraction compensation function was employed by both Chen et al. and Yang et al. (Chen *et al.*, 1997; Yang *et al.*, 2007). Another equivalent compensation employed by Hoffman does not compensate for the gate length as a part of the diffraction compensation, but instead compensates for this factor separately (Hoffman, 2010).

8.3.4 Transmission and Reflection Loss Compensation

The backscatter measurements were compensated for the effects of the transmission loss at the face of the sample and the reflection loss due to the steel reflector not being a perfect reflector (O'Donnell and Miller, 1981). The intensity reflection coefficient used for the compensation is given by Equation 8.7

$$\mathrm{R}^{I}_{w\to r} = \frac{|\tilde{Z}_r - \tilde{Z}_w|^2}{|\tilde{Z}_r + \tilde{Z}_w|^2} \tag{8.7}$$

where $\tilde{Z}_r$ is the complex acoustic impedance of the steel reflector and $\tilde{Z}_w$ is the complex acoustic impedance of the water (Trousil, 2002). The intensity transmission coefficient is complicated by presence of the thin Saran Wrap$^{\mathrm{TM}}$windows at the interface between the cornstarch suspension and the water, and thus is given by Equation 8.8

$$\mathrm{T}^{I}_{w\to s\to c}(f) = \mathrm{T}^{I}_{c\to s\to w}(f) = \frac{4\tilde{Z}_w\tilde{Z}_c}{(\tilde{Z}_w + \tilde{Z}_c)^2 * \cos^2(k_s h) + [\tilde{Z}_s + \tilde{Z}_w * \tilde{Z}_c/\tilde{Z}_s]^2 * \sin^2(k_s h)} \tag{8.8}$$

where $\tilde{Z}_c$ is the complex acoustic impedance of the cornstarch suspension and $\tilde{Z}_s$ is the complex acoustic impedance of the Saran Wrap$^{\mathrm{TM}}$, k_s is the wavenumber in the Saran Wrap$^{\mathrm{TM}}$, and h is the thickness of the Saran Wrap$^{\mathrm{TM}}$(Trousil, 2002).

The transmission and reflection loss compensation is given by Equation 8.9

$$\text{Transmission and Reflection Loss Compensation} = \frac{\mathrm{R}^{I}_{w\to r}}{[\mathrm{T}^{I}_{w\to s\to c}(f)]^2}. \tag{8.9}$$

An example transmission and reflection loss compensation function for a 20% cornstarch suspension in a 51.5% cesium chloride solution is plotted in Figure 8.11.

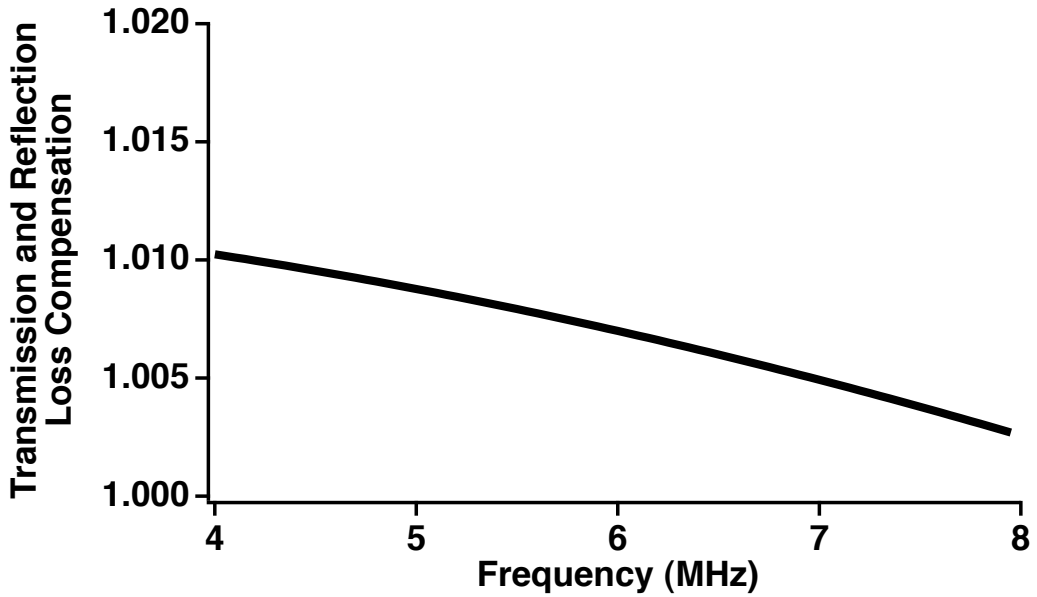

FIGURE 8.11: An example of the transmission and reflection loss compensation function for a 20% cornstarch suspension in a 51.5% cesium chloride solution is plotted as a function of frequency.

8.4 Backscatter Coefficient

An example apparent backscatter transfer function in the linear domain for a 20% cornstarch in 51.5% cesium chloride and water solution was plotted in Figure 8.12. With Equation 8.1, the apparent backscatter transfer function plotted in Figure 8.12, the attenuation compensation function plotted in Figure 8.9, the diffraction effects compensation function plotted in Figure 8.10, and the transmission and reflection loss compensation function plotted in Figure 8.11, an example fully-reduced backscatter coefficient was plotted as a function of frequency in Figure 8.13.

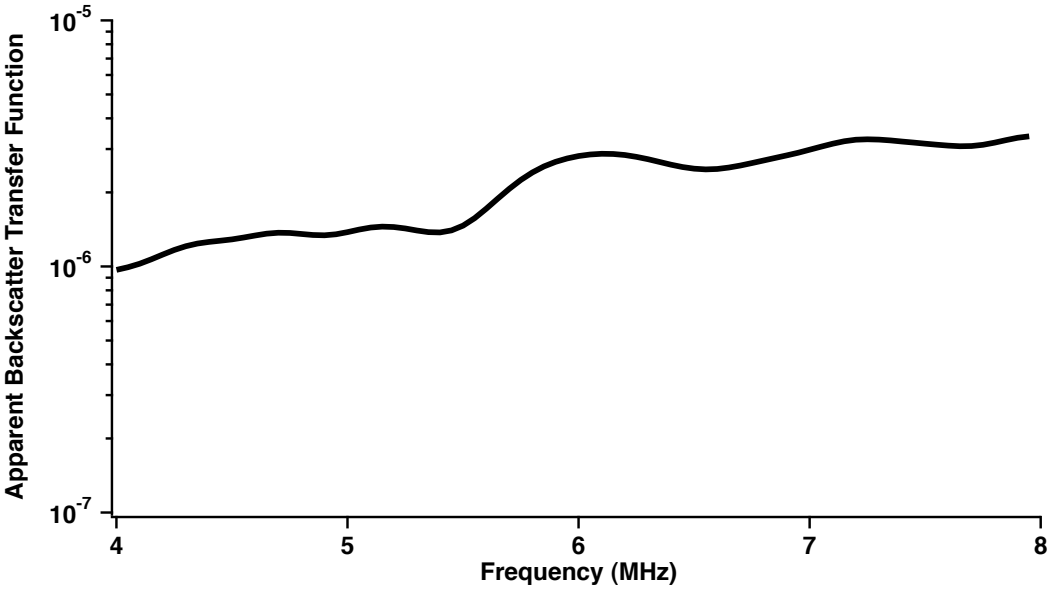

FIGURE 8.12: An example linear apparent backscatter transfer function of a 20% cornstarch in 51.5% cesium chloride solution is plotted as a function of frequency.

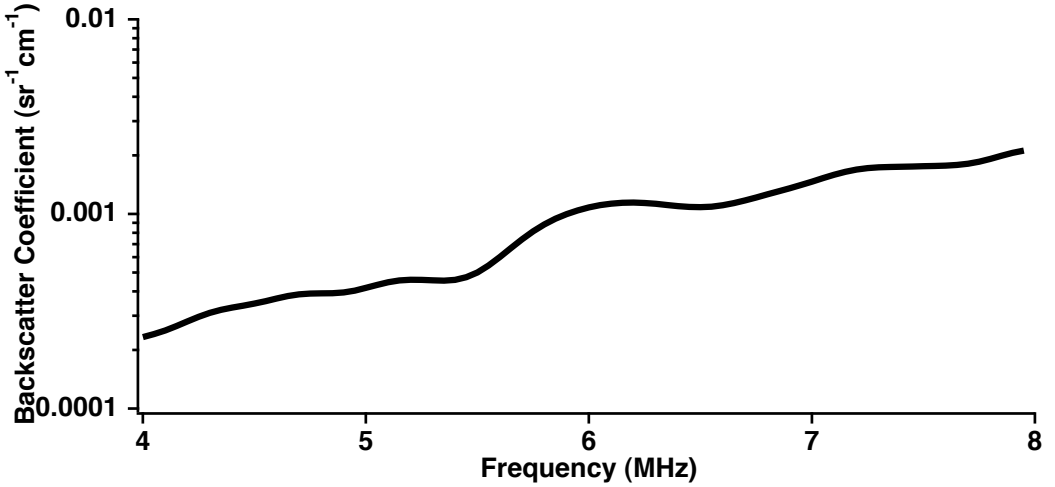

FIGURE 8.13: An example backscatter coefficient of a 20% cornstarch in 51.5% cesium chloride and water solution is plotted as a function of frequency.

8.5 Backscatter Measurements

The fully-reduced backscatter coefficient was measured for five 10% cornstarch suspensions in a 51.5% cesium chloride solution, five 20% cornstarch suspensions in a 51.5% cesium chloride solution, five 30% cornstarch suspensions in a 51.5% cesium chloride solution and five 40% cornstarch suspensions in a 51.5% cesium chloride solution.

8.5.1 10% Cornstarch Suspensions

Backscatter measurements were made on five 10% suspensions of cornstarch in a 51.5% cesium chloride solution as described in Section 8.2. The apparent backscatter transfer function for each of the samples is plotted in Figure 8.14. The apparent integrated backscatter for each sample is shown in Table 8.1. The apparent backscatter transfer function for each sample was compensated for attenuation effects, diffraction effects, and reflection and transmission loss in order to arrive at the frequency-dependent backscatter coefficient as described in Section 8.3. The backscatter coefficient as a function of frequency is plotted in Figure 8.15. The backscatter coefficient at 5 MHz and the frequency exponent of the backscatter coefficient are shown in Table 8.1.

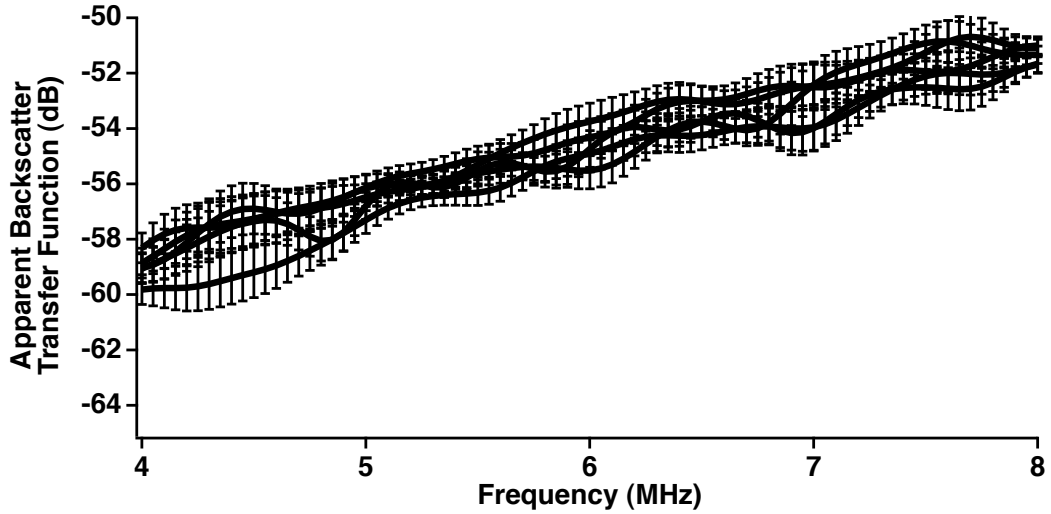

FIGURE 8.14: The apparent backscatter transfer function is plotted for each sample of 10% cornstarch in a density-matched cesium chloride and water solution. The standard deviation of each measurement is also plotted for each sample.

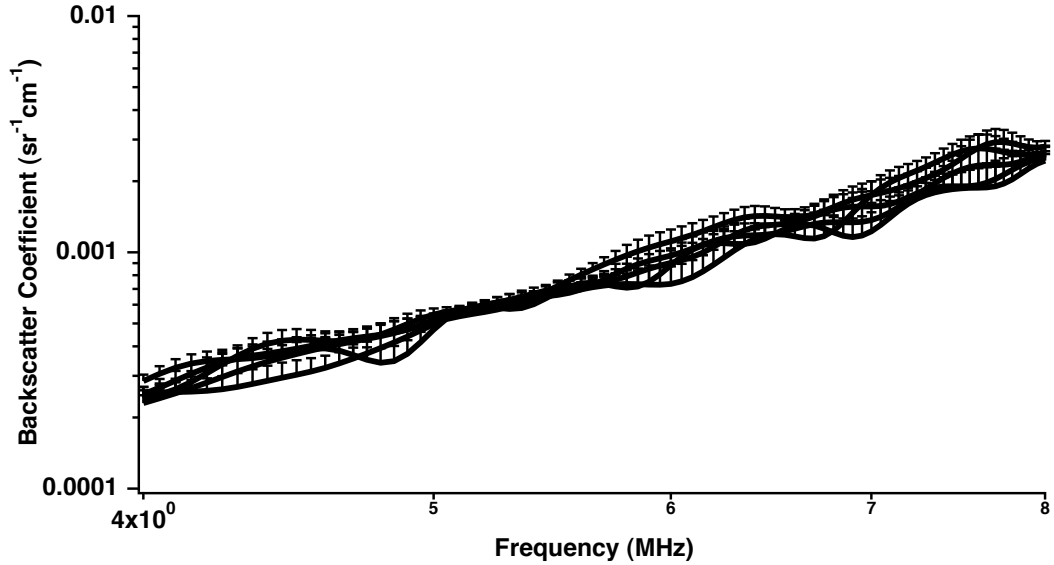

FIGURE 8.15: The frequency dependent backscatter coefficient is plotted for each sample of 10% cornstarch in a density-matched cesium chloride and water solution. The standard deviation of the measurements is also plotted for each sample.

Concentration	Apparent Integrated Backscatter (dB)	Backscatter Coefficient at 5 MHz ($sr^{-1}cm^{-1}$)	Frequency Exponent (f^n)
10% Cornstarch #1	-54.8	$4.97 * 10^{-4}$	3.5
10% Cornstarch #2	-53.7	$5.46 * 10^{-4}$	3.6
10% Cornstarch #3	-53.8	$5.18 * 10^{-4}$	3.3
10% Cornstarch #4	-54.5	$4.71 * 10^{-4}$	3.1
10% Cornstarch #5	-54.1	$5.05 * 10^{-4}$	3.5
Average	-54.2 ± 0.5	$5.07 * 10^{-4} \pm 2.8 * 10^{-5}$	3.4 ± 0.2

TABLE 8.1: The apparent integrated backscatter, backscatter coefficient at 5 MHz, and frequency exponent for each 10% cornstarch suspension is given.

8.5.2 20% Cornstarch Suspensions

Backscatter measurements were made on five 20% suspensions of cornstarch in a 51.5% cesium chloride and water solution as described in Section 8.2. The apparent backscatter transfer function for each of the samples is plotted in Figure 8.16. The apparent integrated backscatter for each sample is shown in Table 8.2. The backscatter coefficient was determined from the apparent backscatter transfer function for each sample by compensating for the effects of attenuation, diffraction, and reflection and transmission loss. The backscatter coefficient as a function of frequency is plotted in Figure 8.17, and the backscatter coefficient at 5 MHz and the frequency exponent of the backscatter coefficient are shown in Table 8.2.

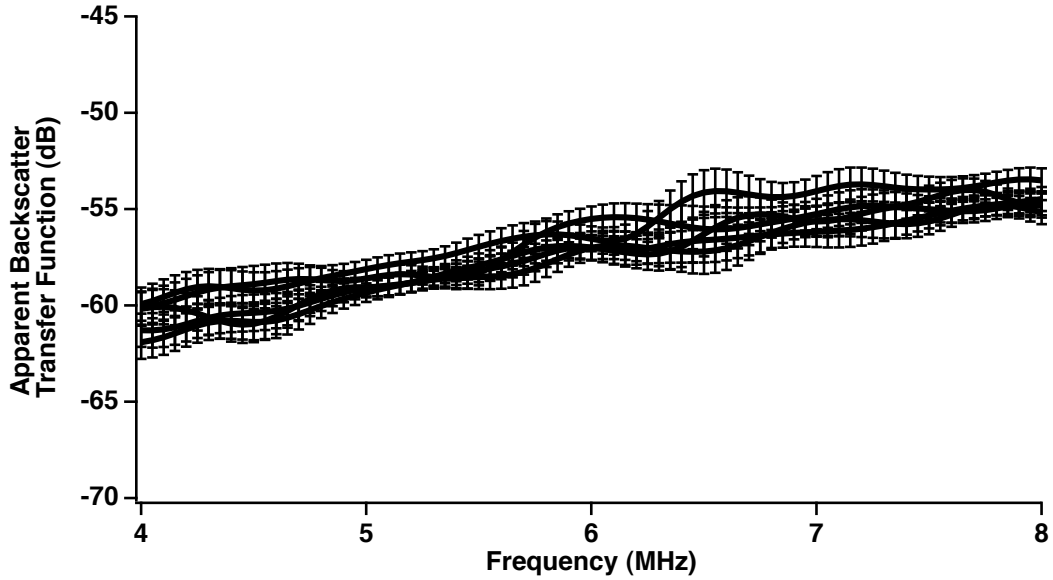

FIGURE 8.16: The apparent backscatter transfer function is plotted for each sample of 20% cornstarch in a density-matched cesium chloride and water solution. The standard deviation of the measurements is also plotted for each sample.

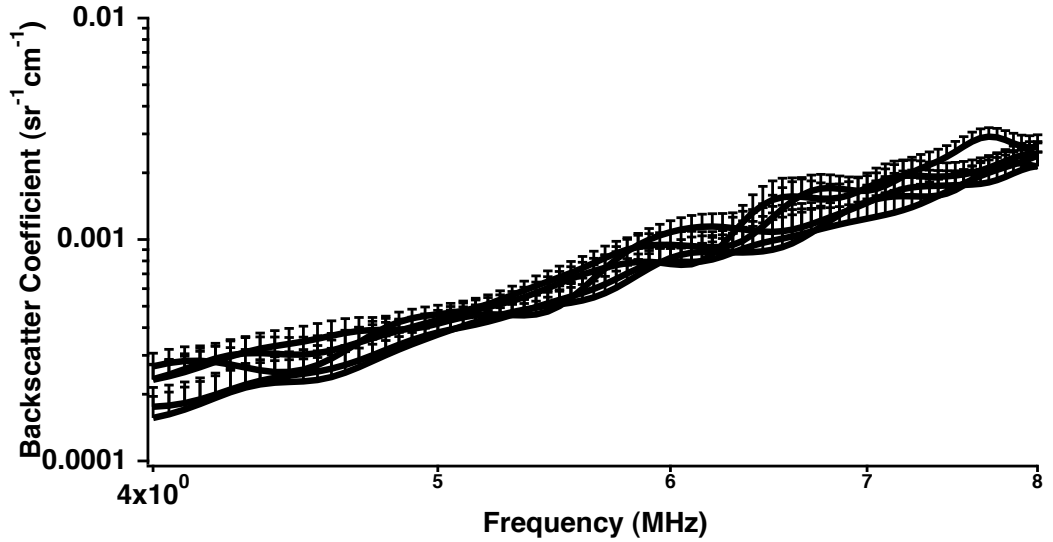

FIGURE 8.17: The frequency dependent backscatter coefficient is plotted for each sample of 20% cornstarch in a density-matched cesium chloride and water solution. The standard deviation of the measurements is also plotted for each sample.

Concentration	Apparent Integrated Backscatter (dB)	Backscatter Coefficient at 5 MHz ($sr^{-1}cm^{-1}$)	Frequency Exponent (f^n)
20% Cornstarch #1	-57.3	$3.72 * 10^{-4}$	3.9
20% Cornstarch #2	-56.8	$4.60 * 10^{-4}$	3.9
20% Cornstarch #3	-57.1	$3.81 * 10^{-4}$	3.7
20% Cornstarch #4	-56.4	$4.17 * 10^{-4}$	3.3
20% Cornstarch #5	-55.8	$4.34 * 10^{-4}$	3.6
Average	-56.7 ± 0.6	$4.13 * 10^{-4} \pm 3.6 * 10^{-5}$	3.7 ± 0.2

TABLE 8.2: The apparent integrated backscatter, backscatter coefficient at 5 MHz, and frequency exponent for each 20% cornstarch suspension is given.

8.5.3 30% Cornstarch Suspensions

Backscatter measurements were made on five 30% suspensions of cornstarch in a 51.5% cesium chloride solution as described in Section 8.2. The apparent backscatter transfer function for each of the samples is plotted in Figure 8.18. The apparent integrated backscatter for each sample is shown in Table 8.3. The apparent backscatter transfer function for each sample was compensated for attenuation effects, diffraction effects, and reflection and transmission loss in order to arrive at the frequency dependent backscatter coefficient as described in Section 8.3. The backscatter coefficient as a function of frequency is plotted in Figure 8.19. The backscatter coefficient at 5 MHz and the frequency exponent of the backscatter coefficient are shown in Table 8.3.

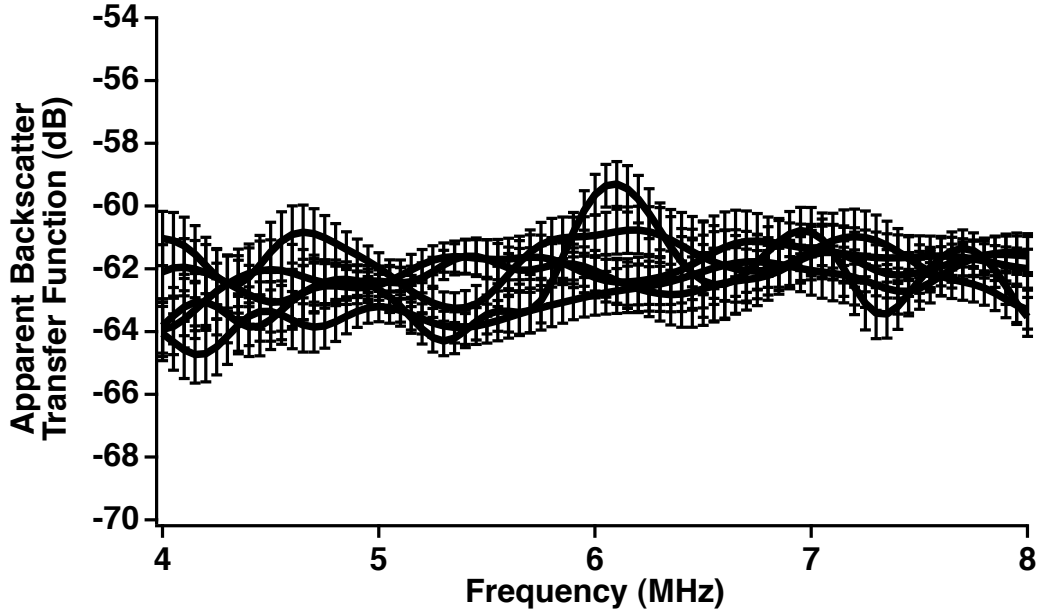

FIGURE 8.18: The apparent backscatter transfer function is plotted for each sample of 30% cornstarch in a density-matched cesium chloride and water solution. The standard deviation of the measurements is also plotted for each sample.

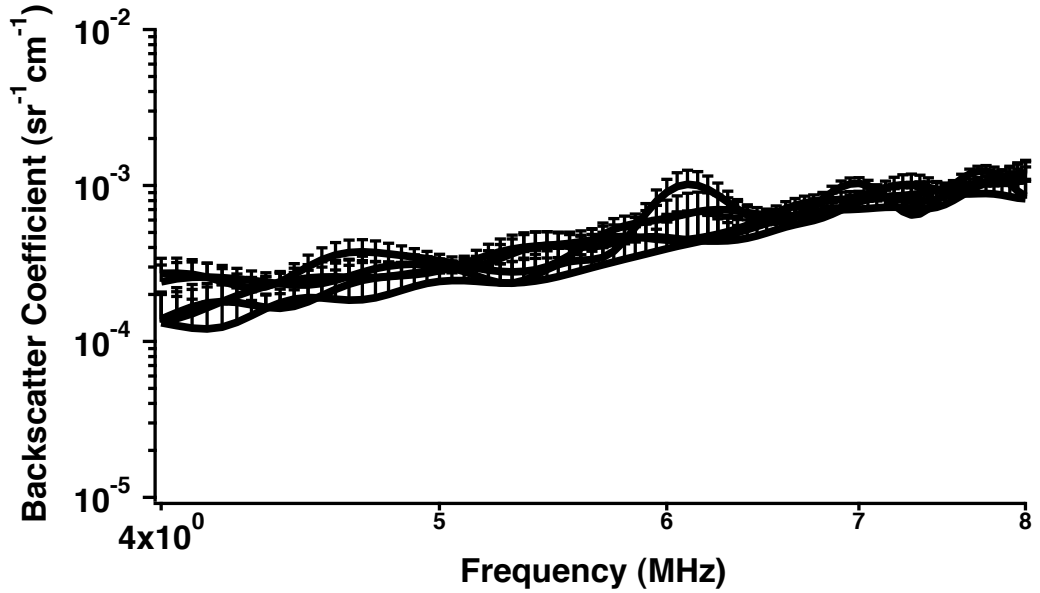

FIGURE 8.19: The frequency dependent backscatter coefficient is plotted for each sample of 30% cornstarch in a density-matched cesium chloride and water solution. The standard deviation of the measurements is also plotted for each sample.

Concentration	Apparent Integrated Backscatter (dB)	Backscatter Coefficient at 5 MHz ($sr^{-1}cm^{-1}$)	Frequency Exponent (f^n)
30% Cornstarch #1	-62.3	$3.06 * 10^{-4}$	2.6
30% Cornstarch #2	-61.9	$3.39 * 10^{-4}$	2.2
30% Cornstarch #3	-62.1	$2.88 * 10^{-4}$	2.7
30% Cornstarch #4	-62.0	$2.84 * 10^{-4}$	3.0
30% Cornstarch #5	-62.7	$2.43 * 10^{-4}$	3.2
Average	-62.2 $\pm$ 0.3	$2.92 * 10^{-4} \pm 3.5 * 10^{-5}$	2.7 $\pm$ 0.4

TABLE 8.3: The apparent integrated backscatter, backscatter coefficient at 5 MHz, and frequency exponent for each 30% cornstarch suspension is given.

8.5.4 40% Cornstarch Suspensions

Backscatter measurements were made on five 40% suspensions of cornstarch in a 51.5% cesium chloride solution as described in Section 8.2. The apparent backscatter transfer function for each of the samples is plotted in Figure 8.20. The apparent backscatter transfer function for each sample was compensated for attenuation effects, diffraction effects, and reflection and transmission loss in order to arrive at the frequency dependent backscatter coefficient. The backscatter coefficient as a function of frequency is plotted in Figure 8.21. The apparent integrated backscatter, the backscatter coefficient at 5 MHz, and the frequency exponent of the backscatter coefficient are displayed in Table 8.4.

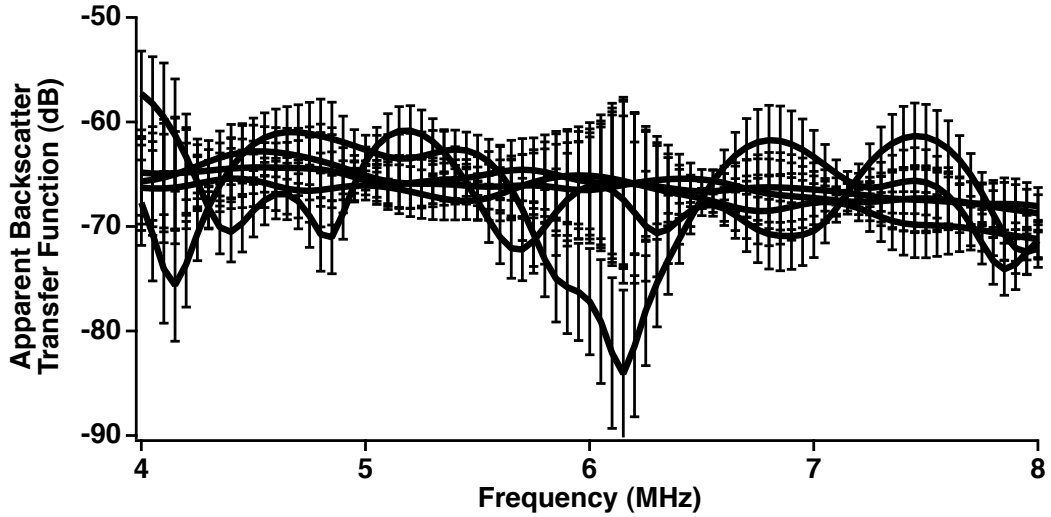

FIGURE 8.20: The apparent backscatter transfer function is plotted for each sample of 40% cornstarch in a density-matched cesium chloride and water solution. The standard deviation of the measurements is also plotted for each sample.

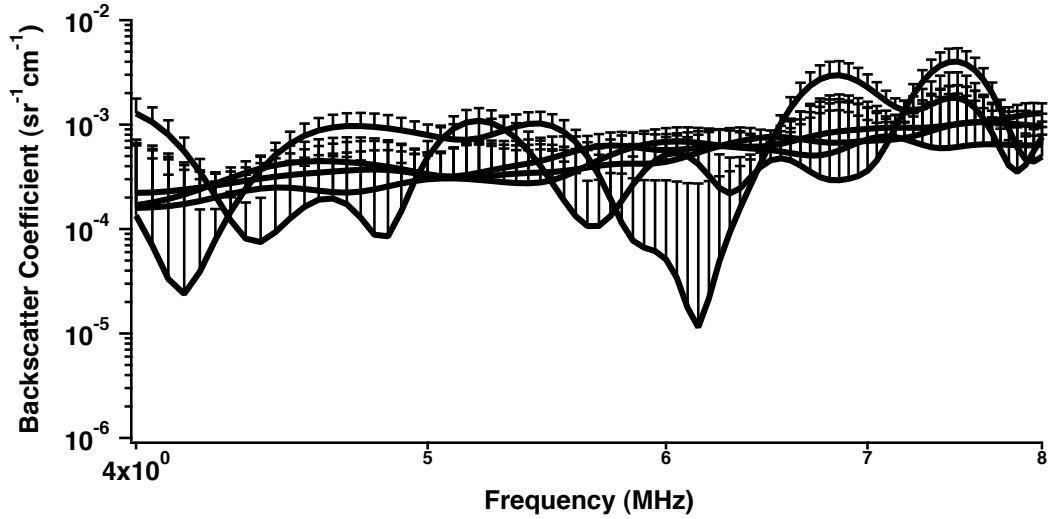

FIGURE 8.21: The frequency dependent backscatter coefficient is plotted for each sample of 40% cornstarch in a density-matched cesium chloride and water solution. The standard deviation of the measurements is also plotted for each sample.

Concentration	Apparent Integrated Backscatter (dB)	Backscatter Coefficient at 5 MHz ($sr^{-1}cm^{-1}$)	Frequency Exponent (f^n)
40% Cornstarch #1	-67.3	$4.83 * 10^{-4}$	2.5
40% Cornstarch #2	-67.5	$4.90 * 10^{-4}$	2.4
40% Cornstarch #3	-67.5	$3.00 * 10^{-4}$	2.2
40% Cornstarch #4	-66.3	$3.36 * 10^{-4}$	2.2
40% Cornstarch #5	-66.2	$3.28 * 10^{-4}$	2.4
Average	-67.0 ± 0.7	$3.87 * 10^{-4} \pm 9.1 * 10^{-5}$	2.3 ± 0.1

TABLE 8.4: The apparent integrated backscatter, backscatter coefficient at 5 MHz, and frequency exponent for each 40% cornstarch suspension is given

8.5.5 Backscatter Coefficient Comparison

The average backscatter coefficient measured for the 10%, 20%, and 30% concentration is plotted in Figure 8.22. As can be seen from the figure, the backscatter coefficient decreases as the concentration of cornstarch increases. This result is reminiscent of the results found for measurements of the backscatter coefficient of red blood cells over a similar range of concentrations (Yuan and Shung, 1988). At these relatively high concentrations of scatterers, the backscatter coefficient is no longer proportional to the scatterer concentration, because the scatterers can no longer be considered randomly distributed (Chen and Zagzebski, 1996).

A theoretical backscatter coefficient can be determined for spherical scatterers whose radius is much smaller than the incident wavelength using Equation 8.10

$$\eta = \frac{W_0(1-W_0)^4}{(1+2W_0)^2}\frac{\sigma_{bs}}{V} \tag{8.10}$$

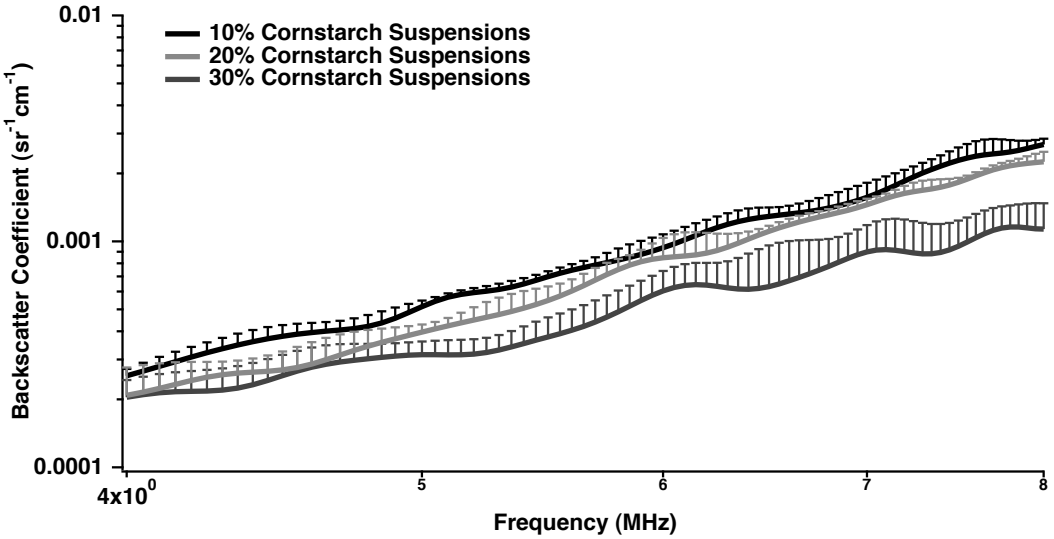

FIGURE 8.22: The average frequency-dependent backscatter coefficient is plotted for the 10%, 20%, and 30% cornstarch suspensions. The standard deviation of the measurements is also plotted for each sample.

where σ_{bs} is the backscattering cross section, W_0 is the volume concentration of the scatterers, and V is the volume of a scatterer (Yuan and Shung, 1988; Lucas and Twersky, 1987; Twersky, 1978). The backscattering cross section at 5 MHz can be found using Faran's theory for spherical scatterers and the properties of a cornstarch particle given by Table 8.5. The volume concentration of the cornstarch was equivalent to the concentrations by mass reported in this chapter, because the suspension was density-matched. The volume of one cornstarch granule was determined by assuming that the cornstarch granules were a sphere with a radius of 7 μm. The theoretical backscatter coefficient at 5 MHz as a function of the volumetric concentration is plotted in Figure 8.23. The theoretical backscatter coefficient at 5 MHz was then compared to the average backscatter coefficient at 5 MHz for the 10% cornstarch suspension, the 20% cornstarch suspension and the 30% cornstarch suspension

Theoretical Parameters	Value of Parameter	Source
Phase Velocity of Host Medium (c_w)	1483 m/s	Experimentally Measured
Phase Velocity of Cornstarch (c_s)	2700 m/s	Inferred from Measurement
Density of Host Medium (ρ_w)	1620 kg/m^3	(Washburn, 1928)
Density of Cornstarch (ρ_s)	1620 kg/m^3	Experimentally Measured
Poisson Ratio of Cornstarch	0.3	(Flores *et al.*, 2007)
Mean Cornstarch Radius	7 μm	Experimentally Measured

TABLE 8.5: The parameters necessary for the theoretical calculation of the backscattering cross section of the cornstarch suspended in density-matched cesium chloride brine.

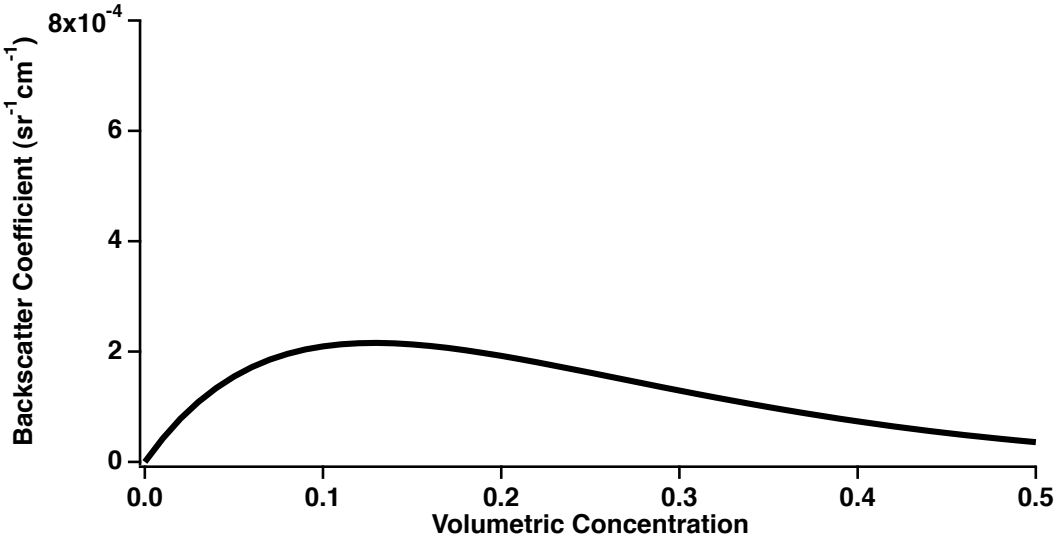

FIGURE 8.23: The theoretical backscatter coefficient at 5 MHz as a function of the volumetric concentration of cornstarch is plotted.

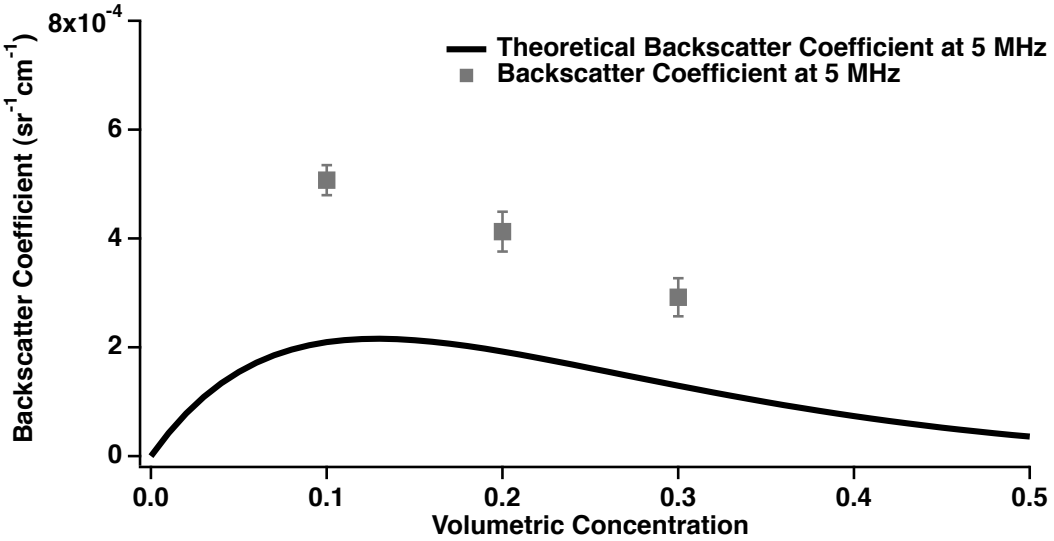

FIGURE 8.24: The theoretical backscatter coefficient at 5 MHz as a function of the volumetric concentration of cornstarch is plotted along with the experimentally measured backscatter coefficient at 5 MHz for three concentrations of cornstarch suspensions.

as shown in Figure 8.24. The trend for both the theoretical and the experimental data agree across this range of concentrations. The lack of detailed quantitative agreement between the theory and experiment is very similar to what was found for red blood cells (Yuan and Shung, 1988). Furthermore, the theory assumes spherical scatterers of a single diameter and thus exact quantitative agreement between the theory and the experiment would be expected.

In order to further confirm the theoretical prediction of the dependence of the backscatter coefficient on concentration of cornstarch, the backscatter coefficient was measured for one sample of a 1% suspension of cornstarch in a 51.5% cesium chloride and water solution, a 2% suspension of cornstarch in a 51.5% cesium chloride and water solution, and a 5% suspension of cornstarch in a 51.5% cesium chloride solution.

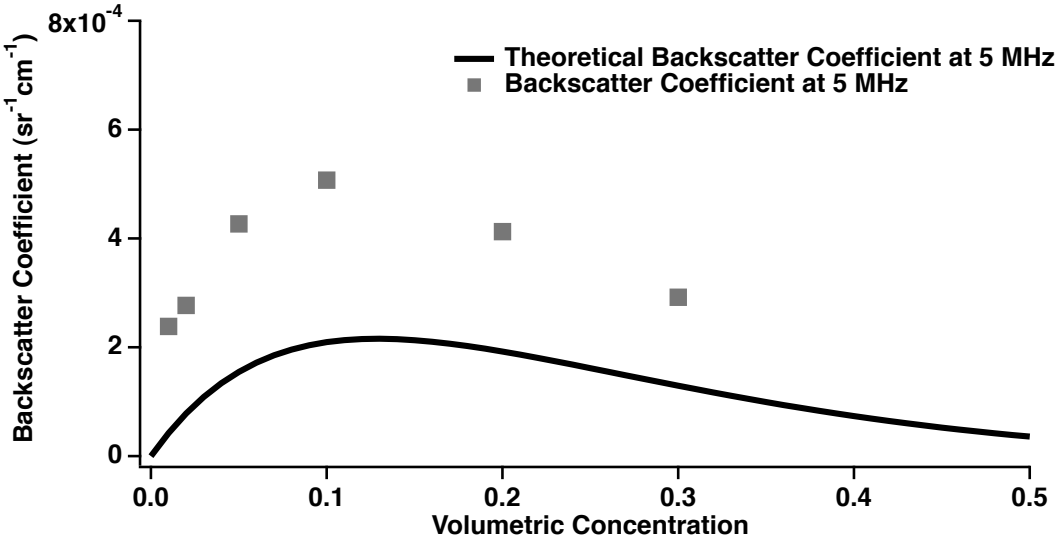

FIGURE 8.25: The theoretical backscatter coefficient at 5 MHz as a function of volumetric concentration of cornstarch plotted along with the experimentally measured backscatter coefficient at 5 MHz for several concentrations of cornstarch suspensions.

The backscatter coefficient at 5 MHz for each of these samples was plotted in Figure 8.25. As can be seen from the figure, the backscatter coefficient at 5 MHz measured for the three samples at lower concentrations seems to suggest that the theory can adequately explain the experimental results.

The average backscatter coefficient at a concentration of 40% cornstarch is plotted as a function of frequency along with the average backscatter coefficients for the 10%, 20%, and 30% cornstarch suspensions in Figure 8.26. As can be seen from the figure, the 40% cornstarch results are substantially more variable and do not follow the trend seen for the other concentrations of cornstarch. The backscatter results at this concentration are still reasonable, but the difficulty of maintaining a homogeneous sample at a concentration of 40% cornstarch increases the uncertainty in the measurements. Thus, it is not surprising that the results at 40% do not follow

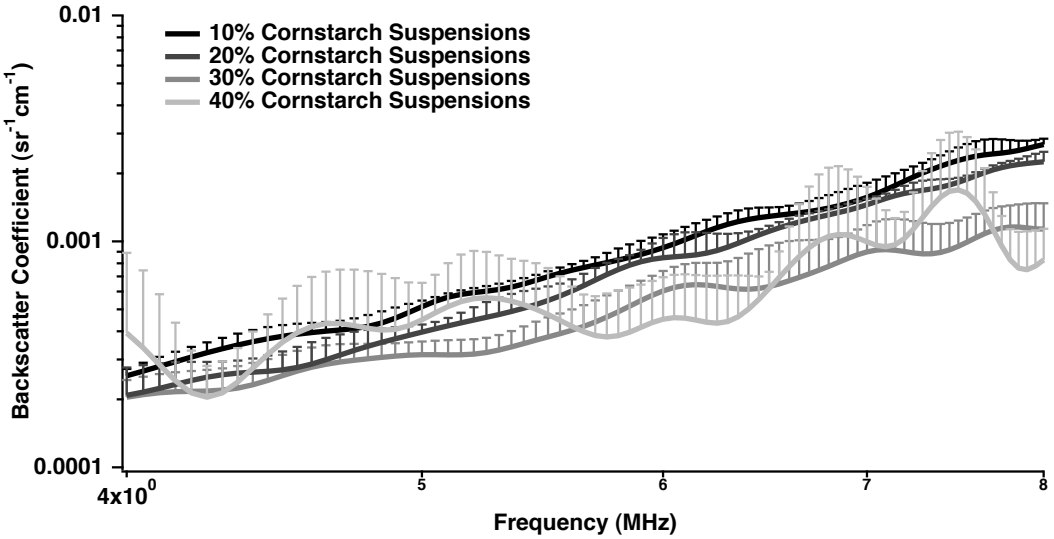

FIGURE 8.26: The average frequency-dependent backscatter coefficient is plotted for the 10%, 20%, 30% and 40%cornstarch suspensions. The standard deviation of the measurements is also plotted for each sample.

the trend found at the lower concentrations.

8.6 Conclusion

This chapter described the experimental measurement method and the analysis method necessary to determine the fully-reduced, frequency-dependent backscatter coefficient. The measurements of the frequency-dependent backscatter coefficient for each concentration of cornstarch suspension studied were presented. The experimental results were explained in terms of a theory used to model the backscatter coefficient of densely packed spherical particles.

Bibliography

Chen, J. and Zagzebski, J. (**1996**). "Frequency dependence of backscatter coefficient versus scatterer volume fraction", IEEE Trans UFFC **43**, 345–353.

Chen, X., Phillips, D., Schwarz, K., Mottley, J., and Parker, K. (**1997**). "The measurement of backscatter coefficient from a broadband pulse-echo system: a new formulation", IEEE Trans UFFC **44**, 515–525.

Flores, A., Bayer, R., Krawietz, K., and Calleja, F. B. (**2007**). "Elastoplastic properties of starch-based materials as revealed by microindentation measurements", Journal of Macromolecular Science, Part B: Physics **39**, 749–759.

Hoffman, J. (**2010**). "Ultrasonic characterization of human coronary arteries and atherosclerotic plaques", Ph.D. thesis, Washington University in St. Louis.

Lucas, R. and Twersky, V. (**1987**). "Inversion of ultrasonic scattering data for red blood cell suspensions under different flow conditions", Journal of the Acoustical Society of America **82**, 794.

O'Donnell, M. and Miller, J. (**1981**). "Quantitative broadband ultrasonic backscatter: an approach to nondestructive evaluation in acoustically inhomogeneous materials", Journal of Applied Physics **52**, 1056–1065.

Sigelmann, R. and Reid, J. (**1972**). "Analysis and measurement of ultrasound backscattering from an ensemble of scatterers excited by sine-wave bursts", Journal of the Acoustical Society of America 1351–1355.

Trousil, R. (**2002**). "Ultrasonic propagation in inhomogeneous media: toward quantitative ultrasonic imaging", Ph.D. thesis, Washington University in St. Louis.

Twersky, V. (**1978**). "Acoustic bulk parameters in distributions of pair-correlated scatterers", Journal of the Acoustical Society of America **64**, 1710.

Washburn, E. (**1928**). *International Critical Tables Vol. 3* (McGraw-Hill).

Yang, M., Krueger, T., Holland, M., and Miller, J. (**2007**). "Anisotropy of the backscatter coefficient of formalin-fixed ovine myocardium", Journal of the Acoustical Society of America **122**, 581–586.

Yuan, Y. and Shung, K. (**1988**). "Ultrasonic backscatter from flowing whole blood. i: Dependence on shear rate and hematocrit", Journal of the Acoustical Society of America **84**, 52–58.

Chapter 9

Summary and Concluding Remarks

This dissertation described the characterization of a suspension capable of discontinuous shear thickening. An aqueous suspension of cornstarch is the classic exemplar of such physical systems. The physics underlying the behavior of such shear thickening suspensions is incompletely understood. Characterization of these suspensions with ultrasound may provide valuable clues into the underlying mechanisms that result in shear thickening behavior. The goal of this thesis was to characterize the acoustic properties of suspensions of cornstarch.

A review of the literature indicated that only limited information concerning the ultrasonic characteristics of suspensions and slurries of starches had been reported and almost none outside of that discussing the monitoring of gelatinization.

Preliminary experiments determined the physical properties of the cornstarch itself, such as its particle size and density, and the reproducibility of the suspension-

making process was examined. Quantitative rheological measurements were made on suspensions of cornstarch in oil; qualitative measurements made on suspensions of cornstarch in water were found to be consistent with literature reports.

The specific experimental techniques and methods of analysis for each type of measurement were individually discussed, developed, and validated. Ultrasonic measurement of the group velocity, the frequency-dependent attenuation properties, the frequency-dependent phase velocity, and the frequency-dependent backscatter properties of the suspensions of cornstarch were reported. Counterintuitive results including negative dispersion and a decrease in the measured backscatter coefficient with increasing particle concentration were understood in terms of widely accepted physical models including internal relaxation processes inferred from dielectric spectroscopy.

In sum, these studies advance the understanding of the physics of cornstarch suspensions and lay the groundwork for future studies probing the physics of the shear thickening.